Size Effect in Tensile Fracture of Concrete and Rock

PROEFSCHRIFT

ter verkrijging van de graad van doctor
aan de Technische Universiteit Delft,
op gezag van de Rector Magnificus prof.ir. K.F. Wakker,
in het openbaar te verdedigen ten overstaan van een commissie,
door het College voor Promoties aangewezen,
op maandag 31 januari 2000 te 16:00 uur

door

Marcel René Antoine VAN VLIET

civiel ingenieur
geboren te Maastricht

Dit proefschrift is goedgekeurd door de promotor:

Prof.dr.ir. J.G.M. van Mier

Samenstelling promotiecommissie:

Rector Magnificus	voorzitter
Prof.dr.ir. J.G.M. van Mier	Technische Universiteit Delft, promotor
Prof.dr. J.M.J.M. Bijen	Technische Universiteit Delft
Prof.dr.ir. R. de Borst	Technische Universiteit Delft
Dr.ir. D.A. Hordijk	TNO Bouw
Prof.dr. B.L. Karihaloo	University of Wales, Cardiff
Prof.ir. A.C.W.M. Vrouwenvelder	Technische Universiteit Delft
Prof.dr.ir. J.C. Walraven	Technische Universiteit Delft

ISBN 90-407-1994-2

Copyright © 2000 by M.R.A. van Vliet

All rights reserved. No part of the material protected by this copyright notice may be reproduced or utilized in any form or by any means, electronic or mechanical, including photocopying, recording or by any information storage and retrieval system, without written permission from the publisher.

Published and distributed by Delft University Press, Delft, the Netherlands.

Stellingen behorend bij het proefschrift

Size Effect in Tensile Fracture of Concrete and Rock

door M.R.A.van Vliet

1. Bij onderzoek naar de schaalafhankelijkheid van de sterkte volstaat het niet om de relatie tussen de sterkte en de proefstukafmeting te bekijken. Alleen een beschouwing waarin zowel de materiaalcompositie en de proefstukgeometrie als de eventuele aanwezigheid van spannings- en/of vervormingsgradiënten aan bod komen, kan leiden tot een verklaring van het waargenomen schaaleffect.

2. Indien de verhouding tussen de maximale korreldiameter en de kleinste proefstukafmeting te klein gekozen wordt, dan leidt dit tot een grote spreiding in de proefresultaten. Deze observatie impliceert dat discussies over een sterkteasymptoot voor zeer kleine proefstukafmetingen geen praktische betekenis hebben.

3. Eénassige trek is buiging.

4. Modellen met experimenteel meetbare parameters zullen de kloof tussen theorie en experiment verkleinen.

5. Anonieme publikatie van onderzoeksresultaten zou de wetenschap ten goede komen.

6. De houding van de wetenschappelijke wereld ten opzichte van jonge onderzoekers is veelal niet bevorderlijk voor hun behoud voor de wetenschap.

7. Bij modelvorming zijn complexiteit en schijnnauwkeurigheid nauw met elkaar verbonden.

8. 

9. Het bedrijven van wetenschap heeft als nevenwerking dat men verleert om niet-ingewikkelde dingen eenvoudig te beschrijven.

10. Het verplicht doorlopen van een typecursus zou een waardevolle aanvulling zijn voor het opleidingsplan van een AIO.

11. Vrijwilligers zetten vaak veel energie in voor niks.

12. Harddisks, woonruimte en tijd hebben gemeenschappelijk dat de efficiëntie tijdens het gebruik daalt bij een toename van de capaciteit.

13. Hoe hoger de opleiding, des te breder de basis.

14. Tot het moment waarop je doet waar je in gelooft, kun je niet weten of je het gelooft of niet.
(Leo Tolstoy)

15. Alle moeite die gedaan wordt om het autorijden onaantrekkelijk te maken, suggereert dat het aantrekkelijker maken van het openbaar vervoer reeds opgegeven is.

16. In tegenstelling tot wat stellingen moeten doen vermoeden, is de algemene ontwikkeling van onderzoekers vaak beperkt.

"Stellingen"[1] attached to the thesis

Size Effect in Tensile Fracture of Concrete and Rock

by M.R.A.van Vliet

1. When investigating size effect on strength, looking at the relation between strength and specimen size is not enough. Only by considering the material composition and the geometry of the specimen, as well as the possible presence of stress and/or strain gradients, can observed size effect be explained.

2. If the ratio between the maximum grain diameter and the geometry of the specimen is chosen too small, a large scatter will occur in the experimental results. This observation implies that discussions about a strength asymptote for very small specimen sizes are not of any practical interest.

3. Uniaxial tension is bending.

4. Models with experimentally measurable parameters would reduce the gap between theory and experiment.

5. The anonymous publication of research results would be beneficial for science.

6. The attitude of the scientific world towards young researchers does not stimulate their retention in science.

7. When modelling, complexity and accuracy can easily be confused.

8. 

9. Assimilating into the scientific community has as side effect that one forgets how to write non-complicated things in an easy way.

10. A compulsory typing course would be a valuable supplement to the training of a PhD student.

11. Volunteers spend a lot of energy for no return.

12. Hard disks, living space and time have in common that efficiency during usage decreases with an increasing capacity.

13. The higher the education, the broader the base.

14. Until you do what you believe in, you don't know whether you believe it or not.
(Leo Tolstoy)

15. The effort to make driving a car unattractive suggests that making public transport more attractive has already been given up.

16. Contrary to what "stellingen"[1] must make believe, the broader interests of researchers are often limited.

---

[1] The statements accompanying a PhD thesis

Acknowledgements

This thesis reports on a research project carried out at the Stevin Laboratory of Delft University of Technology. The financial support of the Dutch Foundation for Technical Sciences (STW) under grant DMB 22.2933 is gratefully acknowledged.

I would like to thank my supervisor, Jan van Mier, for his guidance during the years in the Stevin laboratory. With his continuous availability for (more, or less) technical discussions, as well as a very inspiring attitude towards the rights and duties of a PhD student, he managed to create very pleasant boundary conditions during my research.

Special thanks to my former room mate Adri Vervuurt and former colleague Erik Schlangen. Their lattice knowledge as well as computer tips and tricks I benefitted from until the completion of this thesis.

The size effect experiments which are presented would not have been realized without the expert help of Gerard Timmers. I am grateful for him solving the numerous technical problems we encountered from the beginning until the completion of the experimental program. Furthermore, I would like to thank Allard Elgersma for introducing me in the world of experiments and for the technical assistance he delivered during this project. Thanks to Ger Nagtegaal the computers kept running smoothly. The efforts delivered by the former Measurement and Control group of the Stevin Laboratory are highly appreciated.

Finally I would like to thank the colleagues of the Concrete Structures group for the valuable non-technical diversion, and last but not least, my family and friends for their continuous support and encouragement during the PhD.

Toen hij met zijn kleine-zakenmantred – zip, zip – voorbij wilde lopen hield het jongetje het lucifersdoosje naar hem in de hoogte en rammelde ermee.
– Er zit geld in.
Hij boog zich voorover, speelde verwondering.
– Laat eens zien!
Het jongetje, niet ouder dan vier jaar, schudde zijn hoofd.
– Nee. Als je kijkt zit er géén geld in.
– En als je niet kijkt wèl?
– Ja.
Hij rammelde met het doosje, slim. – Hoor maar. Er zit geld in.

Sybren Polet, Mannekino (1982).

Contents

Symbols and definitions xi

1 Introduction 1
- 1.1 The size effect phenomenon . . . 1
- 1.2 Scope and objectives of current research . . . 2
- 1.3 Outline of the thesis . . . 3

2 State of the art 5

3 Outline of size effect tests 11
- 3.1 Starting points . . . 11
- 3.2 Specimens and materials . . . 13
  - 3.2.1 Material characteristics . . . 13
  - 3.2.2 Specimen shape and size range . . . 18
  - 3.2.3 Manufacturing of specimens . . . 22
- 3.3 Experimental set-ups . . . 27
  - 3.3.1 Testing frames and hinge constructions . . . 27
  - 3.3.2 Loading platens . . . 31
  - 3.3.3 Test control . . . 34
  - 3.3.4 Load eccentricity . . . 36
  - 3.3.5 Deformation measurements . . . 37
- 3.4 Testing procedure . . . 38
  - 3.4.1 Preparation of specimens . . . 38
  - 3.4.2 Size effect tests on concrete and sandstone . . . 39
  - 3.4.3 Impregnation tests . . . 40
- 3.5 Test program . . . 40

4 Verification tests: outline and results 43
- 4.1 Introduction . . . 43
- 4.2 Variation of concrete properties within specimens . . . 43
  - 4.2.1 Problem description . . . 43
  - 4.2.2 Specimens and experimental procedure . . . 44
  - 4.2.3 Test results . . . 45
  - 4.2.4 Conclusions . . . 47
- 4.3 Rotational capacity of hinge constructions . . . 48
  - 4.3.1 Problem description . . . 48

4.3.2 Specimens and testing procedure . . . 49
4.3.3 Test results . . . 50
4.3.4 Conclusions . . . 51
4.4 Effect of test control . . . 51
4.5 Influence of the test set-up . . . 54
4.5.1 Problem description . . . 54
4.5.2 Specimens and testing procedure . . . 55
4.5.3 Test results . . . 56
4.5.4 Conclusions . . . 58

5 Results of size effect tests **59**
5.1 Correction of experimental data . . . 59
5.1.1 Self weight . . . 59
5.1.2 Correction of the force-deformation diagram . . . 59
5.2 Concrete tests (I): specimens stored in laboratory . . . 60
5.2.1 Force-deformation curves . . . 60
5.2.2 Nominal strength . . . 62
5.2.3 Fracture energy . . . 64
5.3 Concrete tests (II): specimens stored in climate room . . . 67
5.4 Felser sandstone tests . . . 72
5.5 Impregnation tests . . . 77

6 Lattice approach to size effect in concrete **83**
6.1 Introduction to lattice modelling . . . 83
6.1.1 The principle of a lattice model . . . 83
6.1.2 Setting up the geometry . . . 85
6.1.3 Material and geometrical input data . . . 86
6.1.4 Failure criterion . . . 91
6.2 Modelling of the size effect experiments . . . 92
6.2.1 Specimens and loading platens . . . 92
6.2.2 Boundary conditions . . . 93
6.2.3 Material and geometrical heterogeneity . . . 95
6.2.4 Overview of input parameters . . . 98
6.3 Regular lattice analyses . . . 99
6.4 Random lattice analyses . . . 102
6.5 Regular lattice versus random lattice . . . 108

7 Interpretation of results: synthesis **111**
7.1 Statistical size effect . . . 111
7.1.1 Application of Weibull theory to experimental results . . . 111
7.1.2 Validity of Weibull theory for present experiments . . . 113
7.2 Effect of nonuniform deformations on the observed size effect . . . 118
7.2.1 Derivation of analytical model for concrete tests . . . 118
7.2.2 Model results . . . 122
7.2.3 Experimental observations . . . 126
7.3 Simulations versus experiments . . . 128

8 Conclusion and future outlook 133

References 137

A Overview results size effect tests 147
A.1 Data of individual tests 147
A.2 Force-deformation curves 149
A.2.1 Concrete tests (I): DRY series 150
A.2.2 Concrete tests (II): WET series 153
A.2.3 Felser sandstone tests 155

B Generation of an aggregate structure 159

C Background of the lattice model 161
C.1 Elastic properties of a heterogeneous regular lattice 161
C.1.1 Lattice model used in the calculations 161
C.1.2 Analytical models 163
C.1.3 Results 166
C.2 Fracture simulations with a regular lattice 168
C.2.1 General aspects of a fracture analysis 169
C.2.2 Effect of strength and stiffness variations of the lattice beams 172
C.2.3 Relation between beam length and minimum aggregate size 175
C.2.4 Influence of the aggregate structure on the fracture behaviour 178
C.3 Improving the computational efficiency 182
C.3.1 Problem description 182
C.3.2 Modelling details 183
C.3.3 Results 185

Summary 189

Samenvatting 191

Curriculum vitae 193

Symbols and definitions

Conventions and definitions

Stresses

In the discussion of the size effect experiments on dog-bone shaped specimens, the stress σ has been computed as

$$\sigma = \frac{F}{A} \tag{1}$$

where

$$A = 0.6Dt \tag{2}$$

In Eq. (1) F is the (measured) force and A the smallest cross-sectional area in the middle of the specimen, which amounts to 60% of the area at the specimen ends. D is the width of the specimen and also represents the characteristic specimen dimension. t is the thickness of the specimen which is kept constant at 100 mm for all specimens. The stress σ is the nominal stress, which means that it is a measure for the force level whereas it does not necessarily represent an actual stress. Following Eq. (1) the nominal strength (or nominal stress at failure) σ_N is defined as

$$\sigma_N = \frac{F_u}{A} \tag{3}$$

where F_u is the ultimate or maximum load that was recorded during the test and A the area of the smallest cross section defined by Eq. (2).

Deformations

During the experiments surface deformations (δ) have been measured with LVDTs and strain gauges over varying measuring lengths L_{meas}. These deformations were the basis for the computation of the strains ε and the crack opening w. The elastic deformation δ_e is defined as

$$\delta_e = \frac{F}{k} \tag{4}$$

where the stiffness k represents the initial slope of the force-deformation curve (see Fig. 1). k is based on a best fit computed with the least squares method, using band widths varying between 20 and 40 data points starting from the origin of the force-deformation curve. Due to the variations in measuring length, type of displacement transducer and specimen composition it was not possible to use a constant band width for all specimens. The most suitable band width for each specimen was determined by a visual check. The plastic deformation δ_p follows from (see also Fig. 1)

$$\begin{aligned} \delta < \delta_u \qquad & \delta_p = \delta - \delta_e \\ \delta \geq \delta_u \qquad & \delta_p = \delta_{p,u} \end{aligned} \tag{5}$$

where δ_u is the total deformation at ultimate load and $\delta_{p,u}$ is the total plastic deformation at ultimate load, both measured over L_{meas}. The crack opening w is defined as

$$\begin{aligned} \delta = \delta_u \qquad & w = 0 \\ \delta > \delta_u \qquad & w = \delta - (\delta_e + \delta_{p,u}) \end{aligned} \tag{6}$$

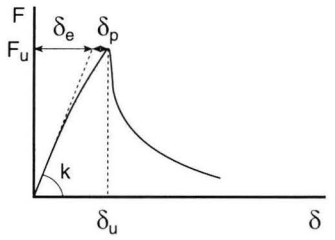


Figure 1 Definition of elastic (δ_e) and plastic (δ_p) deformations until ultimate load.

Fracture energy

According to Hillerborg [38], for uniaxial tensile loading conditions the energy absorbed per unit area in the fictitious crack (the fracture energy G_F, see Fig. 2), can be computed as

$$G_F = \frac{W_F}{A} = \int_0^w \sigma dw \tag{7}$$

where W_F is the work of fracture defined by

$$W_F = \int_0^w F dw \tag{8}$$

The crack width w is defined zero at peak load. The computation of G_F is per definition for complete separation of the crack surfaces, where the crack area A is the *projected* area and not the real area. Although the definition is rather straightforward for prismatic specimens this

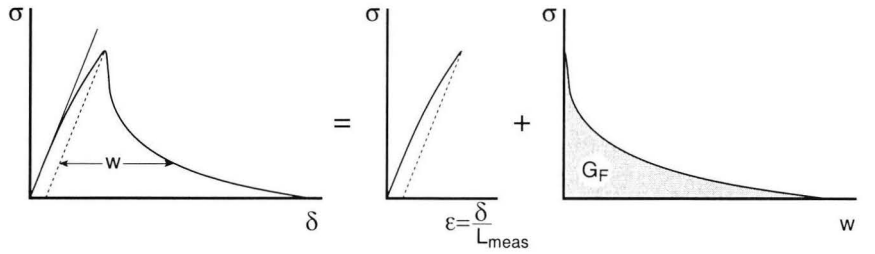


Figure 2 *Subdivision of the total deformation on behalf of the computation of G_F.*

is not the case for the dog-bone shaped specimens which were used in the current research. By introducing a correction factor to accommodate for the fact that the cracks for most specimens did not appear exactly in the middle, the effect of larger values of A on G_F was studied (see [100] for details). The results showed however that this effect was negligible.

The uniaxial tension tests were not continued until complete separation of the two specimen halves for reasons which will be further outlined in Sections 3.4.2 and 5.1.1. Hence, besides G_F also $G_{F_{180}}$ was distinguished, representing the energy which is absorbed during the formation of a crack until a crack opening of $w = 180\ \mu$m . The reason for introducing $G_{F_{180}}$ is that it provides a check for the computed value of G_F. Whereas $G_{F_{180}}$ is purely based on measured deformation values, the crack opening w for zero stress level had to be computed. This was done by linearly extrapolating the stress-crack opening curves until the intersection point with the x-axis, which is illustrated by Fig. 3. The slope of this linear part of the softening curve was computed with the least squares method, similarly to the initial slope k. Now, the number of data points which was used varied between the last 25 or 50, although for the smallest specimens this number could increase up to 100. This is due to the fact that for those specimens the load bearing capacity in the tail of the softening curve was extremely small compared to the capacity of the load cell. Hence, the force measurements fluctuated strongly so that more data were needed to compute the slope. It is mentioned that although linear extrapolation of the softening curve underestimates the computed fracture energy, the method is straightforward. For this reason it has been adopted.

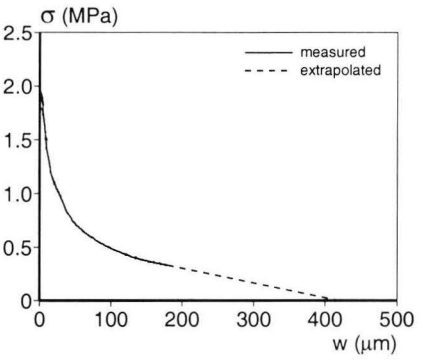


Figure 3 *Linear extrapolation of the tail of the stress-crack opening curve until the intersection point with the horizontal axis.*

List of symbols

a	interval
d	aggregate diameter, beam depth
d_0	critical or transitional beam depth
e	eccentricity
f	strength
f_r	modulus of rupture
h	height of lattice beam
k	stiffness
l	length of lattice beam
l_{ch}	characteristic length
l_f	thickness of cracked boundary layer
m	Weibull modulus
n	number, amount
n_V	number of representative volume elements
p_c	cumulative probability
p_f	probability of failure
r	radius
s	cell size
t	thickness, time
u	displacement
w	crack opening displacement

A	cross-sectional area, sub-cell size
B	width
D	characteristic specimen dimension
E	Young's modulus
F	force, load
G	shear modulus
G_F	fracture energy according to Hillerborg
G_F^*	fracture energy based on the complete area under the $\sigma - \delta$ curve
H	height
K	bulk modulus
K_t	theoretical stress concentration factor for normal stress
L	length, size of lattice mesh
M	bending moment
N	normal force
P_k	relative aggregate volume
V	volume, volume or area fraction
V_r	representative volume
W_F	work of fracture
Z	sectional moment

Greek

α	reduction factor in lattice failure criterion
β	scaling factor in lattice failure criterion
δ	deformation
ε	strain
φ	angle
κ	curvature
ν	Poisson's ratio
σ	stress
σ_0	scale parameter in Weibull function
σ_N	nominal strength

Subscripts

avg	average
ax	axial
b	back
beam	lattice beam property
c	compressive, control
cen	centric
crit	critical
e	elastic
ecc	eccentric
eff	effective
ext	external
f	front
flex	flexural
hom	homogeneous
i	initial, element *i* in a range
lat	lattice
m	measuring, middle
max	maximum
min	minimum
norm	normal
p	plastic
r	reaction
s	scaled, splitting
t	tensile
tot	total
u	ultimate
x, *y*, *z*	directions

Subscripts (continued)

A	aggregate
B	bond
M	matrix

Superscripts

$*$	global (numerical)

Abbreviations

BSE	Back Scatter Electron
CMOD	Crack Mouth Opening Displacement
COD	Crack Opening Displacement
ESEM	Environmental Scanning Electron Microscope
LVDT	Linear Variable Displacement Transducer
RVE	Representative Volume Element
XRD	X-Ray Diffraction
XRF	X-Ray Fluorescence

Chapter 1

Introduction

1.1 The size effect phenomenon

Structural design has evolved from a purely empirical process in the early days, towards an advanced discipline now. Besides experience and well established design rules, sophisticated numerical programs are applied to solve the more complicated problems. Part of the evolution of the design process must be attributed to the application and development of new and in some respects better materials. In parallel, numerical models have to be developed which are capable of simulating the behaviour of these new materials. Before the numerical models can be actually applied however, they have to be validated to determine both their potential and their shortcomings. For this purpose, as well as in situations where models can not be applied, laboratory experiments fulfill a crucial role.

Laboratory experiments are representations of reality, where in the case of structural research full-scale structures or alternatively those parts which are of interest, are subjected to specific loading conditions. The actual size of (parts of) these structures generally exceeds the maximum size of experiments which can still be handled in a laboratory. For this reason laboratory experiments are often scaled versions of the actual structure. The outcome of an experiment can give an indication of, or insight into, the structural behaviour which is to be expected. If the laboratory specimen is smaller than the actual structure, the whole principle is based on the fact that the results obtained in the laboratory should not be influenced by the scale difference. Unfortunately, the latter demand is often not fulfilled. Experience has shown that experimental findings generally vary with the size of the specimen, a phenomenon known as scale or size effect. In general terms, scale or size effect is the variation of material parameters with the material volume. This common definition has also been followed here, although it should be mentioned that an alternative definition can be adopted as well. According to that definition *size effects* are strictly related to the representative volume of a material, which means that they vanish once the representative volume has been reached. *Scale effects* on the other hand, are due to the fact that with an increase of the material volume, the number of weak spots which is present will increase as well. Besides size and scale effects, also *shape effects* can be distinguished. There, a variation of the results must be attributed to the shape of the material volume. This latter effect however, is not investigated here.

Insight into the physical mechanisms underlying size effect is essential to extrapolate experimental findings at laboratory scale to results which can be used in field situations.

Alternatively, when the experiments are used to verify numerical results, these latter should exhibit size effect as well in order to be useful for full scale predictions.

1.2 Scope and objectives of current research

During more than two decades now, the size effect phenomenon has been studied intensively by numerous researchers. Various types of size effect experiments were conducted, and the results were used to verify models that mostly deal with size effect on strength. Those models, of which Bažant's Size Effect Law [6] and the Multi Fractal Scaling Law by Carpinteri [17] are known best, are needed to make predictions for the strength of structures with sizes beyond those which can still be tested in the laboratory. Their main deficiency however, is that they do not incorporate physical mechanisms. Instead, the models have to be fitted to experimental data sets, which mostly results in non-constant values of material parameters for different types of tests. In the author's opinion, this is not the right approach to study, and finally predict, size effect. Instead of functions which have to be fitted on existing data, models should be used in which the physical mechanisms which take place in a material, and eventually can lead to failure of that material, have been incorporated correctly. These models would enable to obtain the correct behaviour of a material volume, irrespective of the type of loading and/or boundary condition which is applied. The basis for such models is a thorough knowledge of the behaviour of the material under consideration.

To study the behaviour of a composite material like concrete a so-called three-level approach can be followed [88]. Inherent to this approach is the definition of three levels of observation: the micro-, meso- and macro-level. With the help of the processes which take place at a certain level, observations can be explained which are made one level higher. To set the scene, the micro-level, which incorporates sizes up to approximately 10^{-4} meter, describes the material at the level of the cement particles. At the meso-level, which reaches sizes of 10^{-1} meter, the aggregates and the cement matrix are distinguished. Even larger sizes belong to the macro-level. There, the concrete is considered a continuum in which no individual material components can be distinguished anymore.

When materials are studied by means of experiment, it is important to discern the difficulties which are inherent to obtaining pure material behaviour. In practice it will be unavoidable that for instance the boundary conditions influence processes which take place inside the material. Hence, the experimental result comprises both the material and the structural behaviour. The same holds true for size effect. The size effect which is observed in a series of experiments can be subdivided in material size effect and various structural size effects. Material size effect is caused by the flaws which are present in the material and which can increase in size as well as number with increasing volume of the material. Structural or fracture size effects on the other hand, depend on the type of failure which occurs in the material. Therefore, to arrive at a true understanding of the nature of size effect, the importance of the individual effects has to be studied rather than considering the size effect as a whole.

The prime objective of the present study is to get more insight into the physical mechanisms underlying size effect in quasi-brittle materials like concrete and rock, rather than only considering the global experimental result. In a combined experimental and numerical program it is tried to distinguish between material and structural size effects in a size range as wide as possible. Besides size effect on strength, also size effect on fracture energy will

be considered. To minimize the structural influences on the experimental result, it is preferred to study size effect under uniaxial tension. A further reason for conducting uniaxial tension tests is the prevailing Mode I failure, which is considered the basic failure mode for quasi-brittle materials. In addition, the tensile testing expertise which exists in the Stevin laboratory is an important reason to focus on uniaxial tension. The increasing attention from the field which has recently been paid to the tensile load bearing capacity of concrete [19], stresses the importance of this type of concrete behaviour for the structural design process.

Although the size effect experiments will be designed as careful as possible, concessions to theoretical demands will be unavoidable because of practical feasibility. Eventual concessions will therefore be accompanied by additional experiments to increase the knowledge of specific influences which are known to be introduced. Numerical simulations will be carried out in parallel to the experiments, thus providing the possibility to get more insight into experimental processes. Using a lattice model to schematize the material at the meso-level, the global behaviour of the specimens can be studied at the macro-level, which coincides with the level of observation in the laboratory experiments.

1.3 Outline of the thesis

It has been attempted to built up the thesis chronologically, so that the order in which the subsequent chapters appear reflects the process which has been gone through. Prior to this description, in Chapter 2 a short introduction is given of the main stream of previous studies dealing with size effect, as well as an outline of the two most used size effect models to date.

The next three chapters treat the experimental part of this study. First, in Chapter 3 a detailed description is given of the way in which the size effect experiments have been conducted. Included are discussions on the design of the experiments, the experimental procedure which has been followed and a description of the experimental set-ups. Thereafter, Chapter 4 describes additional series of verification tests which were conducted to answer questions emerging during the course of the research. These questions concerned, among others, possible influences on the experimental result by the test frame and the type of test control which was applied. Also the influence of casting effects as well as the rotational capacity of the applied hinge constructions was studied in more detail. Finally, the results of the size effect experiments are discussed in Chapter 5. Emphasis is thereby put on the size effect on strength and fracture energy which was observed in the uniaxial tension tests on concrete and Felser sandstone specimens.

The discussion of the experiments is followed by the numerical work which has been carried out. Chapter 6 first gives an introduction of the lattice model that was used, then deals with the applied parameter settings as well as the schematization which was adopted to model the laboratory experiments. In the second part of Chapter 6 the numerical size effect results are discussed. Several aspects of the lattice model, which do not specifically deal with size effect but rather illustrate typical model behaviour, can be found in Appendix C.

In Chapter 7 the observations of experiments and numerical simulations are combined. After deriving a simple analytical model, the influence of structural size effects is quantified in addition to material size effects which were found in the experiments. The thesis is concluded by Chapter 8 which lists the main findings of the study and gives directions for future research.

Chapter 2

State of the art

The fact that materials exhibit size effect has been known for a long time. Yet, during the last decades the size effect phenomenon was studied continuously and with increasing intensity. Besides experimental, analytical and more recently numerical investigations, also the study of literature increased which resulted in references up to the work of Leonardo da Vinci and Galileo Galilei. Hence, it would lead too far here to give an elaborate and complete overview of the research on size effect which has been carried out until now. This has already been done by others, resulting in among others a reference list containing up to 377 entries [9] and an extended review of size effect and other related topics [11]. Instead, a short introduction will be given on the mainstream theories of size effect until the moment this thesis was written.

One of the first main theories of size effect which did, and still does, receive a lot of attention is the classical strength theory. This theory, also known as Weibull or weakest link theory, is purely statistical and based on a distribution of flaws in a material [110]. Furthermore, it postulates that a body consisting of this material is as strong as its weakest component. Whenever the strength of the weakest component is exceeded, the complete body fails since stress redistributions are not taken into account. The statistical size effect on strength according to the weakest link theory will be discussed in more detail in Section 7.1. Suffice it to say here that the predicted strength decrease follows a slope of approximately 1:6 in a bi-logarithmic plot of strength versus size.

In 1972, Walsh reported experimental evidence for a size dependence of the nominal strength of notched concrete beams tested in three-point bending [109]. Compared to the modulus of rupture of unnotched reference prisms, the nominal strength of the beams decreased with increasing size of the uncracked depth d (see Fig. 2.1). This decrease however, was only observed for beams with $d > d_0$, where d_0 can be seen as a critical or transitional depth. For sizes smaller than d_0 it was concluded that stress concentration effects were negligible, which was also interpreted as notch insensitivity of small laboratory specimens.

One year later, Leicester [52] proposed to describe the size effect on the nominal strength with the relation

$$\sigma_N = A_1 D^{-s}, \quad s \geq 0 \tag{2.1}$$

where A_1 is a constant and D the characteristic dimension of the structure. The size coefficient s is a measure of the size effect which occurs for a structure of specified shape and

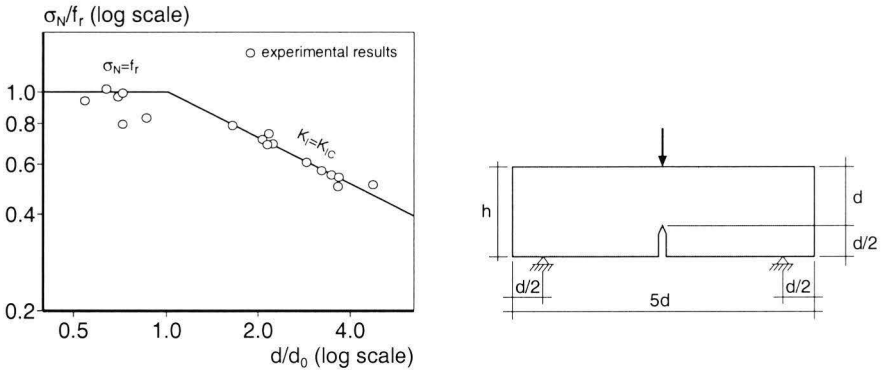


Figure 2.1 *Decrease of the ratio of the nominal strength to the modulus of rupture with the size, as well as the specimen geometry of the tests by Walsh. After [109].*

loading condition, and can be computed from the slope of the $\sigma_N - D$ curve in a log-log plot. As reasons for size effect Leicester identified the material heterogeneity and the presence of notches and other discontinuities in the structure.

Hillerborg et al. [40] showed in 1976 by means of finite element analyses with a cohesive crack model, that unnotched beams under three-point bending exhibit size effect on the modulus of rupture. This result automatically followed from the possibility of reduced stress transfer, after the tensile strength had been exceeded in the most critical point of the beam.

The second major theory of size effect, the so called Size Effect Law (SEL) by Bažant [6], was derived using energy arguments or alternatively dimensional analysis and appeared in 1984. With this Size Effect Law the size effect on geometrically similar, pre-notched structures could be predicted by fitting the expression on a set of experimental size effect data. The SEL, which has as starting points that the material strength for small sizes is bound by the plasticity limit whereas for large sizes the material follows Linear Elastic Fracture Mechanics, describes the transition between these two bounds (see Fig. 2.2a). The remaining assumptions which are made are a constant and thus size independent fracture energy, as well as proportionality between the crack length at ultimate load and the size of the structure. The SEL is written as [11]

$$\sigma_N = \frac{Bf_t}{\sqrt{1+D/D_0}} \tag{2.2}$$

where f_t is a strength parameter like e.g. the tensile strength. The constants B and D_0 must be estimated from a data fit, or follow from the expressions

$$D_0 = c_f \frac{g'(\alpha_0,\theta)}{g(\alpha_0,\theta)} \quad , \quad Bf_t = \sqrt{\frac{EG_F}{c_f g'(\alpha_0,\theta)}} \quad , \quad \theta = 0 \tag{2.3}$$

In Eq. (2.3) c_f stands for the effective length of the fracture process zone at the fracture front in a sufficiently large structure, or, more general, for any material length governing failure.

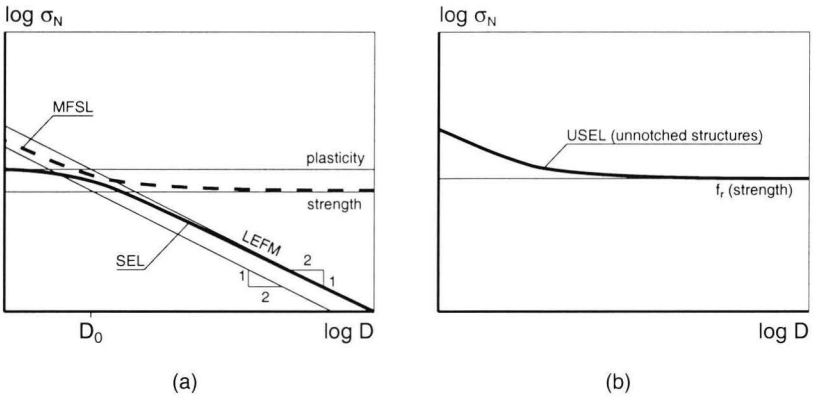


Figure 2.2 *Prediction of size effect by the SEL for notched structures and the MFSL (a), and by the USEL for crack initiation from a smooth surface (b).*

The function $g(\alpha_0,\theta)$ represents the effective dimensionless energy release rate and depends on $\alpha_0 = a_0/D$ and $\theta = c_f/D$, where a_0 is the initial notch length. The value of $\theta = 0$ in Eq. (2.3) follows from the large size asymptotic expansion towards LEFM. g' is the first derivative of the function g with respect to θ ($g' = \partial g(\alpha_0,\theta)/\partial\theta$). The parameter D_0 in Eq. (2.2) represents the intersection point of the horizontal and the descending asymptote, thus indicating a transition in material behaviour (see also Fig. 2.2a). For $D < D_0$ the material tends towards plastic behaviour whereas for $D > D_0$ LEFM governs the failure process. In terms of length or size, D_0 can therefore be seen as a characteristic size for the material under consideration, which for the case of quasi-brittle materials could lead to a dependence on the maximum grain size: $D_0 = \lambda d_{\max}$ [6].

After the first version of the SEL, Bažant and co-workers continued their work, which led to additional formulations for, among others, structures without an initial crack. Eventually, the combined efforts resulted in the formulation of the Universal Size Effect Law (USEL), which is formulated as (see [7, 11])

$$\sigma_N = Bf_t\left[1+\left(\frac{D}{D_0}\right)^r\right]^{-1/2r}\left\{1+s\left[\left(\overline{\eta}+\frac{D}{D_b}\right)\left(1+\frac{D}{D_0}\right)\right]^{-1}\right\}^{1/s} \tag{2.4}$$

where in the first part again the original SEL is found. The part of the expression between braces accounts for the size effect of unnotched structures. In Eq. (2.4) r and s are "parameters not determined by theory for which any value is, in principle, possible" and it is suggested that $r = s = 1$ seems to be most appropriate [11]. $\overline{\eta}$ is an empirical parameter which is defined as $\overline{\eta} = \eta + 1$, where η is a positive empirical constant which for the sake of simplicity may be taken zero [7]. The constant D_b is defined as

$$D_b = \overline{c}_f \frac{\langle -g''(\alpha_0)\rangle}{4g'(\alpha_0)} \quad , \quad \alpha_0 = 0 \quad \wedge \quad g'(\alpha_0) \neq 0 \tag{2.5}$$

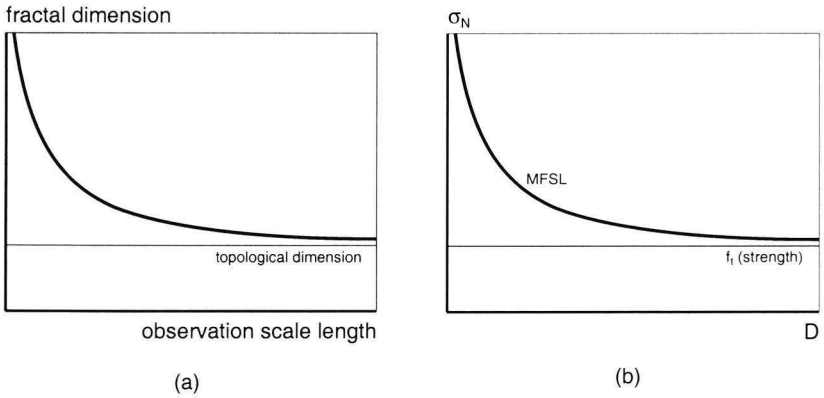


Figure 2.3 *Variation of the fractal dimension with the level of observation (a) and size effect on the nominal strength predicted by the MFSL (b). After [17].*

where $\bar{c}_f = \kappa c_f$ and κ is an empirical constant greater than, but close to one. For crack initiation from a smooth surface, the shape of the Size Effect Law is essentially different as for notched structures, which follows from a comparison between Figs. 2.2a and b. The decreasing LEFM asymptote for large structural sizes has changed into a horizontal asymptote which is defined by a material constant: the modulus of rupture for large sizes (f_r).

The third approach to size effect was presented by Carpinteri in 1992. Contrary to the statistical and deterministic approaches which were discussed before, this explanation for size effect is based on the multifractality of a fracture surface at ultimate load. Thus, the amount of disorder can be expressed by the fractal dimension where the latter parameter increases with increasing disorder of the material. Following this fractal approach, different levels of disorder can be distinguished relative to the size of the structure. For small structural sizes where the influence of the material micro-structure will be strong, maximum disorder will be found. With increasing size however, the degree of disorder decreases until it vanishes. For large sizes the structure can therefore be regarded as homogeneous. The concept of geometrical multifractality can be compared with a continuous variation of the fractal dimension with the scale of observation, as illustrated in Fig. 2.3a. There, it can be seen how the fractal dimension transforms from a high *local* fractal dimension for small scales, towards a constant *global* fractal dimension for large scales. On the basis of the foregoing arguments Carpinteri proposed the Multi Fractal Scaling Law (MFSL) to describe size effect [17, 16]. The MFSL is expressed as

$$\sigma_N = \sqrt{A + \frac{B}{D}} \tag{2.6}$$

where A and B are two constants which have to be determined from a best fit to experimental data using a non-linear least squares algorithm. The prediction of size effect following from the MFSL is opposite to that of the SEL (see Fig. 2.2a), where it could however be argued that the latter should be applied to the case of notched structures only. For small structural sizes the effect of the material micro-structure is predominant, which can also be explained

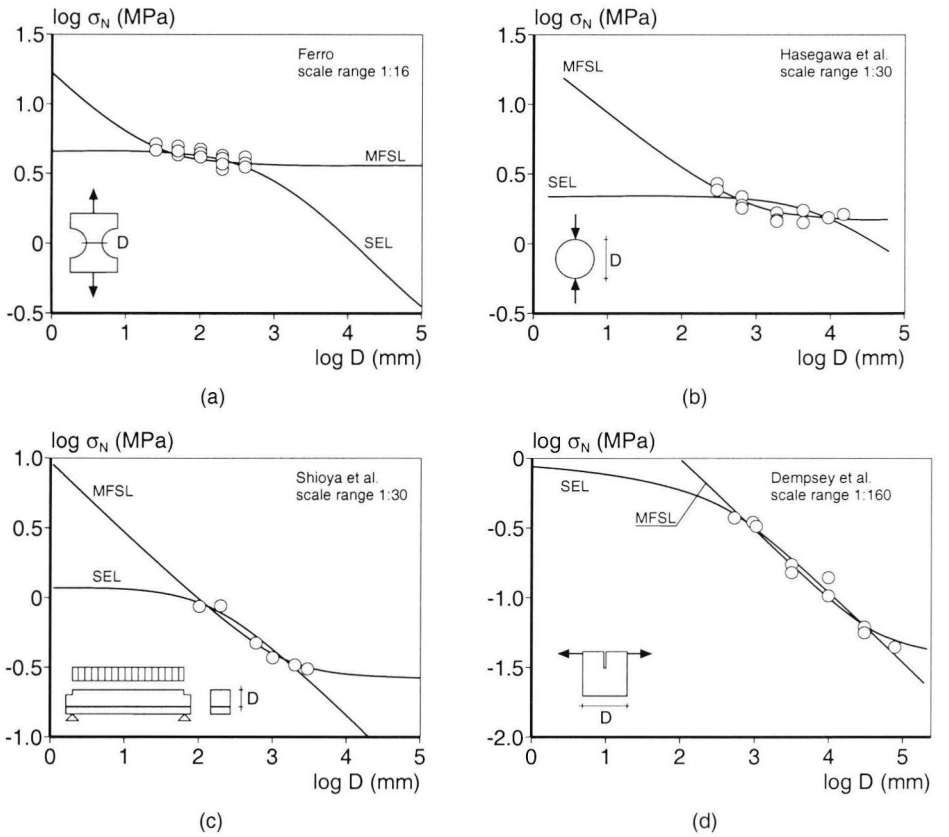


Figure 2.4 *Fits of the Size Effect Law and the Multi Fractal Scaling Law to experimental data of Ferro [26] (a), Hasegawa et al. [28] (b), Shioya et al. [76] (c) and Dempsey et al. [23] (d). Figs. (a), (b) and (c) are after [18], (d) is after [23].*

by a characteristic size of the material flaws becoming comparable to the structural dimensions. Hence, for small sizes the strength tends towards the LEFM strength asymptote with a slope of -1/2. For increasing size on the other hand, the influence of the micro-structure disappears leading to an asymptotic finite strength for large sizes. Similar as for the SEL, an intersection point D_0 for the two asymptotes can be distinguished, which in a bi-logarithmic plot is defined as $D_0 = B/A$ (see Fig. 2.2a).

For an improved understanding of its physical meaning, the MFSL expressed by Eq. (2.6) can be rearranged in the form

$$\sigma_N = f_t \sqrt{1 + \frac{\lambda d_{\max}}{D}} \tag{2.7}$$

where $d_{\max}$ is the maximum grain size and f_t the nominal strength for infinitely large sizes. Now, f_t and λ have to be determined from a fit to experimental data. The material strength

which has been isolated in Eq. (2.7) is governed by the non-dimensional term under the square root, which reflects the influence of the micro-structural disorder (compare Figs. 2.3a and b).

Frequently the MFSL and especially the way in which fractal theory is used, is commented for its lack of physical background. The same comments then easily lead to favoring the SEL over the MFSL since the former is based on mechanical arguments. This opinion is however not shared completely by the author. Models should not solely serve the purpose of perfectly describing reality, but are especially suited to increase our insight into complicated phenomena. Increased insight and understanding can then lead to other models incorporating the major influences which eventually result in a phenomenon which is observed on the macro-scale. It must be realized that the SEL as well as the MFSL do not reveal the sources of a size effect which is observed in experiments. The only information which is obtained is a correlation coefficient, which can be either close to, or far from one. In the process of data fitting both models have the ability to perform well, although the result can also be disappointing depending on the type of test which is considered. Generally, the range of specimen sizes which can be tested is too small to get information about the size effect outside the transition zone between the two asymptotes. To give an impression of fits of the SEL and the MFSL to experimental data, four examples are shown in Fig. 2.4. The test series used are among those with the widest range of sizes to date. For the laboratory experiments this maximum size range is around 1:30, although recently the results of a series of wedge splitting tests were reported in a size range of 1:64 [82]. The largest range of sizes ever tested, 1:160, concerns in-situ fracture tests on first year sea ice at Resolute, North West Territories [1, 59].

To conclude, altogether an impressive amount of size effect studies has been carried out to date, resulting in among others expressions like the Size Effect Law and the Multi Fractal Scaling Law. In order to overcome the restrictions which were mentioned before and which are inherent to the use of this kind of expressions, in this thesis a different approach to study size effect will be followed. Instead of fitting the ultimate stress values to the SEL and the MFSL, which will be possible beyond any doubt, it will be attempted to come to a better understanding of size effect by a thorough analysis of experimental results. In addition to the experiments, analyses with a lattice model will be carried out in order to get more insight into the phenomenon of size effect. In a lattice analysis the material structure is modelled at the meso scale, whereas the behaviour of the structure is studied one level higher, at the macro scale. This makes lattice models especially suited for size effect analyses, since the model parameters are set one level below the level of observation, and do not depend on size. This was first recognized by physicists, e.g. [24, 34, 35], who studied scaling of failure in periodic lattices with breaking thresholds according to various probability distributions. In civil engineering, lattice models were adopted in which a material structure was incorporated [75], whereas examples of this meso-modelling approach to investigate size effect can be found in [14, 48].

Chapter 3

Outline of size effect tests

3.1 Starting points

The design of the size effect tests is based on a number of starting points, which are in summary

- uniaxial tensile loading conditions
- deformation control
- freely rotating boundary conditions
- constant material structure throughout the specimen range

and, rather trivially

- a size range as wide as possible

In this chapter the final design of the size effect tests will be outlined. First however, the choice for, as well as the implications of two of these starting points will be discussed in more detail.

Loading conditions

When performing a literature survey on size effect, a vast number of experimental studies can be found in which specimens of different sizes were tested, see e.g. [18] for an overview. The experimental studies which have been carried out dealt with different types of test. The loading conditions adopted in these tests comprised uniaxial tension, tensile splitting, uniaxial compression, eccentric compression, bending, shear and torsion. As for the specimens, plain concrete and reinforced concrete specimens were studied, both notched and unnotched. The outcome of these previous studies reveals that the magnitude of the size effect is correlated with the type of test. To be more precise: a relation seems to exist between the stress state and the size effect which is observed. Hence, the nature of size effect could be a mixture of both effects originating from the micro-structure of the material and macro-structural effects.

The main aim of this research is to study *material size effects*, as was explained in Chapter 1. Any other effects which could possibly cause a variation of material properties with size should therefore be minimized. In order to minimize the influence of structural stress gradients, thereby offering the best possibility to study a size effect of the material itself, uniaxial tensile loading conditions were preferred in the present research. Another advantage

of uniaxial tensile loading conditions is that Mode I failure takes place, which is considered the most general failure mode for quasi-brittle materials like concrete and sandstone.

Boundary conditions

Another starting point which should be addressed in more detail concerns the type of boundary conditions which is applied in the test. In case of uniaxial tension tests the choice is basically between rotating or fixed boundary conditions, although a third kind of boundary condition has been applied as well, which could be denoted as controlled boundary condition. Rotating boundary conditions imply that the specimen ends can rotate freely during the test. Alternatively, rotation of the specimen ends can be prevented by the bending stiffness of the test set-up in case of fixed boundary conditions. For controlled boundary conditions, three hydraulic actuators are used to ensure that the boundaries of the specimen part which is covered by the control LVDTs are kept parallel during the test. The controlled region can either be the entire specimen [41, 33] or only the middle part of the specimen [26].

The type of boundary conditions which should be applied in a uniaxial tension test is an ongoing matter of discussion to which no definite answer can be given. Each type of boundary condition has its own advantages and disadvantages and, even more important, influence on the outcome of an experiment. Consequently, the experimental result does not reflect the actual material behaviour but a mix of material and structural behaviour. The influence of the boundary conditions can be illustrated by comparing a uniaxial tension test with rotating and fixed boundary conditions respectively (Fig. 3.1). In the case of fixed boundary conditions crack initiation at one side of the specimen results in an eccentricity of the external load, which is followed by a counteracting bending moment of the set-up. Due to this bending moment a second crack initiates at the opposite side of the specimen. This is reflected by a typical plateau in the softening curve (Fig. 3.1). When on the other hand rotating boundary conditions are applied, this counteracting bending moment can not develop and only one crack is found to traverse the specimen. For controlled boundary conditions the structural influences are even stronger than for fixed boundary conditions. By forcing the boundaries of a certain region to remain parallel to each other, a uniform deformation distribution seems to be created. In reality however, only the two boundaries are kept parallel whereas the deformations inside the controlled region change continuously. This results in multiple cracks, which is reflected most clearly in the obtained values for the fracture energy. From a study by Van Mier et al. [91] it followed, that the fracture energy computed for controlled boundary conditions was higher compared to both rotating and fixed boundary conditions. The lowest values for the fracture energy were found for

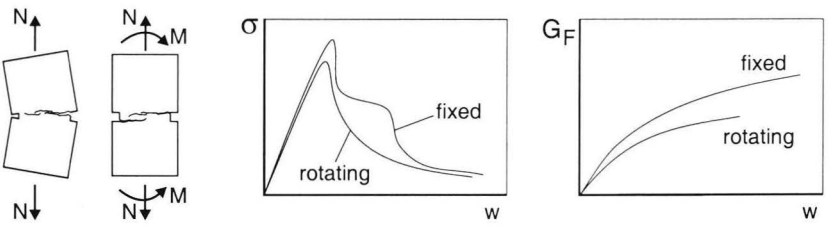


Figure 3.1 Effect of boundary conditions in a uniaxial tension test (after [91]).

rotating boundary conditions, which implies that boundary influences are minimized in this case (see also Fig. 3.1).

Apart from the differences in fracture energy, also the peak load seems to be influenced by the boundary condition which is applied. Uniaxial tension tests on cylinders of which the width as well as the length was varied, tested with fixed and rotating boundary conditions, revealed a tensile strength which was generally lower for freely rotating boundaries [92]. This could be due to the fact that failure can occur at the weakest spot in the specimen, without the boundary conditions influencing this process. It was also observed that the scatter in the strength values was larger for rotating boundary conditions, which again indicates the influence of the applied boundary condition.

To conclude, boundary influences in a uniaxial tension test are minimized when rotating boundary conditions are applied. Despite the fact that the scatter in the test results increases and deformations become highly nonuniform, most of the structural influences caused by the bending stiffness of the test set-up are excluded from the experimental result. This by itself facilitates the reproducibility of the experiments, especially when different set-ups are used like in this research as will be discussed in Section 3.3.1.

3.2 Specimens and materials

Since concrete is a highly heterogeneous material, the micro-structure of concrete and the dimensions of a concrete specimen can not be seen separately. When the specimen dimensions are too small compared to the maximum grain diameter of the concrete mix, the scatter of the test results will be large. This is due to local stress and stiffness fluctuations which can not be averaged out since the total material volume is too small. In this context the term Representative Volume Element (RVE) is often used. For specimen dimensions smaller than the RVE the aforementioned problems arise, which leads to the condition that the smallest specimen should be larger than the RVE. Thus, after choosing the maximum grain diameter of the concrete mix, the smallest specimen dimension is also set. Of course this works the other way around as well. In the present study, neither the material of the specimens, nor the dimensions of the specimens were predefined. The final choices for the maximum grain diameter and the smallest specimen dimension therefore resulted from a coupled process.

With respect to manufacturing the specimens, here the main aim has been to obtain a manufacturing method which would be constant for the entire range of specimens. It may be evident that this point is crucial in a study on size effect, although the practical implications can be considerable. In the following sections the choices for the applied materials, specimens and manufacturing methods will be outlined. If relevant, also the main considerations leading to the final choice are given.

3.2.1 Material characteristics

When studying size effect, various experimental approaches can be followed as was illustrated by Baker [4]. The most common approach, which is followed here as well, is to scale the sizes of geometrically similar specimens while keeping the micro-structure of the material constant. Alternatively, both the size of the specimen and the size of the micro-structure could be scaled simultaneously. An alternative which seems to be identical to the

first approach, is to scale the size of the material micro-structure while keeping the size of the specimens constant. Although this latter alternative *might* seem identical to the first approach which was mentioned, the result can be opposite: the tensile strength reduces while the aggregate size increases [4]. In a relative way this coincides with an increase of the tensile strength with size! The foregoing example is meant to illustrate that care should be taken when discussing size effects. Clear definitions and descriptions of the followed approach are considered to be of vital importance.

Concrete

The concrete mix which was used in this size effect study is, and has been, used frequently in the Stevin laboratory. Experience has shown that the stability as well as the workability of the mix is good. The maximum aggregate size d_{max} is 8 mm, see Table 3.1 for the composition of the mix.

Table 3.1 Concrete mix properties.

Unit content kg/m^3							
8-4*	4-2*	2-1*	1-0.5*	0.5-0.25*	0.25-0.125*	PC	w/c
540	363	272	272	234	127	375	0.5

* aggregate size in mm, PC: Portland Cement (CEM I 42.5 R), w/c: water cement ratio

As will be discussed in Sections 3.2.3 and 3.5 three series of specimens were cast, each series taking from five to ten weeks to be completed. Since the castings were spread over such an extended period of time, it was likely that more than one batch of cement would have to be used. In order to avoid strength differences due to varying quality of different cement batches, all specimens of the first test series were cast using the same batch of cement. That first test series contained specimens of all sizes, and can be considered the main series of experiments to study the size effect of concrete. In order to prevent aging of the cement, the whole batch was stored in an air-tight container. Test series two and three were cast with a second batch of cement.

Closely monitoring the concrete quality of each casting is necessary to ensure that quality differences will not be the source of strength variations observed in the size effect experiments. Therefore, the concrete quality of each casting was determined using a set of twelve 150 mm reference cubes. The second day after casting the cubes were demoulded and placed in a water basin, which was standing in a climate room with a constant air temperature of 20 °C . At an age of 28 days, six cubes were used to determine the uniaxial compression strength, whereas from the remaining six cubes the tensile splitting strength was obtained. Figure 3.2 shows the variation of the average strength values for all batches. The meaning of the gray circles ("batch 2") in Fig. 3.2 will be discussed in detail in Section 3.2.3. For the strength results of the uniaxial tension specimens originating from a specific casting, the reader is referred to Appendix A.

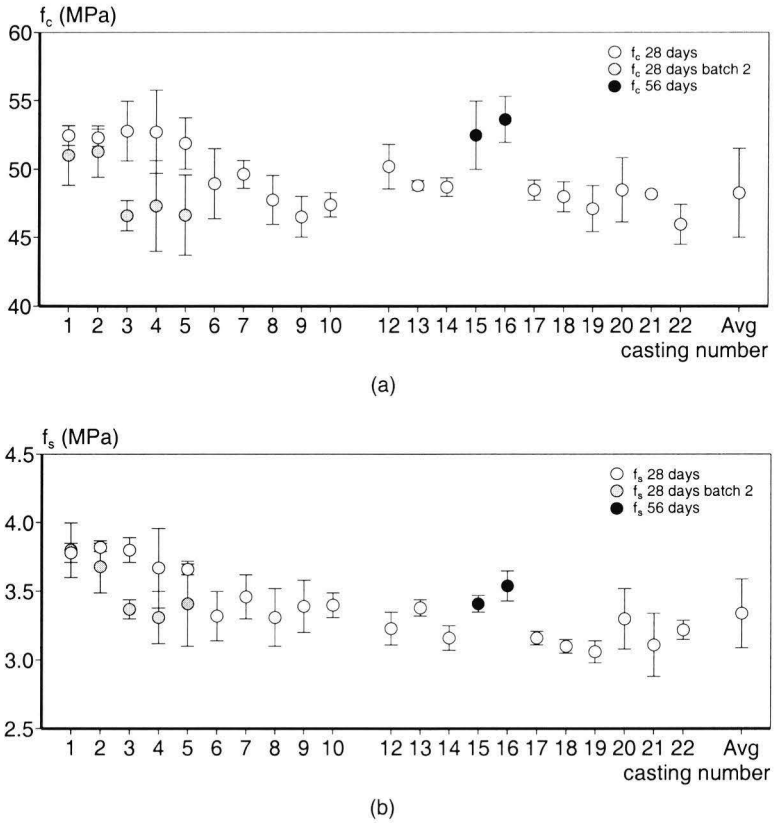


Figure 3.2 *Mean values and standard deviations for 28 day compressive strength f_c (a) and tensile splitting strength f_s (b).*

From Section 3.2.3 will follow that the way in which the reference cubes were cured, as well as their age at testing, was different compared to the uniaxial tension specimens. The strength values of the reference cubes can therefore not be considered representative of the *actual* strength of the uniaxial tension specimens at the moment of testing. Instead, only a mutual comparison of the batch strengths can be made for absolute constant curing conditions. Alternatively, reference cubes could be cured in the same way and tested at the same age as the main specimens, to get an insight into the actual concrete strength at the age of testing. This only makes sense however, when all specimens are stored under controlled climatological conditions. Here, the uniaxial tension specimens were stored under laboratory conditions. Hence, drying out of the cubes would have been different compared to the main specimens, thereby inducing strength differences. Both predicting the strength of the main specimens by the strength of the reference cubes, and mutual comparison of the batch strengths, would therefore have been impossible.

Felser Sandstone

As comparison for the tests on concrete specimens, also one series of size effect tests was carried out on specimens of a natural material. Because of experience with Felser sandstone in the past, this material was used in the present experiments as well. Felser sandstone is a global name for the sandstone originating from a quarry near the city of Kaiserslautern, Germany, and is also referred to as "Eselsfürther" sandstone. Previous experiments have always been carried out on yellow Felser sandstone, whose mechanical properties are extensively described in [36, 106]. In the size effect tests however, red Felser sandstone had to be used since the yellow sandstone could not be delivered on time. The red colour of this type of sandstone is caused by iron oxide which is mostly found inside the quartz grains. After the first verification tests had been conducted, it appeared that although both the yellow and the red Felser sandstone originate from the same quarry, their characteristics are quite different.

The red Felser sandstone exhibits a clear grain structure, with grain sizes generally between 0.15 mm and 0.4 mm and a maximum of 0.7 mm. Figure 3.3a shows the fracture

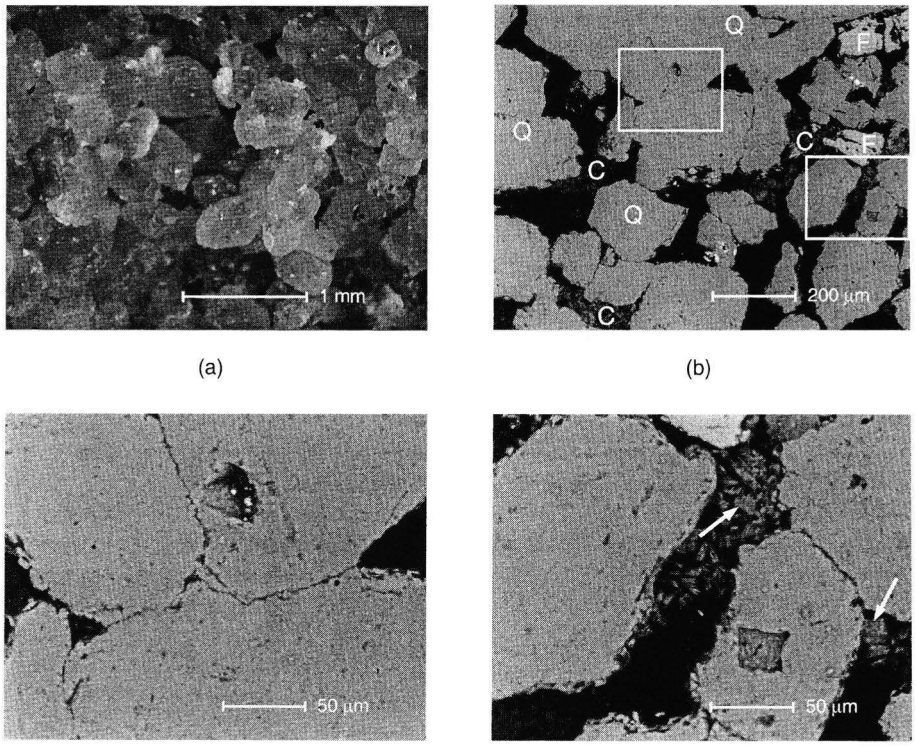


Figure 3.3 *Structure of the red Felser sandstone. Fracture surface (a) and* BSE *micrographs of a polished sandstone surface (b) with close-ups of a grain boundary (c) and voids partly filled with clay minerals (d).*

Table 3.2 *Mineralogical composition and petrophysical properties of red Felser sandstone.*

Grain size (quartz and feldspar)		0.15-0.7 mm	
Rock density (grains and matrix)		2769 ± 22 kg/m^3	
Bulk density		2078 ± 16 kg/m^3	
Porosity		24.9 %	
Grain minerals	Volume %	Matrix minerals	Volume %
Quartz	94		< 1
Feldspar	6		

surface of the red Felser sandstone, giving a good impression of the very open grain skeleton. In Figs. 3.3b,c and d three micrographs are shown of the polished sandstone surface which were made in the ESEM of the micro mechanical laboratory of the faculty of Civil Engineering. The open grain structure again follows from Fig. 3.3b, where sand grains (mostly quartz (Q) and some feldspar (F)), as well as some clay minerals (C) can be seen. Details of Fig. 3.3b are shown in Figs. 3.3c and d. Most of the grains seem to be connected by shared grain faces which probably developed through pressure solution [62] (Fig. 3.3c). Occasionally however, clay minerals are found between the sand grains although they merely seem to fill open spaces between sand grains, rather than serving as a binder. In Table 3.2 the mineralogical composition, as well as some petrophysical properties of the red Felser sandstone are listed. The mineralogical composition has been determined by a combination of a quantitative XRF (X-ray fluorescence) analysis and a qualitative XRD (X-ray diffraction) analysis. The XRF analysis resulted in the percentage by weight of the sandstone minerals, from which the volumetric mineral fractions could be calculated. The porosity of the oven dried red Felser sandstone was determined with a Penta Pycnometer, using Helium to fill the pore volume. The porosity resulting from these measurements is the effective porosity, meaning that only the pore volume which has a direct connection with the open air will be measured. To measure the permeability of the sandstone to gas a Ruska permeameter was used. For the present sandstone however, the material structure appeared to be too open to build up the constant pressure difference which was needed to measure the gas flow through the material.

Although casting and manufacturing effects are absent in the sandstone, and the material has a homogeneous texture, sedimentation layers which cause a strong anisotropy of the mechanical properties are vaguely recognized. The mechanical properties are summarized in Table 3.3. Because of the anisotropic nature of the red Felser sandstone, uniaxial tension tests and uniaxial compression tests were carried out in the direction parallel to the sedimentation layers ($\parallel$) and perpendicular to the sedimentation layers ($\perp$). All tests were conducted on air dried specimens and repeated three times. It must be mentioned however, that for the red Felser sandstone "air dried" appeared to be equivalent to oven dried. After the tests had been finished the remains of the specimens were weighed, and put in an oven for one day

Table 3.3 *Mean values and standard deviations for the mechanical properties of red Felser sandstone. Each value represents the average of three tests.*

	Loading direction	
	$\parallel$ to bedding layers*	$\perp$ to bedding layers
f_t [MPa]	1.22 (0.06)	0.96 (0.03)
f_c [MPa]	40.82 (0.62)	56.69 (2.79)
E_t [GPa]	7.32 (0.34)	11.03 (0.54)
E_c [GPa]	16.97 (0.58)	22.58 (0.18)

*loading direction which was applied in the size effect tests, with the specimen front and back sides parallel to the bedding layers

at 90°C . The specimen weight did not decrease anymore, which indicates that the material structure is open (large pores) and that no water molecules were physically adsorbed. As will be further discussed in Section 3.2.3 it was very beneficial that the sandstone dried so easily. The strength of the material depends strongly on the water content [106], meaning that considerable uncertainties with respect to the strength level will be introduced when the water content is not known.

The uniaxial tension tests were carried out on cylinders with a length of 150 mm and a diameter of 100 mm. At mid length a notch with a depth of 5 mm was cut along the circumference of the specimens. The test procedure was similar to the one to be described in Section 4.3.2. The Young moduli of Table 3.3 are defined by the largest (initial) slope which was found in the uniaxial tension test, and the slope at 50% of the compressive strength in case of the compression tests. Both slopes have been computed using the least squares method and are based on at least ten measuring points. In case of the compression tests these points where equally divided around the 50% strength level, whereas for the uniaxial tension tests the points were taken starting from the origin. During one compression test it was observed that the Young modulus which was found after loading the specimen until 92% of the compressive strength, unloading and again reloading, was only 4% higher compared to the Young modulus of the first loading cycle. This is contrary to yellow Felser sandstone, where an increase of almost 100% was found by Hettema [36]. Whereas in the latter case the strong increase of Young's modulus at reloading is probably caused by compaction, no compaction is found for the red Felser sandstone. This can probably be explained by the small amount of clay minerals which was found between the grains (Table 3.2).

3.2.2 Specimen shape and size range

Designing a specimen shape which is suitable for a new series of tests is less straightforward than it may seem. The shape of the specimen itself can have a profound influence on the eventual test result, even before any effect of the material comes into play. As is the case for many experimental choices, a continuous contemplation has to be made between theoretical demands and practical feasibility. Before looking at the derivation of the specimen shape in

detail, first a remark has to be made on scaling the specimen dimensions. When investigating size effect of material properties, this size effect, if present, follows from variations in the material volume which is considered. Consequently, the dimensions of the specimens in a size effect study should be scaled in 3 dimensions. Because of practical implications however, these 3D size effect studies are rare. Common practice is therefore to scale the specimens in two dimensions while keeping the third dimension constant. This approach has been followed in the present study as well, although it again should be emphasized that this is due to practical restrictions rather than by deliberate choice.

A graphical representation of the design of the specimen shape which was adopted in the present tests, could look like Fig. 3.4. In experiments which are conducted to investigate material properties, the most preferred specimen would be a specimen with periodic boundaries ①. No boundary effects would be present which only blur the actual material effects. In the first step of the design however, the specimen is given finite dimensions ②. These dimensions are characterized by a ratio between the width and the height, and bound by a minimum and a maximum. A prismatic specimen is chosen to minimize shape effects. In the special case of size effect experiments, no preferential area for crack initiation is present so that failure can occur at the weakest spot in the specimen. In this step of the design process the ratio between the width and the height of the specimen is set. The eventual value of this ratio is subject to various considerations. By means of the ratio between the width and the height of the specimen, the distribution of the external forces over the specimen width can be controlled. Furthermore, to ensure that boundary effects are minimized, the area of crack initiation should be away from the boundaries of the specimen. The width of the smallest specimen has a lower bound which is set by the maximum aggregate size d_{max} of the concrete mix to be tested. Hence, a minimum aspect ratio, which is the ratio between the smallest specimen dimension and d_{max}, should be taken of 3 to 5 times d_{max} which is the dimension of the RVE in concrete. The largest specimen on the other hand, determines the maximum ratio between the width and the height. Although a height to width ratio of two will generally ensure the absence of boundary effects in the middle part of the specimen, the amount of concrete needed to cast the largest specimens would be huge. Since it was preferred to make the concrete in the laboratory rather than ordering it at a commercial firm this point was taken into account as well. Altogether, the above considerations resulted in a height to width ratio for the specimens of 1.5 .

To apply the external force on the specimens a connection had to be made between the specimens and the experimental set-up. For this connection steel loading platens were used

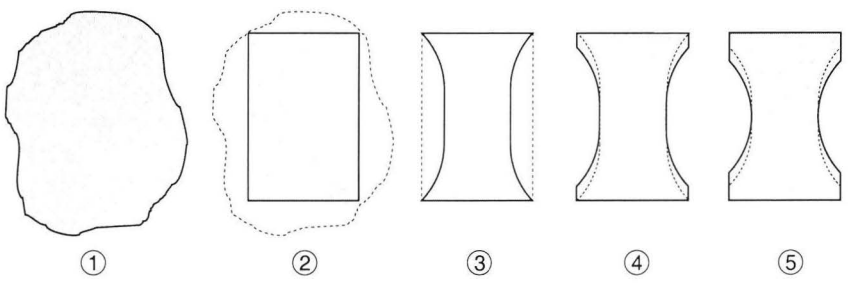


Figure 3.4 Design of the specimen shape for the size effect tests.

which were glued to the specimen ends. Due to differences in Young's moduli and Poisson's ratios of steel and concrete, stress concentrations will develop at the ends of a specimen. In case of a prismatic specimen these stress concentrations often cause failure of the concrete close to the glue layer. Oddly enough this phenomenon is known as glue failure, despite the fact that the concrete fails rather than the glue. When increasing the cross section of the specimen towards the specimen ends, the boundary stresses will be reduced and glue failure can mostly be avoided (Fig. 3.4 ③). To make the specimen ends less sensitive to mechanical damage and to allow for possible solutions in case of glue failure, the shape of the specimen transforms into ④. This shape actually is in good agreement with both practical *and* theoretical demands: the test can be carried out and failure can occur in the prismatic part of the specimen where - in theory - shape effects are absent.

Based on shape ④ in Fig. 3.4 six specimens were cast and tested under conditions comparable to the final test conditions. The final crack patterns for these specimens are shown in Fig. 3.5. Obviously, the chance of the crack occurring in the part of the specimen with the straight edge is small; only two out of six specimens showed this behaviour. Unfortunately this is also what could be expected. Crack initiation in the straight part of the specimen can only be obtained when the stress concentrations at the end of the curved edge are "overruled" by the heterogeneity of the concrete. Since d_{max} of the applied mix was only 8 mm this probability is rather small. When cracking frequently occurs near the curved part of the specimen edge, a dual situation is created: crack initiation at the straight edge *or* at the curved part of the edge. Because of this non-uniqueness interpretation of the results becomes more complicated. Another difficulty which arises for specimens with a straight edge is the huge area in which the deformations have to be controlled for the largest specimens. Since test control would already be a problem by itself (see Section 3.3.3), and the main goal of applying a (partly) straight edge could not be achieved anyway, it was decided to refrain from using this specimen shape.

If the straight part of the specimen edge is simply removed a shape is obtained like ⑤ in Fig. 3.4. The curved edge of the specimen is part of a circle, which facilitates both scaling of the specimens and manufacturing the moulds. The only remaining decision which now has to be addressed is the depth of the circular bays. When performing uniaxial tension tests, it is common practice to reduce the cross section in the middle of the specimen by approximately 20% compared to the cross section at the specimen ends (see e.g. the experimental examples in [91]). The degree in which the cross section is reduced influences the stress concentrations, at least when circular bays are applied like here. This is illustrated in Figs. 3.6a and 3.6b. The figures show the stress contours for the (linear elastic) principal stresses in two dog-bone shaped specimens with cross sections reduced with 20% (Fig. 3.6a) and 40% (Fig. 3.6b)

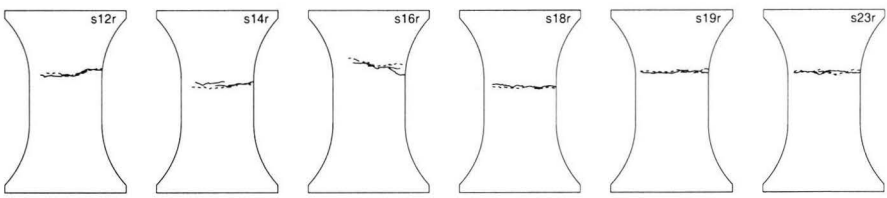
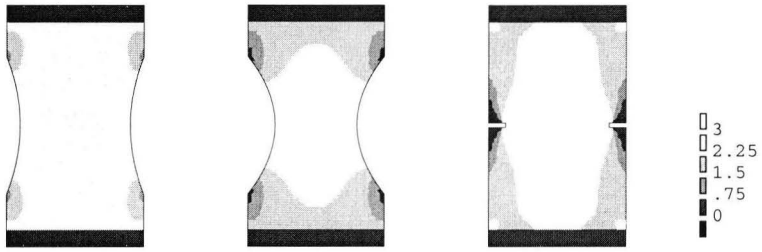


Figure 3.5 Crack patterns for uniaxial tension tests on specimens with straight edge.



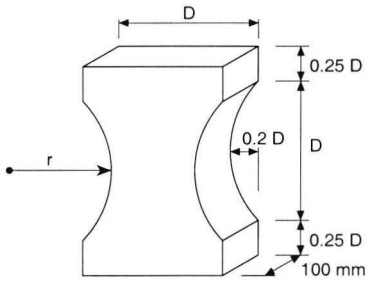
(a) max = 3.55 MPa (b) max = 3.85 MPa (c) max = 8.96 MPa

Figure 3.6 *Stress contours (in MPa) and maximum values for the principal stress (max) due to uniaxial tensile loading in specimen with 20% reduced cross section (a), 40% reduced cross section (b) and notches (c). For all specimens the average stress in the smallest cross section was 3 MPa.*

respectively. To both specimens an external load is applied which yields an average stress ($F/A_{\min}$) of 3 MPa. Compared to the specimen with 20% reduced cross section (Fig. 3.6a) the maximum principal stress is slightly higher for the specimen with the 40% reduced cross section (Fig. 3.6b). The area with high stresses is smaller however, as well is the risk of glue failure which is especially important for the largest specimens. These are the reasons which led to adopting the shape shown in Fig. 3.6b for the size effect tests. The final proportions are shown in Fig. 3.7.

Together with the final shape of the specimen, the size range could be set as well. For the smallest specimen the characteristic specimen dimension D was taken 50 mm, which resulted in a smallest cross sectional width of 30 mm. Consequently, the ratio $D/d_{\max} = 3.75$, which is rather close to the common rule that the smallest structural dimension should be taken at least three to five times the maximum aggregate diameter. By taking $D = 50$ mm for the smallest specimen, it was just possible to adopt six different specimen sizes in a scale range of 1:32. Therefore, it was decided that the test results had to show whether 30 mm for the smallest cross section is too small. The final dimensions for all specimen sizes follow from Fig. 3.7 whereas an impression of the size range can be obtained from Fig. 3.8.

The stress concentration which is caused by the specimen shape can be expressed by a



Type	D (mm)	r (mm)
A	50	36.35
B	100	72.5
C	200	145
D	400	290
E	800	580
F	1600	1160

Figure 3.7 *Specimen shape and dimensions for adopted size range.*

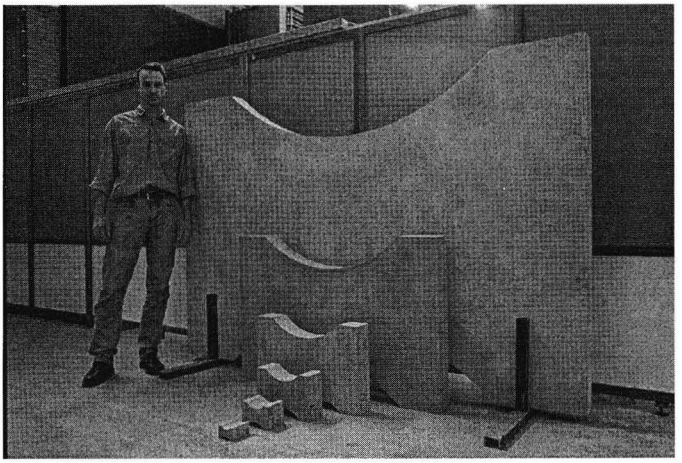


Figure 3.8 Specimen range of size effect tests.

stress concentration factor K_t for the normal stress, following

$$K_t = \frac{\sigma_{max}}{\sigma} \tag{3.1}$$

where the average stress σ follows from F/A_{min} and σ_{max} is the maximum stress in the smallest cross section. Through a linear elastic finite element calculation K_t = 1.28 was found. From Peterson [63, 65] a value of K_t = 1.24 can be deduced which, however, is approximate. For values of the ratio between the smallest width and the maximum width around 0.5 (here $0.6D/D = 0.6$), the approximation of K_t can be as much as 12% too low. The value of K_t = 1.28 agrees therefore fairly well with the result obtained from literature, and will therefore be used in this thesis.

A last remark concerns the use of notches to reduce the cross section. This has not been considered here, for several reasons. First of all huge stress concentrations are introduced, which is shown clearly by Fig. 3.6c. Besides the fact that crack initiation is now limited to only a small area around the notch, the way in which the stress concentrations affect the fracture behaviour of the different specimen sizes is unknown. Another reason concerns the practical problems which can arise during manufacturing of the notch. Damage can for instance be introduced, and since the shape of the notch influences crack initiation, the notch would in theory have to be scaled including its curvature.

3.2.3 Manufacturing of specimens

Concrete

Age of testing

The casting scheme which was followed, resulted from the starting point that the age of the specimens when being tested should be constant within narrow limits. Hydration effects would therefore have to be negligible to minimize the effect of time on the strength variation

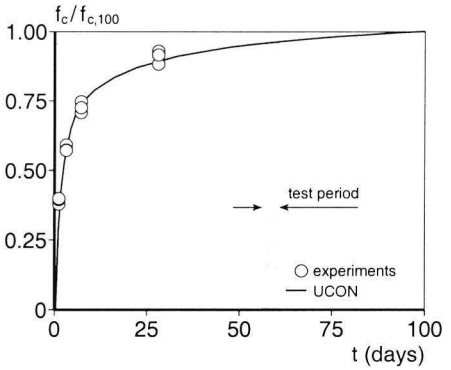


Figure 3.9 Development of compression strength in time

of the specimens. Fig. 3.9 illustrates the time dependent development of the uniaxial cube compressive strength for the concrete mix which was used in the present experiments. The circles represent the strength values of cubes tested at ages of 1, 2, 7 and 28 days respectively. The solid line is a prediction of the development of the compressive strength based on the computed degree of hydration of the mix. The latter is defined as the ratio between the amount of free cement at a certain time, and the initial amount of cement. This prediction was made with the so called UCON system (see [83] for details), using as input values the measured compressive strength as well as the temperature development during hardening of a reference cube. During the first 28 days after casting the main development of the strength takes place. After this period the strength continues to increase, but only very slowly. The age of testing was set at 8 weeks, which effectively meant that the specimens were tested between 56 and 61 days after casting.

Casting scheme

Test preparations included, one specimen could be tested per day, which automatically led to a scheme of one casting per week. Thus, for the main test series (series I), each week specimens of five different sizes were cast in order to distribute the specimen types evenly over the various castings. Casting specimen types E and F simultaneously was thereby impossible because of a number of reasons. The first and main reason was that the mould for either specimen type was placed on the same casting table. A second reason was that testing both specimens in the same week was not possible since time consuming changes of the test set-up were needed due to the large size difference of the two specimens. Thirdly, to cast specimen type E and F at the same time more concrete was needed than could be produced in one batch. Therefore, the first five castings of series I comprised specimen type A, B, C, D and F, followed by five castings with specimens of type A, B, C, D and E (see Table 3.4). Specimen type B and D were cast double for the purpose of verification tests, which will be discussed in Section 4.5. In addition to series I, also a second and third series of concrete specimens was cast (series II and III, Table 3.4) containing a restricted number of specimen sizes which were used for specific experiments.

Table 3.4 Casting scheme.

		Specimen type					
	Casting	A	B	C	D	E	F
Series I	1-5	×	×*	×	×*		×
	6-10	×	×*	×	×*	×	
Series II	12-16	×	×	×	×		
Series III	17-22	×		×		×	

* 2 specimens

Direction of casting

The manufacturing method that was applied for the concrete specimens followed from both practical and theoretical demands. It is known that the direction of casting influences the experimental result due to segregation effects, bleeding and air spaces under the aggregates. All specimens should therefore be cast in the same direction to ensure that casting effects which are present in the specimens are comparable. It is difficult however, to find strong advantages for casting the specimens in vertical or in horizontal direction since both choices have their own (dis)advantages. By casting vertically, casting effects over the cross section of the specimen are avoided and both specimen sides are equal (i.e. mould sides). At the same time gravity effects are introduced however, meaning that very stiff form work is needed to avoid thickness differences over the specimen height and for casting as well as compaction practical problems arise for the large specimens. When alternatively the specimens are cast in horizontal direction, the advantages and disadvantages mentioned previously more or less reverse. Mainly because of practical considerations it was eventually decided to cast the specimens in horizontal position.

Method of casting and compaction

During initial castings, the whole mould was filled with concrete followed by compaction. After demoulding however, the mould side of the specimens appeared to be covered completely with pores and air voids. In the experiments, the entrained air at the mould surface frequently induced crack initiation at the mould side of the specimens. Obviously, the added vibration energy was insufficient to remove the air from the concrete. To facilitate the withdrawal of air from the concrete, it was decided to place the concrete in three layers and to compact each layer separately. The problem of air entrainment and its influence on the experimental result could thus be circumvented. Later however, placing the concrete in three layers appeared to introduce new casting effects. Yet, it was decided to proceed in the same fashion. If casting effects could not be avoided anyway, a solution could be to try to quantify the effects by means of a series of verification tests. For this purpose tensile splitting tests were carried out, which will be discussed in Section 4.2.

The compaction process could be kept constant for specimens of all sizes by using a vibration needle to compact the concrete. The four smallest specimens were compacted with a small vibration needle, whereas a larger needle was used to compact the two largest specimens of the size range.

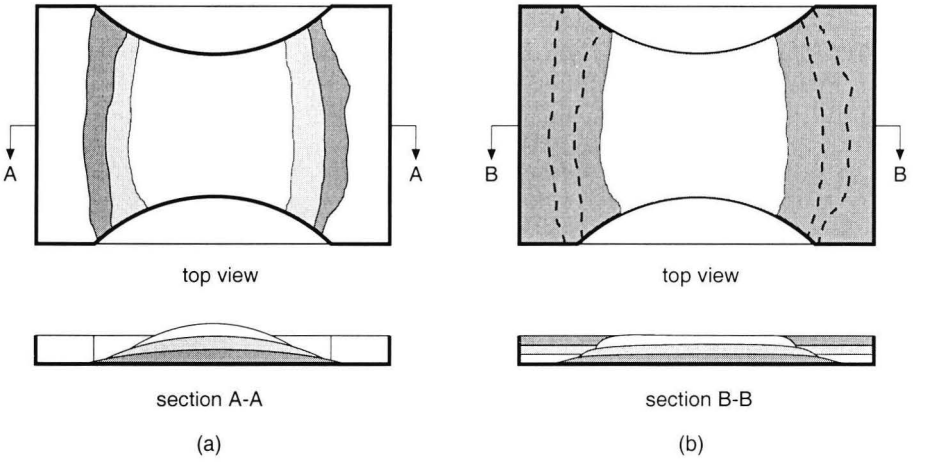


Figure 3.10 *Placing of the concrete for the* F *specimen. Middle part from batch 1 (a) and specimen ends from batch 2 (b).*

In the castings containing a type F specimen, one batch of concrete did not suffice to cast all specimens and cubes. Using two batches to cast the specimens on the other hand, could result in possible differences due to varying batch qualities. Hence, the casting procedure was changed in such a way that all specimens for the main size effect experiments could be cast using concrete from one batch. Thus, the first batch of concrete was used to cast one specimen of type B, C and D, six cubes and the middle section of the F specimen (see Fig. 3.10). The middle part of the type F specimen was taken large enough to ensure that failure would occur within this part of the specimen. The second batch of concrete provided for the second B and D specimen, another six cubes and the outer ends of the F specimen. Since six reference cubes were available from each batch the quality of both batches could be controlled. In Fig. 3.2 the strength results of the second batches can be distinguished by their gray colour.

Curing conditions

Two days after casting all specimens were demoulded. For specimen types E and F this meant that the sides of the mould were removed, whereas the specimen itself was not taken from the casting table until the fourth day after casting. These special measures were taken in order to avoid possible micro-cracking due to the large dead weight of the specimens, in combination with the lower strength of the young concrete. For the same reason, a casting table was constructed (see Fig. 3.11). Since all specimens were cast horizontally, dead weight load acts in the direction of the lowest stiffness when the specimens are lifted from the mould. If the specimens are rotated over 90 degrees however, the dead weight acts in the direction with the highest bending stiffness. The occurring bending stresses will thus be lower and the risk of micro-cracking is reduced. An additional advantage of rotating the specimen is that it can be lifted without cast-in provisions (Fig. 3.11). Any of these cast-in provisions like for instance lifting hooks, could induce stress perturbations during the test.

The curing conditions varied for the specimens of the three test series. For series I and

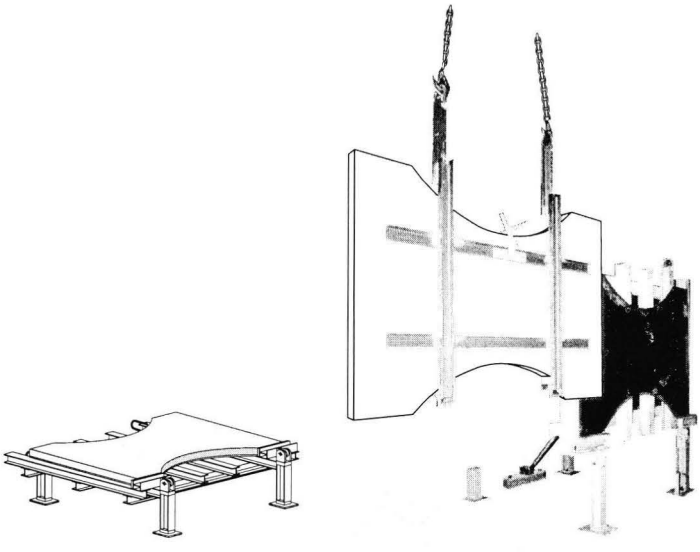


Figure 3.11 *Casting table for specimen type* E *and* F *(left), and demoulding of* F *specimen with lifting frame (right).*

III the specimens were placed in the laboratory after demoulding (approximate conditions 20 °C and 60% R.H.). Series I is therefore also referred to as the "DRY" series. It would have been preferred to store the specimens under water or in a climate room with controlled temperature and relative humidity. The starting point of equal curing conditions for all specimen sizes in addition to the weight and size of the type F specimens, made this very hard however. To check whether noticeable drying differences and shrinkage cracks would occur between specimens of different sizes, series II was cast, which will later be referred to as the "WET" series. The specimens of this series, which were restricted to types A, B, C and D, were placed in the climate room after demoulding. The conditions in the climate room were kept constant at 20 °C and a relative humidity of 95%.

Sandstone

The red Felser sandstone specimens were manufactured at the quarry in Germany and delivered in their final shape. Because of the influences from bedding planes which were mentioned in Section 3.2.1, it was ensured that the direction of the sedimentation layers was the same for all specimens. Furthermore, all specimens were ordered from the same block. Since previous research had shown that the tensile strength of sandstone strongly depends on the moisture content of the material [107], this phenomenon had to be accounted for. In case of differences in moisture content for specimen type A to F, strength variations could be present. Although it was known that this type of sandstone is highly permeable, also the

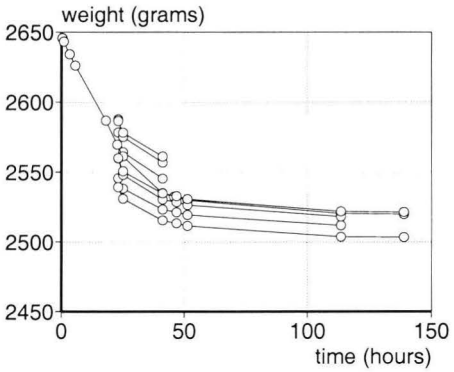


Figure 3.12 *Drying out of red Felser sandstone cylinders (l=150 mm, Ø100 mm) in laboratory conditions.*

weight loss was monitored of cylinders with a length of 150 mm and a diameter of 100 mm. The cylinders were stored under laboratory conditions (approximately 20 °C and 60% R.H.). The moisture content of the red Felser sandstone specimens was found to become constant in less than one week (Fig. 3.12). It must be mentioned however, that the start of the measurements was not at a state of complete saturation of the sandstone. Instead, the measurements reflect the amount of water which was already present in the sandstone, increased with the water which was absorbed during drilling and sawing of the specimens.

Since the tests shown in Fig. 3.12 do not reflect the drying out which can be expected for larger volumes, it would be preferred to test the sandstone specimens under controlled moisture conditions. This could be either a constant laboratory moisture content after oven-drying of the specimens, or fully saturated. Both situations were unrealistic however from a practical point of view. Hence, it was decided to store the specimens in the laboratory before testing, long enough though to ensure that a stable moisture condition had developed. For specimen type A, B and C this meant storage in the laboratory for 7 weeks, type D 10 weeks and type E to F for at least 13 weeks.

3.3 Experimental set-ups

3.3.1 Testing frames and hinge constructions

The size effect tests were carried out in three different loading frames. It has already been mentioned that, in general, and for uniaxial tension tests in particular, the experimental set-up can have a profound influence on the test result. This is especially the case for uniaxial tension tests with fixed boundary conditions since the effect of the bending stiffness of the loading frame is directly incorporated in the experimental result. When rotating boundary conditions are applied on the other hand, the bending stiffness of the frame is not of importance. The normal stiffness however, could theoretically still be a point of concern. When the specimen is loaded elastic energy is stored in the frame, which will be freed when the force decreases in the softening regime. This will result in deformation of the specimen in addi-

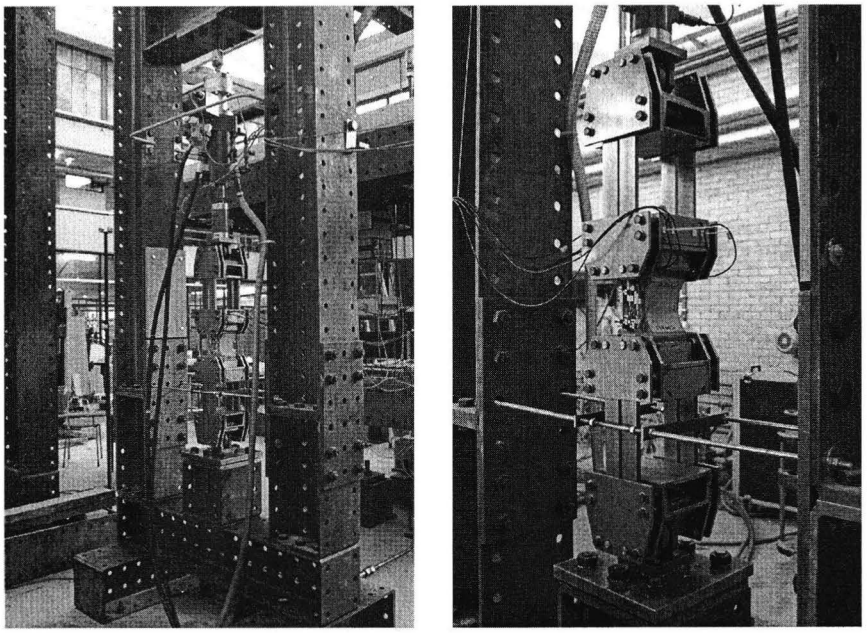


Figure 3.13 *Small experimental set-up for the testing of specimen type* A *and* B.

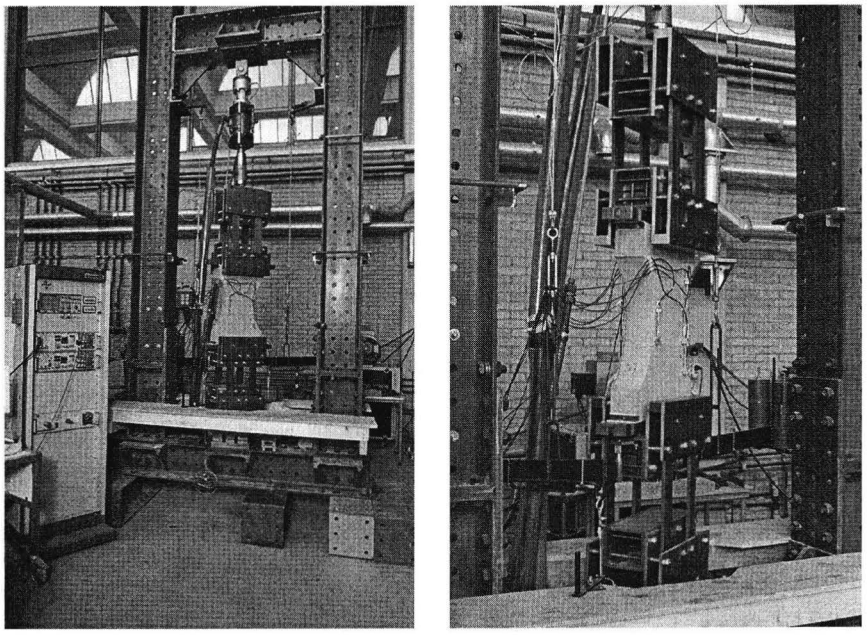


Figure 3.14 *Intermediate-sized experimental set-up for the testing of specimen type* C *and* D.

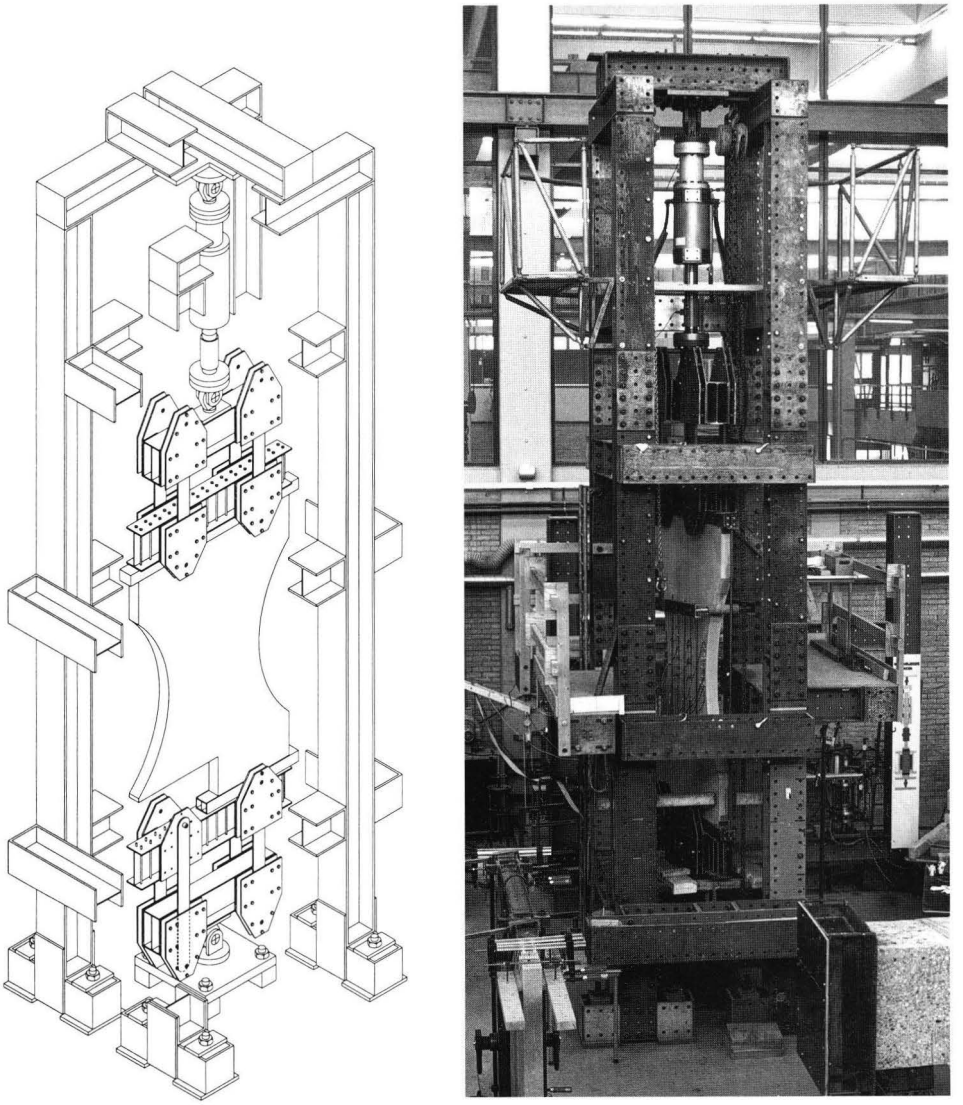


Figure 3.15 Large experimental set-up for the testing of specimen type E *and* F.

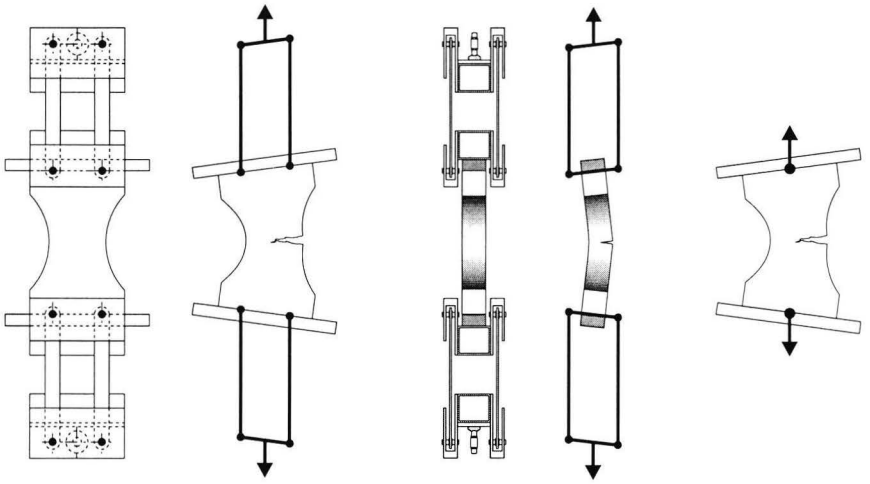


Figure 3.16 *Principle of the hinge construction (type D) for free rotations in two orthogonal directions. In-plane direction (a), out-of-plane direction (b) and schematization (c).*

tion to the deformation due to the external force which is exercised by the hydraulic actuator. Since the deformations measured on the specimen surface are used as feed-back signal for test control, these additional deformations will be noticed. They can also be accounted for assuming the reaction time of the experimental set-up is short enough.

The fact that the loading frame influences the experiment means that it would be preferred to use one single frame in which all tests can be conducted. A range of specimens with various sizes then means, however, that the set-up has to be adjusted for each new specimen size that is to be tested. The present scheme in which specimens of five different sizes had to be tested each week did not allow for using only one experimental set-up. Also when accuracy is considered, using only one single frame is not preferred since it implies that for

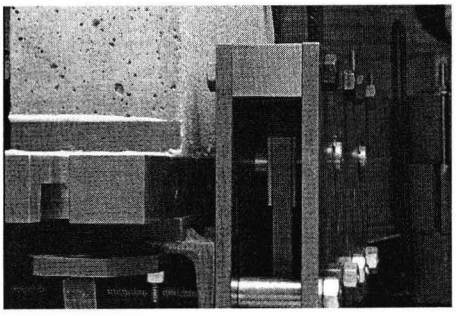


Figure 3.17 *Situation of rotation point in the glue layer between specimen and loading platen.*

the small specimens the load and the displacement of the piston will only be a fraction of the total capacity of the experimental set-up. For both reasons it was decided to conduct the uniaxial tension tests in three different experimental set-ups, with two subsequent specimen sizes being tested in the same set-up. Both the smallest experimental set-up (specimen type A and B) and the intermediate-sized experimental set-up (specimen type C and D) were built in a single frame consisting of two columns (Figs. 3.13 and 3.14). Inside each frame a load cell and a hydraulic actuator were placed, both with a capacity of 100 kN and for the latter a stroke of ± 20 mm. To conduct the tests on specimen type E and F a double frame was used with four columns, an actuator with a capacity of 400 kN and a stroke of ± 100 mm and a load cell also with a capacity of 400 kN (Fig. 3.15). All actuators were connected to the frames by means of hinges.

Inside each frame a hinge construction was placed which allowed for free rotations of the specimen ends in two orthogonal directions (Fig. 3.16). The special shape of the hinge constructions followed from the demand to locate the rotation point exactly at the end of the specimen, or, to be more precise, in the glue layer between specimen and loading platen (Fig. 3.17). Since only the specimen is then incorporated in the system length this was considered to be the best way of testing the specimen material.

The principle of the hinge construction becomes more transparent when reducing the construction to the basic scheme. This is illustrated in Fig. 3.16 for a type D specimen. Both ends of the specimen are connected to a hinge construction consisting of two horizontal cross bars and four pendulum bars, two on the front side and two on the back side. The pendulum bars are connected to the cross bars through hinges, which allow for a rotation of 360 degrees in the in-plane direction and 8 degrees in the out-of-plane direction. By means of the pendulum bars the external force which is exercised by the hydraulic actuator is subdivided in four forces. These four forces in the pendulum bars are then distributed over the width of the specimen by the cross bar to which the loading platens are fixed.

In each loading frame a hinge of different size is placed, designed for specimens of type B, D and F respectively. Hence, a specimen of one size smaller can be tested in the same hinge construction by raising the lower hinge over a distance equal to half the specimen size. The extra space is filled with massive steel bars, to ensure that the elastic deformations of the set-up do not increase considerably (see Figs. 4.10a and c). Adjusting the position of the lower hinge was relatively easy for the smallest and the intermediate-sized set-up, and could be done between two tests in a testing week. The large set-up could remain unchanged for several weeks since the E and F specimens were cast in two groups of five specimens each.

To account for the possibility that differences between the three set-ups would affect the experimental results a series of verification tests was incorporated in the test program. These verification tests comprised tests on specimens of type B in the intermediate-sized loading frame, and tests on type D specimens in the large frame. By comparing the results of these verification tests with results on B and D specimens conducted in the small and intermediate-sized frame respectively, possible differences would be noticed (see Section 4.5 for details).

3.3.2 Loading platens

The steel loading platens that were used in the size effect tests provided for the connection between specimen and experimental set-up. As will be discussed in Section 3.4.1, the loading platens were glued to the specimen ends prior to testing. The other side of the loading platens

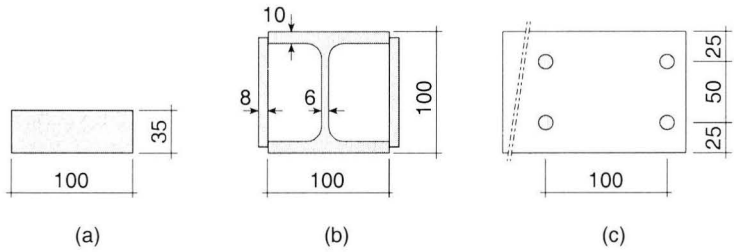


Figure 3.18 *Applied loading platens for specimen type* A *to* D *(a),* E *and* F *(b) and bolt pattern (c). Measures in mm.*

could be fixed to the upper and lower cross bar of the lower and upper hinge respectively, by two rows of bolts. Two types of loading platens were used, depending on the specimen type. For specimen type A, B, C and D massive steel loading platens were used with a cross section as shown in Fig. 3.18a. The loading platens for the E and F specimens were taken more robust, based on a standard H-shaped beam which was reinforced with additional steel plates on the sides (Fig. 3.18b). For the length of the loading platens see Table 3.5. The number of bolts which was used to fasten the loading platens varied with the size of the specimen (Table 3.5). Regardless of the total number of bolts, the bolt pattern was kept centric with respect to the centre of the specimen (Fig. 3.18c). To be able to use a set of loading platens in different set-ups, the bolt dimensions as well as the hole pattern were kept constant. Note that the height of the loading platen was incorporated in the design of the hinge construction since the point of rotation had to be in the glue layer. As a consequence, a special set of loading platens was used to conduct the verification tests on the type D specimens in the large set-up (see also Table 3.5).

The (bending) stiffness of the loading platens in addition to the number of bolts which is used, decides whether the test will proceed successfully. This appeared for the type C specimens in the initial stage of the research. It is noteworthy that the bending stiffness lies between the stiffness of the loading platen itself, and the composed stiffness of loading platen and cross bar of the hinge construction. The actual stiffness thereby depends on how tight the bolts are fastened. For the case which is considered here the composed stiffness

Table 3.5 *Details on loading platens for all specimen sizes.*

type	A	B	C	D	D[1]	E	F
length [mm]	130	130	320	600	500	984	1784
number of bolts	2×2	2×2	2×2	2×4	2×4	2×8	2×16
steel angles[2] [mm]	10x1.5	15x2	20x2	20x2	50x5	50x5	50x5

[1] D test in large set-up, [2] numbers represent width x thickness

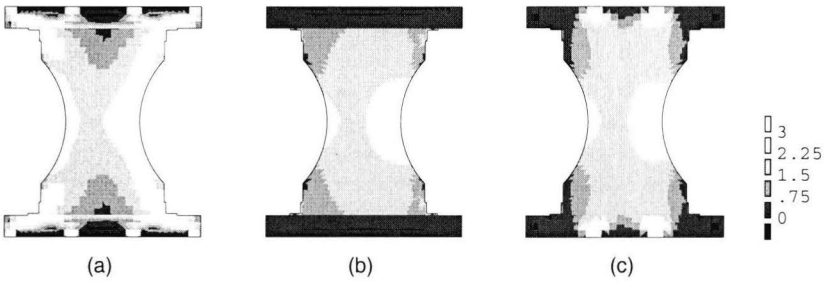


Figure 3.19 *Stress contours (in MPa) for an eccentrically loaded type* C *specimen with low-stiffness loading platens (a), stiff loading platens (b) and low-stiffness loading platens connected to the set-up with 2 instead of 4 bolts (c).*

of loading platen and cross bar was approximately 57 times higher than the stiffness of the loading platen only. At first, the loading platens of the C specimens were fastened to the hinge constructions with 2×4 instead of 2×2 bolts, resulting in glue failure for each test which was carried out. In case of a very loose connection between loading platen and cross bar of the hinge, the bolt forces are distributed over the specimen width through the bending stiffness of the loading platens only, see Fig. 3.19a. High bending stresses then occur at the edges of the specimen ends and induce glue failure. When alternatively the loading platens are bolted tightly to the cross bars, the bending stiffness of the loading platens transforms into the composed bending stiffness of loading platen *and* cross bar. Bending of the loading platens is now restricted and glue failure is prevented (Fig. 3.19b). In practice however, the bolts could not be tightened too strongly since small deformation differences sometimes induced cracking of the glue layer. The solution hence existed in not using the outer bolts (Fig. 3.19c).

To prevent cracking of the glue layer during fastening of the long row of bolts in the loading platens, a slightly different preparation procedure was adopted for the E and F type

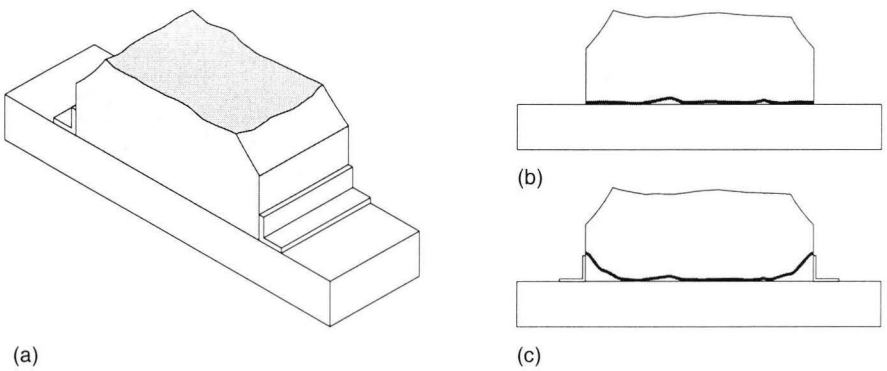


Figure 3.20 *Steel angle glued in corner between specimen and loading platen (a), boundary crack in specimen without steel angle (b) and with steel angle (c).*

specimens. Contrary to the smaller specimens, for the E and F specimens the entire cross bars were taken out of the set-up. Thus, the loading platens could already be bolted to the cross bars before glueing. Next, cross bar and loading platen were glued to the specimen ends. Although this was rather cumbersome because of the large weight of cross bar and loading platen (175 kg), glue failure could be restricted to one single test. To achieve this, one other precaution had to be taken as well since despite careful preparation of the specimens, glue failure could otherwise not be prevented for the larger specimens. It was found that the problem of glue failure due to high tensile stresses and shear stresses in the specimen [47, 106], could be solved in a rather easy and straightforward manner. By glueing small steel angles in all four corners between specimen and loading platens (see Fig. 3.20 and Table 3.5) the risk of glue failure could be eliminated almost completely. This was simply due to the fact that by placing the steel angles cracks could not develop in a straight line anymore (Fig. 3.20b), but were forced to branch off instead (Fig. 3.20c). It should be mentioned that in those tests where glue failure occurred, the cracks always developed in the first millimeters of concrete rather than in the concrete-epoxy interface.

3.3.3 Test control

The complete experimental set-ups consisted of one of the three loading frames, a Schenck regulation system and the hydraulics. The scheme of the control and loading system is shown in Fig. 3.21. Two different Schenck regulation systems were used. The first system comprised two independent regulation circuits, of which circuit 1 was part of the small experimental set-up (A/B specimens), whereas circuit 2 was connected to the large experimental set-up (E/F specimens). The second regulation system was part of the middle sized set-up (C/D specimens). There, contrary to the small and the large experimental set-up, an external time base was used rather than the built-in time base of the Schenck regulation system. This external function generator was controlled by software running on a PC. The Schenck regulation system is the central part of the closed loop servo-controlled experiment, and provides the control signal for the servo valve of the hydraulic actuator. Test control could thereby be switched between displacement control (piston), load control and strain (or deformation) control. In case of displacement control, the feed-back signal was provided by the displacement transducers inside the pistons. These had measuring ranges of ± 25 mm and ± 20 mm for the two smallest set-ups and ± 100 mm for the large set-up. The loads were measured by load cells placed between the hydraulic actuator and the upper hinge construction. The load cells had the same capacity as the hydraulic actuators in the various test rigs, namely 100 kN for the small and intermediate set-up and 400 kN for the large set-up.

All uniaxial tension tests were conducted under deformation control. The deformations needed for test control were measured by LVDTs. To be able to perform stable tests a system was adopted for test control similar to that used in [53]. The system is based on two principles. Firstly, applying a constant, relatively small, measuring length for the control LVDTs which is kept constant for all specimen sizes. Secondly, using the maximum deformation measured by a single LVDT as feed-back signal ("MAX" control), rather than the average signal of two or more LVDTs. The measuring length adopted for the control LVDTs was 75 mm (65 mm for the type A specimens). With increasing specimen size, the zone were crack initiation may take place increases as well due to the geometrical similarity for all specimen sizes. To control the deformations occurring in a larger zone, a number of control LVDTs

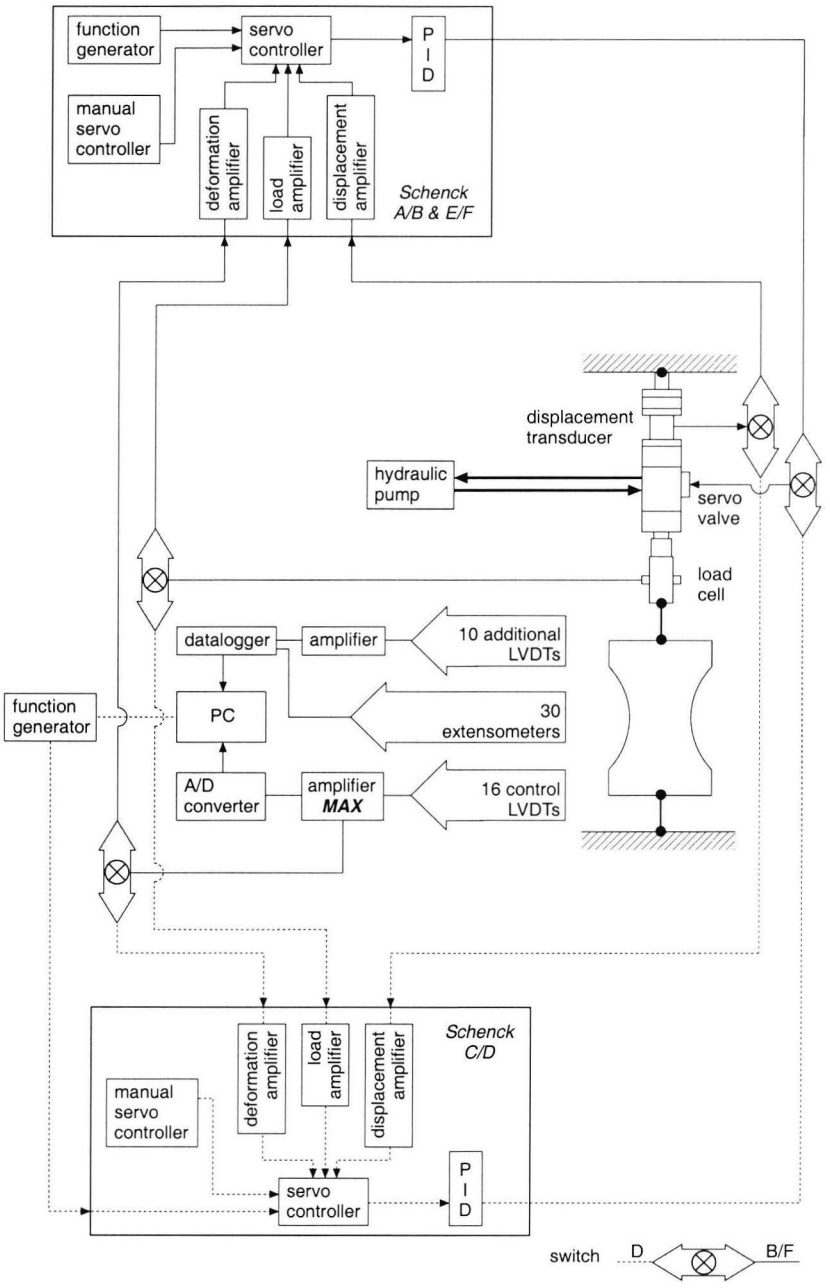


Figure 3.21 *Overview of experimental set-ups for* A / B *and* E / F *tests (upper part) and* C / D *tests (lower part).*

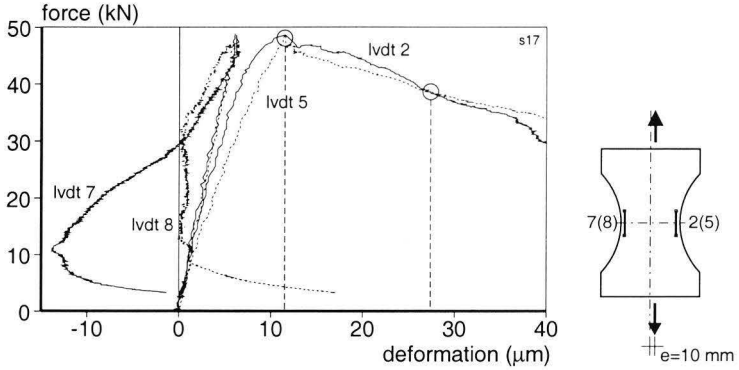


Figure 3.22 *Principle of test control during a test on a type* D *specimen. The numbers between brackets (figure on the right) indicate the* LVDTs *placed at the back.*

was placed in line along the edges of the specimen (see Fig. 3.23b). The control LVDTs were connected with a specially developed device which continuously checked up to 16 LVDTs for the one measuring the largest deformation. This LVDT was used to control the test. When the next instant another LVDT measured a larger deformation test control was switched to that LVDT.

An example of a test in which this switching of control LVDT took place several times is given by Fig. 3.22. Until peak load, the test is controlled by LVDT 5 which is placed on the back side of the specimen (right side of Fig. 3.22). Immediately after peak load, the crack propagates through the specimen to the front and continues to grow there. Consequently test control is switched to LVDT 2. At a crack opening displacement (COD) of 27 μm again a change of control LVDT takes places when LVDT 5 takes over from LVDT 2.

3.3.4 Load eccentricity

The size of the zone in which crack initiation can be expected increases with the specimen size. Because of the constant measuring length of 75 mm which was applied for the control LVDTs, the number of LVDTs which had to be placed in line on each edge of the specimen could be up to five for a type F specimen. The control device which was used to check all LVDTs for the one measuring the largest deformation could only handle a maximum of 16 LVDTs, whereas 20 LVDTs were needed to perform a test on a F specimen. To overcome this problem a small load eccentricity was applied in the uniaxial tension tests. Because of this eccentricity it could be ensured that crack initiation would take place at the side of the specimen with the largest number of control LVDTs. The eccentricity was taken such, that at peak load a tensile state of stress was present in the entire cross section. Furthermore, the eccentricity was scaled with the size of the specimens. According to the theory of linear elasticity, the maximum stress in the outermost fibre of the cross section follows from

$$\sigma_{max} = \frac{F}{A}\left[1 + \frac{6e}{0.6D}\right] = 1.2\frac{F}{A}, \qquad e = \frac{D}{50}\ (\text{mm}) \tag{3.2}$$

where A is the cross-sectional area, $0.6D$ the width of the smallest cross section and e the eccentricity of the external load F. The maximum stress is thus independent of the specimen size. In the experiments, the eccentricity of the external load was obtained by glueing the specimen eccentrically to the loading platens.

3.3.5 Deformation measurements

During a uniaxial tension test, the specimen was fully instrumented in order to obtain deformation readings over the complete surface of the middle part of the specimen. These measured deformations can roughly be subdivided in three groups, namely control deformations, scaled deformations and additional deformations. All measurements were taken both on the front and the back of each specimen, and in principle all specimens were instrumented in the same way. With decreasing specimen size however, the surface became too small to place all measuring points, so that the measured deformations were restricted to the main scaled deformations and those used for test control. Here, the measurements taken on the specimens will be illustrated by means of a B and a D specimen (Fig. 3.23).

The deformations that were used for test control were measured with LVDTs (Solartron A6G), which were calibrated for measuring ranges of ± 500 μm and ± 1000 μm for the concrete tests and sandstone tests respectively. The LVDTs were placed along the edges of a specimen, both on the front and the back side (see Fig. 3.23). Each LVDT was placed in a holder, which could be clamped in a measuring point which was glued to the concrete (Fig. 3.24b). The measuring length of the LVDTs placed along the edges of a specimen (L_c) was 75 mm, except for the A specimens. Since their length was only 75 mm there the effective measuring length for the control LVDTs was 65 mm.

For the scaled measurements LVDTs were used as well, and the measuring length (L_s) scaled with the size of the specimen. In case of the A and B specimens the scaled measurements were only taken in the middle of the specimen, whereas for the larger specimens scaled measurements were taken at positions left and right of the specimen middle as well (Fig. 3.23). For the scaled measurements on specimen type D, E and F extra equipment was needed because of the large measuring lengths (240 mm to 960 mm respectively). There, the measuring configuration comprised a steel rod which was clamped in a measuring point at

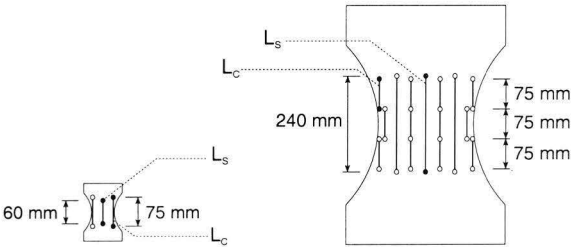


Figure 3.23 *Placement of displacement transducers on specimen type* B *(a) and* D *(b).* L_c *refers to constant control measuring length;* L_s *to scaled measuring length.*

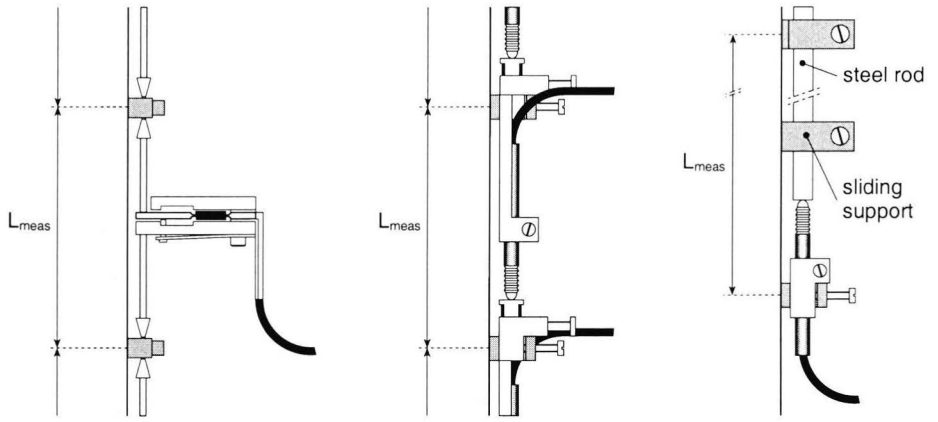


Figure 3.24 *Measurement configurations for extensometers (a), control* LVDTs *(b) and scaled measurements for specimen type* D, E *and* F *(c).*

the top end of the rod (Fig. 3.24c). The lower end of the rod was led through an additional support which allowed for frictionless movements in vertical direction. An LVDT which was clamped in a third measuring point was used to measure the vertical displacements of the lower end of the steel rod.

The third kind of deformation measurements was conducted with extensometers (measuring range ± 1 mm), that were developed by the Measurement and Instrumentation group of the Stevin Laboratory (Fig. 3.24a). Basically, these extensometers measure the displacement between two measuring points through the bending of a thin metal strip to which a strain gauge is attached. The applied measuring length for the extensometers was 75 mm, analogous to the control LVDTs.

Depending on the type of measuring device, the signals were first amplified (LVDTs), or directly retrieved by a data logger in case of the extensometers. Finally, all deformation signals as well as the output signals of the Schenck regulation system (load, function signal, feed-back signal and piston displacement) were collected in one data scan, by a measuring program running on the PC (see Fig. 3.21). The data scans were made at fixed time intervals, starting with 5 seconds and step-wise increasing until 40 seconds in the tail of the softening curve.

3.4 Testing procedure

3.4.1 Preparation of specimens

Concrete series I, III and sandstone

In the week prior to testing, the specimens were taken out of their storage in the laboratory. First the cement skin and loose concrete parts were removed from the specimen ends with

a steel brush. Hence, the connection was improved between the glue and the aggregates embedded in the matrix material. After blowing the roughened surface with pressurized air, the surface of the concrete as well as the steel loading platens were scoured thoroughly with acetone. Next, the loading platens were glued to the concrete using a two-component epoxy resin (VN-PCI BWD lijm). In addition, in the corners between specimen and loading platens small steel angles were glued. The reason for applying these steel angles was that they proved to be very effective in almost completely eliminating the risk of glue failure, as was explained before (see Section 3.3.2). For the sandstone scouring the ends of the specimens sufficed since the surface already consisted of open material. The loading platens and angle steels were glued to the sandstone specimens analogous to the concrete specimens.

After the epoxy had hardened, which took about six hours, the specimens could be lifted and the measuring points could be glued on the front and back side of the specimens. This concluded the test preparations, making the specimen ready to be placed in the test set-up. To facilitate handling the specimens, but also to protect the glue layer in case of the larger specimens, the loading platens were connected. This connection consisted of steel strips which were bolted to the loading platens so that a stiff frame was created around the specimen.

Concrete series II

The preparation of the concrete specimens of series II was slightly different. Since these specimens had been cured at a relative humidity of 95%, drying out of the specimens during preparation was prevented as much as possible. The day prior to testing the specimens were taken out of the climate room. Around the specimen a wet cloth was wrapped which was covered with a sheet of plastic, leaving only the specimen ends free. After brushing the ends of the specimens they were blown dry with pressurized air and scoured with acetone. After the loading platens had been glued to the ends of the specimen no part of the concrete surface was exposed to the open air anymore. One day later, which was the day of testing, the plastic was cut away at the places were measuring points had to be glued. After the measuring points had been glued to the specimen surface, the specimen was placed in the test set-up. Next, the remaining plastic foil was removed and the test started.

3.4.2 Size effect tests on concrete and sandstone

As soon as the specimen was bolted to the hinge constructions and the measuring devices were mounted to the specimen, the test procedure could start. Because of the flexible nature of the test set-up, which can be compared best with a chain consisting of several rings, this procedure had to be rather special. The first difficulty was to determine the point of zero load and zero deformation. Secondly, before the test could be started under deformation control a small pre-load had to be applied. Finding a situation in which no load acted on a specimen was not possible since a specimen is not only loaded by the hydraulic actuator, but also by its own weight and the weight of the lower hinge construction. The consequent deformations thereby vary with the position of the displacement transducer. For this reason the control LVDTs were set to zero after the specimen was bolted to the upper and lower hinge construction. The actual origin of the deformations measured by each transducer was obtained by back calculation as will be outlined in Section 5.1.2. After setting the LVDTs to

zero, the displacement of the piston was increased manually until an increase of the load was observed. At that moment control of the test was switched to load control. In load control the load was increased until a prescribed load level which varied with the size of the specimen. At this load level the tensile stresses inside the specimens were large enough to obtain clear deformation readings of the control LVDTs, so that control of the test could be switched to deformation control. For the concrete specimens, the prescribed load levels were 0.5 / 0.7 / 2.25 / 2.5 / 15 and 25 kN for the specimens of type A, B, C, D, E and F respectively. When deformation control was active, the ramp of the function generator was started which meant the actual start of the test. The deformation rate was kept constant during the test at 0.028 μm/s for the concrete specimens and 0.056 μm/s for the sandstone specimens. This higher deformation rate for the sandstone specimens was inherent to the measuring range of the control LVDTs. Since the sandstone deformations were much larger than those of concrete, the measuring range of the control LVDTs was increased from ± 500 μm to ± 1000 μm . By doubling the deformation rate as well, the loading speed remained the same. Each test was continued until the first control LVDT went out of range.

3.4.3 Impregnation tests

The idea behind these tests (series III) was to use impregnation techniques for getting more insight into the fracture patterns inside the specimens, in addition to the deformation measurements carried out on the surface of the specimens. Besides ultimate load, three values for the control deformation were chosen, at which the specimen was unloaded after a test procedure had been followed similar to one described in the previous section. These deformation values were 50 μm , 100 μm and 300 μm respectively. After the specimen had been unloaded and only a small residual force was left, the loading platens were connected by steel strips to avoid further deformations. Subsequently the specimen was taken out of the experimental set-up. Next, a small container was glued around the cracked middle section of the specimen. The container was filled with a low viscosity two-component epoxy (VN-PCI epoxy injectiehars 2055) to which fluorescent dye (Struers EPO dye) had been added. Specimen and container were then placed in vacuum for approximately 40 minutes. After the air pressure had been restored, the epoxy could harden.

The second part of the impregnation tests consisted of cutting the specimens. First the specimen ends including the loading platens were removed, followed by cutting all specimens in slices with a diamond saw (see Fig. 5.18). Because of the impregnation with epoxy, this could be done safely without the risk to damage the cracked specimens. Finally the slices were photographed in a dark room under ultra-violet light.

3.5 Test program

In this section an overview is given of the experiments which have been conducted. The tests listed are not only size effect tests, but also include verification tests meant to elucidate the influence of the experimental set-up. The name convention is based on the experimental variables and is built up as follows:

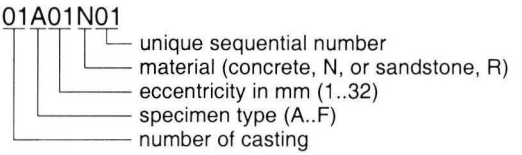


Table 3.6 Size effect tests on concrete, series I (stored in laboratory).

Specimen type					
A	B	C	D	E	F
01A01N01			01D08N04		01F32N06
02A01N07	02B02N08	02C04N09	02D08N10		
03A01N13	03B02N14				03F32N19
04A01N20		04C04N23			04F32N26
05A01N27		05C04N30	05D08N31		05F32N33
06A01N34	06B02N35	06C04N37	06D08N38	06E16N40	
07A01N41*	07B02N42	07C04N44	07D08N45		
08A01N48				08E16N54	
09A01N55		09C04N58		09E16N61	
10A01N62		10C04N65		10E16N68	

* only peak load

Table 3.7 Size effect tests on concrete, series II (stored in climate room).

Specimen type			
A	B	C	D
12A01N69	12B02N70	12C04N71	12D08N72
13A01N73	13B02N74	13C04N75	
14A01N77	14B02N78	14C04N79	14D08N80
15A01N81	15B02N82	15C04N83	15D08N84*
16A01N85	16B02N86	16C04N87	16D08N88

* only peak load

Table 3.8 Verification tests for influence of the test set-up, series I (stored in laboratory).

Specimen type			
B	B[1]	D	D[2]
04B02N21	04B02N22	04D08N24	
			07D08N46
08B02N50	08B02N49	08D08N52	08D08N53
09B02N57	09B02N56	09D08N59	09D08N60
10B02N63	10B02N64	10D08N66	

[1] B tested in intermediate-sized set-up, [2] D tested in large set-up

Table 3.9 Impregnation tests on concrete, series III (stored in laboratory).

Maximum deformation	Specimen type		
	A	C	E
Peak	18A01N104	18C04N105	18E16N106
50 μm	20A01N92	20C04N93	
100 μm	19A01N89	19C04N90	
300 μm	21A01N95	22C04N99	

Table 3.10 Size effect tests on sandstone.

Specimen type					
A	B	C	D	E	F
00A01R04	00B02R07	00C04R10	00D08R13	00E16R16	00F32R19
00A01R05	00B02R08	00C04R11	00D08R14	00E16R17	00F32R20
	00B02R09	00C04R12	00D08R15	00E16R18	00F32R21

Chapter 4

Verification tests: outline and results

4.1 Introduction

The results presented in this chapter all belong to experiments which were conducted in addition to the main size effect tests. Several reasons existed for conducting these verification tests. One reason was to ensure that the assumptions which were made in the experimental design were actually met during the main experiments, like in case of the rotational capacity of the hinge constructions. As for the effect of test control and casting effects, specific experimental observations were studied in more detail by means of the verification tests. Finally, already when designing the experiments it was known that certain structural effects were possibly introduced during testing, which in turn could influence the experimental result. In this respect again the casting effects are mentioned, as well as using three different experimental set-ups for conducting the size effect experiments. The presence of these structural effects does not necessarily mean that the eventual result can not be used or will be of lower quality. Getting insight into, and thoroughly understanding these introduced effects is however regarded as very important. The obtained knowledge can then be used to interpret the results of the main tests.

4.2 Variation of concrete properties within specimens

4.2.1 Problem description

The dog-bone shaped specimens which were used in the uniaxial tension tests were cast horizontally as was discussed in Section 3.2.3. Consequently, one side of the specimen had been in contact with the mould (mould side) whereas the other specimen side consisted of the casting surface (casting side). In the uniaxial tension tests crack initiation frequently occurred at the casting side of the specimens, especially for the larger specimen sizes. Purely the effect of casting the specimens horizontally could be an explanation for this observation, as was reported by Scheidler [67]. Crack initiation at the casting side can be attributed to a lower strength and stiffness of the concrete surface layer. Both parameters are lower because of segregation effects as well as a higher water-cement ratio due to bleeding. In the present case however, the casting effect was likely to be even stronger because the concrete was cast in three layers whereas each layer was compacted after being cast. This could mean

that the mould side of the specimen had been compacted three times, the middle part of the specimen twice and the casting side only once. To be able to quantify this casting effect on the strength and stiffness of the concrete throughout the specimen, a series of verification tests was carried out in the experimental set-up developed by Vervuurt [103].

4.2.2 Specimens and experimental procedure

The verification tests comprised deformation controlled tensile splitting tests on thin notched plates with dimensions $125 \times 168 \times 15$ mm^3 (Fig. 4.1b). To manufacture the tensile splitting specimens two concrete blocks with the dimensions of a type D specimen were cast (Fig. 4.1a). Analogous to the dog-bone shaped specimens the blocks were cast in three layers which were vibrated separately, and placed in the laboratory during hardening. At an age of 6 weeks the tensile splitting specimens were sawn from the bottom (mould side), the middle and the top layer (casting side) of the blocks, as shown in Fig. 4.1a. After the specimens had been sawn, they were placed in plastic bags to prevent drying out until the time of testing. Apart from the position of the specimen in the block, also the way in which the notch was introduced was varied. To study a possible influence of the wall effect as well as drying out on crack initiation, a steel strip was used to make a cast-in notch in half of the specimens, whereas for the remaining specimens the notch was sawn.

Two hours before testing the specimens were taken out of the plastic bags. On top of the specimens the loading platens were glued, and a steel strip was glued to the bottom of the specimen for vertical support. This is shown in Fig. 4.1b together with the loading configuration. The loads F are applied through a symmetric double working hydraulic actuator with a capacity of 1 kN. The separate loads can be measured by two load cells that are attached to each piston. The tensile splitting tests were carried out under displacement control. As feed-back signal the average deformation (CMOD) was used, which was measured by two LVDTs that were placed over the notch on both the front and the back side of the specimen. The LVDTs had a measuring length of 15 mm and the applied deformation rate was 0.06 μm/s.

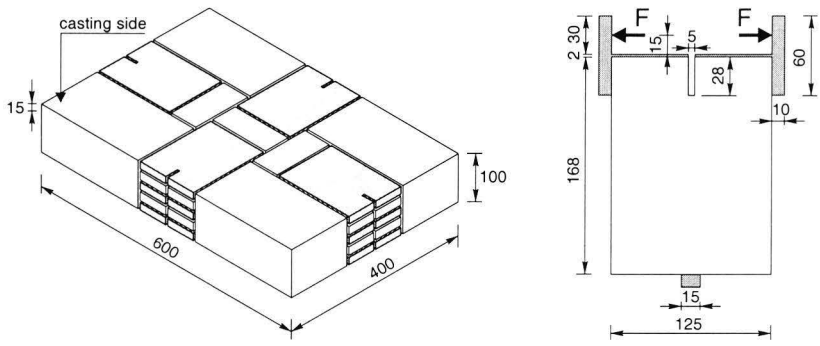


Figure 4.1 *Method of specimen manufacturing (a) and adopted specimen geometry (b). Measures in mm.*

4.2.3 Test results

In Fig. 4.2 the load-CMOD curves are shown which were recorded during the tensile splitting tests on specimens originating from the three layers in each block. For a full discussion of the test results the reader is referred to [96]. The final crack patterns which are shown beside each graph are the average path of the cracks on the front and the back surface of a specimen. The load in the graphs is the average of the two loads that were measured by the load cells, divided by the actual thickness of the specimen in order to compensate for thickness variations. As for the CMOD, the average was taken of the displacements measured by the LVDT on the front and on the back side of the specimen.

In Fig. 4.2 the influence of the layer from which a specimen originated is reflected by the length of the tail of the softening curve. For the bottom layer (Figs. 4.2e,f) the tail extends for most specimens until an average CMOD of 170 μm . The specimens from the top layer however (Figs. 4.2a,b), generally did not reach these values for the CMOD since failure of the specimen occurred long before. This indicates that the inhomogeneity of the top layer is larger compared to the bottom layer, which could also be the explanation for the fact that no effect of the notch type can be distinguished (Fig. 4.2a vs. 4.2b). A slight effect of the type of notch is found when comparing Figs. 4.2c and d. Due to more vertical initial crack growth a higher ductility is found for the specimens with cast-in notches. For non-vertical initial crack growth more brittle post-peak behaviour is observed, which agrees with findings by Vervuurt [103]. A possible explanation for the more vertical initial crack growth in case of cast-in notches could be the wall effect and shrinkage cracks around the notch. Consequently, the concrete is locally weakened and crack growth will take place perpendicular to the applied load. As soon as the crack reaches a part of the specimen with a higher strength and stiffness crack arrest occurs, attended by a change of the direction of crack growth [103].

The effect of the notch type is rather insignificant when compared to the influence of the position in the block. In the consideration of the obtained values for the ultimate load F_u and the specimen stiffness k, the type of notch will therefore not be considered separately. Fig. 4.3 illustrates the relation between F_u, k and the layer from which the specimen originated. The stiffness of the specimen is thereby taken as the maximum value of the initial slope of the load-CMOD curve, which has been computed with the least squares method for the first 10 measuring points. In Table 4.1 the mean values and their standard deviations are listed. Both strength and stiffness of the specimens clearly increase from the top layer (casting surface) to the bottom layer (mould side). This shows that a clear casting effect is present, and also explains the observations of crack initiation at the casting side of the dog-bone shaped specimens in the uniaxial tension tests. In comparison with the mould side, the casting side of the uniaxial tension specimens does not only have a lower strength, but will also exhibit larger deformations. These can be attributed to the lower stiffness of the casting side, which is caused by a lower aggregate content due to segregation effects. Note however, that the strength and stiffness variation is not necessarily continuous over the thickness of the block. For block 1 the properties of the middle and bottom layer are almost equal, whereas for block 2 they continue to increase. Similar observations were made in the uniaxial tension tests. For the large specimens both crack initiation and the largest deformations occurred without exception at the casting side of the specimen. This was not the case for the smaller specimens however, which can be attributed to the fact that reproducing a certain concrete composition facilitates with increasing specimen size.

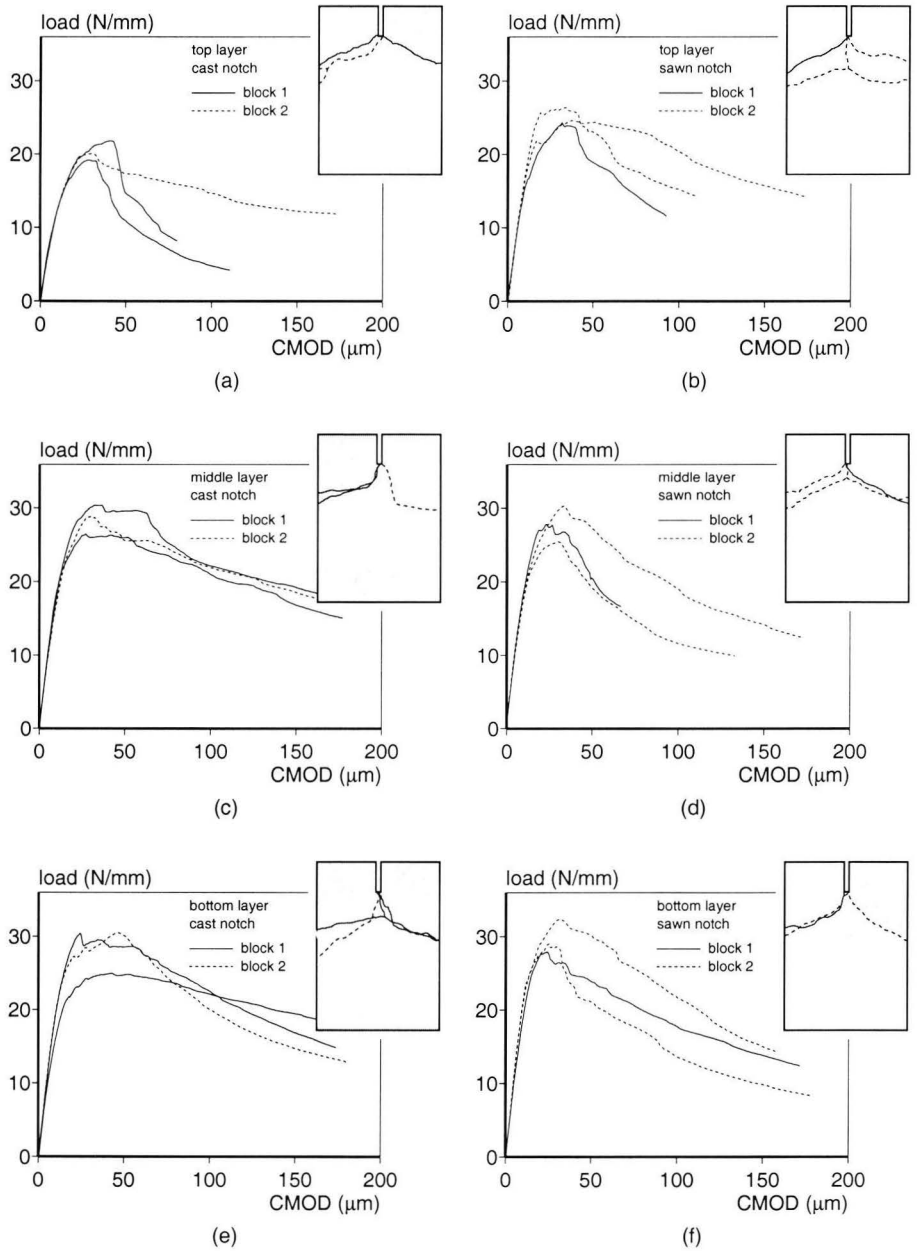


Figure 4.2 *Load-*CMOD *curves and final crack patterns for the tensile splitting tests on specimens originating from three layers of each concrete block.*

Table 4.1 *Mean values and standard deviations for the ultimate load F_u and the initial stiffness k for each layer.*

Layer	F_u [N/mm]		k [GPa]	
	Block 1	Block 2	Block 1	Block 2
Top	21.82 (2.59)	23.76 (3.26)	1.63 (0.16)	1.72 (0.18)
Middle	28.29 (1.99)	28.26 (2.49)	2.12 (0.08)	2.10 (0.14)
Bottom	27.84 (2.72)	30.69 (1.64)	2.15 (0.13)	2.43 (0.08)

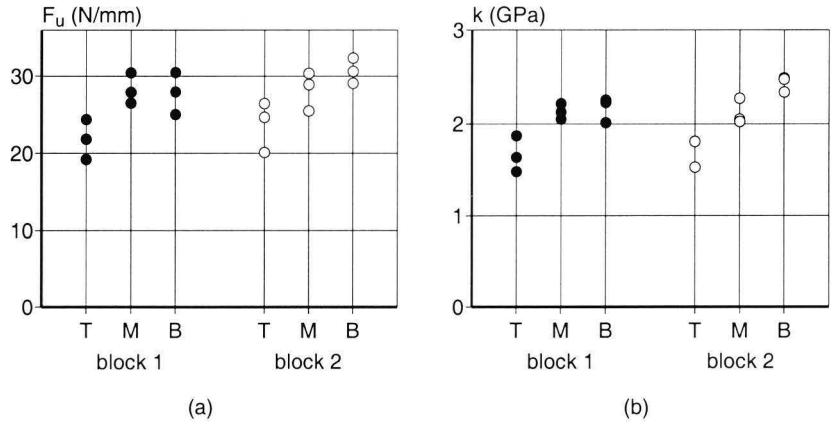


Figure 4.3 *Values for the ultimate load F_u (a) and the initial stiffness k (b) of the splitting tests.*

To allow for a broader use of the obtained stiffness values over the block thickness, the specimen stiffnesses k have been converted to Young's moduli E using an inverse method (see [103] for details). In short, the values for the Young moduli have been derived using a linear elastic finite element calculation of a splitting test in combination with the measured k values. The resulting mean values and standard deviations for E are summarized in Table 4.2. In addition, also the mean value of E is given, measured during uniaxial compression tests on three prisms with dimensions $100\times100\times400$ mm^3. These prisms were cast in one layer and compacted on a vibration table, contrary to the blocks from which the tensile splitting specimens were sawn. Despite the manufacturing differences, it is still noteworthy that even Young's moduli of the bottom layer from the blocks are still lower than those of the prisms. Similar observations were made by Stroeven [80]. He found that the average value for the Young modulus of small concrete volumes, was significantly lower than the overall Young's modulus of a concrete volume which was several times larger.

4.2.4 Conclusions

To get an insight into the variation of the concrete strength and stiffness parallel to the direction of casting, a series of verification tests was carried out. These tensile splitting tests

Table 4.2 *Average values and standard deviations for computed and experimentally determined Young modulus (E).*

Layer	E [GPa] Block 1[1]	Block 2[1]	Prism[2]
Top	20.93 (2.28)	22.11 (2.51)	
Middle	27.09 (1.19)	26.91 (1.94)	32.58 (1.08)
Bottom	27.54 (1.87)	30.99 (1.20)	

[1]computed, [2]experimentally determined

revealed a clear increase of both the strength and the stiffness going from the casting surface to the mould side of a concrete block. Although this concrete inhomogeneity in the present case can be attributed to the adopted casting method, similar effects will, to a lesser extent however, always be present in a concrete specimen. With the obtained results the larger deformations and crack initiation at the casting side of a specimen can be explained, which were frequently observed in the uniaxial tension tests.

4.3 Rotational capacity of hinge constructions

4.3.1 Problem description

The outcome of a uniaxial tension test is very sensitive to boundary influences, which was discussed in detail in Section 3.1. Although the application of freely rotating boundary conditions in the size effect tests was a starting point, it later became beneficial as well. When rotation of the specimens ends is prevented, the bending stiffness of the test frame comes into play since rotations of the specimen are counteracted by the set-up. With three test frames of different sizes it would be very difficult to ensure identical boundary conditions. By applying hinges between specimen and test frame this problem is reduced to a great extent.

Hinges are not perfect however, and it is difficult to tell which moment capacity is still allowable without noticeably affecting the experimental result. After the analysis of the preliminary tests it was found that in many tests snap-through behaviour occurred. In such cases a sudden load drop was observed in the descending branch. Simultaneously, the deformations at the side of the specimen opposite to the side of test control increased strongly. This phenomenon will be discussed in detail in the next section, here it is just mentioned because at that time it gave rise to doubts with respect to the rotational capacity of the hinge constructions. The phenomenon looked similar to the well known "bumps" which are found in the descending branch of uniaxial tension tests with fixed boundary conditions, and could therefore indicate that the moment capacity of the hinges was too large.

It was decided to conduct a series of uniaxial tension tests which were similar to tests that were previously carried out [92]. Those tests focused on the differences between rotating and fixed boundary conditions and served therefore as a basis for the verification tests.

4.3.2 Specimens and testing procedure

Since the verification tests had to show the presence, or rather the absence, of any influences of the experimental set-up on the test result, effects of the specimen shape had to be excluded. In this respect one has to think in particular of the shape of the cross section, which is known to influence the place of crack initiation in a uniaxial tension test. In case of a rectangular cross section cracks will always initiate at a corner. For a circular cross section on the other hand, no predestined crack initiation takes place [89, 88]. Hence, cylindrical specimens were used. To avoid the directional preference for crack propagation which is induced by the load eccentricity, the specimens were loaded concentrically.

For practical reasons, the tests were conducted in the small and the intermediate-sized set-up only. The dimensions of the specimens are shown in Fig. 4.4, where it is mentioned that the lengths were kept equal to those of the B and the C specimens. To facilitate a comparison of the results a notch was made along the circumference of the specimens. Thus failure would always occur at mid length.

The specimens were manufactured from two concrete cubes with a width of 300 mm, and were placed in the climate room after being demoulded (20°C , 95% R.H.). Two weeks after casting, four cylinders were cored out of each block parallel to the direction of casting. The short cylinders were obtained from the large ones by cutting off the outer parts from two cylinders of each block. Thus, the notched middle planes of all specimens originated from the same height in the block. After manufacturing of the cylinders had been completed, they were placed in a fresh tap water basin in the laboratory. The cylinders were tested four weeks after casting. During test preparation the notch was filled with wet cloth and covered with tape, which were both removed before the test was started.

To control the test four LVDTs with a measuring length of 75 mm were placed around the notch (see Fig. 4.4b). All tests were conducted similarly to the size effect tests, i.e. by using the maximum signal of the four LVDTs for feed-back.

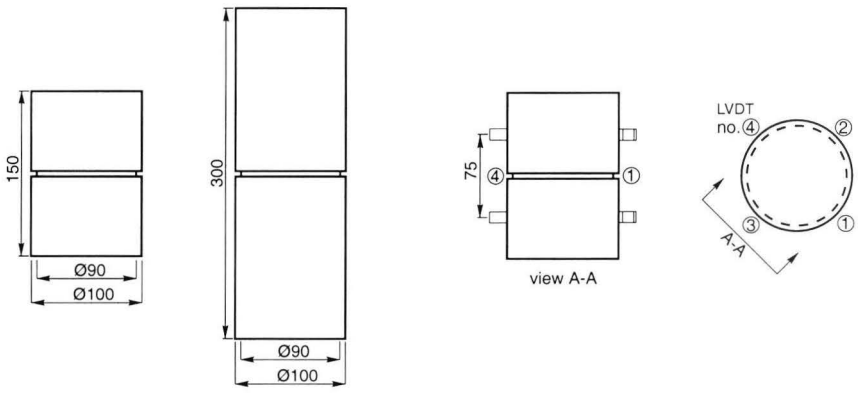


Figure 4.4 Applied specimens (a) and placement of the LVDTs *(b). Measures in mm.*

4.3.3 Test results

A general observation for uniaxial tension tests with rotating boundary conditions on cylindrical specimens is that the deformations along the circumference of the specimens increase continuously. This was also the case for the present tests, as is shown in Fig. 4.5a for a test which can be considered representative. Note that the result concerns a test on a 300 mm cylinder in the intermediate-sized set-up. Since the dimensions (and thus the moment-capacity) of the hinges increased with the size of the set-up, the tests on the 300 mm cylinders are more critical than those on the short cylinders conducted in the small set-up.

Although an inspection of the individual force-deformation curves did not reveal limitations of the rotational capacity, a quantitative verification was carried out as well. Using the deformations measured by the four LVDTs the specimen rotations in the in-plane and the out-of-plane direction can be computed. These rotations are denoted φ_1 and φ_2 respectively, and follow from

$$\varphi_1 = 360\left[\frac{(\delta_1+\delta_2)-(\delta_3+\delta_4)}{2r\sqrt{2}}\right], \qquad \varphi_2 = 360\left[\frac{(\delta_1+\delta_3)-(\delta_2+\delta_4)}{2r\sqrt{2}}\right] \tag{4.1}$$

where for r the radius of the unnotched specimen has been taken. For fixed boundary conditions these rotations are found to be close to zero, and if a small increase occurs, it is later followed by decrease as is shown by the thick lines in Fig. 4.6. When rotations of the specimen are not restricted however, φ_1 and φ_2 should increase irrespective of the magnitude of the rotation. Looking at Figs. 4.6a and b it may be clear that the specimens could rotate freely. The curves of Fig. 4.6a however, do show a deficiency of the hinge construction in the small set-up. All specimens fractured namely in the same way, which is indicated by the fact that the in-plane (φ_1) and out-of-plane (φ_2) rotations are consistently grouped. From the definition of φ_1 and φ_2 follows that the crack always must have initiated under LVDT 2, followed by propagation towards LVDT 3. The individual LVDT readings of all verification

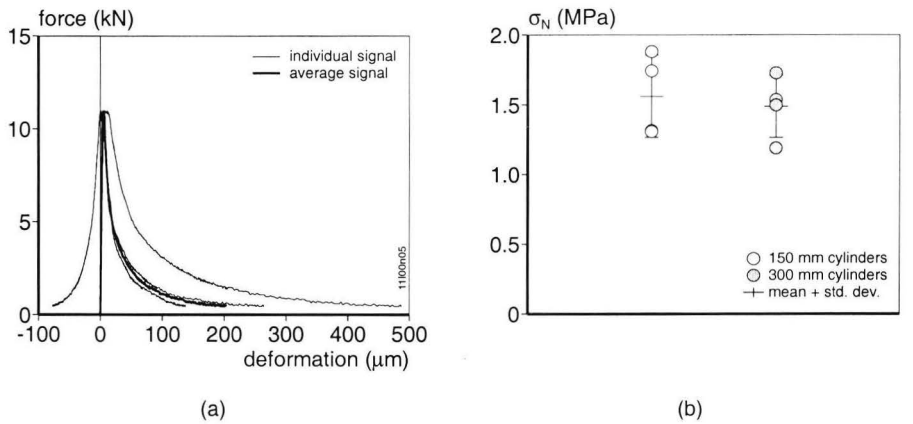


Figure 4.5 *Typical result for the deformations measured along the circumference of a 300 mm cylinder (a) and strength results for all verification tests (b).*

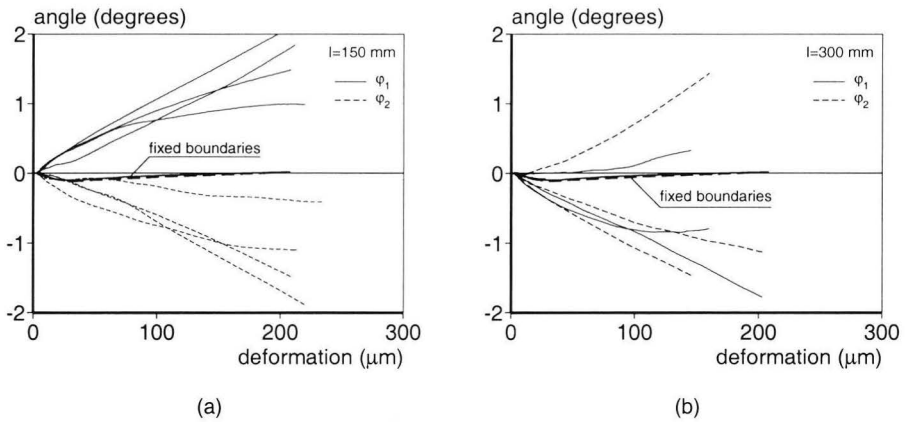


Figure 4.6 *Development of the rotations in the in-plane and the out-of-plane direction for the tests on cylinders with a length of 150 mm (a) and 300 mm (b).*

tests confirm this suspicion, meaning that the smallest pair of hinges exhibits directionality. A possible explanation could be that the pendulum bar at the right back side is slightly longer than the other bars, thus causing an unequal distribution of the external force. It is unlikely however that this strongly influences the peak strength, see Fig. 4.5b. The strength values for the short and the long cylinders are comparable which shows that in this respect the two hinge constructions perform similarly. Note that the strength values actually *must* be comparable. According to strength theory, only in case of unnotched specimens a lower strength could be expected for the 300 mm cylinders. By applying a notch however, and supposed the stress concentration caused by the notch overrules any material structural effects, the effect of volume differences between the short and the long specimens disappears because now the plane of crack initiation is fixed. Hence, no statistical size effect will occur.

4.3.4 Conclusions

The tests on centrically loaded cylindrical specimens showed that free rotations of the specimen ends could take place in both the small and the intermediate-sized test set-up. It was also found however, that the smallest pair of hinges exhibits directionality which caused consistent crack initiation at the right back side of the specimen. Despite this directionality, a comparison of the tensile strength values which were obtained in each set-up did not show consistent differences.

4.4 Effect of test control

This section varies slightly from the other sections in the present chapter because the discussions do not concern a separate, strictly defined series of experiments. Instead, the tests which are described were part of the approximately 75 preliminary tests carried out to check the experimental set-ups and to study the effect of various parameter settings on the exper-

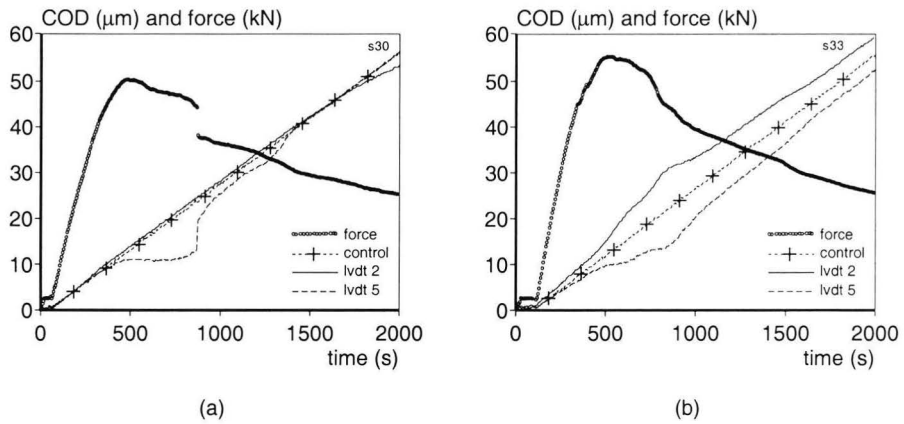


Figure 4.7 COD *signals for a test with* MAX *control (a) and* AV2 *control (b) respectively.*

imental result. In these preliminary tests, which were mainly carried out on type D specimens, snap-through behaviour was frequently observed. This behaviour was characterized by a sudden increase of the deformation at the side of the specimen opposite to the side of deformation control (see Fig. 4.7a). Simultaneous with the deformation increase a load-drop occurred. At first, this typical behaviour was suspected to be induced by a certain moment capacity of the hinges as was discussed in the previous section. Later however, it was recognized that the snap-through behaviour could be due to the type of test control which was applied (see [97] for a detailed elaboration).

The feed-back signal which has been used in the tests was the maximum deformation measured by one of the control LVDTs. In Fig. 4.7a LVDT 2 and LVDT 5 correspond with the two control LVDTs in the middle and at the right side of a D specimen (see also Fig. 3.22). LVDT 2 is glued to the front side, LVDT 5 to the back side of the specimen. The maximum deformation is measured under LVDT 2, which is therefore used to control the test. When at t=900 seconds the deformation under LVDT 5 at the back side of the specimen suddenly increases, this is not "noticed" by the control system since the signal of LVDT 5 remains smaller than the current feed-back signal. A possible scenario could therefore be that along with the deformation increase under LVDT 5 also the total axial deformation increases. This would result in an immediate decrease of the external load by the control system which is reflected by the load-drop. In addition to the tests with the regular, "MAX" control, additional

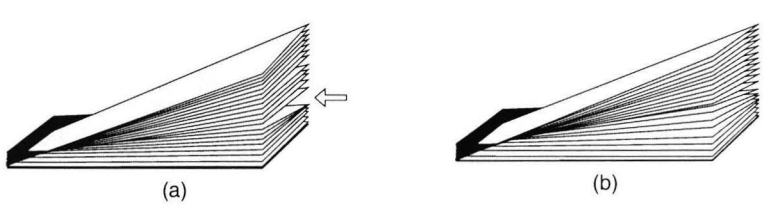


Figure 4.8 Deformation of the specimen middle under MAX *(a) and* AV2 *(b) control.*

tests were conducted in which the type of test control was varied. In these tests the average signal of LVDTs 2 and 5 was used as control signal (AV2 control), as well as the average signal of all four LVDTs around the specimen middle (AV4 control).

A typical result of a test with AV2 control is shown in Fig. 4.7b. Since the deformation measurements at both the front and the back side of the specimen are incorporated in the control signal, no unstable post-peak behaviour is observed anymore. The fact that the deformations of the specimen now increase more gradually is also reflected by Figs. 4.8a and b. The figures show schematically the deformations measured by the four LVDTs at the corners in the middle of the specimen until a post-peak load level of 25 kN. Whereas for MAX control a displacement jump is found at the back side of the specimen, this jump does not occur when AV2 control is applied. Instead of the average signal of only two LVDTs also the average signal of all four LVDTs can be used for test control. From the tests in which this AV4 control was applied however, only one out of four could be conducted in a stable manner. Because of the dimensions and the asymmetry of the cross section, the difference between the average signal and the maximum signal probably became too big.

It must be realized that the type of test control which is applied can induce or prevent (locally) unstable crack growth. This can be illustrated as follows (see also Fig. 4.7). For AV2 control the deformations measured by both control LVDTs are monitored, although the signals are averaged and thus damped. A test with MAX control is considered, where the signal of LVDT 2 is used for feed-back. If the deformations under LVDT 5 (on the opposite specimen side) start to increase, bending of the specimen in the out-of-plane direction will take place. As a consequence the deformations measured by LVDT 2 decrease. This will however not be allowed by the control system, which might even compensate the decreasing deformation of LVDT 2 by increasing the external force. If this would happen it would be the exact opposite of the desired action of the control system. The crack propagation at the back side of the specimen should namely be controlled rather than stimulated.

MAX control is not ideal since crack growth can easily take place outside the controlled area without being noticed by the control system. When instead an average signal of two or more LVDTs is used for test control this problem is solved, but due to the averaging the control signal becomes too weak. Especially for large dimensions of the cross section in combination with rotating boundary conditions a considerable difference can develop between

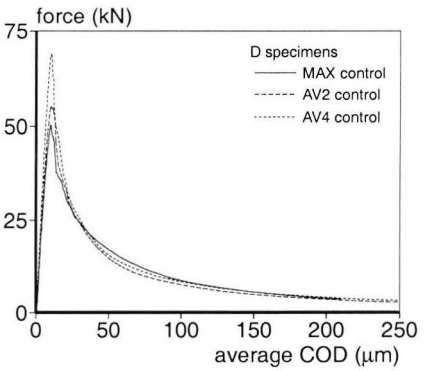


Figure 4.9 Average COD *curves for* D *specimens tested with* MAX, AV2 *and* AV4 *control.*

the maximum signal and the average signal. Surely this can be overcome by amplifying the control signal but then also the noise increases whereas the accuracy remains the same. A method that, because of a lack of time, could not be applied here anymore, but which seems promising in the light of the foregoing discussion, would be *rate* control. If the LVDT measuring the maximum deformation rate would be used for feed-back, test control would always focus at the location of crack growth which is exactly as it should be.

The remaining question is whether the average load-deformation response of the specimen is influenced by the type of test control. Partly, this question is answered by Fig. 4.9. In the figure, the average deformation signal of the four LVDTs around the specimen middle is shown for three tests with different types of test control. Apart from the variation in ultimate load the curves show a strong resemblance. This indicates that despite apparent differences between the deformation readings of the individual LVDTs, the average load-deformation response of the specimens does not seem to be influenced by the type of test control.

With respect to the ultimate load which is recorded in a test, some additional remarks have to be made. Because of the age difference of the tests shown in Fig. 4.9 (MAX: 59 days, AV2: 109 days and AV4: 140 days), no definite conclusions can be drawn with respect to a possible relation between the ultimate load and the type of test control. Differences in deformation rate for instance, could have played a minor role however. Since the *applied* deformation rate was the same in all tests, the *actual* deformation rate differed. The difference in actual deformation rate is simply due to the fact that an average signal is smaller than a maximum signal. Because of the larger deformation rate a slightly higher strength might be found for the tests in which an average deformation signal is used for test control (see e.g. [55]). Another aspect concerns the placement of the control LVDTs. In some tests with MAX control on prisms, it almost seemed as if the main crack eventually developed under the LVDT which was placed closest to the edge of the specimen. If this would be true, it would mean that for prismatic specimens the spot where failure will eventually take place could be depicted by the placement of the control LVDTs. Tests by Van Mier showed that the position of the control LVDTs can influence the value of the ultimate load as well [90]. In his tests the control signal was varied between the average signal of two LVDTs in the middle of the specimen, and the average signal of four LVDTs at the specimen edges. In the latter tests a higher strength was found. The reason was that the control LVDTs positioned at the edges prevented large deformation gradients to develop over the specimen width. For the specimens with middle control these deformation gradients *did* develop leading to lower values of the ultimate load.

Although some of the previous considerations are rather speculative, they could be interesting to be studied in more detail. Especially in discussions on material behaviour and characteristic material parameters, a thorough knowledge of these external influences on the experimental result is essential.

4.5 Influence of the test set-up

4.5.1 Problem description

In Section 3.3.1 the experimental set-ups were described in which the size effect tests have been carried out. It was mentioned that three different test frames were used, each with

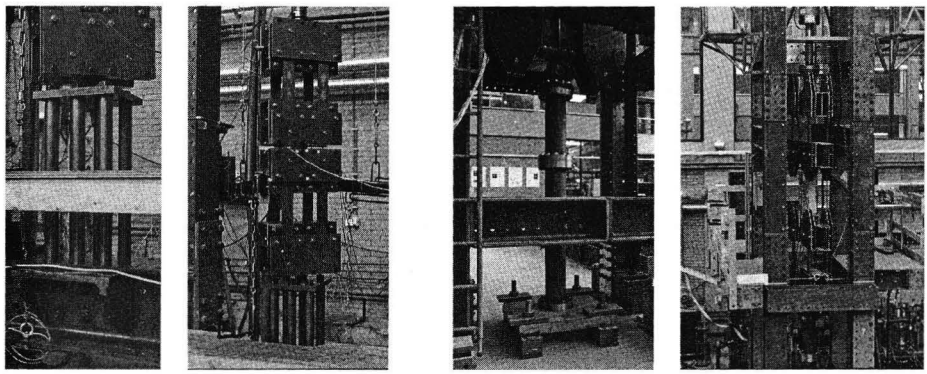
its own hinge construction, hydraulic cylinder and control unit. In each hinge construction specimens of two sizes were tested. The hinges were designed for the largest specimen (type B, D and F) to be tested in the hinge which was placed in the small, intermediate and large loading frame respectively. This actually meant that specimen type A, C and E was placed in an oversized hinge construction.

Although the choice for three experimental set-ups had to be made because of practical considerations, it was realized that it could have implications for the test results as well. Generally speaking, test results incorporate material as well as structural behaviour, where the latter behaviour is induced by among others boundary effects which incorporate influences of the test frame. This influence of the test frame has always been a hot issue in discussions on tensile testing. A coupling between the (in)stability of a uniaxial tension test and the axial as well as the rotational stiffness of the test frame resulted in minimum requirements for these stiffnesses in order to obtain stable tests, e.g. [64, 31, 39]. As soon as closed-loop control systems were applied the frame stiffness became less crucial for test stability, although it was recognized that boundary conditions strongly affect the result of a uniaxial tension test, e.g. [84, 118, 22]. To see whether a noticeable effect of the experimental set-up is present in the current test results, additional experiments were carried out. These experiments comprised uniaxial tension tests similar to the tests of the main series, but now specimens of a specific size were tested in a larger hinge construction than the one that was normally used. Since the larger hinge construction was placed in a larger test frame, the latter was also varied. Possible effects of the experimental set-up on the test result could then be distinguished by comparing the outcome of the tests on specimens tested in their "own" frame, and the ones tested in a larger frame.

4.5.2 Specimens and testing procedure

Boundary effects can be illustrated most clearly when they are strongly exaggerated. Therefore specimen type B and D were tested in a larger set-up. Consequently, they were tested in a hinge construction which was four times oversized instead of two times as in the regular tests. To compensate for the smaller height of the B and D specimen, the lower hinge of the intermediate-sized and the large set-up respectively was moved upward. The extra space was filled by six massive steel rods with a diameter of 50 mm in case of the intermediate-sized frame, whereas a massive steel column with a diameter of 180 mm was placed under the lower hinge of the large frame (see Figs. 4.10a and c). The large area of the spacers had to ensure that in the verification tests the elastic deformations of the experimental set-up would not increase compared to the regular tests.

The specimens which were used for the verification tests originated from the castings of the main size effect tests (series I). Since the verification tests were conducted after the main test series had been completed, by then the specimens had reached ages between 150 and 220 days. For this reason the results of the verification tests were not only compared to the results of the main series, but also to new test results obtained in the regular frames. Thus, the specimens were tested in pairs, both coming from the same casting but tested in different set-ups.



(a) (b) (c) (d)

Figure 4.10 *Upward translation of the lower hinge construction in the verification tests for the intermediate-sized set-up (a) and the large set-up (c). Figures (b) and (d) give an overview of the two experimental set-ups.*

4.5.3 Test results

If structural influences of the experimental set-up would be present in the test result, this could first of all be reflected by the average force-deformation curves. In Fig. 4.11 the curves of the verification tests have been gathered with the force-deformation curves for the B and the D specimens which were recorded in the main test series. Figures 4.11a and c show the results for the specimens tested in their "own" set-up. Apparently the age difference hardly influenced either the stiffness or the softening curve of the specimens, since the results for the verification tests are in, or close to the band with the original results. The softening curves for the specimens which were tested in the larger set-up (Figs. 4.11b and d) are more spread, although the scatter in the force signal makes a comparison with the original curves rather difficult. This scatter however, also illustrates a problem which was encountered in the verification tests. By testing specimens in a hinge construction which was strongly oversized, the weight of the hinge constructions became relatively large compared to the self weight (and dimensions) of the specimens. Thus, it could happen that the system of specimen and hinges started to vibrate after for instance sudden crack growth had occurred. If this happened, restoring test control in order to damp out the vibration was practically impossible. When instead of the fluctuating force-deformation signals the envelopes of these curves are compared with the gray shaded areas, the agreement is still good.

Besides the softening curves, also the peak loads for tests in different set-ups can be compared. In Fig. 4.12b the nominal strengths following from the verification tests on the D specimens are compared with the results of the main series. Whereas the gray circles are on average the same as the original values, the white circles are situated consistently lower. Theoretically, this could be due to the fact that the specimens were tested in an oversized set-up. If so, the same result would have to be found for the type B specimens in Fig. 4.12a. Since the white circles are there situated above average, different effects must have been at play for the B and the D specimens. In the tests on the D specimens (Fig. 4.11d) vibrations

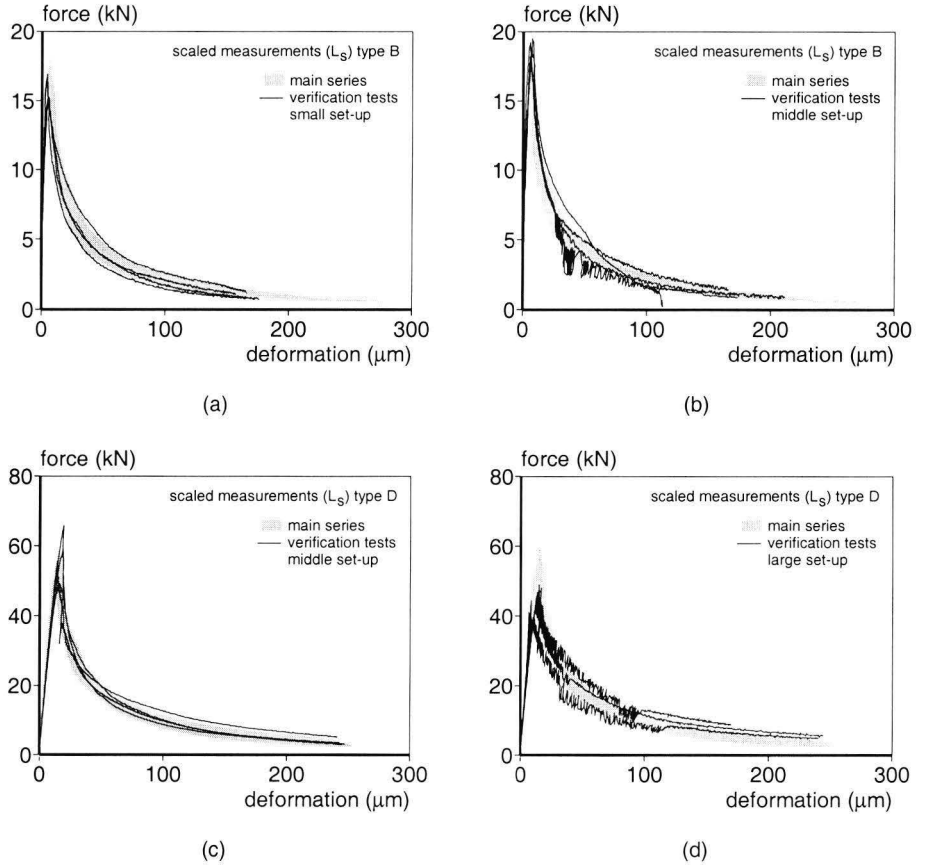


Figure 4.11 *Force-deformation curves obtained in both the small and the intermediate-sized set-up (a,b) and the intermediate-sized as well as the large set-up (c,d).*

occurred already before peak load. The low nominal strength values found in those tests are therefore likely to be caused by the vibrations in the large set-up. Hence, the influence of the control system and the dimensions of the set-up in relation to the specimen dimensions are coupled. In other words, the fact that the specimens were tested in a larger set-up indirectly influenced the experimental result. With respect to dimensions of the set-up one must think of dynamic effects due to the length of the hydraulic system. These effects can affect the oil pressure, and thus the servo valve and the hydraulic actuator.

In two out of four tests on the B specimens in the intermediate-sized set-up, it was observed that the crack propagated in the out-of-plane direction instead of from the right to the left side. As a consequence, the effect of the load eccentricity disappears and a higher ultimate load can be found. This observation could be an explanation for the fact that, on average, the nominal strength values for the B specimens tested in the intermediate-sized set-up (white circles) are relatively high. The larger dimensions of the hinges in the intermediate-

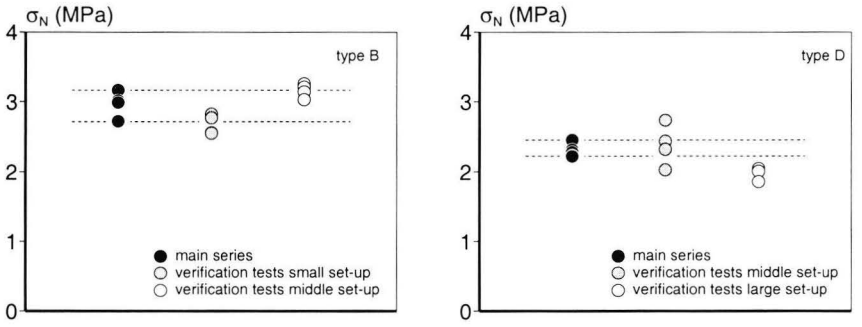


Figure 4.12 *Nominal strengths resulting from the verification tests compared to the values which were found in the main series. The dashed lines mark the range in which the results of the main series are situated.*

sized set-up can have reduced the influence of the eccentricity of the B specimens. It is mentioned that in the main test series, crack propagation in the out-of-plane direction was only observed incidentally.

4.5.4 Conclusions

By testing specimens of the same size in two different set-ups, it was found that problems are introduced when the discrepancy between the size of the specimen and rest of the set-up becomes too large. Consequently, test stability and increasing structural effects influenced the experimental result. It must be emphasized however, that these effects can not be attributed to a set-up by itself. Apart from local variations, the shape of the softening curves of specimens which had been tested in different set-ups hardly varied. The fluctuations in nominal strength which were found are linked to the verification tests and the way they were designed. A translation of the findings of these verification tests to the main test series is therefore not only difficult, but would probably also lead too far.

Chapter 5

Results of size effect tests

5.1 Correction of experimental data

The results which are presented in this chapter are directly retrieved from the experimental data. Compared to the raw experimental data however, the data which were used have been corrected in two ways. The first correction concerns the subtraction of the self weight above the final crack. Secondly, the measured deformations had to be corrected in order to find the origin of the force-deformation curve, which could not be done during the experiment.

5.1.1 Self weight

During a test, the external load was measured by the load cell which was positioned directly under the hydraulic actuator in all experimental set-ups (see Figs. 3.13, 3.14, 3.15 and 3.21). Before the specimen was placed in the experimental set-up the load was calibrated to zero. Consequently, the weight of the upper hinge construction was excluded from the measured external force. The weight of the upper loading platen and the weight of the specimen part above the final crack however, were still included in the external force and had therefore to be subtracted. The values needed for this weight correction were measured after the test had been completed. For practical reasons it was more convenient to do this outside the set-up. Hence, the specimen would be removed from the set-up in one piece, i.e. before it had been fractured completely. The two specimen halves were then separated manually, followed by the weighing of the two specimen halves including the loading platens.

Note that due to the position of the load cell and the flexible nature of the set-up, the external load can be subdivided in two parts. The active part is exercised by the hydraulic actuator and can be controlled by the closed loop control system. The second part of the external load however, is passive. It comprises the self weight of the lower specimen half as well as the lower hinge construction. Although this part of the load is automatically recorded by the load cell it could not be controlled, since building up compressive forces was impossible because of the hinges.

5.1.2 Correction of the force-deformation diagram

In order to find the origin of a force-deformation curve, a uniaxial tension test is usually started in compression. A deformation scan at zero load level can then be used to correct the

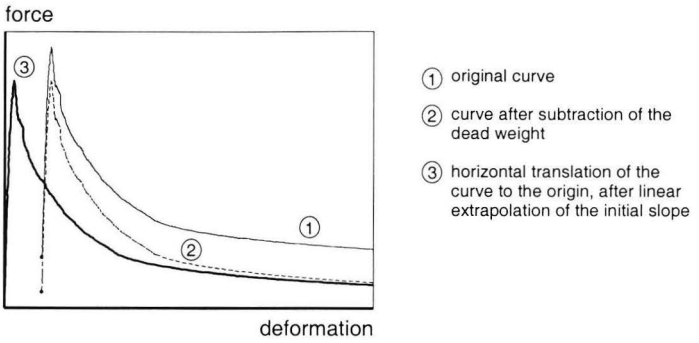


Figure 5.1 Corrections made on the original experimental data.

deformations which were measured during the test. In the present tests however, this method could not be adopted since no compressive forces could be applied due to the flexibility of the hinges. Moreover, unless a certain minimum tensile load was present, the exact load was even unknown. This uncertainty was caused by the lower hinge construction, whose self weight was only fully activated when the hinge was (vertically) stretched. Because of the previous reasons the origin of the force-deformation diagram was retrieved through back analysis. After the raw experimental data (① in Fig. 5.1) had been corrected for the self weight (② in Fig. 5.1), the initial slope of the curve was linearly extrapolated until the intersection point with the x-axis. Thus, the deformation value is obtained which has to be used to correct the data, leading to the final curve which is denoted by ③ in Fig. 5.1. Since the measured deformations depend on both the measuring length and the position of the measuring device on the specimen surface, the described correction procedure has been carried out for all individual LVDTs.

5.2 Concrete tests (I): specimens stored in laboratory

5.2.1 Force-deformation curves

The tests on the concrete specimens which had been stored in the laboratory (series I), will for the sake of simplicity be referred to as the DRY tests. In Figs. 5.2a and b the force-deformation curves for all individual tests are presented. For each specimen size at least four successful (i.e. with a complete softening curve) tests were conducted (see Figs. 5.2a and b). The deformations in Fig. 5.2 are the average of the scaled measurements (L_s) in the middle of the specimen at the front and the back side (see Fig. 3.23). Because of the scaled measuring length, the initial slope of the curves is the same since also the force scales with the cross section of the specimen. Just beyond peak load, the slope of the softening curve with respect to the vertical axis decreases for larger specimen sizes. This is due to the increase of the elastic deformations within the measuring length, which even results in a negative slope for the F specimens. Note that since these deformation signals were only measured and not used as feed-back signal, the negative slope of the softening curve beyond peak did not cause problems with test control. If on the other hand these scaled measurements would have

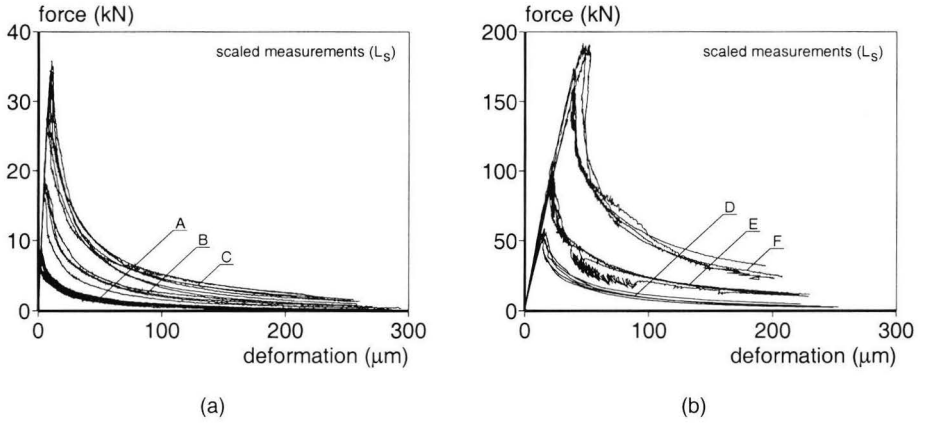


Figure 5.2 *Overview of all force-deformation curves which were obtained for specimen type* A, B, C *(a) and* D, E, F *(b).*

been used as control signal, no post-peak behaviour could have been retrieved for the largest specimens because of snap-back. This increasing risk of snap-back behaviour for increasing measuring length was among others illustrated by Hordijk [42], and encountered in uniaxial tensile size effect tests by Ferro [26].

Testing the largest specimens was not more difficult than testing the smaller specimens due to the constant, small, measuring length and the use of the maximum rather than the average deformation signal for test control. In combination with the largest specimens, the adopted system for test control could however lead to experiments exhibiting constant, small, load fluctuations. Because of the shape of the specimens the preferential area for crack initiation increased with the size. Consequently, for the large specimens test control sometimes switched between LVDTs which were placed quite far apart. This phenomenon, as well as the fact that the response time of the largest test set-up was lower because of among others the length of the hydraulic system, could result in small load jumps. With respect to test stability, the stiffness of the largest test set-up did not cause special difficulties. Only during problems with a bad servo-valve in the hydraulic actuator of the large set-up, a stiffness effect was noticed. Due to the bad servo-valve small vibrations were encountered in some experiments, which hardly damped out because of the size of the set-up and the flexible character of the hinge constructions. These vibrations are reflected in some parts of the softening curves of the type E and F specimens. After replacing the servo-valve, vibrations were not noticed anymore.

Fig. 5.2 suggests that the nonlinearity which is observed before ultimate load is reached, increases with the size of the specimen. In order to get a better impression on this matter the total strains at ultimate load have been computed, both for the average scaled measurements (Fig. 5.3a) and for the control signal (Fig. 5.3b). By subtracting the elastic strain from the total strain at peak load, also the plastic strain has been computed for both measurements. In Fig. 5.3a it is found that the total strains at peak load decrease with increasing size of the specimen. In the next section it will be shown that the same trend is found for the nominal strength which indicates that the magnitude of the strains follows the external load. The

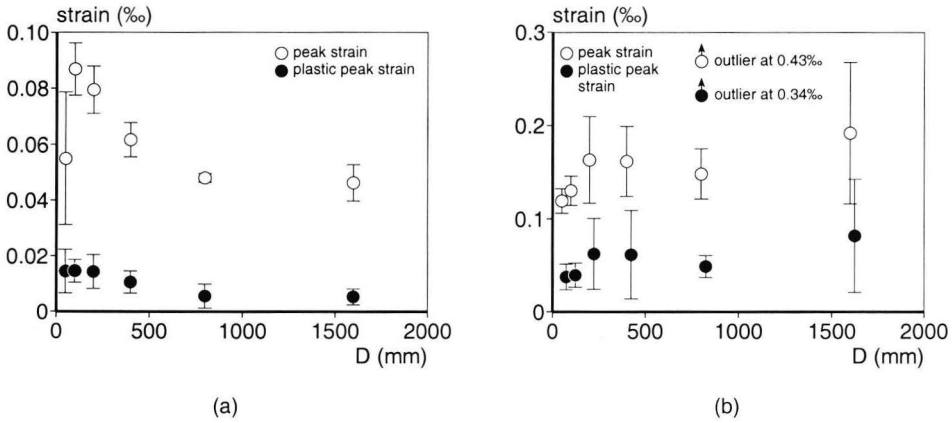


Figure 5.3 *Total strain and plastic strain at ultimate load computed from the average scaled signal (a) and the control signal (b).*

plastic strains, or the nonlinearity, appear to be constant for specimen type A, B and C, followed by a decrease for larger sizes. This indicates that scaled measuring lengths smaller than 120 mm (type C), do not cover the complete zone in which micro-cracking occurs. The size of this zone seems to be size independent, which follows from the decrease of the plastic strains for the three largest specimens. This picture is confirmed by Fig. 5.3b. Going from specimen type A to C, the position of the control LVDT is more and more inside the zone with stress concentrations along the edge in the specimen middle. The total strain at peak load, as well as the plastic strain therefore increase towards specimen type C. For even larger specimen sizes however, the highly stressed zone extends beyond the measuring length of the control LVDT which leads to approximately constant deformations within the measuring length.

With respect to the scatter in the total strains which have been computed from the scaled measurements (Fig. 5.3a), it is pointed out that this scatter is especially high for the smallest specimens. Since the measuring length for those specimens was only 30 mm, the initially large and later decreasing scatter can be related to the work of Müller [58]. He found a direct relation between the standard deviation of the strains measured on the surface of a uniaxially loaded concrete prism on the one hand, and the ratio of $d_{\max}$ and the measuring length on the other hand.

5.2.2 Nominal strength

Using the ultimate loads which were recorded during each test, the nominal stresses at failure were computed according to Eq. (3) in the chapter Symbols and Definitions. Thus, the size effect on strength is found for the present tests, see the bi-logarithmic plot of Fig. 5.4. The mean values and standard deviations are summarized in Table 5.1. For specimen type B and larger sizes, the nominal strength consistently decreases. The strength difference between the B and the F specimens was found to be as large as 37%.

For the smallest specimens, the strength values show a scatter which covers almost the

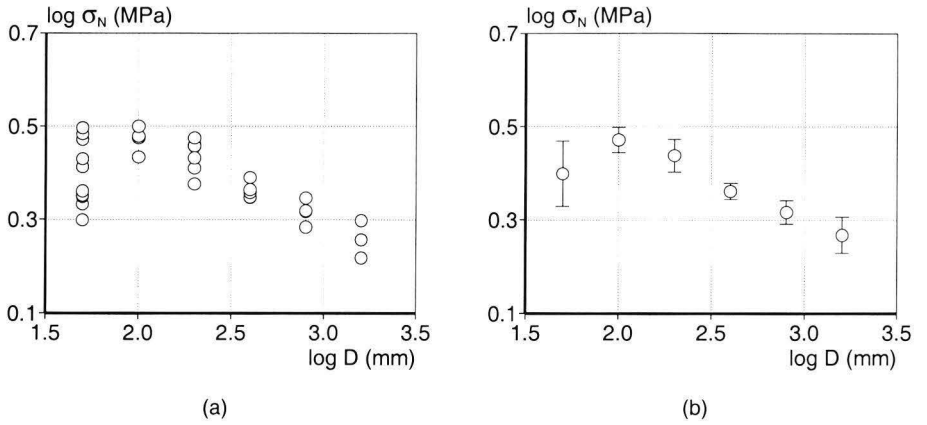


Figure 5.4 *Individual values (a) and mean values (b) of nominal strength σ_N vs. specimen size D. The specimen size D should not be confused with the specimen type* D.

complete range in which the strength results for the larger specimen sizes are lying. Partly this is due to the fact that ten tests were conducted on A specimens, a number which is much higher than for the other specimen types (see Table 5.1). This however, is only part of the explanation as will also be illustrated in Section 7.3. Another explanation for the large scatter of the A specimens is the small aspect ratio of $D/d_{\max} = 3.75$, leading to a too small specimen volume compared to the representative volume. Already during the design stage of the experiments it was doubted whether this aspect ratio would be large enough. Due to the shape of the specimens, failure will take place close to the middle of the specimen which has a width of only 30 mm in case of the A specimens. Whether an 8 mm aggregate, or more general one of the largest aggregates, is present in this middle section or not, can have a distinct influence on both the stiffness and the ultimate strength of the specimen. If such an aggregate is present large stress concentrations will develop in its vicinity. As a consequence, the ultimate load will reduce since the possibilities for stress redistributions are restricted because of the small dimensions of the cross section of the A specimens. The scatter in the strength values is similar to findings by Kadleček and Špetla [49]. They concluded however, that the maximum size of the aggregates could be as large

Table 5.1 *Mean values for the nominal strength of the concrete tests of the DRY series. The numbers between brackets indicate the number of tests and the standard deviation.*

Type (nr)	A (10)	B (4)	C (7)	D (5)	E (4)	F (4)
σ_N [MPa]	2.54	2.97	2.75	2.30	2.07	1.86
	(0.41)	(0.19)	(0.21)	(0.09)	(0.12)	(0.16)

as one third of the smallest specimen dimension. Yet, the smallest specimen dimensions are not only of importance with respect to the maximum aggregate diameter. Also the influence of wall effect on the experimental result will be strongly related to the dimensions of the specimen. Especially for the smallest specimens it will be evident that wall effect will be present in a considerable part of the smallest cross section. Consequently, a larger variation of the concrete strength can be expected for these specimens, as well as strength values which on average will be lower. With increasing size of the specimen, the influence of wall effect will fade away. The low strength of the A specimens is probably also partly due to a lower degree of hydration compared to the larger specimens. Since the smallest specimens have a large specific area they will easily dry out, leaving less water for hydration of the cement. Altogether the results for the smallest specimens should be considered with reservation.

The specimens of different sizes were cast using ten different batches of concrete. Although the four smallest specimen sizes of the DRY series were spread over the various castings, it could not be avoided that an order was present for the E and the F specimens. The F specimens originated from the last five castings whereas the E specimens came from the first five castings. Due to the fact that the first casting was in January, whereas casting ten was made in June, seasonal differences are present between the castings. These differences concern the conditions during and after casting in terms of temperature and relative humidity, which could have led to variations in the concrete quality. When looking at Fig. 3.2 it actually seems as if the average strength after 28 days was higher for the first castings. By correcting the results of the uniaxial tension tests with respect to the average batch strength, it was verified whether the size effect on the nominal strength was influenced by variations in concrete quality (see [100] for details). No clear influences were found however.

5.2.3 Fracture energy

The fracture energy, which can be seen as a (partial) measure for the ductility of a material, is often considered to be a material parameter. This means that the value should be unique, and thus constant, for a specific material which among others implies that the fracture energy must be independent of size. Most studies on the size dependence of the fracture energy show a tendency towards a constant value for large sizes. For small sizes however, the fracture energy increases with size. Planas, Elices and Guinea [27, 66, 25] pointed out that after corrections for different possible sources of energy dissipation, as well as the energy consumed in the tail of the softening curve, an almost size-independent fracture energy was found for three-point bend tests.

For the present tests the fracture energy G_F has been computed following the method which is outlined in the chapter Symbols and Definitions. Apart from the fracture energy for complete separation of the two specimen halves, also the fracture energy until a crack width of 180 μm is considered ($G_{F_{180}}$). In Fig. 5.5a both values for the fracture energy, based on the average scaled measurements in the middle of the specimens, are shown as a function of the specimen size. The global development for G_F as well as $G_{F_{180}}$ is comparable, indicating that the linear extrapolation of the force-deformation relation seems to be a reasonable assumption. Differences between G_F and $G_{F_{180}}$ increase slightly with size. This can be attributed to the relatively high load bearing capacity of the largest specimens at the moment the test had to be stopped.

The total work which is exercised by the external load can be subdivided in the work

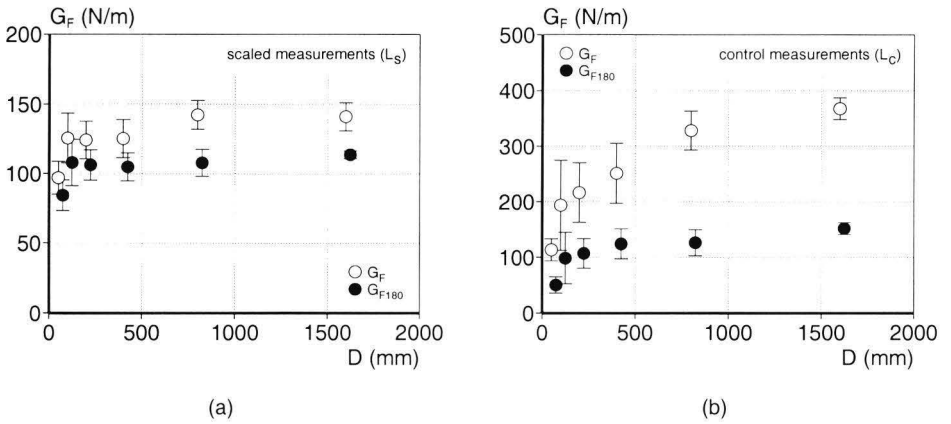


Figure 5.5 *Fracture energy for the DRY series, based on scaled measurements in the specimen middle (a), and control measurements at the specimen edge (b).*

exercised by the axial force ($W_{F_{ax}}$) and the work of flexure ($W_{F_{flex}}$). Hence

$$W_{F_{tot}} = W_{F_{ax}} + W_{F_{flex}} \tag{5.1}$$

If the work is computed using the measurements based on the scaled measuring length L_s, the flexural component $W_{F_{flex}}$ is omitted almost completely, leaving only $W_{F_{ax}}$. If, on the other hand, the total work is based on the deformations measured within the control measuring length L_c, $W_{F_{flex}}$ *is* included. This results in larger values for both G_F and $G_{F_{180}}$, as is illustrated by Figs. 5.5a and b respectively. Besides the contribution of $W_{F_{flex}}$, another reason for the higher G_F values of Fig. 5.5b compared to Fig. 5.5a is the fact that absolute deformations are used, rather than an average deformation composed from measurements on the front and the back of the specimen. The weaker convergence of G_F towards a constant value in Fig. 5.5b compared to Fig. 5.5a is due to the rotating boundary conditions. Rotations of the specimen come therefore into play, which means that along with the increasing width for larger specimens, larger deformations will be found at the edges of those specimens. Consequently, the fracture energy increases as well. In any case, in the light of the definition of the fracture energy, using an absolute deformation value at a specimen edge to compute the crack width can be questioned. The (average) crack width will be strongly overestimated, and via the work of fracture also the fracture energy. This problem is circumvented by using an average deformation value, like for the average scaled measurements. There, apart from the smallest specimens, an almost constant fracture energy is found. This could indicate that the relative amount of damage which develops during crack propagation is not strongly correlated with the size. It is emphasized however, that the thickness of the uniaxial tension specimens was kept constant at 100 mm. If something like a "process zone size" exists, it could be very well possible that for larger specimen sizes the thickness of the specimens is too small to enable such a process zone to develop fully. This could be the reason for the fracture energy going towards a more or less constant value. If the thickness of the specimens would have been larger, higher values for the fracture energy might have been found for larger sizes, meaning

Table 5.2 *Mean values for the fracture energy of the DRY series. The numbers between brackets indicate the number of tests and the standard deviation.*

	Scaled measurements		Control measurements	
Type (nr)	$G_{F_{180}}$ [N/m]	G_F [N/m]	$G_{F_{180}}$ [N/m]	G_F [N/m]
A (9)	84.5 (11.1)	97.0 (11.8)	140.7 (11.6)	190.8 (15.8)
B (4)	108.1 (16.8)	125.7 (18.0)	178.9 (36.7)	255.0 (64.7)
C (7)	106.3 (11.0)	124.2 (13.6)	185.8 (21.2)	273.6 (42.8)
D (5)	104.9 (10.1)	125.2 (13.7)	199.3 (21.7)	300.9 (43.2)
E (4)	107.8 (9.7)	142.3 (10.3)	201.0 (18.7)	362.7 (28.1)
F (4)	113.6* (2.8*)	141.1 (10.2)	221.6 (8.7)	394.3 (15.7)

* mean value and standard deviation based on 3 instead of 4 tests

that G_F would have continued to increase, thus converging towards a constant value for even larger specimen sizes. In this respect a series of wedge splitting tests is mentioned that was carried out by Trunk [82]. He found a continuous increase of G_F until a certain level, which among others depended on the maximum aggregate size which had been used.

The reason for the low G_F values of the A specimens remains unclear. To see whether the scatter in the nominal strength has been of influence on G_F, the individual G_F values of all tests have been normalized with respect to the nominal strength. The result is a value with the dimension of length, which can be seen as a measure for the ductility (Fig. 5.6a). Surprisingly, an almost constant increase of this value is found for increasing specimen size, and the sharp decrease in the value for the A specimens does not occur anymore. This does

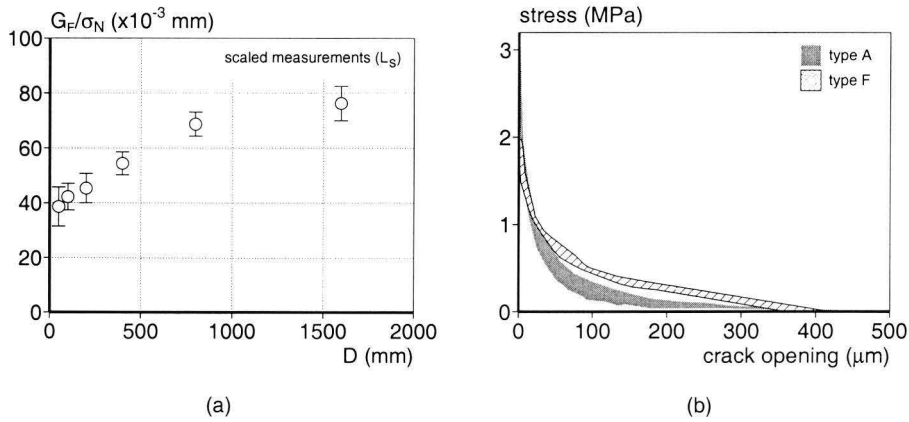


Figure 5.6 *Normalized fracture energy based on the scaled measurements (a), and band width for the stress-crack opening curves of the A and the F specimens (b).*

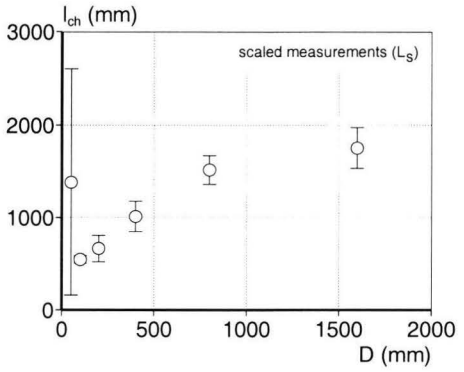


Figure 5.7 Variation of the characteristic length l_{ch} with the size of the specimen.

not only show that the influence of the nominal strength on G_F is considerable, but also questions designating a parameter like G_F, which is clearly influenced by a non-constant parameter like the strength, as a material parameter. When speaking purely in terms of ductility, an increase is found with size (Fig. 5.6b) which would be even more obvious after normalizing the curves in Fig. 5.6b with respect to the stress.

It should be mentioned that a measure for the ductility of a material, close to the one discussed before, is known as the characteristic length l_{ch}. The characteristic length is defined as [64]

$$l_{ch} = \frac{G_F E}{f_t^2} \tag{5.2}$$

where E is the Young modulus of the specimen, which for the present specimens is computed using the average scaled deformation in the middle of the specimen (see Eq. (7.8)). The tensile strength f_t equals the nominal strength. As Fig. 5.7 shows, also l_{ch} increases with size, similar to the values of Fig. 5.6a. The question which concerned the influence of the scatter in strength on the low G_F values of the A specimens, can not be answered however. Due to among others the short scaled measuring length of the A specimens (L_s = 30 mm), now the scatter in computed Young's moduli obscures any possible effect of the scatter in the nominal strength for the A specimens.

5.3 Concrete tests (II): specimens stored in climate room

The decision to store the specimens of the DRY series in the laboratory until the moment of testing, was mainly based on practical considerations. To check whether the curing conditions in the laboratory had a negative effect on the observed size effect because of for instance drying shrinkage, it was decided to conduct a second series of size effect tests. The specimens of this second, so called "WET", series comprised only the four smallest specimen sizes. These specimens are more easy to handle and could therefore be placed in a climate room under controlled conditions (20°C , 95% R.H.). Basically, the tests of the WET

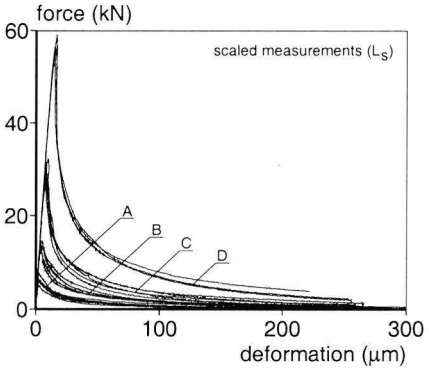


Figure 5.8 Overview of force-deformation curves for the specimens of the WET series.

series were carried out in the same way as those of the DRY series. The main difference is the number of used LVDTs, which for the WET series was restricted to the LVDTs needed for the control and the scaled measurements. Hence, the time needed for preparations, and in which the specimens could dry out, was reduced. In Fig. 5.8 the recorded force-deformation curves are collected, again based on the average scaled measurements in the middle of the specimens.

The values of the nominal strength which were found in the WET tests are listed in Table 5.3. As follows from Fig. 5.9, the strength of the specimens in the WET series is generally lower compared to the specimens of the DRY series. Furthermore, also the size effect on strength is different since the strength increases, instead of decreases, with the size of the specimens. The lower strength of the WET series can be related to results reported in literature. In [60] for instance, it is shown that the strength of concrete decreases, when being stored under conditions with increasing relative humidity. water. For concrete which has been stored under water, even lower strength results are found. The strength of concrete is suggested to be related to the cohesive forces between the solid particles [57]. Hence, for wet concrete these forces might be lower because of a decreased surface energy due to water adsorption. With this explanation for the lower strength in general, the question of the observed increase of strength with specimen size is still not answered.

Despite all precautions which were taken to prevent the specimens of the WET series from drying out, it might very well be that the specimens *did* dry out after they were taken out of the climate room. During the preparation of the specimens the sealing might have been insufficient which can have resulted in the development of eigen-stresses and thus lower values for the ultimate load. As soon as the test was started, the specimens were completely uncovered so that dehydration and the consequent increase of eigen-stresses could take place freely. Because of the extensive starting procedure for an experiment, as well as the low loading rate, the latter effect can have been considerable. Compared to the DRY series, where the eigen-stresses due to differential shrinkage had averaged out at the time of testing, the eigen-stresses in the WET series will have been much higher. Eigen-stresses would have the most significant effect on the behaviour of the small specimens because of their large specific area. For the D specimens only a small part of the cross section will dry out, meaning that the eigen-stresses would be less significant. This could be an explanation for the fact that

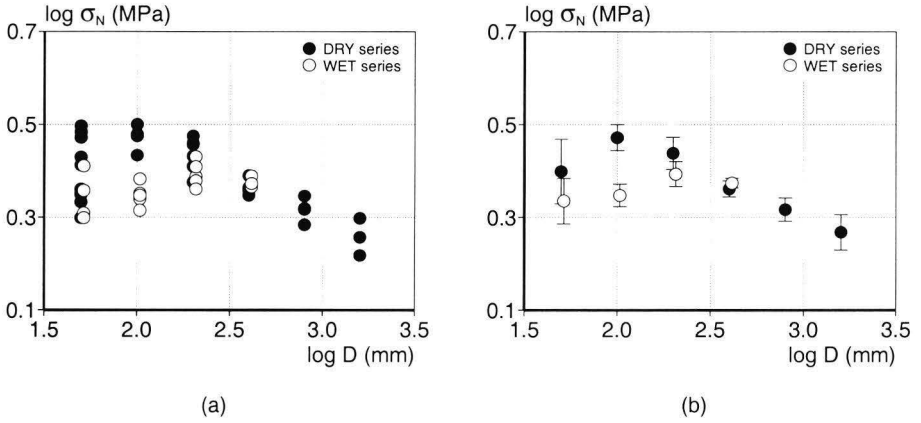


Figure 5.9 *Individual values (a) and mean values (b) for the variation of the nominal strength in the DRY and the WET series.*

the type D specimens from both the WET and the DRY series show similar strength values. Following this line of reasoning would also imply that for specimens larger than type D, the WET series might show the same size effect on strength as was found for the DRY series. The results of the present tests can be related to the work of other researchers. Hordijk [42], found a lower strength for specimens that were kept in a water basin until being tested, compared to specimens which had been placed in the laboratory 2 weeks prior to testing. This is in agreement with experiments conducted by Bonzel and Kadleček [15], which show the significance of eigen-stresses in concrete specimens which are taken out of the water and dry in air. The first 7 days after the specimens of a comparable concrete mix had been taken out of the water, a strong decrease of the tensile strength was measured. Afterwards however, the strength increased again. It is stressed that the foregoing does not imply that curing the specimens in air results in a higher strength than in a situation in which specimens are prevented from drying out. Mechtcherine [56] compared the uniaxial tensile strength for unsealed and sealed concrete specimens, and found higher values in the latter case.

The differences in nominal strength between specimen type A, B, C and D of the WET and the DRY series respectively, can also be deduced from the pre-peak force-deformation curves. In Fig. 5.10, the control signals of different tests are compared, which resemble the signal of the LVDT covering the area where crack initiation will eventually take place. Figs.

Table 5.3 *Mean values for the nominal strength of the concrete tests of the WET series. The numbers between brackets indicate the number of tests and the standard deviation.*

Type (nr)	A (5)	B (5)	C (5)	D (4)
σ_N [MPa]	2.17 (0.25)	2.23 (0.13)	2.48 (0.16)	2.37 (0.06)

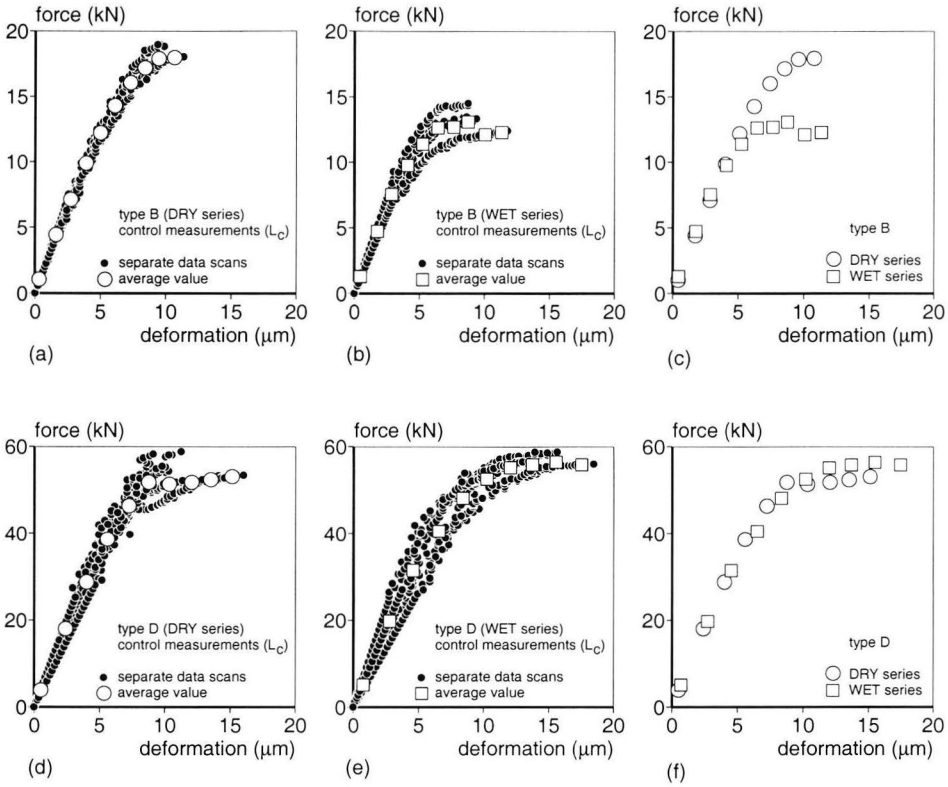


Figure 5.10 *Pre-peak load-deformation response of type* B *specimens (a)-(c) and type* D *specimens (d)-(f) for the DRY series (a),(d) and the WET series (b),(e). The filled circles represent the individual scans of all tests whereas the large white symbols are the average values of all tests.*

5.10a,b,d and e show the individual scans which were made during all tests on type B and type D specimens of the WET and the DRY series. In addition, also the average values for all tests have been computed which are compared in Figs. 5.10c and f. The latter figures show that for the type B specimens of the WET series considerable pre-peak nonlinearity is found, whereas for the B specimens of the DRY series the load increases linearly almost until peak load. Although these deformation differences are found for some of the D specimens as well, the peak loads are far less affected.

A final remark concerns the scatter of the test results. Just like in the DRY series, also for the strength values of the A specimens in the WET series a larger scatter is found than for the other specimen sizes. Contrary to the DRY series however, the number of results is now constant for all specimen types. These results therefore support the conclusion that the aspect ratio of $D/d_{\max} = 3.75$ for the type A specimens was too small. Furthermore, also for the specimens of the WET series, wall effect is expected to have a distinct influence on the experimental result. Due to the wall effect, the concrete in the boundary zones of

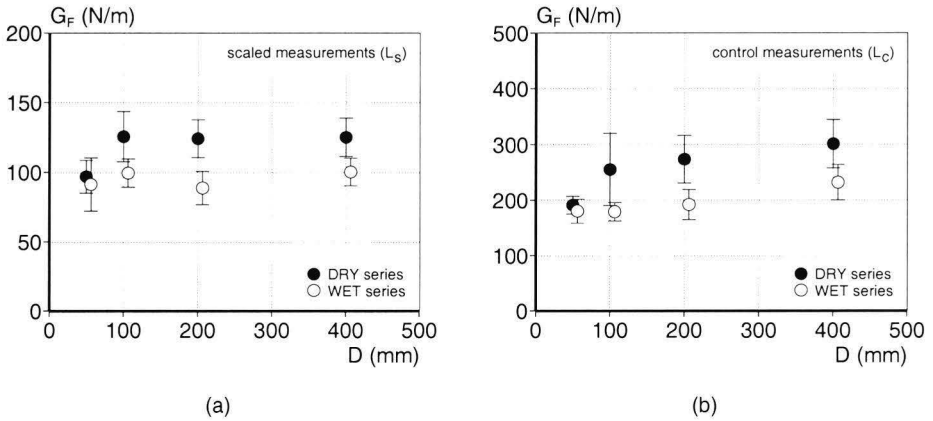


Figure 5.11 *Fracture energy for the WET series, based on scaled measurements in the specimen middle (a), and control measurements at the specimen edge (b).*

the specimens exhibits a higher porosity and can therefore dry out more quickly than the inner specimen parts. Hence, the eigen-stresses which develop due to drying out of the outer specimen zones are expected to be highest for the A specimens. For larger specimens the part of the cross section which dries out will be smaller, meaning that also the eigen-stresses will be less significant. This could be an explanation for the fact that for the type D specimens from both the WET and the DRY series comparable strength values were found.

The results for the fracture energy of the WET series are illustrated by Figs. 5.11a and b. The corresponding values are listed in Table 5.4. Basically, the size effect on G_F seems to be the same as for the DRY tests, irrespective of the use of the scaled measurements (Figs. 5.11a) or the control measurements (Figs. 5.11b). In case of the scaled measurements, G_F does not depend on the size of the specimens. For the control measurements on the other hand, G_F increases slowly. These observations are restricted to the rather small range of only four specimen sizes. When considering the complete set of results for the DRY series, a small further increase of G_F was found for specimen type E and F. Despite this increase, still a constant value for G_F can be found for the range of specimens B to F, which is situated within the standard deviations. Apart from specimen type A, the variation in fracture energy

Table 5.4 *Mean values for the fracture energy of the WET series. The numbers between brackets indicate the number of tests and the standard deviation.*

		Specimen type (nr)			
	Measurements	A (5)	B (5)	C (5)	D (3)
G_F [N/m]	scaled	91.5 (19.2)	99.6 (10.1)	88.9 (12.1)	100.4 (9.9)
	control	180.2 (21.4)	179.0 (16.2)	191.8 (27.1)	231.8 (32.0)

for the WET and the DRY series agrees well. This again indicates that the fracture energy which was found for the A specimens in the DRY series is too low, which is due to the scatter of the nominal strength as was illustrated in Fig. 5.6.

The absolute values for the fracture energy which are found for the WET tests are consistently lower than for the DRY tests. This was also found by Mechtcherine [56], who compared the fracture energy of sealed and unsealed specimens. For the unsealed specimens a higher value for G_F was found, both in uniaxial tension tests and in three point bending tests. By scanning the fracture surfaces of both types of specimens, the unsealed specimens showed a roughness which was much higher than that of the sealed specimens. This can be attributed to a larger amount of micro-cracks, which developed during the shrinkage process which took place in the unsealed specimens. Due to these distributed micro-cracks, first of all more macro-cracks will develop. In addition, the macro-cracks will branch rather than going straight through the specimen. Both mechanisms will lead to a higher value for the fracture energy.

5.4 Felser sandstone tests

In addition to the size effect tests on concrete, a second, completely different material was tested in order to get additional insight into the size effect phenomenon. Because of experience in the past, the specimens of this series were made of Felser sandstone. After testing the specimens of type A, B and C it appeared that the maximum range of the LVDTs, which was 500 μm , was rather small because of the large deformational capacity of the sandstone (compare Figs. 5.12 and 5.2). The measuring range of the LVDTs was therefore changed to 1000 μm for the remaining tests on specimen type D, E and F.

In Figs. 5.12a and b an overview is given of the recorded force-deformation curves, where for the deformation again the average deformation of the scaled measurements in the middle of the specimen has been taken. Due to problems with one of the two LVDTs a curve from a test on an E specimen is missing, although the ultimate load for this test has been recorded.

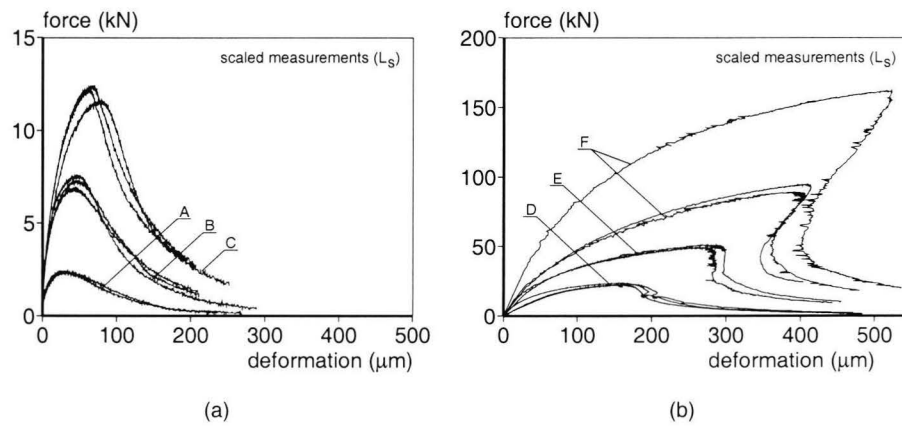


Figure 5.12 Overview of force-deformation curves for the sandstone specimens.

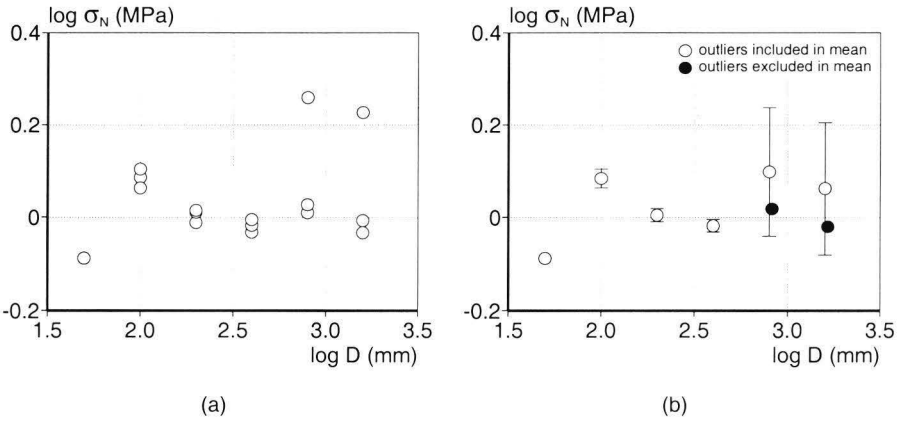


Figure 5.13 *Individual values (a) and mean values (b) of σ_N vs. D for the sandstone specimens.*

A comparison between Fig. 5.12 and Fig. 5.2 shows that the sandstone behaves completely differently from concrete. The material has a lower stiffness, is weaker and shows a much higher pre-peak nonlinearity compared to concrete. Despite the fact that the Felser sandstone is a natural material the overall reproducibility of the tests was rather good, which can be attributed to the homogeneous composition of this type of sandstone. Only for specimen type E and F one out of three tests for each specimen type showed a completely different behaviour, which is not unusual in rock testing [74, 114]. As a result a strength was found which was much higher compared to the other two specimens of the same dimension. In Fig. 5.13a the strength values of the sandstone specimens are shown. The recorded strength of the two A specimens was remarkably low, whereas for the E and the F specimens two extremely high strength values were found. Although a special request was made for manufacturing specimens out of the same block of sandstone, it can not be ascertained that this has actually been the case. This doubt is supported by additional tests on the remains of the F specimens. Using an Equotip impact device, the hardness of all F specimens was measured in the vicinity of the final crack. With these hardness numbers, the unconfined compressive strength was approximated using the relation given in [105]. The results of this simple check,

Table 5.5 *Mean values for the nominal strength of the sandstone tests. The numbers between brackets indicate the number of tests and the standard deviation.*

Type (nr)	A (2)	B (3)	C (3)	D (3)	E (3)	F (3)	E* (2)	F* (2)
σ_N [MPa]	0.82	1.22	1.01	0.96	1.30	1.20	1.04*	0.96*
	(-)	(0.06)	(0.03)	(0.03)	(0.45)	(0.42)	(-)	(-)

* outliers not incorporated in mean value

revealed that the approximated compressive strength of one F specimen was more than twice as high compared to the compressive strength of the other two specimens. For this specific specimen also the extremely high nominal tensile strength was found. Despite the rather global character of the verification, the findings confirm the assumption that the sandstone of the high strength E and F specimen should be considered not representative within the present test series. The layered composition of this red Felser sandstone, as well as the possible presence of faults and weak spots can explain the low strength of the A specimens. Because of their small size, the A specimens could have been manufactured entirely from the material of a weak bedding layer. With respect to weak spots, specimens of larger sizes will be less sensitive for the presence of such local inhomogeneities since more possibilities for stress redistributions exist. Local inhomogeneities in a small specimen on the other hand, will govern the experimental result and in this case the ultimate strength which is found.

When supposing that the high strength E and F specimen are outliers, the resulting mean values for the largest specimens are comparable to the values found for the smaller specimens. This is illustrated in Fig. 5.13b by the filled circles. Hence, the size effect in the sandstone tests, if present at all, is only mild and already vanishes for specimens larger than type C. Another conclusion could however be that the higher strength of the B specimens is actually due to a locally higher strength of the block from which the specimens originated. In that case the sandstone experiments do not show size effect on strength. The last hypothesis would be supported by results obtained by Wijk [114, 113]. From a vast series of uniaxial tension tests on Bohus granite cylinders followed that the uniaxial tensile strength was independent of the material volume. It was also found that the uniaxial tensile strength measured in point load tests agreed well with the strength resulting from the uniaxial tension tests. In the point load tests a size effect was present however, which was attributed to the loading conditions and consequent stress distributions near the loading points. The general conclusion was therefore that in absence of these concentrated loads the granite did not exhibit size effect, and that "modest stress concentrations due to bending in the uniaxial strength test do not appear to influence the test result" [113]. In the present tests a similar observation was made. The strength results of the sandstone series are namely confirmed by three uniaxial tension tests without load eccentricity, on cylinders with a length of 150 mm and a diameter of 100 mm. At half-length a notch with a depth of 5 mm was sawn along the circumference of the cylinders. The average strength which was found for these three tests amounts to 1.22 MPa [98]. Since the area of the smallest cross section of the cylinders differs only 6% from the cross sectional area of the type B specimens in the size effect tests, their strengths should be comparable. That this is actually the case follows from Table 5.5. Apart from the red Felser sandstone being insensitive for modest stress concentrations, this also might confirm that the results of the sandstone type B specimens are not higher by coincidence, but due to a size effect on the nominal strength.

Also for the red Felser sandstone the fracture energy has been computed. Since the number of values for each specimen size was restricted however (see Table 5.6), the results have to be considered with some reservation. In first instance G_F was computed in the same fashion as for the concrete tests (black circles in Fig. 5.14). This means that the inelastic or bulk energy which is dissipated by micro-cracks developing in the area outside the localized crack, is neglected (area denoted by "I" in Fig. 5.15). A study by Elices et al. [25], as well as own findings, show that for concrete the influence on G_F of neglecting bulk energy dis-

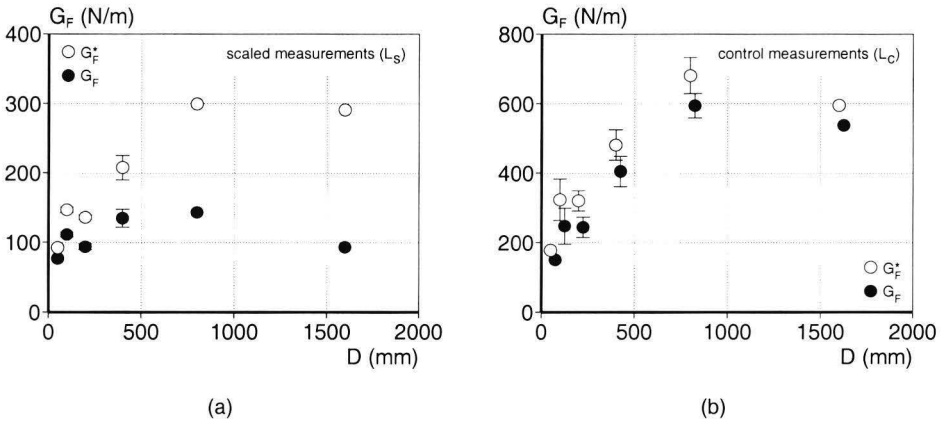


Figure 5.14 *Fracture energy for the sandstone series, based on scaled measurements in the specimen middle (a), and control measurements at the specimen edge (b).*

sipation is restricted to only a few percent. This is however not the case for the red Felser sandstone, at least not for the values of the fracture energy based on the scaled measuring length. Figures 5.15a and b illustrate the areas on which, according to the adopted definition by Hillerborg, G_F is based for the scaled measurements and the control measurements respectively (area "II"). Alternatively, a fracture energy G_F^* is considered which takes into account bulk energy dissipation as well. Hence, G_F^* is represented by the total area under the stress-deformation curve $A_I + A_{II}$ (Fig. 5.15), assuming that the fracture process already starts in the pre-peak regime. In other words, the nonlinearity must be due to irreversible processes in which energy is dissipated, rather than elastic deformations which occur because

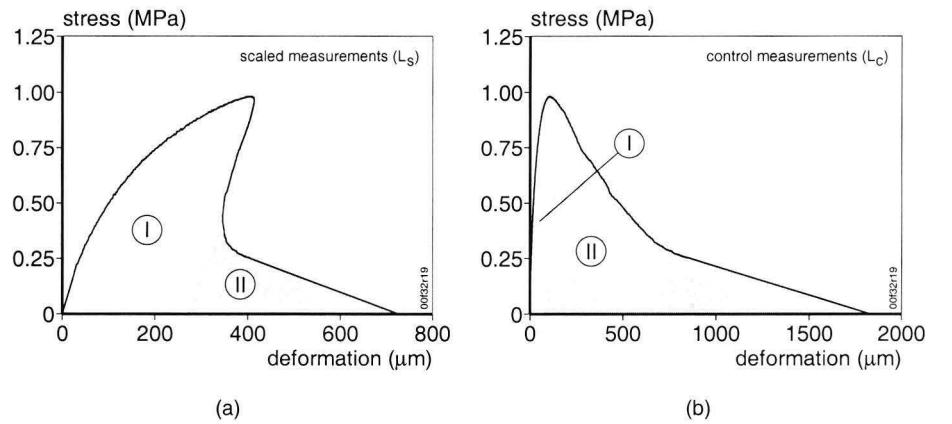


Figure 5.15 *Deformation signal for a scaled measurement (a), and a control measurement (b) of a sandstone type* F *specimen. A_{II} is the area which defines G_F, whereas G_F^* is defined by $A_I + A_{II}$.*

Table 5.6 *Fracture energy for the sandstone tests. G_F refers to the fracture energy according to Hillerborg, whereas G_F^* is based on the total inelastic deformations.*

	Scaled measurements		Control measurements	
Type (nr)	G_F [N/m]	G_F^* [N/m]	G_F [N/m]	G_F^* [N/m]
A (2)	76.7 (-)	92.6 (-)	150.3 (-)	177.9 (-)
B (3)	111.3 (3.7)	147.0 (3.8)	247.3 (51.4)	323.2 (60.3)
C (3)	93.8 (4.4)	136.2 (3.2)	243.9 (29.3)	320.3 (29.5)
D (3)	135.1 (13.0)	208.1 (17.6)	404.8 (43.6)	481.1 (43.8)
E (3)	143.3* (-)	299.6* (-)	594.6 (35.1)	681.0 (52.5)
F (2)	93.2 (-)	291.1 (-)	538.1 (-)	595.4 (-)

* mean value based on 2 instead of 3 tests

of for instance sliding in the clay minerals or deformation of the pores. The actual reason for the nonlinearity, can however not be given on basis of the available experimental results.

The variation of the fracture energy with size which results from the sandstone tests is in some aspects comparable to the results of the concrete tests. For the control measurements the fracture energy is found to increase strongly with size, which was found in the concrete tests as well (Fig. 5.14b vs. Fig. 5.5b). In case of the sandstone however, the increase is steeper which might be due to the fact that the ratio between the maximum grain diameter and especially the thickness of the specimens is much higher than for the concrete specimens. For the scaled measurements (Fig. 5.14) this increase is found as well, but only for G_F^*. Remarkably, the difference between G_F and G_F^* increases nonlinearly. No final explanations are available for the observed size effect on the fracture energy in the sandstone tests. It is however likely that answers must be sought in the peculiar material structure of this type of sandstone. In Section 3.2.1 it was shown that the material exhibits a clear, very open grain structure. The individual grains have silicate bonds and are sometimes connected by thin clay layers. Failure of these bonds could be the reason for the strong nonlinearity which is observed, and which simultaneously indicates a large capacity to redistribute stresses. Whether G_F^* prevails over G_F can only follow from additional tests, which could give information on the nature of the pre-peak nonlinearity.

A last remark concerns the decrease of the fracture energy for the F specimens (see Fig. 5.14 and Table 5.6). It is believed that this decrease is artificial, and due to the fact that the tests on the F specimens had to be stopped relatively early. As a result, the linearly extrapolated descending branch of the $\sigma - w$ relation, which is used to compute the fracture energy, intersects the x-axis at a deformation which is probably too small. A similar situation was encountered for the C specimens, which like the F specimens show values for the fracture energy which seem too low. It can be expected however, that the fracture energy converges towards a constant value. Despite the small maximum grain size of the sandstone, apparently a very large ratio between minimum specimen dimension and maximum grain diameter has to be maintained before this plateau is reached.

5.5 Impregnation tests

Test series III comprised a limited number of impregnation experiments, in which partly fractured specimens were impregnated with fluorescent epoxy. After hardening of the epoxy the specimens were sliced up. Thus, it was attempted to get more information about the fracture process inside the specimens. Apart from an A, C and E specimen which were loaded until ultimate load, three A and three C specimens were fractured until a maximum deformation of 50 μm , 100 μm and 300 μm respectively. Alternatively, the specimens could have been fractured until specific post-peak load levels. The choice for such a deformation criterion or a force criterion depends on the scatter which is expected. Within the observed scatter, it must be possible to make comparisons between specimens of the same size at different fracture stages, as well as comparisons between specimens of different sizes with the same stage of fracturing. In case of a deformation criterion, the post-peak load level at which unloading is started varies. Especially in the steep part of the softening curve these variations can be strong. A force criterion on the other hand will show fluctuations in the deformation stage at unloading, in addition to the fact that the criterion is sensitive to variations in ultimate load for the subsequent specimens. This problem has to be circumvented by applying a relative force criterion rather than an absolute force criterion. By looking at the results of the DRY series, it was found that the test results, especially towards the tail of the softening curve, would be comparable best if a deformation criterion was applied. A second reason for choosing a deformation instead of a force criterion to compare the fracture stage of different specimens, was the intention to relate the deformation measured at the specimen surface to the fracture inside the specimens. In Table 5.7 the loads are listed at which the deformation criterion, and thus the moment of unloading, was reached. A comparison of the consequent load levels relative to peak load shows that apart from the 50 μm results, the deformation and loading stages in both the type A and type C specimens are well comparable.

In Fig. 5.16 the force-deformation curves are shown of the type A and type C specimens which were loaded beyond ultimate load. After unloading, the deformation of the specimens was fixed at a low force level. The crack openings which were found in the specimens can therefore be related to the deformations which were measured after unloading (Fig. 5.16). It must be noted however, that the applied method of internal crack visualization has its limitations. When no cracks can be seen it does not necessarily mean that they do not exist. The only conclusion which can be drawn is that within the limitations of the present impregnation method no other cracks were found than those visible on the pictures. As a reference for

Table 5.7 *Absolute and relative residual force values at which the specimens of the impregnation tests have been unloaded.*

	type A		type C	
δ [μm]	F [kN]	F/F_u [kN]	F [kN]	F/F_u [kN]
50	2.25	0.34	19.44	0.63
100	1.72	0.24	7.77	0.24
300	0.79	0.10	3.28	0.10

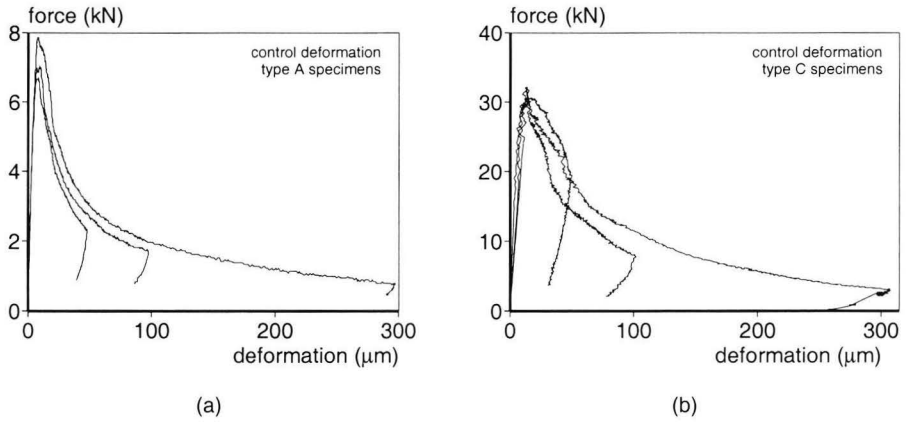


Figure 5.16 *Force-(maximum) deformation curves of the impregnation tests on type* A *specimens (a) and type* C *specimens (b) for three unloading stages.*

the other test results presented in this thesis, in Fig. 5.17 also the force-deformation curves have been included which are based on the average scaled deformations in the middle of the specimens.

After the fractured specimens had been impregnated, the specimen ends were removed (Fig. 5.18a). Next, the remaining middle part of the specimen was cut in seven slices with a thickness of approximately 10 mm as is illustrated in Fig. 5.18b. The distance between the back side and the front side of two subsequent slices was approximately 4 mm.

Differences between the three deformation stages which are considered, can be distinguished most clearly for the C specimens. When comparing the force-deformation curves of the C specimens which were loaded until 50 μm and 100 μm respectively (Fig. 5.16b), a difference in ductility is observed. In the experiments such a "ductile" control signal like for

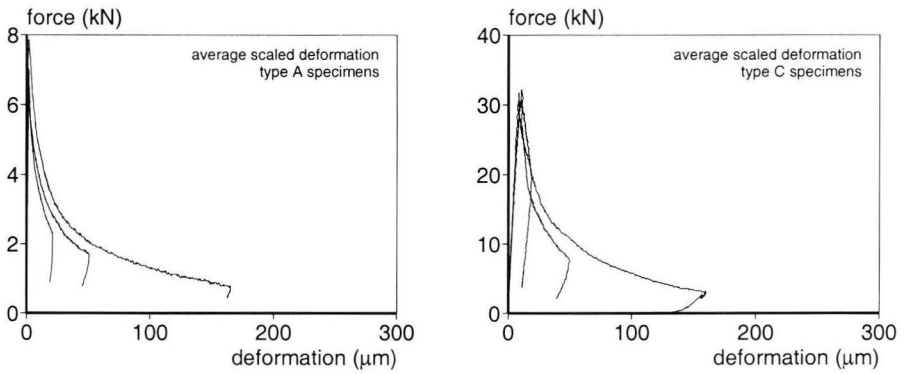


Figure 5.17 *Force-(average scaled) deformation curves of the impregnation tests on type* A *specimens (a) and type* C *specimens (b) for three unloading stages.*

the 50 μm specimen indicated that the deformations were distributed unevenly over the cross section. This coincides with bending in the out-of-plane direction. To visualize the (impregnated part of the) main crack inside the two specimens, a crack map was constructed for each specimen by measuring the crack length on the front and the back side of each slice. These measured crack lengths are represented by the thick lines in Fig. 5.19, where the gray shaded area gives an approximation of the shape of the impregnated crack, within the limitations of the applied method of impregnation. The aforementioned uneven deformation distribution is reflected well by the crack pattern (Fig. 5.19). In the C specimen which was loaded until a deformation of 100 μm the crack front is curved, which is in agreement with findings of other researchers (see e.g. [5, 81, 85]), and which could have implications for the computation of G_F for partially cracked specimens [50]. The curved crack front can partly be attributed to the composition of the outer layers of the specimens, where a higher water-cement ratio and a disturbed mix composition will lead to a lower strength. In addition, micro-cracks due to drying out will cause crack propagation along the circumference of the specimen. With respect to uneven deformation distributions and the curved crack front, it could be argued that using impregnation methods to visualize internal crack patterns is restricted to cracks which are in direct connection with the specimen surface. Nevertheless, also acoustic emission experiments on beams made of mortar and steel fibre reinforced concrete respectively [51, 112], showed the curved shape of the crack front.

In the impregnation experiments, several indications were found of a lower matrix density of, and/or small cracks in the outer specimen layers. Comparison of Fig. 5.20a and b shows for instance the difference between a crack map at the surface of the specimen, and at a small distance from the surface. It must be mentioned that the nature of the surface cracks is unknown, which means that the cracks are probably induced by a combination of differential

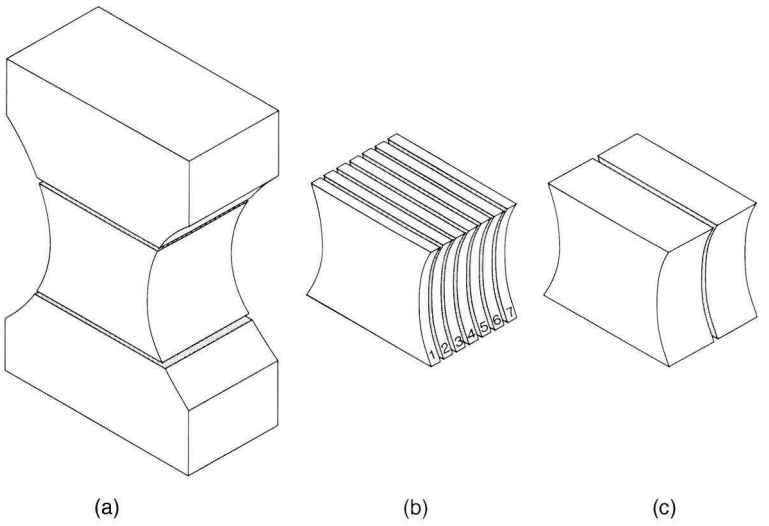


Figure 5.18 *Cutting procedure after impregnation of a fractured specimen. Removal of the specimen ends (a), followed by cutting the specimen in slices (b) or a single cut for the manufacturing of thin sections (c).*

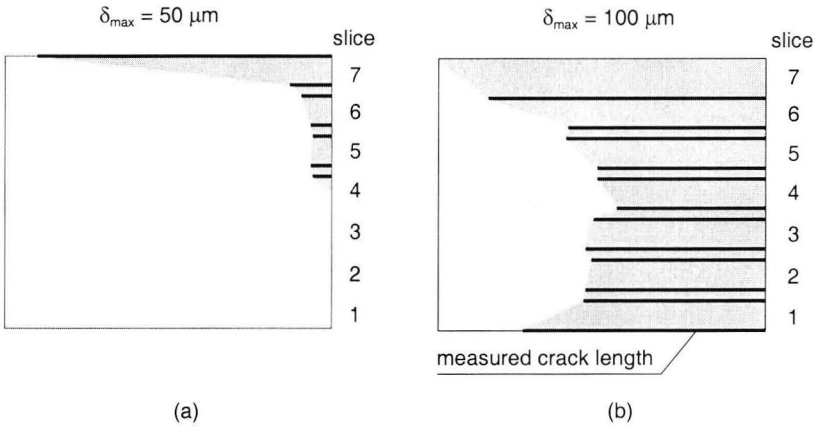


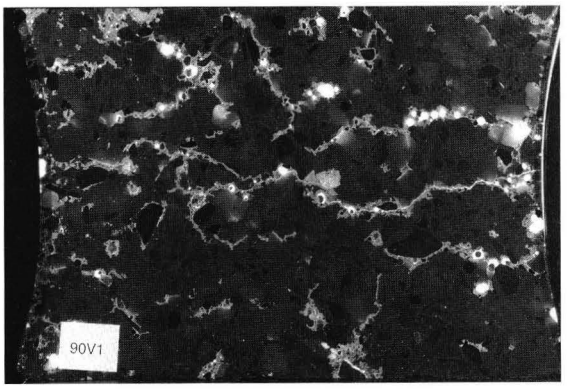
Figure 5.19 *Top view of the reconstructed cracks in the type* C *specimens which were loaded until a maximum deformation of 50 μm (a) and 100 μm (b) respectively.*

shrinkage and the external loading. Besides the impregnation of surface cracks at the front and the back side of the specimens, it was also found that a zone with a width between 1 and 4 mm along the sides of the specimens had been impregnated. Although no discrete cracks could be distinguished in these zones, the density of the matrix was probably low enough for the epoxy to penetrate. A similar phenomenon was actually observed in the specimens with the larger cracks widths. There, a zone with a width of a few millimeters was impregnated on both sides of the discrete crack.

The cracks which were found in the C specimens loaded until deformations of 100 μm and 300 μm respectively were very different with respect to the tortuosity. In all slices of the specimen loaded until 100 μm, a thin, discrete crack was found like shown in Fig. 5.20b. Most of the slices of the C specimen which had been loaded until a deformation of 300 μm however, showed a crack zone which was wider and more branched. Although these observations are made on single specimens, it is interesting that the difference in crack pattern nicely agrees with the difference in force-deformation curves. From Fig. 5.17b follows that the more tortuous crack path coincides with the most ductile softening curve.

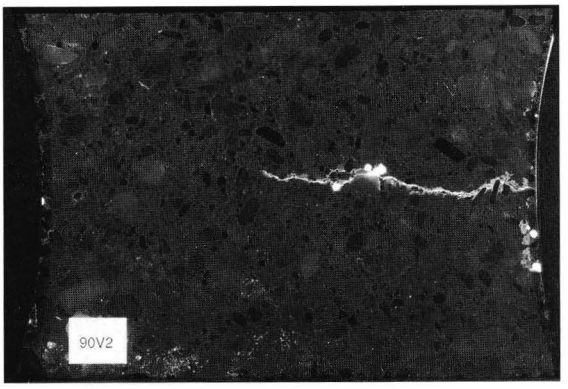
To conclude the main results of the impregnation tests, some comments will be made concerning the specimens which were loaded until ultimate load. Since the deformations at ultimate load were only small and no localized fracture was expected yet, a limited number of thin sections was made instead of regular pictures of the specimen slices like shown in Fig. 5.20.

Contrary to the specimens which were cut in slices, the specimens from which thin sections were made were only cut in two parts, approximately halfway the thickness of the specimen (see Fig. 5.18). The cut was made in such a way that the final position of the thin section was 50 mm from the front surface as well as 50 mm from the back surface of the specimen. A close inspection of the thin sections did not reveal any discrete cracks, whereas micro-cracks where found throughout all thin sections. This is not surprising, since already in 1963 Hsu [46] found that even before any load was subjected to concrete prisms, already



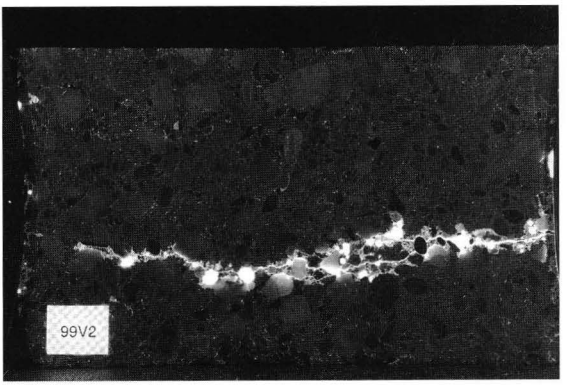
C type
surface
$\delta_{max} = 100\ \mu m$

(a)



C type
depth $\approx$ 14 mm
$\delta_{max} = 100\ \mu m$

(b)



C type
depth $\approx$ 14 mm
$\delta_{max} = 300\ \mu m$

(c)

Figure 5.20 *Crack patterns at the specimen surface (a) and at a depth of approximately 14 mm under the surface (b) for a type* C *specimen loaded until a maximum deformation of 100 μm . Figure (c) is made at the same position as (b) but in the* C *specimen loaded until a maximum deformation of 300 μm .*

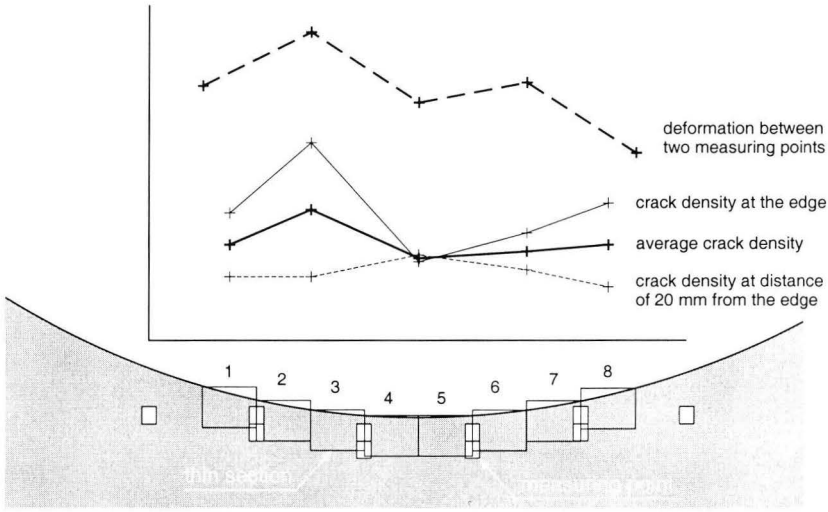


Figure 5.21 *Comparison of the average deformations measured at the right edge of an* E *specimen, and the crack density which was found in thin sections originating from the middle plane of the specimen at the right edge.*

12 % of the aggregate perimeters in a cross section was cracked. For the E specimen, which had been loaded until ultimate load, eight thin sections of approximately 30×40 mm^2 were made along the right (most stressed) edge. For each of the thin sections the density was determined of cracks between 1 and 10 μm wide, in zones with a width of 10 mm along the edge of the specimen and at a horizontal distance of 20 mm from the edge. In Fig. 5.21 these crack densities are plotted as a function of the position of the thin section in the specimen. In addition, the average deformation is plotted in the figure which was measured by the control LVDTs at the front and the back side of the specimen. Fig. 5.21 shows that in the zone along the specimen edge generally a higher crack density was found compared to the zone at a distance of 20 mm from the edge, and thus coinciding with the inner specimen part. Furthermore, the average crack density of both zones agrees well with the deformation readings of the LVDTs at the specimen surface. Although no discrete crack was found in thin sections 2 or 3, the average crack density is clearly higher than in the other thin sections. This could indicate that crack localization would have started right there.

Chapter 6

Lattice approach to size effect in concrete

6.1 Introduction to lattice modelling

6.1.1 The principle of a lattice model

A lattice model is based on the concept of discretizing a continuum by line elements. Hrennikoff [43], who was one of the first to study this approach, used it to overcome the mathematical difficulties which are incorporated in the solutions of the theory of elasticity. In the 80's, lattice models again came into fashion. This time it was in theoretical physics that the model's excellent capabilities were recognized for introducing heterogeneity in an easy and natural way [35]. The electrical breakdown of resistor networks was studied, but also mechanical failure of various lattice configurations containing spring elements with one, two or three degrees of freedom. These latter studies on periodical lattices mostly had a phenomenological character and were thus not directly related to real materials. In Delft, a lattice model has been developed by Schlangen and Van Mier [72]. Contrary to the former models used by physicists, in their model the simulation of quasi-brittle material behaviour was of main importance. This model has been adopted in the present study as well, to be used in parallel to the experiments in order to get more insight into experimental observations that were made.

One of the main characteristics of quasi-brittle materials like concrete and certain types of rock is their high degree of heterogeneity. This heterogeneity can be easily incorporated in a lattice model, by assigning different strength and/or stiffness values to the individual lattice elements (meso-level). Then, in a mechanical analysis, lattice elements are subsequently removed from the mesh in order to model crack initiation and propagation. Interesting thereby is, that even when purely elastic-brittle material behaviour is assigned to the lattice elements the computational result automatically incorporates softening, which is another characteristic of quasi-brittle materials. This principle can be illustrated by the simple example of Fig. 6.1. Consider a system of five parallel bars with length l, which can only transfer normal forces and which can rotate freely in the nodes (Fig. 6.1a). All bars have the same normal stiffness EA, where E is the Young modulus and A the cross-sectional area, and each bar i can transfer a maximum force $F_{\max,i}$. When the system is given a uniform vertical displacement u, bar i fails at a displacement

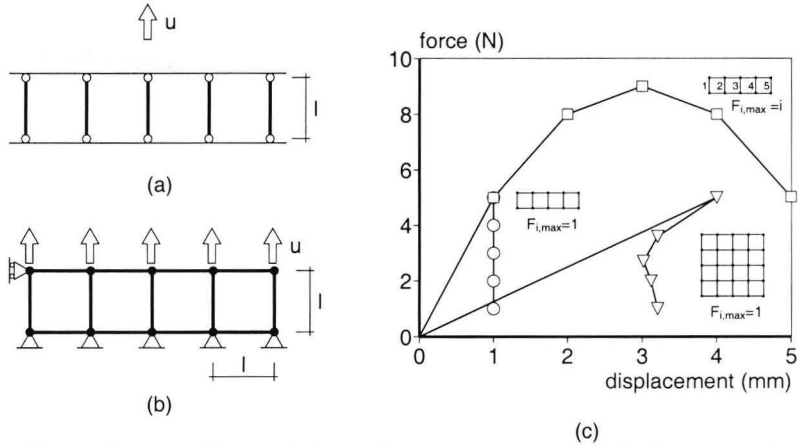


Figure 6.1 *System of 5 parallel bars (a), equivalent square lattice consisting of beam elements (b) and behaviour of 3 different lattice configurations (c).*

$$u = u_i = \frac{F_{\max,i}\, l}{EA} \tag{6.1}$$

and the total force which is transferred by the homogeneous system follows from

$$F_{\text{tot}} = \sum_{i=1}^{m-n} \left(\frac{EA}{l}\right)_i u = (m-n)\frac{EA}{l}\, u \tag{6.2}$$

where m stands for the total number of bars, and n represents the number of bars which already failed. For this simple case, the same relations hold when instead of the system of five parallel bars, a square lattice of beam elements is taken which can transfer normal forces, shear forces and bending moments (Fig. 6.1b). Suppose $l = 1$ mm. The most elementary case which now can be considered is the failure of a homogeneous lattice. In other words, all springs have the same stiffness ($EA = 1$ N) and a strength of $F_{\max} = 1$ N. Hence all springs fail at the same value of u (Eq. 6.1), and the force transmitted by the lattice decreases as soon as the first beam has failed: the global behaviour of the lattice is elastic-purely brittle (Eq. (6.2) and circles in Fig. 6.1c). When however instead of a constant strength different strength values are assigned to the subsequent beams, the behaviour of the lattice changes completely. Despite the fact that the individual beams behave purely brittle, softening behaviour is obtained for the lattice as a whole (squares in Fig. 6.1c). Another typical case which can be modelled concerns the effect of the elastic energy which is stored in the system. The influence of this elastic energy on the global model behaviour can be illustrated by loading a homogeneous lattice with four layers until complete failure (triangles in Fig. 6.1c).

In the present example heterogeneity has been introduced by a "random" variation of the beam strength. Yet, other, more structured ways, can be applied as well. The introduction of an aggregate structure in the lattice will be discussed in Section 6.1.3, whereas in Appendix

C.2.2 the influence of variations of different parameters on the lattice behaviour will be discussed in more detail.

Although modelling heterogeneity and the consequent effect on the global material behaviour can be easily achieved, lattice models have their shortcomings as well. These shortcomings concern the predictive capabilities in the quantitative sense, as well as the huge computational demands. In the author's opinion, lattice models suit best the group of qualitative models, which can be applied to study phenomena inherent to a specific material. The material structure can be easily incorporated by setting the material parameters one level below the level of observation. Application of the model to real structural sizes however, then lies beyond reach.

6.1.2 Setting up the geometry

A continuum can be discretized by a lattice in various ways. One can consider 2D or 3D models, with regular or random geometries and overlapping or non-overlapping lattice elements. Also the number of degrees of freedom per node can be varied. These different approaches will not be discussed here since overviews can be found in e.g. [71, 103]. It is mentioned though, that a study on various 2D lattice geometries which incorporated heterogeneity, showed that only small differences occurred in the computational result [104]. Large differences on the other hand, were found in the performance of lattices with 1, 2 or 3 degrees of freedom per node respectively. This led to the conclusion that beam models are best suited for simulating the fracture behaviour of heterogeneous materials like concrete [71].

In the present study two types of lattice models have been adopted which both have a triangular geometry (Fig. 6.2). The first type of lattice is a regular triangular lattice in which the nodes are placed at equal distances in a triangular pattern, see Fig. 6.2a . Consequently, all lattice elements have the same length, and when the elements are assigned the same geometrical and material properties, such a lattice is homogeneous and isotropic. This is fully true when periodic boundary conditions are applied, whereas the isotropy approximately holds for finite lattice dimensions, which is discussed in detail in Appendix C.1.

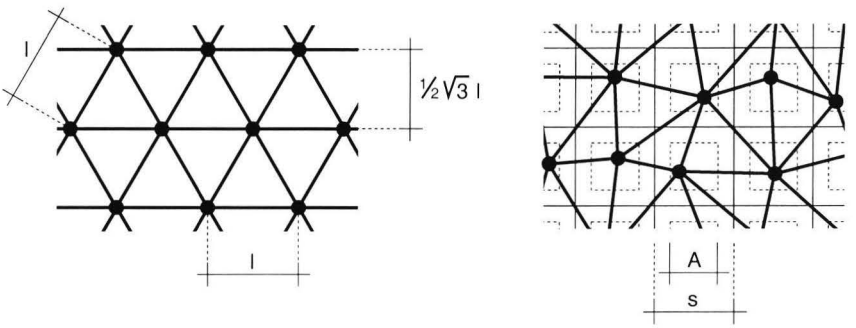


Figure 6.2 Adopted regular (a) and random (b) triangular lattice.

The second type of lattice which has been used is the random triangular lattice illustrated in Fig. 6.2b. The basis for the construction of the latter lattice is a regular square grid with cell size s. In addition, sub-cells with size A are defined with the condition $0 < A \leq s$. Within each sub-cell the (x,y) coordinates of a node are generated at random using a uniform distribution. Using Voronoi triangulation the nodal connectivities are then determined, which means that the three nodes which are closest to each other are connected by lattice elements. Even when the geometrical and material properties are the same for all lattice elements, a random lattice is heterogeneous due to the length variation of the lattice elements. The heterogeneity of a random lattice can be controlled by the value of A. When $A < s$ is chosen, this basically means that the degree of randomness is decreased [103], which can be beneficial for preventing the generation of very short lattice elements. In the simulations presented in this thesis $A = s$ has been adopted, since also in the materials to be modelled a large degree of heterogeneity is present at the meso-structural level.

6.1.3 Material and geometrical input data

In the lattice model which has been developed in Delft, the nodes are connected by Bernoulli beams which in the 2D case have rectangular cross sections. The global, or overall behaviour of the lattice can be controlled by assigning geometrical and material properties to the beam elements. It is mentioned that within the simulations which are discussed in this thesis, all beam elements of a lattice had the same cross-sectional dimensions. Variations have only been applied to the strength and the stiffness of the individual beams.

Regular lattice

Starting with the global elastic properties, the global Young modulus E and the global Poisson ratio ν depend on the chosen beam length l, the (local) Young modulus E_{beam} and the beam height h. The thickness t of the lattice beams does not influence the result of a lattice analysis. It can therefore be either taken unit thickness, or be chosen equal to the thickness of the specimen which is being modelled. Since ν only depends on l and h whereas it is independent of E_{beam}, the value for h has to be fixed first. In case of a homogeneous regular lattice with periodic boundary conditions, an analytical expression for ν in the elastic stage can be derived by comparing the strain energy of a unit cell of the lattice and an equivalent continuum area [71]. This expression reads

$$\nu = \frac{1 - \left(\frac{h}{l}\right)^2}{3 + \left(\frac{h}{l}\right)^2} \tag{6.3}$$

The value of E not only depends on l and h, but also on E_{beam}. The Young modulus of the lattice beams is the only remaining parameter which influences the elastic behaviour of the lattice, and which has not been set yet. In a similar fashion as for ν, and again for a homogeneous regular lattice with periodic boundary conditions, the analytical expression for E can be found to be (after [70])

$$E = 2\sqrt{3}\,\frac{E_{\text{beam}}\,A}{l}\left[\frac{1+\left(\frac{h}{l}\right)^2}{3+\left(\frac{h}{l}\right)^2}\right] \tag{6.4}$$

where $A = bh$ is the cross sectional area of the beams.

Expressions 6.3 and 6.4 are valid for regular lattices with periodic boundary conditions where consequently no boundary effects can occur. For lattices with finite dimensions however, boundary effects are present which can affect the global elastic properties. To study the range of validity for expressions 6.3 and 6.4, E and ν were computed for (approximately square) homogeneous regular lattices of different sizes L. The lattice size L is defined as B/l for a regular lattice and B/s for a random lattice, where B stands for the width of the lattice mesh (see Fig. 6.3). As for the input parameters $l = 1$ mm, $h = 1/\sqrt{3}$ mm and $E_{\text{beam}} = 31255$ MPa were chosen. More information on the calculation of E and ν can be found in Appendix C.1.1. In Fig. 6.4 the results are shown for five regular lattice meshes with $L = 4$, 10, 20, 40 and 80, where E^* and ν^* have been introduced for the numerically obtained elastic properties. Since for finite lattice sizes isotropy of the lattice is not guaranteed anymore, the numerical values for the elastic properties in x and y direction have been shown separately.

The main observation in Fig. 6.4 is that for loading in the y direction, computational and analytical results agree well. In addition, for the Young modulus the numerical and analytical values are in good agreement irrespective of the direction which is considered. Especially for lattice sizes $L \geq 20$ only minor differences were found between E^* and E. In those cases Eq. (6.4) can therefore be used safely for setting E_{beam}. For the Poisson ratio the ratio of ν_y^* and ν is very sensitive for changes in L. In case $L < 20$, this probably must be attributed to a combination of the mesh geometry and the way in which the mesh was loaded. To calculate E_x^* and ν_y^*, only the outer nodes of the vertical boundaries at $x = 0$ and $x = B$ were displaced and not the "inner boundary nodes" at $x = 0.5l$ and $x = B - 0.5l$. Hence, the difference between the smooth horizontal and irregular vertical boundaries increases strongly for very

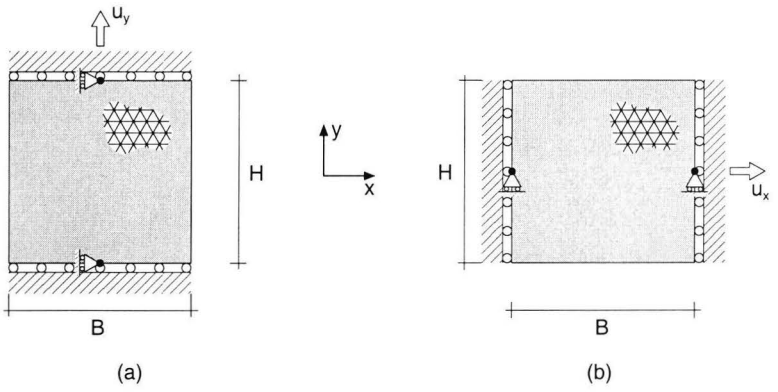


Figure 6.3 *Applied models for the computation of Young's modulus and Poisson's ratio in the x and y directions.*

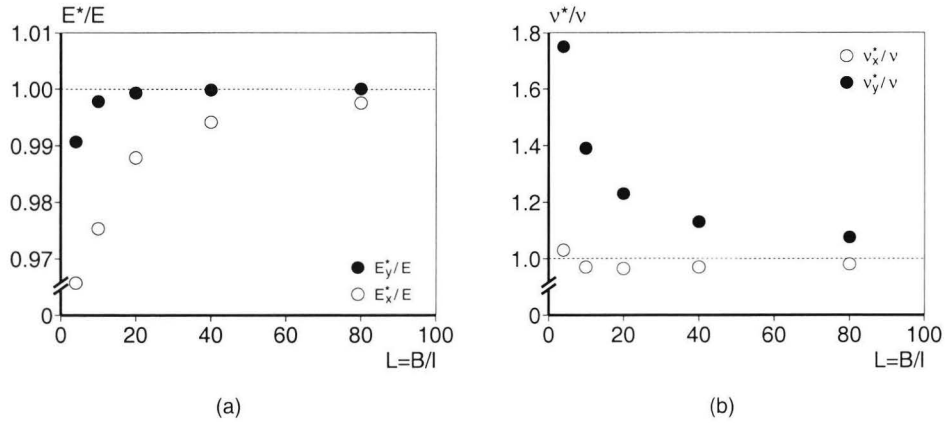


Figure 6.4 *Difference between the numerically and analytically obtained values for the Young modulus (a) and the Poisson ratio (b) for different sizes L of a regular lattice.*

small lattice sizes. Yet, for $L \geq 20$ the regular lattice performs quite acceptable since also in experiments the scatter in measured Poisson's ratio can be considerable.

For the sake of completeness the degree of anisotropy for the same lattice meshes has been included as well (Fig. 6.5). From the figure it follows that with respect to Young's modulus the lattice can be considered quasi-isotropic. For the Poisson ratio directional differences up to 40% were obtained for $L = 4$. When multiaxial loading cases are considered this could become of importance, so that taking $L \geq 40$ would be advisable. In case of uniaxial loading it is best to keep the loading direction perpendicular to the base of the triangles which corresponds with the values of E_y^* and ν_x^*.

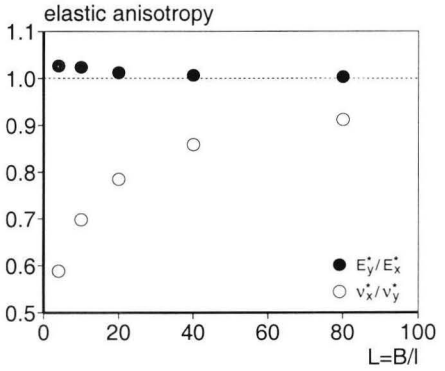


Figure 6.5 *Relation between the degree of anisotropy for the elastic properties of a homogeneous regular lattice and the lattice size L.*

Random lattice

For a random lattice, E^* and ν^* are tuned in exactly the same way as for the regular lattice. Analytical expressions however, are not that beneficial anymore since due to the dependence of E^* and ν^* on l, the expression would include a summation over all beam elements. To allow for an easier access of the values of h and E_{beam} which are needed to tune E^* and ν^*, Vervuurt [103] derived empirical relations which are shown graphically in Fig. 6.6. The relations are fits through the results of Poisson's ratios calculated on numerous random meshes of 50×50 nodes. Note that the x-axis of Fig. 6.6a has been recalculated from h/s to h/l_{avg} using the values of the average beam length l_{avg}, which were computed for the random meshes [103]. By doing so, the results for a regular lattice could be incorporated in the figure as well. Thus, it is found that for a regular lattice and a random lattice with maximum degree of randomness ($A = s$) the relation between ν^*_{avg} and h/l_{avg} is fairly close.

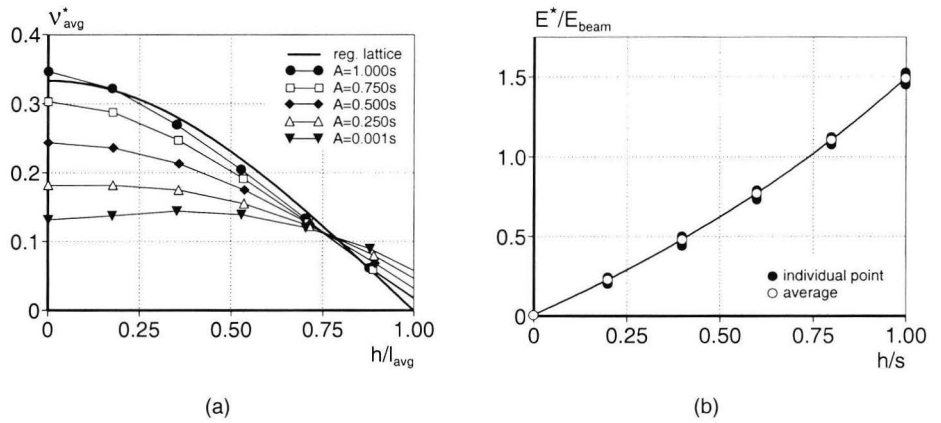


Figure 6.6 *Relation between ν^*_{avg} and h/l_{avg} for a regular triangular lattice and a random lattice with varying randomness (a), and between h/s and E^*/E_{beam} for a random lattice ($0 < A \leq 1$), after [103].*

Introducing the concrete meso-structure

In a heterogeneous material like concrete a clear material structure is observed at the meso-level. This material structure can be roughly subdivided into three different phases: aggregates, (interfacial) bond and matrix. In addition, porosity could be considered a fourth phase, which, however, has not been done in this study. Each of the three phases has its own characteristic strength and stiffness. Thus, depending on the type of cement, aggregate and possible additives, concrete with certain characteristics can be developed. By introducing this material structure in the lattice model not only the elastic properties of concrete can be modelled (see Appendix C.1 for the 2D case and [54] for the 3D case), but also the typical fracture behaviour of a specific type of concrete [103].

Several methods can be adopted to introduce a concrete material structure, or alternatively the effects of such a material structure, in a lattice mesh. These methods can be subdivided in graphical and statistical methods. In the latter case strength or stiffness distributions could be adopted to introduce heterogeneity in the lattice. In case of the graphical

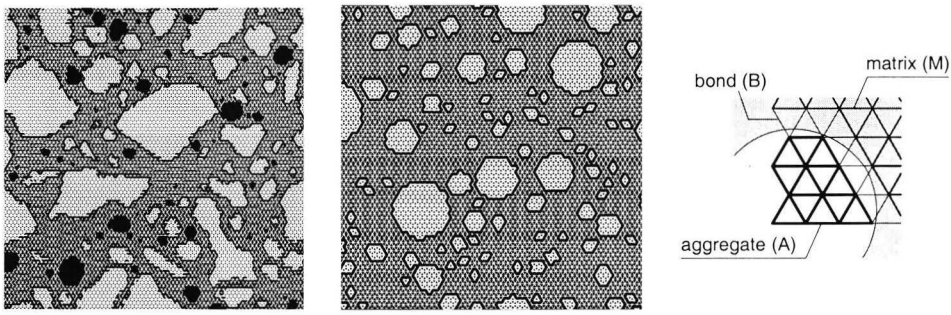


Figure 6.7 *Projection of a scanned aggregate structure including pores, after [71] (a) or a computer generated aggregate structure (b) on top of a lattice.(c) illustrates the way in which properties are assigned to the beams of the three phases which are distinguished in this study.*

methods, which are usually adopted in the current model, a picture of an aggregate structure is projected on top of the lattice. This can for instance be a picture of a scanned, "real", concrete aggregate structure (meso level) like shown in Fig. 6.7a [71], where concrete has been modelled as a four phase material including pores. Alternatively however, a simplified computer generated aggregate structure can be used (Fig. 6.7b), where the aggregate distribution is based on e.g. a Fuller curve [68, 108] (see also Appendix B). The generated aggregates can then be placed in the concrete area using a random procedure [68], a procedure resembling the casting process in which the aggregates are dropped in the concrete area at random horizontal positions [104], or more advanced procedures taking into account dynamic interactions of the aggregate particles [79]. The way in which the meso-structure is eventually translated to the lattice beams however, does not depend on the way in which the picture of the aggregate structure was obtained.

After projecting the aggregate structure on top of the lattice, aggregate properties are assigned to the beams falling inside an aggregate whereas matrix properties are assigned to the beams situated outside the aggregates. Lattice beams which cross the circumference of an aggregate are assigned interface or bond properties (see also Fig. 6.7c). Since the model is linear elastic, and the behaviour of the lattice beams purely elastic-brittle, these material properties only concern the strength values (f_{t_A}, f_{t_B} and f_{t_M}) and the stiffness values (E_A, E_B and E_M) of the three phases. In a qualitative sense, the result of a lattice simulation only depends on the ratios of these values: f_{t_A}/f_{t_M}, f_{t_M}/f_{t_B}, E_A/E_M and E_M/E_B (see also Appendix C.2.2). Quantitatively however, the computational results *do* depend on the magnitude of the strength and stiffness values which have been assigned to the beam elements. Instead of using the strength values for matching the outcome of a lattice analysis with experimental results, the use of a tuning parameter is more transparent. Such a tuning parameter is available in the model as well and will be discussed in the next section. The ratios which have generally been applied in lattice analyses, as well as the individual values on which they are based are listed in Table 6.1. A limited discussion of these ratios and their effect on the numerical result can be found in Appendix C.2.2. For studies including systematic variations of the strength and stiffness ratios the reader is referred to [68, 73, 103].

Table 6.1 General input parameters for lattice simulations.

Units in MPa									
f_{t_A}	f_{t_B}	f_{t_M}	E_A	E_B	E_M	f_{t_A}/f_{t_M}	f_{t_M}/f_{t_B}	E_A/E_M	E_M/E_B
10.0	1.25	5.0	70000	25000	25000	2.0	4.0	2.8	1.0

It may be evident that the introduction of an aggregate structure, and thus a variation of E_{beam} within the mesh, has its implications for the tuning of the global stiffness of the lattice mesh. Eq. (6.4) as well as the empirical relation shown in Fig. 6.6b now do not apply anymore. The global stiffness can therefore only follow from a mechanical analysis as discussed in Appendix C.1. Note however, that during the tuning process only the stiffness *values* E_A, E_B and E_M are varied. The stiffness *ratios* E_A/E_M and E_M/E_B on the other hand, always remain the same. Furthermore, a linear relation exists between the global Young modulus and the Young moduli which are assigned to the beam elements.

When an aggregate structure is projected on a lattice, the discretization of the aggregate structure depends on the ratio $l/d_{\min}$. The effect of varying this ratio is illustrated in Appendix C.2.3. Generally speaking, maintaining $l/d_{\min} \leq 0.5$ for a regular lattice ensures that even the smallest aggregate particles are incorporated in the lattice.

6.1.4 Failure criterion

When performing a fracture analysis on a lattice mesh, a failure criterion has to be chosen. Again several methods can be adopted, based on fracture mechanics, energy dissipation or strength theory. With respect to strength criteria, variations from the criterion discussed hereafter are e.g. the nodal stress criterion [71] or a Mohr-Coulomb like stress criterion [95]. In the current model usually a tensile strength criterion is adopted which has shown to perform well for uniaxial tensile loading conditions, and which is based on the maximum stress in a beam element. This "effective" stress σ_{eff} is composed from the normal force N, and a part of the maximum bending moment M in one of the two nodes (i, j) through

$$\sigma_{\text{eff}} = \beta\left(\frac{N}{A} + \alpha\frac{|M_i,\, M_j|_{\max}}{Z}\right) \tag{6.5}$$

where A is the cross-sectional area and $Z = (1/6)th^2$ the sectional moment of the beam. The influence of the factor α on the computational result is rather small and mainly governs the length of the tail of the softening diagram which is found. For examples of the effect of variations of α the reader is referred to [68, 103]. In the present simulations, the generally applied value of $\alpha = 0.005$ has been used.

The factor β in Eq. (6.5) is a pure scaling parameter. The idea behind β is that it can be used to fit the average peak load of a number of uniaxial tension tests, and a set of simulations of the same test including the same concrete composition. Once the value for β has been set, it remains unchanged while varying the specimen geometry and/or the loading conditions. It is noteworthy that by setting β the same effect is obtained as by a variation of the strength

values f_{t_A}, f_{t_B} and f_{t_M}, while keeping the *ratios* f_{t_A}/f_{t_M} and f_{t_M}/f_{t_B} constant. As mentioned before, using the scaling parameter β for this purpose is however preferred for the sake of clarity. In the simulations presented in this thesis the parameter β has not been used, so $\beta = 1.0$.

In each step of a fracture analysis the lattice mesh is loaded by external forces or prescribed displacements, and for each element σ_{eff} is computed following Eq. (6.5). Then, the element with the highest stress over strength ratio is removed from the mesh. This procedure is repeated until the mesh has completely fractured. It is mentioned that due to the linear elastic nature of the model the load which is applied to the lattice mesh can be a unit load. The external load in calculation step n, at which the most critical element i fails, can namely be found by back-calculation through

$$F_{\text{ext,crit}} = \frac{f_{t,i}}{\sigma_{\text{eff},i}} F_{\text{ext}} \tag{6.6}$$

In all simulations which have been carried out only *one* beam element was removed from the mesh during each loading step. By removing more than one element per step the speed of a computation can be considerably increased, although the possibility for stress redistributions during the fracturing process decreases. In case the number of beams that is removed per step remains small however, no large deviations occur in the computational result [37]. Here this matter has not been looked into.

6.2 Modelling of the size effect experiments

In this section the numerical modelling of the size effect experiments will be discussed. Uniaxial tension tests on specimens of five different sizes were modelled with regular and random triangular meshes, with and without particle overlay respectively. Although it has been attempted to enhance the models and to keep them as small as possible, the total computer time needed was still huge. Depending on their size, the simulations have been run at the following Silicon Graphics workstations: an Indigo with R4000 processor, three Indy's of which two had a R4600 and one a R4400 processor, an Origin 200 with 4×R10000 processor and an Origin 2000 with 4×R10000 processor. The CPU time needed varied from 2.3×10^4 sec. to 5.5×10^6 sec. which corresponded with runtimes from 7 to more than 3800 hours for a complete fracture analysis on a lattice with particle overlay.

6.2.1 Specimens and loading platens

In the numerical schematization of the specimens it was attempted to model the laboratory experiments as closely as possible. Since a 2D lattice model was used however, effects in the out-of-plane direction could not be incorporated in the analysis. To be able to model a large size range within the available computational capacity, the part of the specimen which was modelled with a lattice had to be kept as small as possible. Meanwhile it had to be ascertained that modelling only a part of the specimen with lattice elements would not affect the numerical result. In Appendix C.3 the effect of partly replacing the lattice mesh by continuum elements is outlined in more detail. Based on the results which are discussed there, the

total mesh was reduced by only applying lattice elements in that part of the specimen where cracks were expected. The remainder of the specimen and the loading platens were represented by 4-noded plane stress elements. For the dog-bone shaped specimens this implied that in the middle of the specimen a zone with a height of approximately 80 mm was modelled with lattice beams. Compared to the laboratory specimens, this meant that failure could occur in the zone in the middle of the specimen which was covered by the control LVDTs with a measuring length of 75 mm. By applying a lattice mesh with a height of 80 mm, the nodal displacements at the measuring points were just outside the area where possibly stress disturbances are induced due to the transition from lattice to continuum mesh. Apart from the type A specimen, all specimens were modelled with a combined lattice-continuum mesh. Since the total height of the type A specimens was only 65 mm, the whole specimen was modelled with a lattice. To connect the lattice and the continuum mesh, first all boundary nodes of the lattice were placed at a straight horizontal line (see also Appendix C.3.2). Then, linear dependencies ("tyings") were prescribed between the translational degrees of freedom of the nodes at the lattice-continuum boundary.

All elements representing the specimen, i.e. lattice beams as well as plane stress elements, were given unit thickness (1 mm). In case of the plane stress elements representing the loading platens however, a thickness of 1×10^5 mm was taken to ensure a uniform distribution of the external forces. The external forces have been applied as point loads at the positions of the bolts in the actual loading platens (see Section 3.3.2). The number of forces thereby depended on the specimen type (Table 3.5). By varying the magnitude of the force per bolt, the load eccentricity was incorporated.

6.2.2 Boundary conditions

In the experiments boundary conditions were chosen which allowed for free rotations of the specimens in two orthogonal directions. Furthermore, the rotation point was situated in the glue layer between specimen and loading platens. Because of the way in which the hinge constructions were designed in the experimental set-up, the whole of specimen and hinge constructions remained flexible until a certain tensile force had been applied. Consequently, modelling the complete system of specimen and hinges similarly as in the experiments, leads to a schematization which allows for rigid body rotations of the specimen (Fig. 6.8a). To arrive at a stable system resembling the schematization which is shown in the most right picture of Fig. 3.16, two alternatives are available. In the first alternative, the supports are placed at the bottom of the lower loading platen, whereas the upper loading platen remains unsupported. The external forces are applied at the upper loading platen. In this schematization the specimen can move freely in horizontal direction, but the rotation points are not situated between specimen and loading platens. A second alternative is shown in Fig. 6.8b. The rotation points are now situated correctly, which however also means that horizontal movements of the specimen boundaries are prevented. For both schematizations which are shown in Fig. 6.8 a lattice simulation has been made. In the simulation shown in Fig. 6.8a, the specimen is loaded through a vertical displacement of the upper hinge construction. The load eccentricity is introduced by means of an eccentric adjustment of the pendulum bars to the loading platens. In the simulation of Fig. 6.8b however, the load eccentricity is incorporated in the external forces. Both simulations gave identical results, despite the fact that negative diagonal terms were present in the stiffness matrix of the system shown in Fig. 6.8a.

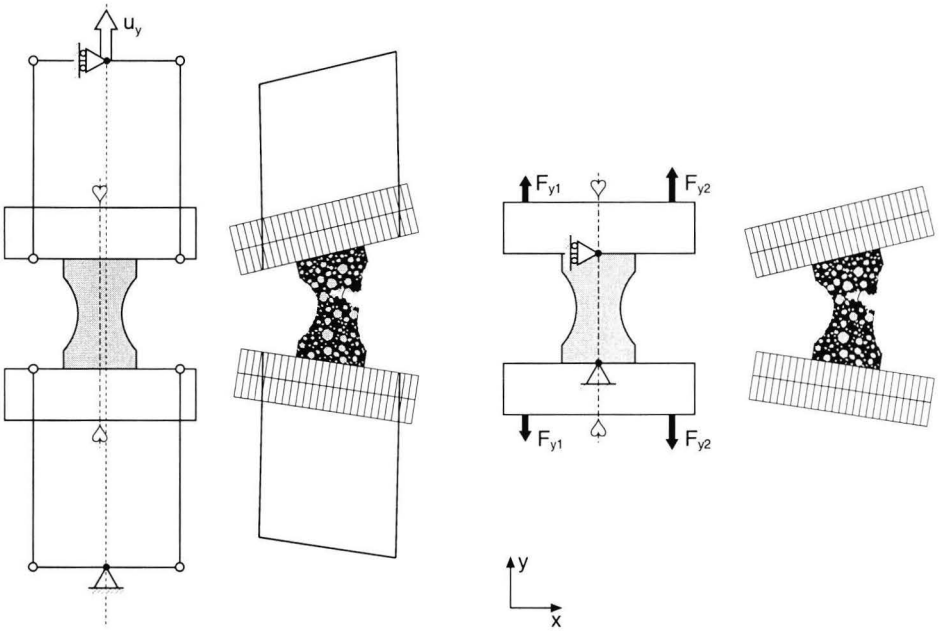


Figure 6.8 *Lattice model of type* A *specimen including hinge construction (a) and with simplified rotating boundary conditions (b). The fractured models are shown after removal of 175 beams.*

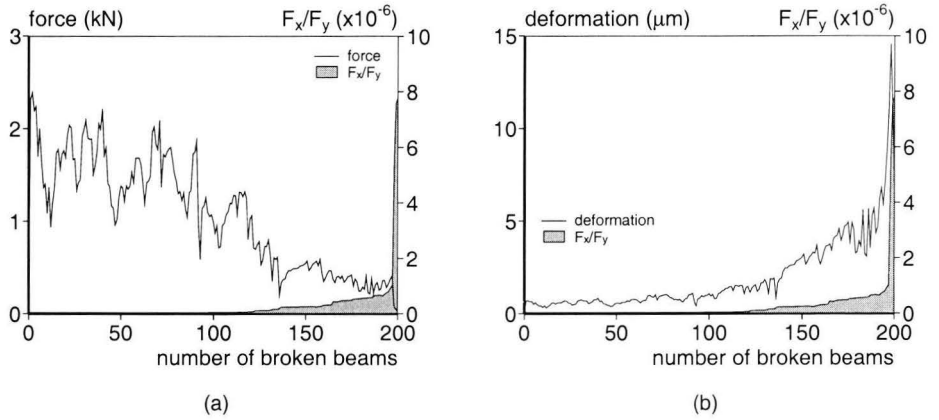


Figure 6.9 *Ratio of the horizontal reaction force and the (vertical) external force, in comparison with the external force (a) and the deformations computed in the specimen middle (b) for the simulation of Fig. 6.8b.*

When a simplified representation of the hinge constructions by means of supports does not affect the numerical result, the remaining question concerns the development of horizontal reaction forces in the system of Fig. 6.8b. Fig. 6.9 shows the ratio of the horizontal reaction force F_x and the total (vertical) external force F_y as a function of the number of beam elements which has been removed. In addition, also the external force (Fig. 6.9a) and the deformation in the middle of the specimen are shown (Fig. 6.9b). The latter was measured as illustrated in Fig. 3.23. From the graphs in Fig. 6.9 follows that horizontal forces develop when the specimen has almost fractured through. At that stage the rotation of the specimen halves increases, and the specimen middle undergoes a displacement in horizontal direction. Since at that moment the load-bearing capacity of the specimen is only small and the magnitude of the horizontal forces is almost negligible, hardly any influence will be found on the computational result. Therefore, and also because of the simple but representative schematization, the experiments have been modelled following Fig. 6.8b.

6.2.3 Material and geometrical heterogeneity

The laboratory experiments and the numerical simulations are not only connected by the shape of the specimens, but also by the material structure. Although the laboratory specimens are heterogeneous and each of them is unique as for the meso-structure, their *degree* of heterogeneity is similar. The degree of heterogeneity is namely related to the maximum aggregate size, which is invariable with the specimen size. In the simulations this constant degree of heterogeneity is reflected by the (average) length of the lattice beams, which is the same for all meshes. For the regular lattice a beam length of 1 mm was chosen. For the random lattice a cell size s of 1 mm was applied, which together with a randomness of 1 ($A = s$), leads to a slightly larger average beam length of $1.14s = 1.14$ mm [103]. In the case of the random lattice heterogeneity is automatically incorporated through the geometry of the mesh. For the regular lattice however, heterogeneity was explicitly introduced by projecting an aggregate structure on top of the lattice.

Just like the laboratory experiments, a heterogeneous lattice mesh is unique. Because of the consequent scatter in the results, simulations with a certain type of mesh and for a certain specimen size would have to be repeated. This was not possible however, because of the large amount of time which was needed to run the simulations. Therefore a different approach was followed. This approach has as additional advantage that a main feature of numerical simulations is benefitted as well, namely the possibility to test specimens of different sizes but with identical meso-structures.

In case of the random lattice, a rectangular set of nodes on an area of 1600×2400 mm^2 was generated, which covers the area of a type F specimen. All random lattice meshes for the smaller specimens were generated using the same set of nodes. The specimens were thereby placed on top of the nodes in such a way that the coordinates of the point 0 (see Fig. 6.10a) on the right hand side, in the middle of the specimens, coincided.

For random as well as regular lattice simulations additional heterogeneity was introduced by an aggregate structure in the mesh. For this purpose computer generated aggregate structures were used, rather than scanned, digital images. Obtaining digital images of real aggregate structures in the sizes which were needed would take a lot of effort, leaving the question whether it is worth while to apply this method for introducing heterogeneity. It is mentioned that this question is strongly related to the state of the art of the lattice model which has

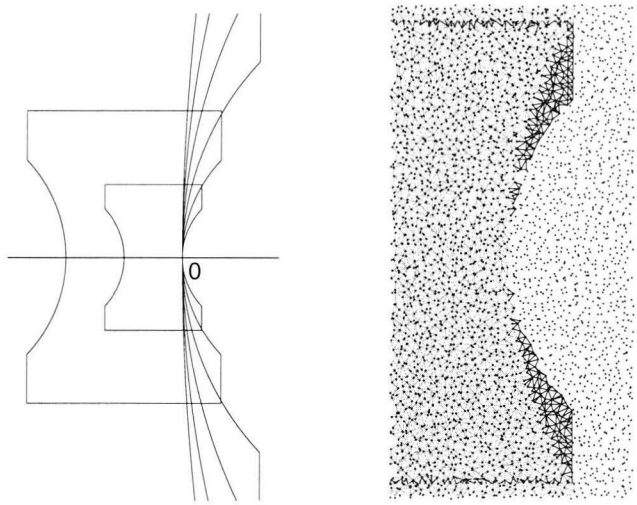


Figure 6.10 *Placement of meshes of different sizes on nodal data set (a) and example of construction of the* A *mesh (black) and the* B *mesh from the set of nodes (b).*

been used. From the simulations which are described in Sections C.2.3 and C.2.4 follows that the result of a lattice computation mainly depends on the ratio between weak and strong elements in the mesh. Hence, when this ratio remains constant, geometrical differences between aggregate structures will not drastically change the load-deformation response or the crack pattern resulting from a simulation (see also Fig. C.22). The basis of the aggregate

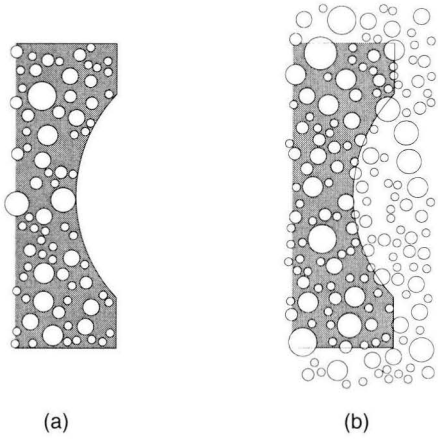


Figure 6.11 *Aggregate structure at the boundary of a cast (a) and a sawn specimen (b).*

structure was an aggregate distribution which was generated using Eq. (B.1). Based on the concrete mix which was applied in the laboratory specimens, the input parameters were taken $P_k = 0.65$ and $2 \leq d \leq 8$ mm. The aggregates were placed randomly in the generation area, as described in Appendix B.

In order to obtain similar aggregate structures for all specimen sizes it would be most easy to generate a large rectangular aggregate structure. Analogous to the generation of the random meshes, the aggregate structures for all specimens could then be cut from this large aggregate structure like is illustrated in Fig. 6.11b. Since the specimens were cast in dog-bone shaped moulds rather than sawn from a concrete block, a wall effect is present along the specimen edges (Fig. 6.11a). Compared to a sawn specimen, the concrete along the boundaries will therefore be weaker, which is partly due to a smaller amount of aggregates and a higher water-cement ratio. To take this wall effect into account while maintaining the same aggregate structure throughout the specimen, the following procedure has been adopted. First an aggregate structure was generated for a type F specimen, thus covering the largest area for which a particle overlay was needed. The smaller specimens were then placed on this particle overlay in the same way as illustrated in Fig. 6.10a. For the area without particles along the right boundary of each specimen, additional particles were generated for each specimen type. Parts of the resulting aggregate structures for specimen type A-E are shown in Fig. 6.12. Note that a wall effect is only introduced along the right boundary of the specimens. At the upper and lower boundary of the lattice mesh the concrete continues, so cutting the aggregates there is a natural thing to do. It could not be avoided though to cut the aggregates at the left boundary as well. This will hardly influence the numerical result however, provided of course the crack initiates at the right side of the specimen.

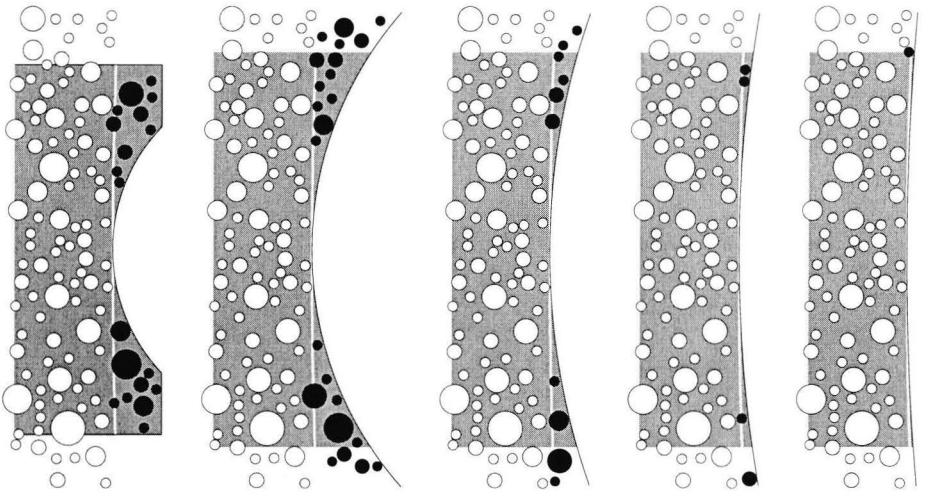


Figure 6.12 Applied aggregate structures for specimen type A-E *(left to right).*

6.2.4 Overview of input parameters

The input parameters which have not been discussed until now concern the strengths and the stiffnesses, as well as the dimensions of the cross section which have been assigned to the beam elements. As has already been pointed out in Section 6.1.3, the ratios of the strength and stiffness values for the subsequent phases determine the lattice behaviour. Except for the ratio f_{t_M}/f_{t_B}, all ratios were kept the same as in Table 6.1. The ratio f_{t_M}/f_{t_B} was chosen slightly lower than four to avoid excessive micro-cracking before peak load (see Appendix C.2.2). Starting point for tuning the beam height and the phase stiffnesses were a Poisson's ratio $\nu = 0.2$ and a global stiffness $E^* = 25000$ MPa for a mesh consisting purely of matrix material. An overview of all input parameters is given in Tables 6.2 and 6.3.

Table 6.2 Geometrical input parameters of the size effect simulations.

		Measures in mm				
		s	A	l	h	t
Lattice	regular	-	-	1.0	0.577	1.0
	random	1.0	1.0	-	0.615	1.0
Continuum	matrix[1]	-	-	-	-	1.0
	concrete	-	-	-	-	1.0
	steel	-	-	-	-	1.0×10^5

[1] mesh without particle overlay $2 \leq d \leq 8$ mm for the lattice

Table 6.3 Material properties of the size effect simulations.

		Units in MPa							
		ν	E	E_A	E_B	E_M	f_{t_A}	f_{t_B}	f_{t_M}
Lattice	regular	-	-	87514	31255	31255	10.0	1.50	5.0
	random	-	-	88522	31615	31615	10.0	1.50	5.0
Continuum	matrix[1]	0.2	25000	-	-	-	-	-	-
	concrete[2]	0.2	29956	-	-	-	-	-	-
	concrete[3]	0.2	28744	-	-	-	-	-	-
	steel	0.3	210000	-	-	-	-	-	-

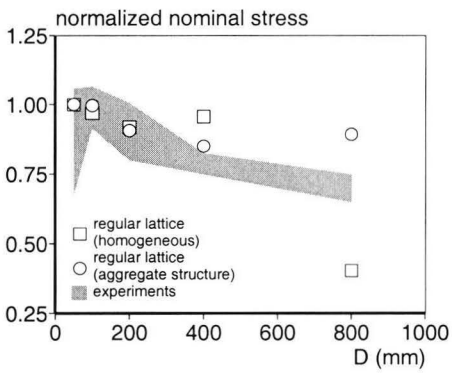
[1] mesh without particle overlay $2 \leq d \leq 8$ mm for the lattice, [2] in combination with regular lattice, [3] in combination with random lattice

6.3 Regular lattice analyses

The size effect simulations which have been carried out on regular lattice meshes comprised two sets of simulations. One set of homogeneous regular lattices and a second set of regular lattices in which an aggregate structure was incorporated. The presence of the aggregate structure, or rather heterogeneity in general, has a distinct influence on the size effect which is found. In Fig. 6.13 the results of both sets of simulations are shown, along with the band width of the individual experimental values. All results have been normalized in order to enable mutual comparisons. For the simulations the results of each set were normalized with the highest value of that set. In case of the experiments, all individual strength values have been normalized with the highest, *average*, strength value, which was found for the type B specimens (see Table 5.1).

In the homogeneous simulations no stress redistributions can take place, so that the ultimate load is reached after the first beam element has been removed from the lattice (see the table in Fig. 6.13). For specimens A, B and C the nominal stress is found to decrease gradually. The results of specimens D and E on the other hand fluctuate so strongly that, within the limited number of available results, it is hard to tell which of them (if any) follows a certain trend. A definite answer to this question can only be given after additional computations would have been made. If however the strength of the E specimen would give a true indication of the size effect for a homogeneous regular lattice, this size effect would be enormous. Alternatively, the low strength of the E specimen could also be due to imperfections in the mesh. In this respect one has to think of stress concentrations at the boundary between the continuum and the lattice, which still might be present despite all precautions which have been taken to ensure a smooth transition between both meshes. The smaller the lattice beams are with respect to the area in which the stress concentrations act, the stronger the influence of those stress concentrations will be. Thus, the external load at which a beam falling inside a higher stressed area fails will be especially low, which could be the reason for the low strength of the E specimen.

Contrary to the homogeneous case, stress redistributions can take place when heterogene-



Type	Removed beams at ultimate load	
	Homogeneous	Aggr. structure
A	1	66
B	1	306
C	1	389
D	1	365
E	3	1029

Figure 6.13 *Normalized nominal stresses for the regular lattice simulations with and without aggregate structure. The table lists the number of beam elements which had been removed at the moment the ultimate load was reached.*

ity is included in the lattice, like for the regular lattice with aggregate overlay. As a result, the number of beam elements which must fail before peak load is attained increases considerably. This follows from the table in Fig. 6.13, and is also illustrated graphically in Fig. 6.14 where the crack patterns at peak load are shown. The number of beams which fail until peak load approximately increases with the specimen size. As a matter of fact this could be expected, since also the areas with stress concentrations in the middle of the specimen scale with the specimen size. Looking back at Fig. 6.13 it can be seen that the nominal strength for the heterogeneous lattice first decreases with size and later increases again. The explanation for this phenomenon probably has to be sought in the width of the lattice zone. In comparison with the experiments, the area which is modelled with a lattice for specimen type A, B and C resembles the area covered by control LVDTs. This means that both in the simulations and the stable laboratory tests, cracks develop only in this specific area. In the experiments, crack localization outside this area would automatically have led to sudden failure. Contrary to the single row of LVDTs on the small specimens, in the experiments three and five rows of control LVDTs were placed on specimen type D and E respectively. Moreover, the crack frequently localized in these zones outside the middle of the specimen. Since this is not possible in the simulations, the development of micro-cracks could very well be restricted by the parts of the specimen modelled with continuum elements (see also Fig. C.24 and Fig. C.27 in Appendix C). Because of the relatively small lattice area less damage can develop, leading to a value for the ultimate load which is artificially high. Thus an increase of the nominal strength for specimen D and E is observed.

It is noteworthy that the crack patterns at peak load, at least for specimen type A, B, C

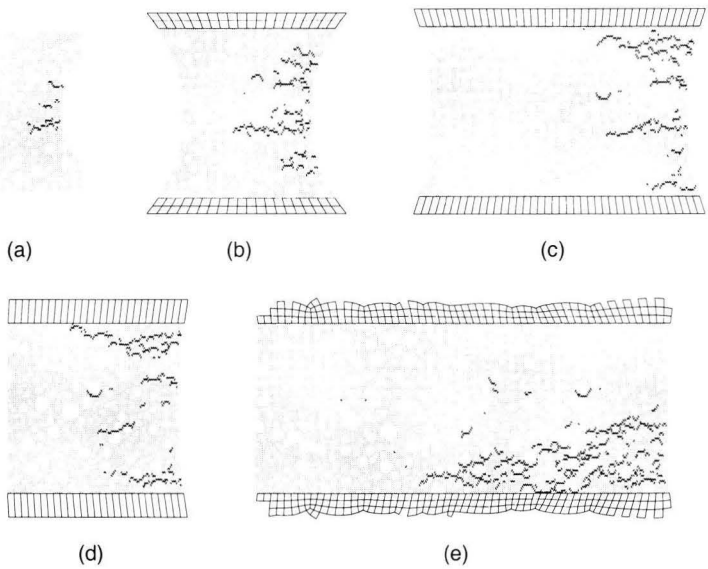


Figure 6.14 *Crack pattern at ultimate load for the regular lattice meshes with aggregate structure of specimen type A (a), B (b), C (c), D (d) and E (e) respectively. Figures (d) and (e) only represent the right side of the lattice mesh.*

and D, are all quite similar, which would be expected for the same aggregate structure. The reason for a size effect is therefore incorporated in the size of the highly stressed zones and the possibilities for stress redistributions in relation to the size of the specimen. With respect to the latter remark one has to consider the same amount of beams breaking in a small and a large specimen. The small specimen might be almost fractured through whereas at the same moment the large specimen has only partly failed.

All simulations were continued until the specimens had completely separated in two parts. In Fig. 6.15 the computed force-deformation curves are shown which resulted from the simulations on the heterogeneous regular lattices. Using these deformations, as well as the COD (or control) measurements at the right side of the specimen, the fracture energy was computed following the procedure described in the chapter Symbols and Definitions. In addition, this was done for a maximum crack width of 25 μm and 100 μm respectively. From

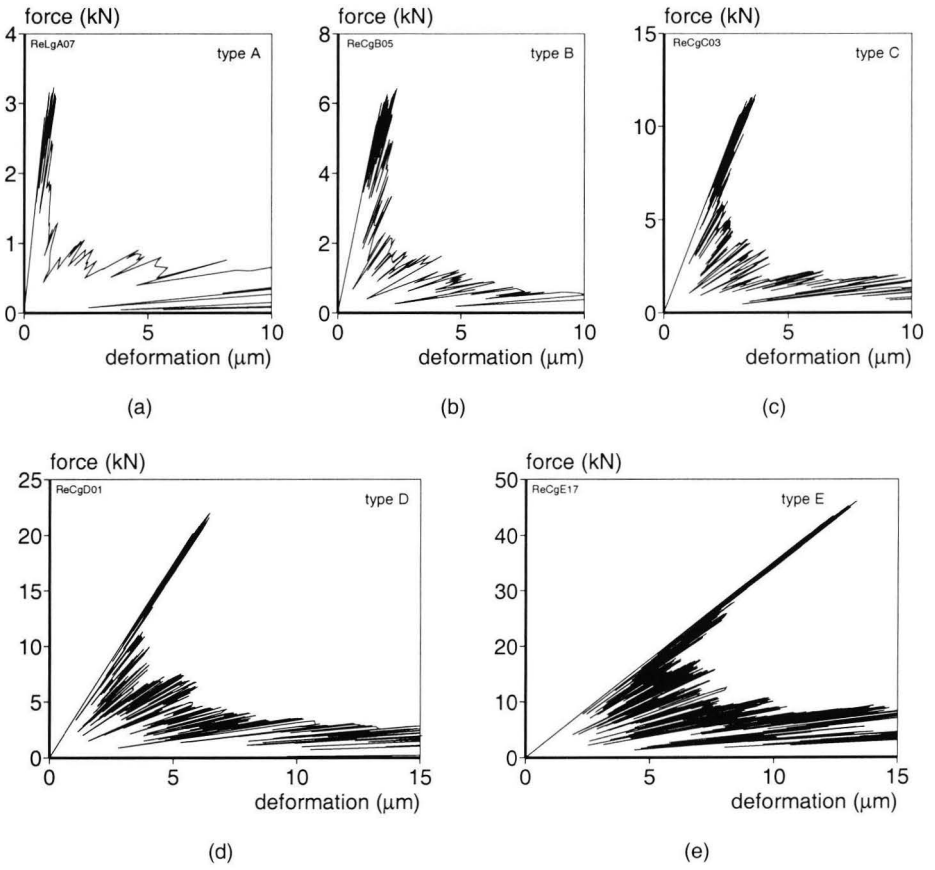


Figure 6.15 *Computed force-deformation curves for the regular lattice meshes with aggregate structure of specimen type* A *(a),* B *(b),* C *(c),* D *(d) and* E *(e), based on the scaled deformation measured in the specimen middle.*

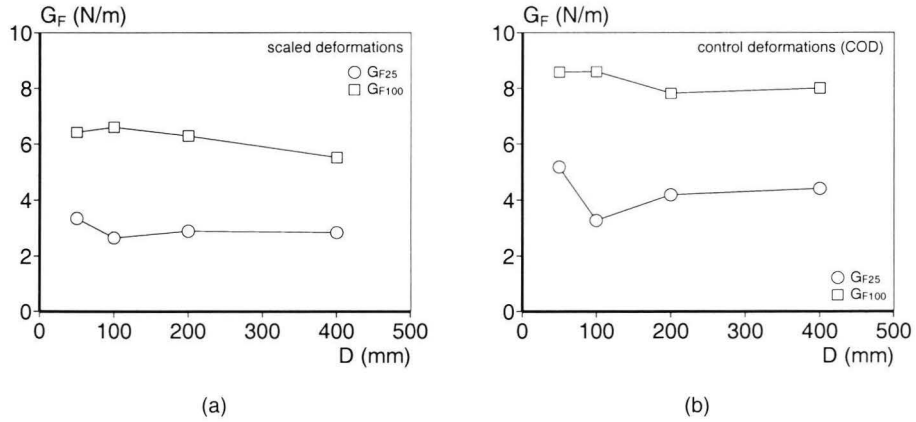


Figure 6.16 *Fracture energy computed from the regular lattice simulations with aggregate structure (eccentric loading), using the deformations measured in the specimen middle (a) and at the right side of the specimen (b).*

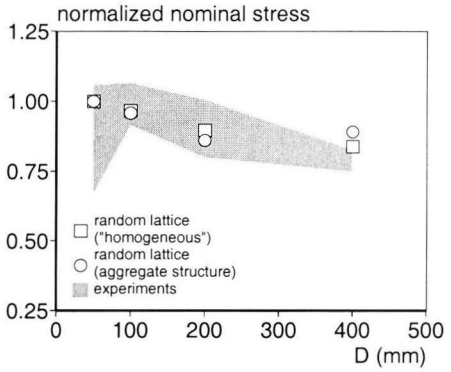
the results shown in Fig. 6.16 follows that for a larger maximum crack width, differences in fracture energy between the subsequent specimen sizes average out. For a maximum crack width of 100 μm, a more or less constant fracture energy is found. For the fracture energy computed from the COD measurements higher values are found, which is due to the fact that the work of bending is incorporated as well.

6.4 Random lattice analyses

In addition to the size effect simulations on regular lattices, also simulations on random lattices were carried out. The only difference between these simulations was the type of lattice that was applied. The continuum mesh as well as the aggregate structure were identical.

Even when no aggregate structure is incorporated in the mesh, a random lattice exhibits a heterogeneous behaviour due to the variation in beam length. This leads to small stress redistributions before the ultimate load is reached (see also the last column of Table 6.4), resulting in a behaviour which is strongly comparable to that of a regular lattice with aggregate structure. The computed size effect on the nominal strength for the random lattice is shown in Fig. 6.17, where the random lattice without aggregate structure is referred to as "homogeneous". When comparing Figs. 6.17 and 6.13, it is found that both types of random lattice behave quite similar as a regular lattice with aggregate structure. The presence or absence of an aggregate structure in the random lattice is reflected by the number of beam elements which fails before peak load, or, again, the degree of stress redistributions which occurs. This is illustrated in the table which accompanies Fig. 6.17. In conjunction with the last column of Table 6.4, it seems as if with an increasing number of beams failing before peak load, the difference between the failure load of the first beam element (F_1) and the ultimate load (F_u) increases as well.

Analogous to the regular lattice with aggregate structure, also for the random lattice with



Type	F_1/F_u	
	"Homogeneous"	Aggr. structure
A	0.89	0.71
B	0.88	0.66
C	0.94	0.66
D	0.90	0.57

Figure 6.17 *Normalized nominal stresses for the random lattice simulations with and without aggregate structure. The table shows the ratio between the failure load of the first beam and the ultimate load, as a measure for stress redistributions.*

aggregate structure it was found that the nominal strength increased again for specimen type D. The crack patterns at ultimate load of Fig. 6.18, show how the height of the zone in which micro-cracking occurs increases with the specimen size. For the D specimen this height is again restricted by the height of the lattice mesh, leading to the artificially high value of the nominal strength for this specimen. Since cracking in a "homogeneous" random lattice is much more discrete, there this effect is not found. This will be illustrated further on in this paragraph (Fig. 6.23).

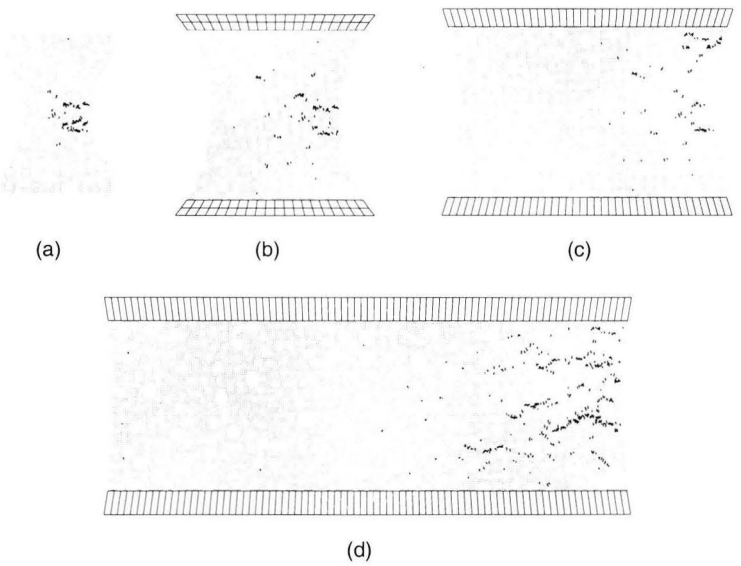


Figure 6.18 *Crack pattern at ultimate load for the random lattice meshes with aggregate structure of specimen type A (a), B (b), C (c) and D (d) respectively.*

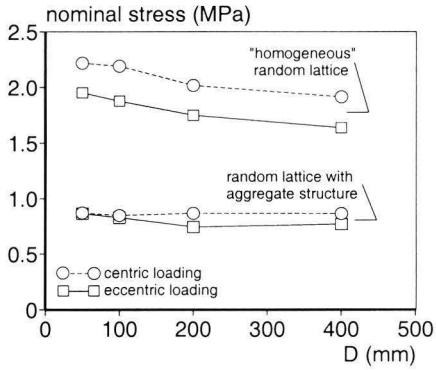


Figure 6.19 *Computed nominal stresses for random lattices with and without aggregate structure under centric and eccentric loading respectively.*

Until now, all results which have been presented concerned simulations in which the loading configuration was eccentric, like in the experiments. In order to get more insight into the effect of this load eccentricity simulations were carried out in which the load was applied centrically. These simulations comprised the regular lattice meshes as well as the random lattices. The following discussions however, will be restricted to the outcome of the random lattice simulations.

The results of the centric as well as the eccentric simulations have been gathered in Fig. 6.19, both for the random lattice with and without aggregate structure. In addition to Fig. 6.19, a comparison of some characteristic values is given in Table 6.4. In the table the ratio of the load in the centric and the eccentric loading case (F_{cen}/F_{ecc}) is shown, which is known to be 1.20 in the homogeneous, linear elastic case (see Eq. (3.2) in Section 3.3.4). This ratio

Table 6.4 *Results for the random lattice simulations with centric loading vs. those with eccentric loading. The number between brackets denotes the step at which the centric load has been taken.*

	Type	Side of crack initiation	$F_{cen,step}/F_{ecc,1}$	$F_{cen,u}/F_{ecc,u}$	Peak step	
					Cen.	Ecc.
"Homo-geneous"	A	Right	1.17 (1)	1.14	9	8
	B	Right	1.18 (2)	1.17	24	11
	C	Left	1.19 (6)	1.15	19	9
	D	Right	1.18 (1)	1.17	14	11
Aggregate structure	A	Left	1.13 (1)	1.01	49	68
	B	Left	1.15 (1)	1.02	113	87
	C	Right	1.14 (1)	1.17	328	94
	D	Left	1.16 (2)	1.12	712	345

has been computed at ultimate load and, in most cases, at the first step of the computation, i.e. for the load which was needed to remove the first beam element. If another step was chosen, this was just to enable computing the ratio at removal of exactly the same element, in both the centric and the eccentric simulation.

For the "homogeneous" random lattice the results of the simulations with and without load eccentricity are quite comparable. This follows quantitatively from Table 6.4, as well as from the graphical illustration in Fig. 6.19. The difference between the results of both loading cases is more or less constant, and purely due to the load eccentricity. This conclusion is supported by the centric and eccentric simulations on homogeneous regular lattices. There, the ultimate load was always reached at step one and the difference between the ultimate load in the centric and the eccentric case was independent of the specimen size. More interesting therefore, is the outcome of the random lattice simulations with aggregate overlay. For the removal of the first beam element the ratios between the force in the centric and the eccentric simulation are again governed by the load eccentricity. At ultimate load however, it is found that the ratios have increased or decreased. A decrease of the ratio is found in those simulations where the path of the discrete cracks does not coincide for both loading cases. When micro-cracking occurs at a weaker (or more stressed) spot in the mesh than was the case for the eccentric simulation, the peak load will be lower. The factor F_{cen}/F_{ecc} is then found to decrease as well. The second situation which can be considered concerns an increase of the ratio F_{cen}/F_{ecc} towards peak load, like is found for specimen type C. For this specimen the area where cracks occur *is* the same in both simulations, but the number of beam elements which has been removed at peak load is much higher in the centric case. It seems that due to this larger amount of micro-cracks, the consequent stress redistributions allowed for a further increase of the external load. This in return led to an increase of the ratio F_{cen}/F_{ecc}. Looking again at Fig. 6.19, it can be seen that for the centric simulations almost no size effect appears.

In summary, it seems that two different effects have to be distinguished, which both influence the ultimate load.

1. The ultimate load depends on the weakest spot which is present in the material *and* where failure can actually occur. If, like in the case of load eccentricity, higher stresses occur in a stronger part of the material, failure can occur there which results in a nominal strength which is relatively high.

2. The ultimate load depends on the degree in which stress redistributions can take place, since stress redistributions lead to an increase of the external load.

Also for the eccentrically loaded random lattices with aggregate structure, the fracture energy G_F has been computed until a maximum crack width of 25 μm and 100 μm respectively. Contrary to the regular lattice (Fig. 6.16), the results for the random lattice which are shown in Fig. 6.20, are much more similar to the experimental results which were presented in Figs. 5.5a and b. G_F tends to increase with the specimen size, although this increase becomes smaller for large sizes. With respect to the values of $G_{F_{100}}$ it is mentioned that they must be regarded with some reservation. Due to the two-dimensional nature of the lattice simulations which are presented here, the resulting behaviour is very brittle. A crack opening of 100 μm is therefore relatively large, meaning that the fracture energy can be strongly influenced by

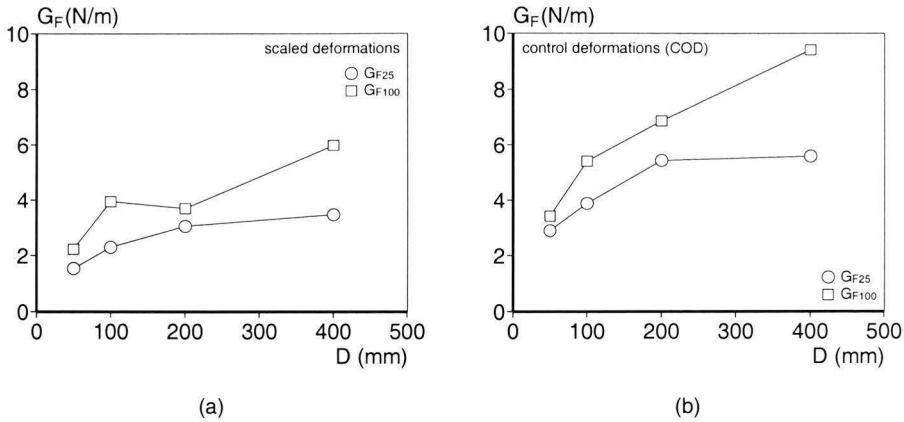


Figure 6.20 *Fracture energy for the random lattice simulations with aggregate structure, using the deformations measured in the specimen middle (a) and at the right side of the specimen (b).*

the load bearing capacity of only a small number of lattice beams. Furthermore, since not more than one simulation has been carried out for each specimen size, the computed values for G_F can only be regarded as indicative for a possible behaviour or trend.

The general observation until now is that in particular the behaviour of a random lattice with aggregate structure comes close to the concrete behaviour in many aspects. To conclude the observations of size effect in a lattice, a comparison is made between the crack patterns in random meshes of different sizes but with the same aggregate structure. The deformed meshes of four specimens are shown in Fig. 6.21, where each specimen has reached a COD of 5 μm. All specimens show one localized crack with branches and surrounded by micro-cracks. The micro-cracks partly developed before peak load was reached. Also during the propagation stage of the localized crack however, new micro-cracks develop in its vicinity. This fracture process can be directly related to the distribution of beam strengths in the random lattice. Hence, the random lattice can be compared with a regular lattice with a strength distribution [68, 69] or a regular lattice in which small particles have been included [2, 3]. Basically, the lattice behaviour which is obtained depends on the ratio between weak and strong elements in the mesh which is discussed in detail in Appendix C.2.4. Whether this on-going development of micro-cracks during the propagation phase also take place in real experiments, would have to follow from experimental observations.

For all specimens of Fig. 6.21 the main crack localized at the same spot in the material. Along with the COD of 5 μm, the length of the localized crack is found to vary which leads to different deformation states of the four specimens. The vertical deformations of the A specimen vary almost linearly over the width of the specimen. With increasing size of the specimen, the nonlinearity of the deformations increases as well. This is illustrated by Fig. 6.22, where the vertical deformations of the upper lattice boundary have been plotted as a function of the distance to the right specimen edge. To facilitate a mutual comparison, the deformations of each specimen size have been normalized with the maximum deformation which was computed for that specimen size. It can be expected that this transition from

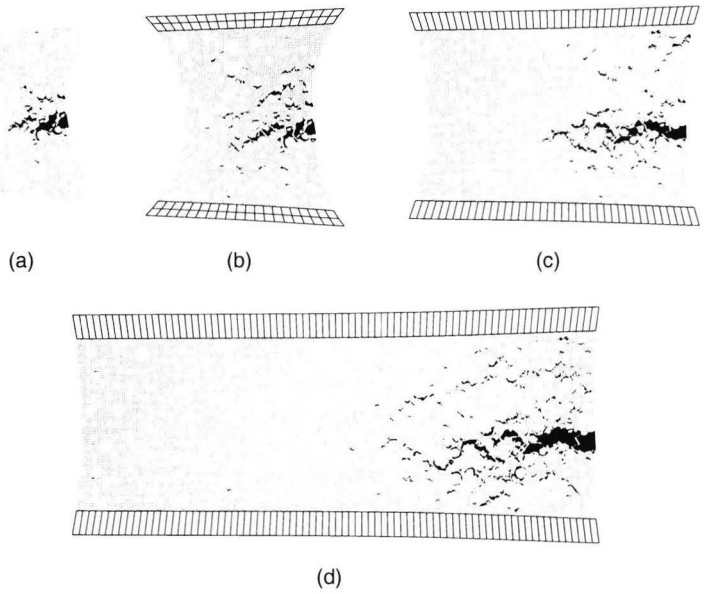


Figure 6.21 *Random lattice meshes with aggregate structure, of type* A *(a),* B *(b),* C *(c) and* D *(d). All specimens represent a deformation stage with a* COD *of 5 μm.*

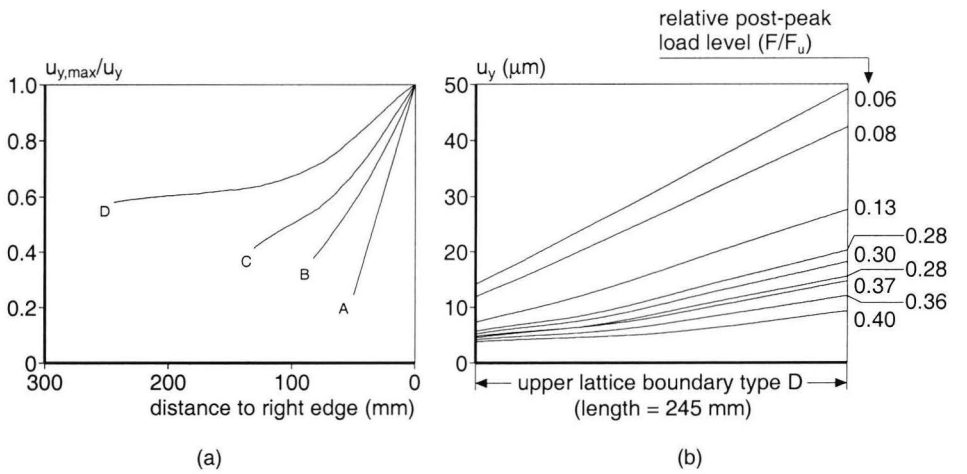


Figure 6.22 *Normalized vertical deformation of the upper lattice boundary at a* COD *of 5 μm for the random lattices with aggregate structure (a), and post-peak deformation evolution for upper lattice boundary of the* D *specimen (b).*

nonlinear specimen deformations at peak load, to linear deformations once a stress-free crack has developed throughout the specimen, occurs for each specimen size. An example of such a transition is given in Fig. 6.22b, which shows the deformation evolution of the upper lattice boundary of the D specimen of Fig. 6.21d, beyond peak load.

6.5 Regular lattice versus random lattice

In Appendix C.2.2 it has been illustrated that the outcome of a lattice analysis strongly depends on the kind of heterogeneity which is included in the lattice mesh. Furthermore, also the amount of weak lattice elements relative to the total amount of elements influences the observed lattice behaviour to a great extent. In addition to the various size effect simulations which have been discussed, here it is intended to give a comparison between the results for the different lattices which have been adopted. Hence, the type C lattice is taken as example, modelled with a regular and a random lattice, both with and without aggregate structure respectively. For these lattices the final crack pattern as well as the force-deformation curves are collected in Fig. 6.23, where the elastic deformations have been subtracted from the total deformations. Table 6.5 lists some characteristic values for each simulation.

For the homogeneous regular lattice computation, the typical characteristics are that ultimate load is reached in step one, followed by a straight crack through the mesh. This results in a smooth softening branch together with a value for G_F which is very low. As soon as an aggregate structure is included the behaviour of the lattice becomes much more ductile. Before peak load stress redistributions occur and crack growth and crack localization go together with branching and bridging so that a much higher value for the fracture energy is obtained. It is interesting to see that already a random distribution of (geometrical) beam properties, as is the case for the "homogeneous" random lattice, gives strongly comparable results. However, fewer beams fail before peak load and the localized crack is not as tortuous as for the regular lattice with aggregate structure. Yet the variation of beam lengths can easily make up for this in terms of ductility. When incorporating an aggregate structure in the random lattice as well, the aforementioned effects become even more extreme.

Note that also for these four simulations, the approximate relation between the ratio F_1/F_u (table in Fig. 6.17) and the number of beams which fail before peak load is found (Table 6.5). In other words, with an increasing number of beam elements failing before peak

Table 6.5 *Comparison of characteristic values for different lattice models used to schematize the type C specimen.*

Lattice type	Aggregate structure	F_1/F_u	Peak step	$G_{F_{15}}$ [N/m]
Regular	-	1.00	1	0.41
	×	0.83	389	2.26
Random	-	0.94	9	2.43
	×	0.66	94	3.68

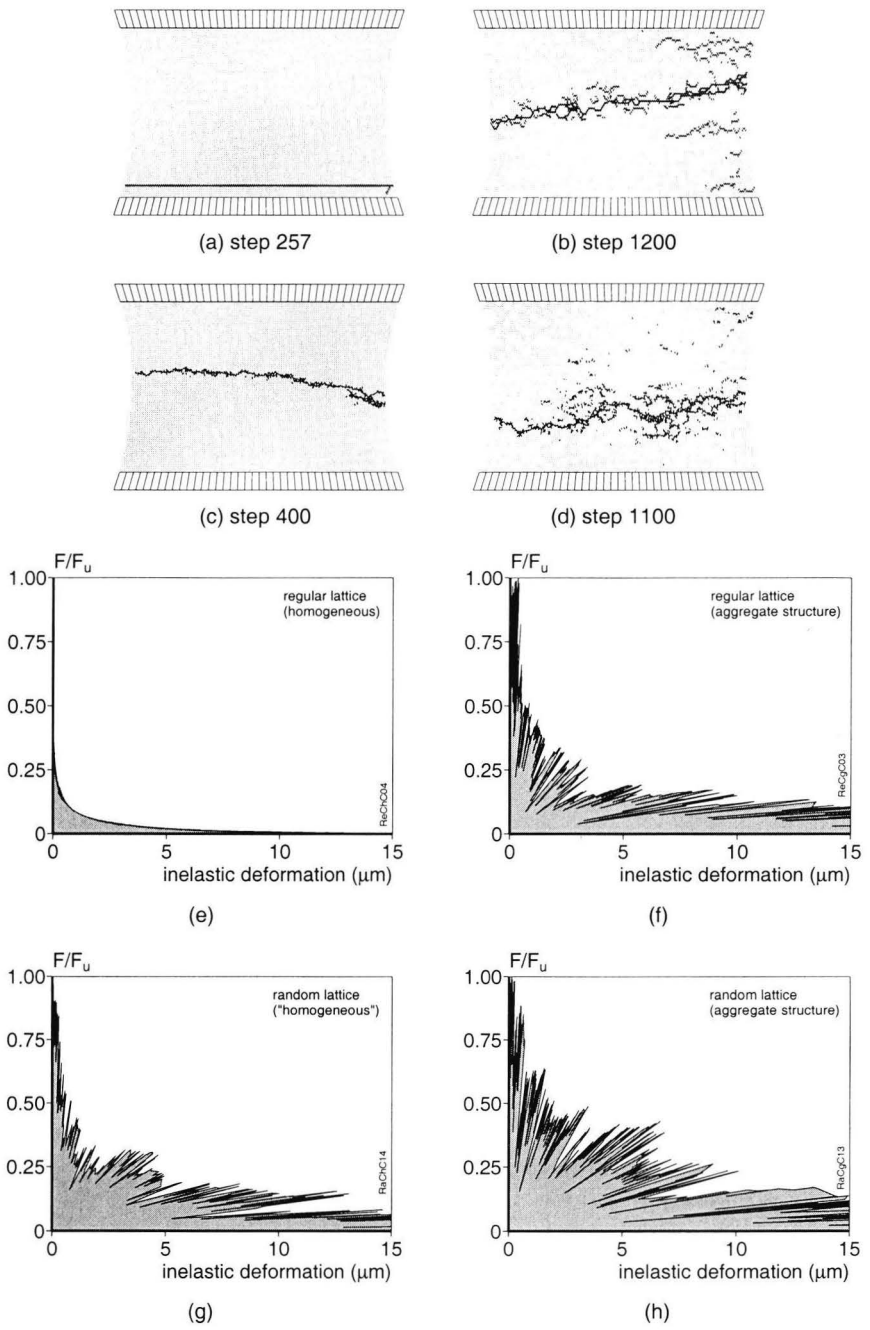


Figure 6.23 *Final crack patterns and force-deformation curves for specimen type* C *modelled with a regular lattice without (a,e) and with aggregate structure (b,f), and a random lattice without (c,g) and with aggregate structure (d,h).*

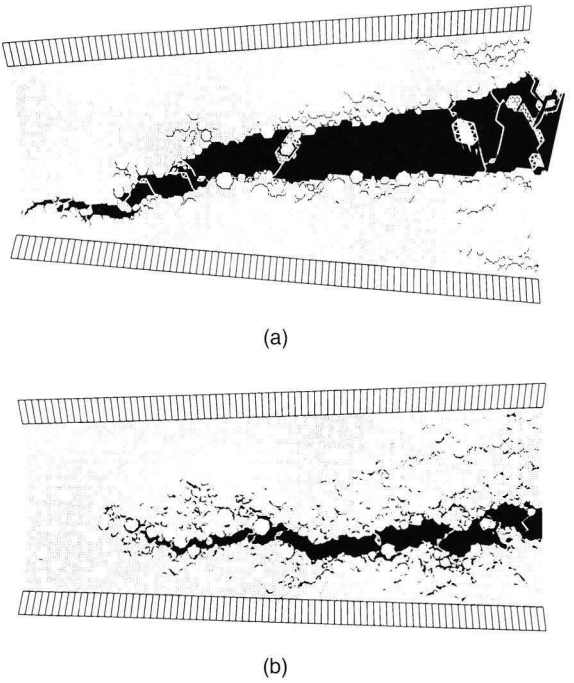


Figure 6.24 *Deformed regular (a) and random mesh (b) of type* D *specimen after the removal of 2250 lattice beams.*

load, the ratio F_1/F_u decreases.

When considering a regular and a random lattice, both with the same aggregate structure, a comparison can be made like for the D specimen which is shown in Fig. 6.24. From both lattices 2250 beam elements have been removed. In the regular lattice (Fig. 6.24a) the beams were mainly removed during the formation and propagation of the localized crack. In the random lattice on the other hand (Fig. 6.24b), apart from the localized crack also additional micro-cracks developed in the vicinity of the macro-crack. This is purely due to the length variation of the beam elements in the random lattice, meaning that a comparable result would be obtained when a strength distribution is applied in e.g. the matrix phase of the regular lattice. On the one hand one could argue that in the latter case the distribution is known exactly, which could be preferred. On the other hand it means that the characteristics of the distribution would have to be chosen (average and width), which will be difficult to do in a straightforward manner. By applying a random lattice this problem is automatically circumvented. The result is a mesh which does not exhibit directionality and which incorporates variations of properties in a wide range of magnitudes.

Chapter 7

Interpretation of results: synthesis

7.1 Statistical size effect

In the first chapters of this thesis it was mentioned that the size dependence of the nominal strength has been known for a long time. An extensive literature review by Bažant and Chen [9] starts by mentioning findings of Leonardo da Vinci, already in the 16th century. At that time, Da Vinci stated that an inverse proportionality existed between the length of a cord and its strength. Later that statement was rejected and/or more refined but the basic principle remained intact: the strength decreases with, in this case, an increasing length of the cord. Four centuries passed until Weibull proposed a statistics based strength theory which became widely accepted [110, 111]. Application of Weibull's theory, now even known as classical strength theory, is restricted however, since the effect of stress-redistributions is not taken into account. Consequently, the ultimate load which can be born by a piece of material purely depends on the distribution of flaws in that piece of material. If the strength of the weakest spot is exceeded, the ultimate load has been reached and total failure takes place. Due to this purely brittle material behaviour Weibull's theory is also called the weakest link theory.

7.1.1 Application of Weibull theory to experimental results

Since the weakest link theory is based on failure types in which stress redistributions are absent or only play a minor role, its application is restricted to uniaxial tension tests. These tests are generally considered to be typical examples of material failure under a uniform state of stress. Failure occurs at the weakest spot in the material, and since no stress redistributions take place this is inherent to failure of the complete specimen. Consequently, size effect under uniaxial tension should be considered to be a statistical size effect which implies that it follows Weibull theory. For other types of tests however, the load can increase further after exceedance of the tensile strength which can be attributed to the specimen geometry and/or the stress distribution within the specimen. In the latter cases a strong size effect is found, which is explained by fracture mechanics and energy-based approaches, e.g. [7, 8, 61].

Here uniaxial tension tests are discussed, so let us take a closer look at the size effect according to Weibull theory. In its most general form, the probability of failure of a solid, p_f, can be written as a function of its volume and some parameters which are considered to be material parameters. This function is given by [110, 12]

$$p_f = 1 - e^{-n_V \left(\frac{\sigma - \sigma_u}{\sigma_0}\right)^m} \quad , \quad n_V = V/V_r \tag{7.1}$$

The solid is schematized as a volume V, which is subdivided in n_V representative volume elements V_r. Such a volume V_r can be regarded as the smallest volume which can both be treated as a continuum and which is still representative for the material. In Eq. (7.1) σ stands for the externally applied stress, σ_u is the largest stress at which the failure probability is zero (strength threshold or datum parameter), σ_0 is the scale parameter and m the shape parameter or Weibull modulus which can be found by a fit on experimental data.

When substituting V in Eq. (7.1) by $V = D^n$, where D is the characteristic dimension and n is the number of dimensions, an inverse proportionality between σ_N and D can be derived following (see also [12])

$$\sigma_N \propto D^{-n/m} \tag{7.2}$$

This relation can now be applied to the present test results. In the case of two dimensional similarity like in the present investigation, $n = 2$. The value for the Weibull modulus m follows from a series of tensile tests on concrete conducted by Zech and Wittmann [117] as $m = 12$, leading to

$$\sigma_N \propto D^{-1/6} \tag{7.3}$$

In other words, in a log-log plot the nominal strength of concrete should decrease inversely proportional to the specimen size with a ratio 1:6. This relation is shown graphically in Figs. 7.1a and b for the test results of the DRY and the WET series respectively. It is realized that the value of $m = 12$, and thus the inverse proportionality of 1:6 between log σ_N and log

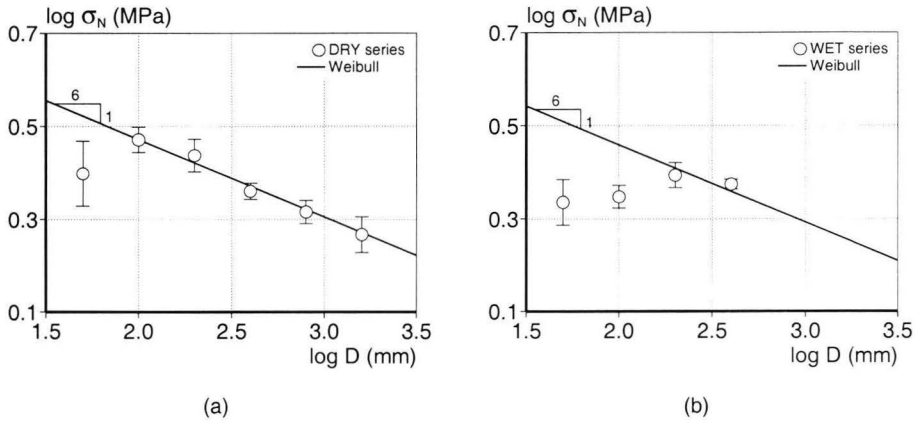


Figure 7.1 *Comparison between Weibull theory and results of DRY series (a) and WET series (b) respectively.*

D, is non-unique, since it depends among others on the concrete grading and the coefficient of variation of the experimental results. Hence, the value of $m = 12$ should merely be seen as an approximation for uniaxial tension tests on concrete. A second remark concerns the application of Weibull theory to failure of concrete. In concrete, stress redistributions and thus progressive failure will always occur to some extent, the degree of stress redistributions being dependent on among others the state of stress. Hence, applying Weibull theory to concrete failure would already involve a more advanced kind of Weibull theory, compared to the original version which purely dealt with instant failure of the complete structure. Keeping the foregoing considerations in mind the agreement between the results of the DRY series and the size effect predicted by Weibull theory is evident, and even more impressive when considering that the Weibull relation has been derived instead of having been fitted to the experimental results. A natural conclusion would therefore be that the observed size effect in the uniaxial tension tests is a pure material or statistical size effect. When looking at the results of the WET series however, no agreement is found between the experiments and the Weibull relation. If a material size effect is present, then it is completely overruled by other, possibly structural, effects which appeared during the tests.

7.1.2 Validity of Weibull theory for present experiments

Comparison of the size effect according to Weibull theory with the experimental results of two series of uniaxial tension tests, shows almost perfect agreement for the DRY series whereas total disagreement is found for the WET series. The question is therefore raised whether classical strength theory is actually applicable here. To answer this question the starting points have to be reviewed, which are a uniform state of stress and the absence of stress redistributions. In order to get more insight into the fulfillment of these starting points in the present experiments, a representative test on a type B and a type F specimen will be evaluated in more detail.

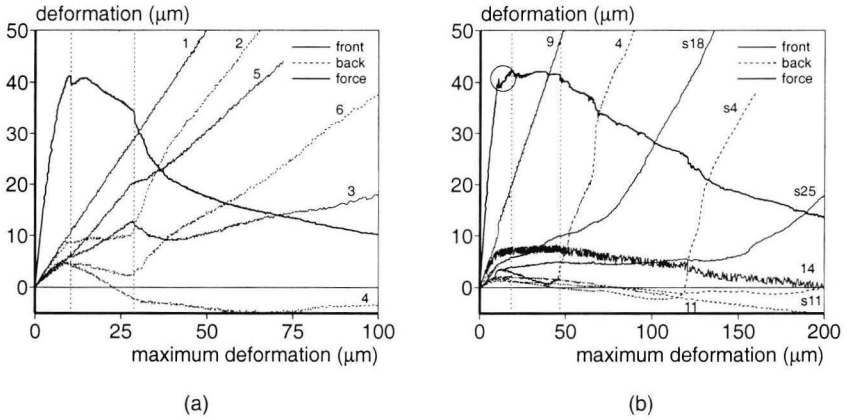


Figure 7.2 *Deformation readings in failure zone for* B *specimen (a) and* F *specimen (b), see also Figs. 7.3b,c. The ultimate loads are 17.9 kN for the* B *specimen and 190.7 kN for the* F *specimen respectively.*

As was already pointed out in Section 3.3.5, multiple displacement transducers were placed on a specimen during a test. Figs. 7.2a and 7.2b show the measured deformations in the failure zone of a type B and a type F specimen as a function of the maximum or control deformation (see Figs. 7.3b,c for transducer numbers). As a reference also the external force is plotted against the maximum deformation, where it is mentioned that the magnitude of the force is not related to the values on the y axis. For both specimens the LVDT placed in the right front corner of the specimen measures the largest deformation and is therefore used to control the test. The deformations measured by the other LVDTs are smaller and roughly depend on their position on the specimen surface. When the crack, which propagates through the specimen from the right side towards the left side, passes a displacement transducer the measured signal increases strongly. Before this moment however, the deformations measured by that particular LVDT are mainly elastic.

Two typical stages in each test have been marked by the dotted vertical lines in Figs. 7.2a and 7.2b. The first line indicates ultimate load. The second line marks the moment at which the deformation at the back side of the specimen, next to the right corner, starts to increase rapidly. Whereas the load for the type B specimen increases almost linearly until peak load, this is not the case for the type F specimen. Here the load starts to increase linearly, followed by a strong nonlinearity before peak load, which has been marked with a circle in Fig. 7.2b. Already during this stage of the experiment the deformation readings of LVDTs 4 and 9 start to deviate increasingly. For the type B specimen on the other hand, hardly any deviation of the deformation readings on the front and the back side (LVDTs 1 and 2) was found before ultimate load.

The second dotted vertical line corresponds in case of the B specimen with the moment when a small load drop occurs. This is probably due to the fact that the length of the crack front suddenly decreases after having increased continuously before. Although the same happens for the F specimen, an equally abrupt load drop was not observed there. A possible reason might be the more gradual failure which is observed in the large specimens, like for instance at peak load. When the deformations at the back of the specimen start to increase, all deformations measured on the front side are larger than those on the back side. This shows that crack propagation is not purely from the right to the left side, but an intermediate form between propagation in the in-plane and the out-of-plane direction. This change of the preferential direction for crack growth can to some extent be attributed to the shape of the cross section, which is further elaborated in Section 7.2.2.

Following the above considerations, it would be interesting to verify whether a relationship exists between the ultimate load level and the deformation state of a specimen until peak load. In Figs. 7.4 and 7.5 the deformations of the transducers covering the final crack are shown at ten loading stages until ultimate load (see also Fig. 7.3a). For the type B specimen the measurements of the LVDTs in the middle of the specimen have not been incorporated since their measuring length is 60 mm, instead of the 75 mm for all the other measurements. Consequently, the measured deformations in the middle will be about 20% lower than at the edges, purely due to the different measuring lengths, which would give a wrong impression. Thus, the actual deformations on the front and back side of the type B specimen are like the ones shown in Fig. 7.5, rather than varying linearly.

In Fig. 7.4 little difference is found between the deformation of the front and the back side of the type B specimen. Whereas no deformation gradient is present over the specimen thickness (out-of-plane direction), a deformation gradient *is* found in the in-plane direction,

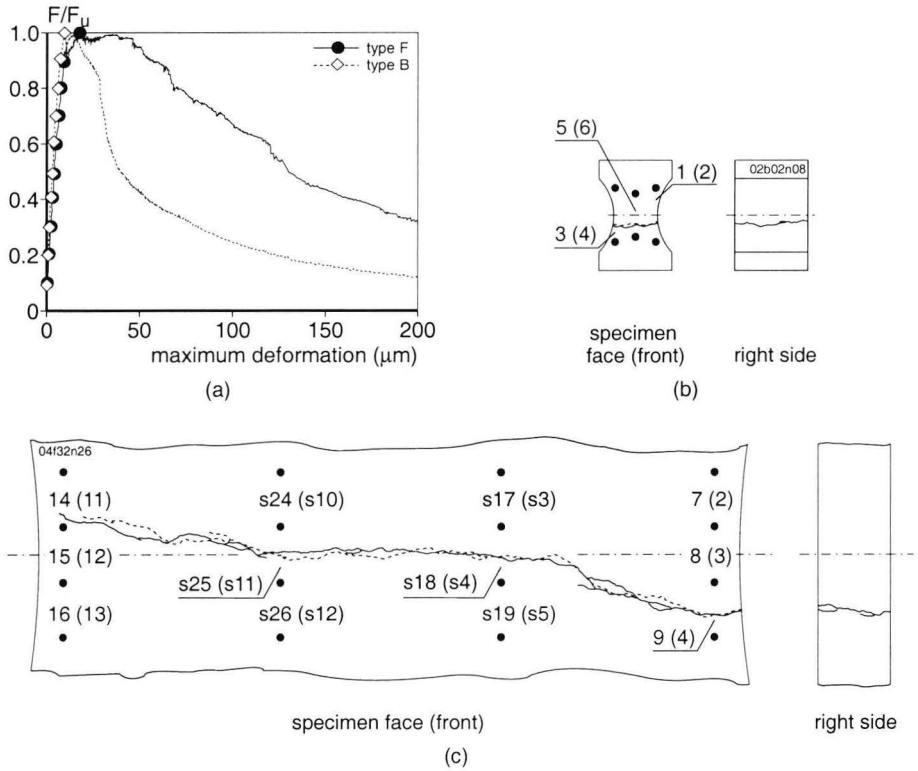


Figure 7.3 *Different loading stages for the type* B *and type* F *specimen at which the deformations are shown in Figs. 7.4 and 7.5 respectively (a), final crack pattern and transducer configuration for the type* B *specimen (b) and the type* F *specimen (c). The numbers between brackets indicate the transducers at the back side of the specimen.*

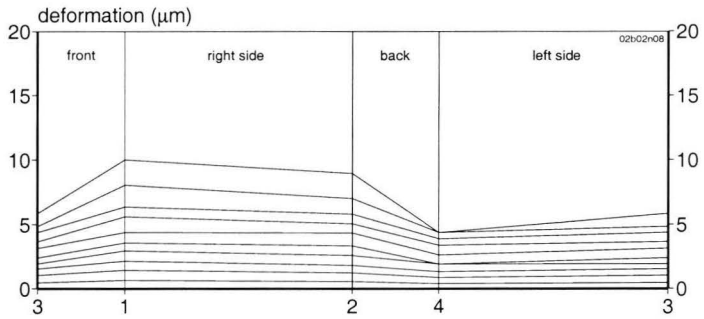


Figure 7.4 *Deformation of type* B *specimen (of Fig. 7.2a and Figs. 7.3a,b) during 10 loading stages until ultimate load. For the placement of the transducers indicated at the x-axis, see Fig. 7.3b.*

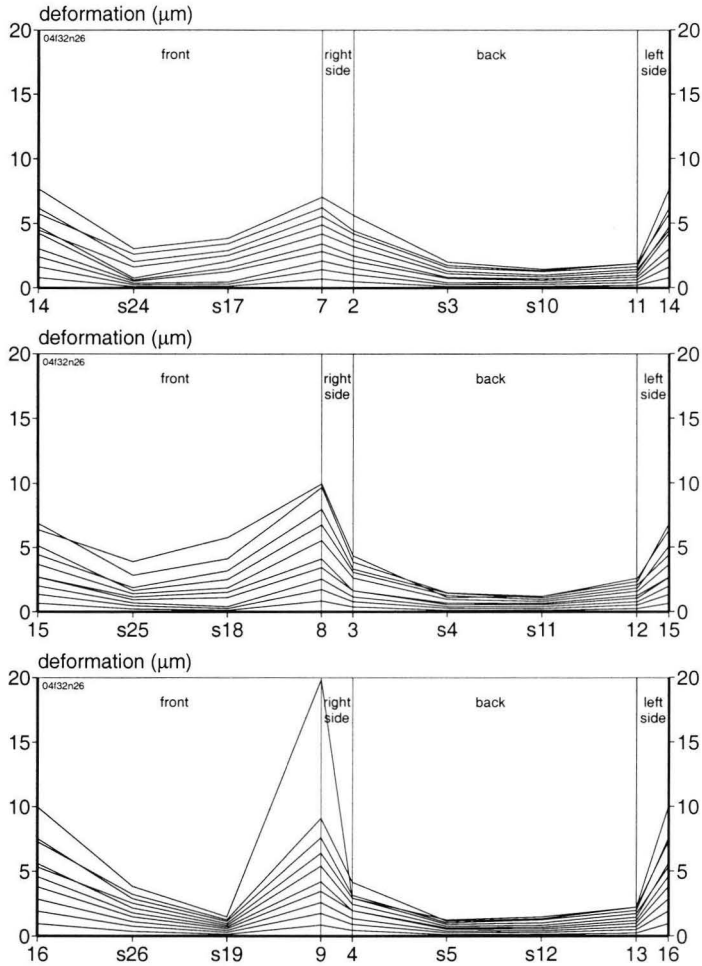


Figure 7.5 *Deformation of type* F *specimen (of Fig. 7.2b and Figs. 7.3a,c) during 10 loading stages until ultimate load. For the placement of the transducers indicated at the x-axis, see Fig. 7.3c.*

mainly due to the load eccentricity. The observations made for the type F specimen are quite different, see Fig. 7.5 which shows the measurements of three rows of displacement transducers in the specimen middle. Again crack initiation takes place at the front right corner of the specimen. Contrary to the type B specimen however, a clear deformation gradient is present over the specimen thickness (out-of-plane direction). The variation of the deformations on the front and the back side of the specimen reflects the influence of the specimen shape.

From the foregoing it follows that at peak load, in the out-of-plane direction almost uniform as well as highly nonuniform deformations were observed for two different specimens.

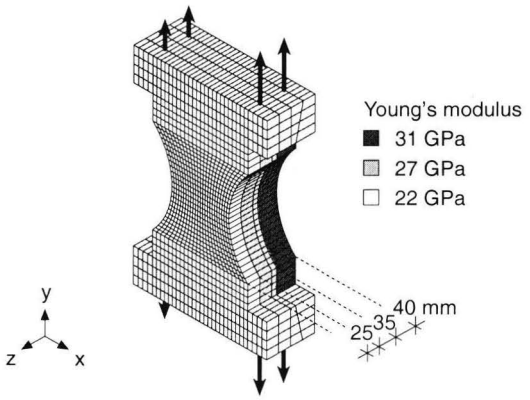


Figure 7.6 Model for eccentrically loaded specimen with inhomogeneous cross section.

Furthermore, it is noteworthy that for the type B as well as the type F specimen the crack starts at the front side. For both specimens this was the casting side (upper side of the specimen during casting), whereas the back side was the mould side (lower side during casting). These observations can be directly related to casting effects, as was discussed in Section 4.2.

The detailed examination of two experiments revealed that the behaviour before ultimate load can hardly be seen as that of homogeneous specimens with a uniform deformation distribution. It may therefore not be straightforward to consider only the nominal strength σ_N, and not take into account the actual pre-peak deformations in the critical cross section of the specimen as well. With respect to the ultimate load and a possible size effect this actual deformation distribution might be equally, if not more important than the properties of the material itself.

Now, a closer look will be taken at the nature of the specimen deformations, or rather strains, until ultimate load. The strain and consequently the stress distribution within the specimens is affected by the specimen shape, the eccentricity of the external force and internal eccentricities. In the first loading stages these internal eccentricities can, among other causes, be due to the inhomogeneity of the cross section as was shown in Section 4.2. As a consequence, certain areas of the specimen are more strained which leads to more micro-cracking. These micro-cracks in return lead to a further decrease of the local stiffness and can therefore increase the internal eccentricity. To obtain more insight into the actual strain distribution in the specimens, a simple linear elastic calculation has been carried out on the 3D finite element model shown in Fig. 7.6. The model represents a type C specimen subjected to a load of 4 kN which is applied with an eccentricity $e_x = 4$ mm in x direction. Inhomogeneity of the specimen has been incorporated by subdividing the specimen into three layers with an arbitrarily chosen thickness (see Fig. 7.6), and stiffness values according to Table 4.2.

Fig. 7.7 shows the strain distribution along the edges of the cross section in the middle of the specimen. Note the strain gradient over the specimen thickness which is caused by the material inhomogeneity. Because of this material inhomogeneity, the centre of stiffness and the centroid of the cross section do not coincide anymore. Hence, the external load, which is applied centrically in z direction, becomes eccentric thereby causing a moment M_z with

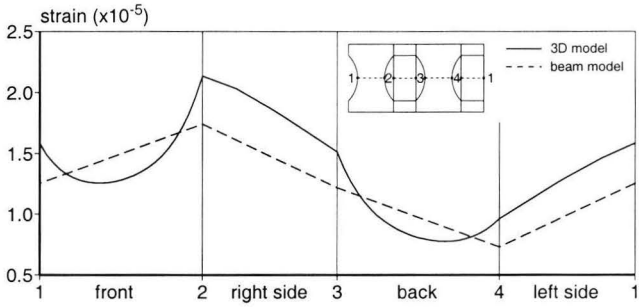


Figure 7.7 *Strain distribution along the edges of the smallest cross section of an eccentrically loaded inhomogeneous specimen (for the 3D model see Fig. 7.6).*

respect to the elastic centroid and thus bending in the out-of-plane direction (see also Fig. 7.8). With the given load eccentricity e_x and material inhomogeneity (e_z), the most strained part is the front corner on the right hand side of the specimen. The information which already followed from Figs. 7.4 and 7.5 is thus confirmed. The deformations and/or stresses which occurred in the specimens during the tests were highly nonuniform. To be more precise, nonuniformity of stresses and strains is introduced by the shape of the specimens, the eccentricity of the external load and material inhomogeneities due to the casting process. None of these causes however, was expected to induce any size effect. In case of the specimen shape and the load eccentricity two dimensional similarity was ensured, and casting effects are likely to be distributed randomly over the specimens. This led to the idea that the actual stress and strain gradients at the time of testing, could have had an important influence on the ultimate load level which was eventually recorded. Despite the fact that the results plotted in Fig. 7.1a follow the Weibull relation so nicely, the question can therefore be posed whether for the present experiments classical strength theory is applicable, or at least dominant, at all. This matter has been studied using a simple analytical model which is outlined in the next section. The basic idea behind the model is that predictions can be made for the ultimate load of each experiment, by using the initial deformation measurements as input for the model. By comparing the predicted ultimate load values with the values which were actually recorded in the experiment, the influence of the deformation gradients becomes more transparent.

7.2 Effect of nonuniform deformations on the observed size effect

7.2.1 Derivation of analytical model for concrete tests

Hereafter, the basics of the model will be given whereas additional information can be found in [101]. In the model, the homogeneous specimen follows Bernoulli beam theory (i.e. plane sections remain plane), and failure is assumed to take place in the smallest cross section. The stress-strain relation in this cross section is defined by Hooke's law, leading to failure of the specimen as soon as the critical stress σ_{crit} is reached in any point. Let us now take

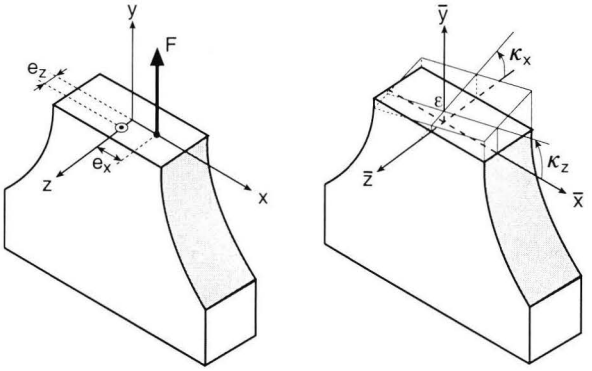


Figure 7.8 Schematization of the forces and deformations in the specimen middle.

a closer look at the deformation or strain gradients which were mentioned in the previous section, and which are shown schematically in Fig. 7.8. The first strain gradient is found in the in-plane direction due to the eccentricity e_x of the external load F. Although the external load is applied centrically in the out-of-plane or z direction, a strain gradient in this direction was found in the experiments as well. Since the specimens were cast horizontally, the stiffness and strength of the concrete were found to vary over the thickness of the cross section (Section 4.2). Due to this material inhomogeneity, the centre of stiffness and the centroid of the cross section do not coincide anymore. Hence, the external load becomes eccentric with an eccentricity e_z which leads to bending in the out-of-plane direction (Fig. 7.8).

The assumption of a homogeneous specimen which was made earlier, suggests that no bending would take place in z direction since in the experiments $e_z = 0$. The strain gradients in z direction however, will follow directly from the experimental measurements as will be explained hereafter. Hence, the analogy can be used between a centric load acting on an inhomogeneous cross section with non-coinciding centroid and centre of stiffness, and an eccentric load acting on a homogeneous cross section. The model which has been applied is therefore the same as illustrated in Fig. 7.8, except for the centre of stiffness which now coincides with the centroid of the cross section so that $\bar{x} = x$ and $\bar{z} = z$.

The strain distribution in the cross section can be obtained by superimposing its components (see also Fig. 7.8)

$$\varepsilon(x,z) = \varepsilon + \kappa_z x + \kappa_x z \tag{7.4}$$

where ε stands for the axial strain in the centre of stiffness indicated by the origin of the ($\bar{x}$, $\bar{y}$, $\bar{z}$) axes in Fig. 7.8. κ_z and κ_x represent the curvature of the specimen in the $x-y$ and the $z-y$ plane (or around the z-axis and the x-axis) respectively. They are defined as

$$\kappa_z = \frac{1}{r_z} = \frac{\partial \varepsilon(x,z)}{\partial x}, \qquad \kappa_x = \frac{1}{r_x} = \frac{\partial \varepsilon(x,z)}{\partial z} \tag{7.5}$$

where r_z and r_x are the radii of curvature around the z- and x-axis respectively. Following the model, the highest strain will be found in one of the corners in the middle of the specimen. Until now, only a constant normal strain and bending strains in two orthogonal directions have been incorporated in the model. If again the specimen of Fig. 7.6 is considered, the strain distribution along the specimen edges can also be computed with Eq. (7.4). After rewriting in terms of the externally applied force F and its eccentricity with respect to the centre of stiffness (e_x, e_z), the strain distribution follows from

$$\varepsilon(\bar{x},\bar{z}) = \frac{F}{EA} + \frac{Fe_x}{EI_z}\bar{x} + \frac{Fe_z}{EI_x}\bar{z} \tag{7.6}$$

in which EA, EI_z and EI_x are the normal stiffness and bending stiffnesses of the composite cross section with respect to the $\bar{z}$ and $\bar{x}$ axis respectively. For the same values of $F = 4$ kN and $e_x = 4$ mm the resulting strains along the edges are presented by the dashed line in Fig. 7.7. As can be seen, the bending effects are incorporated correctly and the only difference between the numerically and analytically computed strains along the edges is the influence of the specimen shape. When instead of the strain distribution in the entire cross section only the *maximum* strain is of interest, the effect of the specimen shape can be easily incorporated through a theoretical stress concentration factor K_t. K_t is defined as $\sigma_{\max}/\sigma$, where $\sigma_{\max}$ is the maximum stress in the smallest cross section of a centrically loaded homogeneous specimen and σ is the average stress. For the present specimen geometry $K_t = 1.28$ (see Section 3.2.2). Note that K_t depends on the ratios $D/0.6D$ and $r/0.6D$ where r is the radius of the circular edge. D and $0.6D$ stand for the width of the specimen at the end and in the middle respectively. Since these two ratios are constant for all specimen sizes, the same is true for K_t, making it a constant, purely geometrical factor. For the sake of simplicity only the stress concentration factor for the normal stress has been incorporated in the model. The stress concentration factor for the bending stress, which is lower, has been omitted.

After rewriting Eq. (7.4), an expression for the critical strain in a corner point with positive coordinates (x_c, z_c) is found following

$$\varepsilon_{\text{crit}} = \left[K_t \frac{1}{EA} + \frac{\kappa_{zi}}{F_i}x_c + \frac{|\kappa_{xi}|}{F_i}z_c\right]F_u \tag{7.7}$$

In Eq. (7.7), E, κ_{zi} and κ_{xi} are computed from deformation measurements which were made in the laboratory experiments. The Young modulus E represents the maximum slope of the average $\sigma - \varepsilon$ curve and is obtained using the least squares method. Once the maximum slope has been found, E can be computed from the scaled measurements in the middle of the specimen through (see also Figs. 3.23 and 7.9)

$$E = \frac{\sigma}{\varepsilon} = \frac{FL_s}{A_{\text{avg}}\overline{\delta_m}} = \frac{\overline{k_m}L_s}{A_{\text{avg}}} \tag{7.8}$$

where $\overline{\delta_m}$ stands for the average deformation measured on the front and the back side in the specimen middle (Fig. 7.9), and A_{avg} represents the average cross-sectional area within the scaled measuring length L_s.

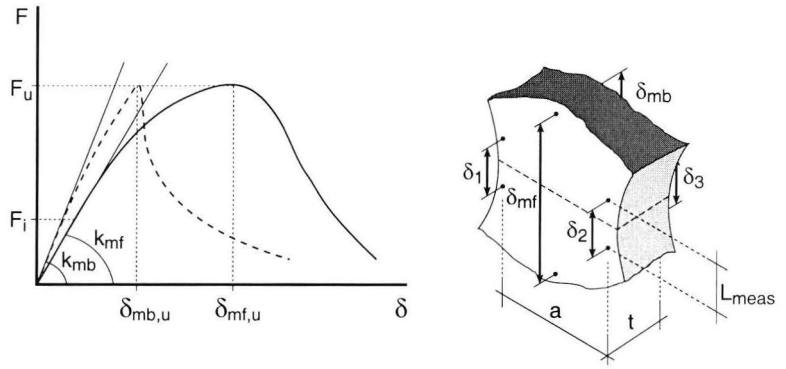


Figure 7.9 *Determination of material parameters from measurements (a) and measurement configuration (b).*

The curvatures κ_z and κ_x in Eq. (7.4) represent the slope of the strain field and can therefore be computed from the deformation differences which were measured at the specimen surface. With increasing load however, κ_z and κ_x increase as well and possibly even nonlinearly. For this reason the *initial* curvatures κ_{zi} and κ_{xi} have been introduced in Eq. (7.7), which vary linearly with the external load F thereby neglecting nonlinear deformations. For each test, κ_{zi} and κ_{xi} were computed at a load level F_i using the maximum slope of the $F-\delta_j$ curves of the subsequent displacement transducers (see Fig. 7.9). The expressions for κ_{zi} and κ_{xi} are

$$\kappa_{zi} = \frac{F_i\left[(k_2^{-1}-k_1^{-1})+(k_3^{-1}-k_4^{-1})\right]}{2aL_{\text{meas}}}, \quad \kappa_{xi} = \frac{F_i\left|k_{mf}^{-1}-k_{mb}^{-1}\right|}{tL_s} \tag{7.9}$$

where k_j are the slopes of the various $F-\delta_j$ curves with subscripts according to Figs. 3.23 and 7.9. It is mentioned that applying the thickness t in Eq. (7.9) implies that the deformations are measured right at the specimen surface. In reality however, the LVDTs are situated at a small distance off the specimen surface, which has been neglected here. This was done because the influence on the computational results of taking a value slightly greater than t is negligibly small. Moreover, due to possible rotations of the LVDTs and the measuring points (see [88] for details), other uncertainties are present in the measurements, which reduces the relevance of a greater value of t.

The only remaining unknown in Eq. (7.7) is $\varepsilon_{\text{crit}}$. Following Hooke's law $\varepsilon_{\text{crit}}$ can be computed from σ_{crit}, which can be regarded as the local material strength. Since the Young modulus computed for the different specimens varied quite a lot (especially for the smallest specimens), setting σ_{crit} and computing $\varepsilon_{\text{crit}}$ through E, seems more straightforward than setting a constant value for $\varepsilon_{\text{crit}}$. The value for the critical or local failure strength is, arbitrarily using the average strength of the type B specimens (Table 5.1), set as

$$\sigma_{crit} = \sigma_N \left[K_t + \frac{6e_x}{0.6D} \right] = 4.39 \text{ MPa} \tag{7.10}$$

with $e_x = 2$ mm and $D = 100$ mm. As a matter of fact any other value for σ_{crit} could have been chosen, since this would merely affect the height and scatter of the computed σ_N values. The scaling of the results for different specimen sizes however, remains the same. With

$$\varepsilon_{crit} = \frac{\sigma_{crit}}{E} \tag{7.11}$$

F_u follows directly from Eq. (7.7), giving a "prediction" for σ_N after division by A.

7.2.2 Model results

The model which is described in the previous section has been applied to the concrete experiments of the DRY and the WET series. In Figs. 7.10a and b the mean values and standard deviations of the model calculations are compared with the experimentally measured nominal strength values for both test series.

Keeping in mind that the value for σ_{crit} in Eq. (7.10) was chosen rather arbitrarily, the mutual differences between σ_N values of different specimen sizes must be compared for the model as well as the experiments. The absolute difference between the model values and the experimental values is variable since the magnitude of the model values directly depends on the applied value for σ_{crit}, and can therefore vary. In case of the DRY series (Fig. 7.10a), the model calculations agree fairly well with the global response of the experiments. Yet, for the small specimen sizes, too low values are found for the nominal strength. In this respect the results of the WET series seem to be in better agreement (Fig. 7.10b), since also for the type B specimens a relative strength level is found which is in accordance with that of the

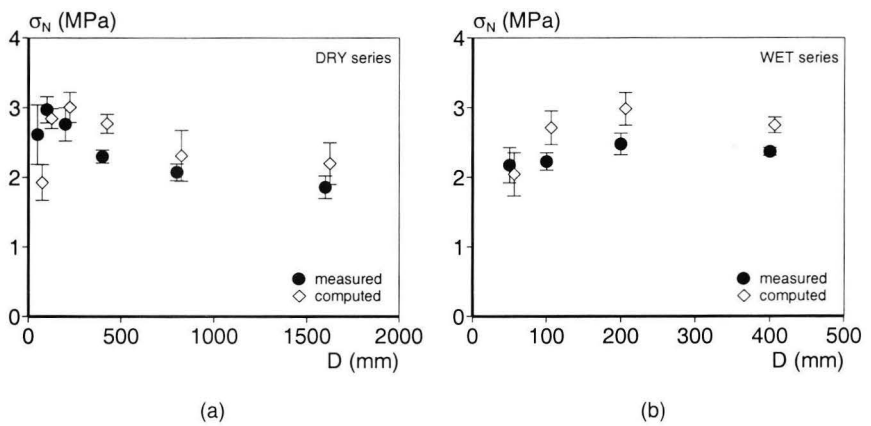


Figure 7.10 *Mean values of measured and computed nominal strengths for the DRY series (a) and the WET series (b).*

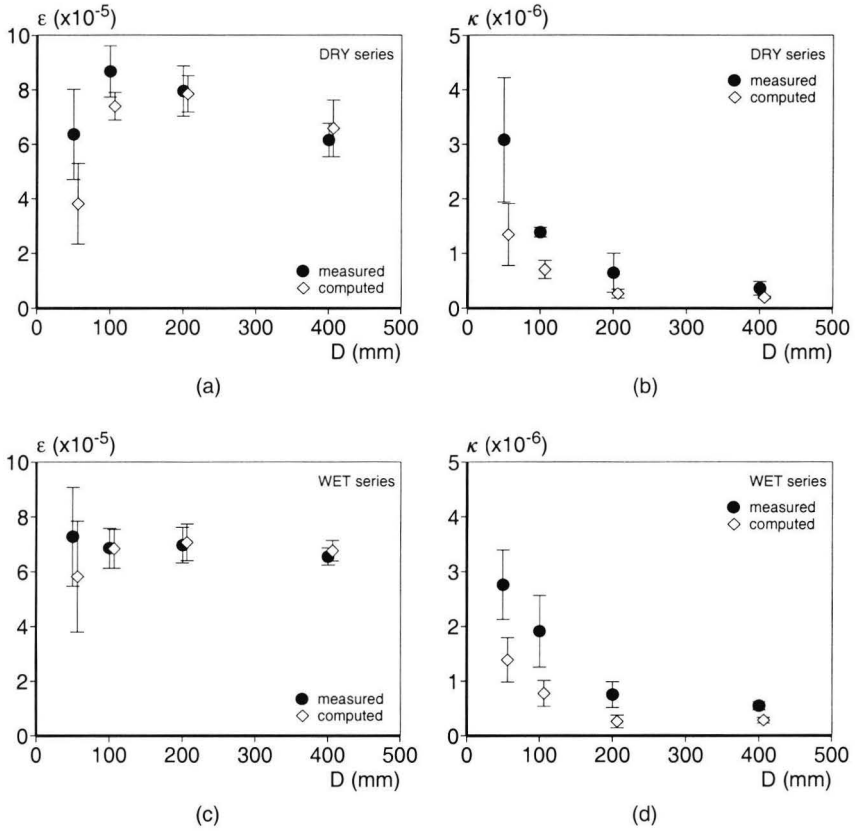


Figure 7.11 *Measured and computed mean values of normal strain (a, c) and total curvature (b, d) for the DRY series (a,b) and the WET series (c,d).*

experiments. The nominal strength of the A specimens however, is again far too low from a relative point of view. The basis for the predicted nominal stresses is the normal strain ε in the centroid of the cross section and the curvatures κ_x and κ_z, from which the total curvature κ can be composed as

$$\kappa = \sqrt{\kappa_x^2 + \kappa_z^2} \tag{7.12}$$

In Fig. 7.11 the measured and computed values for ε and κ are compared. A general observation is that the computed values for κ are lower than the measured ones, which can be attributed to neglecting the nonlinear deformations. Since the experimental κ values on the other hand are based on the deformations measured at ultimate load, they do incorporate nonlinearities. Hence, compared to the experiments, one would expect to obtain too high values for the computed ε and σ_N when the computed values for κ at ultimate load are too low. The actual findings, however, are completely opposite. The experimentally obtained

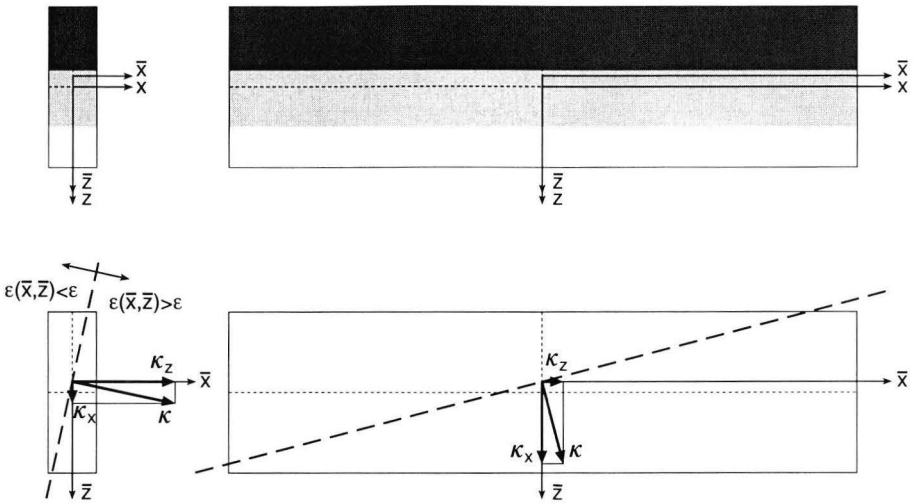


Figure 7.12 *Small and large specimen, both with the same inhomogeneous cross section as shown in Fig. 7.6. The thick dashed line represents the axis perpendicular to the resulting curvature κ, around which bending will take place. Note that the illustrations are not scaled properly and thus purely phenomenological.*

values of σ_N are higher, despite the presence of considerable strain gradients over the cross section. This could indicate that the material structure overrules the influence of the strain gradients, which is for instance the case for an 8 mm grain in a type A specimen, situated in an area with a very high strain gradient (see also [32]). Another explanation can be found in the statistical interpretation of the curvatures. A high value for the curvature implies that the highest strains will only act in a small part of the cross section. The probability of a weak spot being present in this part of the cross section is therefore small as well. As a consequence, high ultimate loads will be found for small specimens which exhibit high strain gradients. In the experiments this phenomenon could very well occur, whereas it is absent in the computations leading to differences between the two sets of σ_N values.

A comparison of the measured curvatures at peak load for the DRY and the WET series (Figs. 7.11b and d) shows that in the WET series, the curvature of the type B specimens was relatively high compared to the curvatures of the other specimen sizes. This could be an explanation for the low value of the mean nominal strength of those B specimens. Note that in case of a higher average σ_N value for the B specimens the size effect for the WET series becomes similar to that of the DRY series, with as main difference the lower strength level.

The curvatures κ_x and κ_z can also be used to get additional insight into some experimental observations. To illustrate this a closer look is taken at the effect of the cross section dimensions on the preferential direction for crack growth. Consider a small and a large specimen, both with an inhomogeneous cross section (see Fig. 7.12). Since the inhomogeneity of the two cross sections is identical, they only differ by their width. For each of the two cross sections a model can be made like is shown in Fig. 7.8, where the eccentricity of the load is scaled according to the size of the specimen. With the available data the centre of stiffness as

well as κ_x and κ_z can be computed for each cross section. The centre of stiffness was defined as the origin of the principal axes of the inhomogeneous cross section, which in this case does not coincide with the centroid of the cross section. Each cross section will bend around a line through the centre of stiffness. The computed curvatures κ_x and κ_z can be represented as components of the vector $\boldsymbol{\kappa}$, which by definition point in the direction of the largest strain. $\boldsymbol{\kappa}$ is known to be perpendicular to the neutral axis, and thus to the line around which bending of the cross section takes place for a combination of bending and normal force. The angle γ between $\boldsymbol{\kappa}$ and the $\bar{x}$-axis can be computed as

$$\gamma = arctan\left(\frac{\kappa_x}{\kappa_z}\right) \tag{7.13}$$

and is found to increase with the size of the specimen, or rather the width of the cross section. As a consequence also the line around which the cross section bends rotates, so that for the small specimen mainly bending in the in-plane direction takes place whereas the large specimen bends more in the out-of-plane direction. This is exactly what follows from the experiments as can be seen in Figs. 7.4 and 7.5. Note that in case of a homogeneous cross section $\kappa_x = 0$ and thus $\gamma = 0$. The specimen will then only bend in-plane and the crack propagates from the right to the left side. The foregoing considerations are purely linear elastic and can therefore not be applied to a fractured cross section. This however does not change the basic idea, which is that for given inhomogeneity the shape of the cross section influences the deformation of, as well as fracture initiation in a specimen.

In the analysis of the experiments with the model formulation of Eq. (7.7), a relation is set between the ultimate load which is found in a test and the presence of deformation gradients during that test. This becomes more transparent when Eq. (7.7) is rewritten in terms of the ultimate stress σ_u and the critical stress σ_{crit}. If the situation at ultimate load is considered, the initial curvatures in x and z direction can be replaced by the actual curvatures at ultimate load, leading to the expression

$$\sigma_u = K_t^{-1}\left[\sigma_{\text{crit}} - Ex_c\kappa_z - Ez_c|\kappa_x|\right] \tag{7.14}$$

Note that $\sigma_u = \sigma_N$ and that $\sigma_{\text{crit}} = f_t$. Especially the latter definition might seem to be very straightforward, although the author does not share that opinion. Often the tensile strength f_t is used as a well defined material property, whereas in reality f_t at most denotes an average strength at which a specimen failed under a uniaxial, centrically applied load. This however is not the issue here, leaving the remark that σ_{crit} or alternatively f_t must be regarded as a local failure stress. Equation 7.14 shows how the global, nominal strength can be reduced due to stress concentrations induced by the specimen shape, or strain gradients induced by for instance material inhomogeneity or eccentricity of the external load. If a prismatic homogeneous specimen is considered, $K_t = 1$ and $\kappa_z = \kappa_x = 0$ so that the ultimate stress is found to be equal to the critical or tensile strength. Interesting is that for instance Bažant and Li [10] and Zhu [119] on a different basis arrived at a similar expression for the modulus of rupture of unnotched plain concrete beams. Bažant and Li extended their expression to the case of a combined moment and normal force, giving

$$f_r = f_t + El_f\kappa_z \tag{7.15}$$

where f_r is a global strength limit, which for the case of pure bending follows from $f_r = 6M_u/bh^2$. f_t is again the tensile strength and l_f is the (assumed constant) height of a layer in the most stressed part of the cross section, where micro-cracking and stress redistributions take place. κ_z represents the curvature or the strain gradient over the height of the beam. Remarkable is that in Eq. (7.15) f_r and thus F_u increase with increasing κ_z, which is contrary to Eq. (7.14) and the experimental results discussed in the next section. A possible explanation could be that a "basic loading case" has to be distinguished, like uniaxial tension with small bending effects *or* mainly bending. Depending on such a basic loading case size effect will be governed by a combination of statistical and deterministic size effect, or a mainly deterministic size effect induced by stress redistributions.

7.2.3 Experimental observations

In the previous section it was shown that a relation exists between strain gradients and the observed size effect in the present tests. The question whether the observed size effect on strength actually was a size effect on strain gradients has not been answered however. If so, the strain gradients, or in other words the amount of bending, would depend on the size of the specimen. In Fig. 7.13 the relation between the nominal strength and the amount of bending is shown for the individual tests of the DRY and the WET series. Both parameters are based on experimentally measured values. The amount of bending is represented by the ratio between the largest flexural strain in one of the corners (ε_{flex}), and the axial or normal

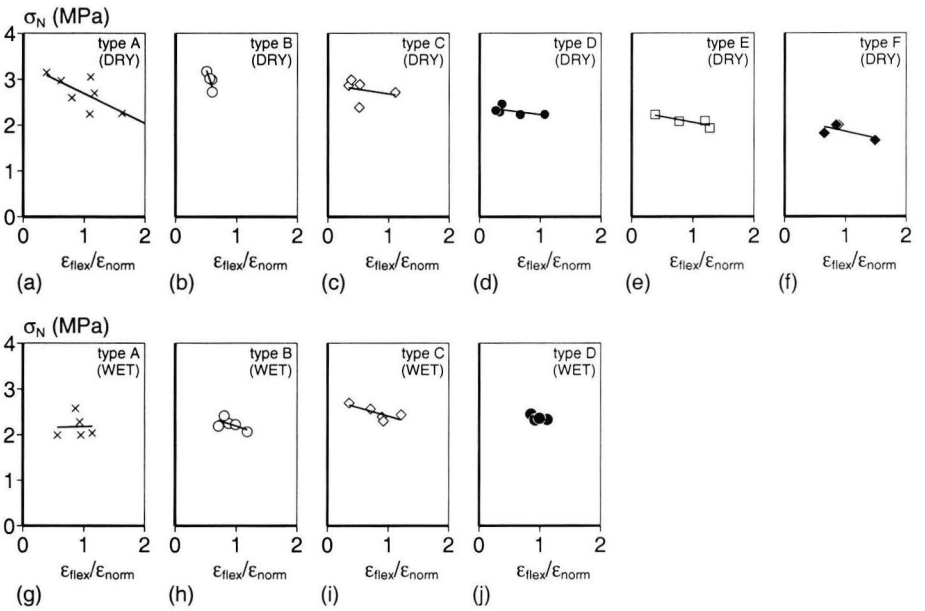


Figure 7.13 *Relation between the nominal strength and the amount of bending for the specimens of the DRY series (a-f) and the WET series (g-j). The straight lines represent the linear regression through the individual data points.*

strain in the centroid of the cross section (ε_{norm}). Thus, in the case of a pure normal force without bending the ratio $\varepsilon_{flex}/\varepsilon_{norm}$ would be zero.

When first focusing on the DRY series (Figs. 7.13a to f) it is observed that apart from the type A and B specimens, the decrease of the nominal strength with increasing ratio $\varepsilon_{flex}/\varepsilon_{norm}$ is approximately the same for all specimens. Moreover, for all specimen sizes various degrees of bending were present in the tests. This shows that the nominal strength differences are not likely to be due to a size effect in the occurring strain gradients. It must be mentioned, however, that due to the larger volumes of the big specimens a better reproducibility could be achieved during the casting process. Consequently, stiffness differences due to casting effects will be present more consistently in the large specimens compared to the small specimens. Also for the WET series a consistent relation between the nominal strength and the amount of bending was found, even for the type B specimens. The fact that this relation does not hold for the type A specimens of both series indicates that bending effects are overruled. In this respect again the dominating influence of the material structure, wall effect and the small aspect ratio are mentioned.

Finally, in Fig. 7.14 the results of the linear regression of the $\varepsilon_{flex}/\varepsilon_{norm}$-$\sigma_N$ points per specimen size are collected for the DRY and the WET series, together with the regression for all data points of each series. Again consistency is observed. Note that the slope of the regression lines in Fig. 7.14a is approximately the same, whereas the strength level at which the lines are situated follows the specimen size. The regression lines for the small specimens are situated at higher strength levels and reversely those for the large specimens are found at lower strength levels. This indicates that the strength results incorporate another effect as well, for instance a statistical size effect, which would be in accordance with the findings in Section 7.1.1. In case of the WET series no relation exists between the specimen size and the strength level at which the regression lines are situated. In addition to the fact that the measured curvatures were higher in the WET tests compared to the DRY tests, it is concluded that in the WET series structural bending effects overruled a material size effect.

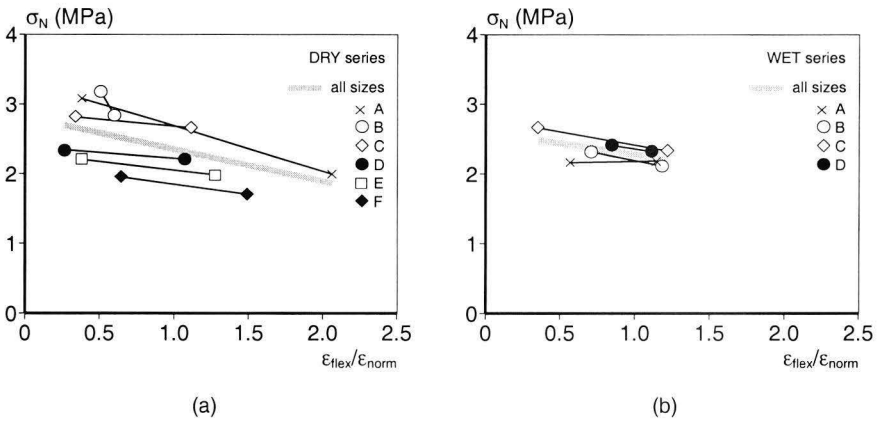


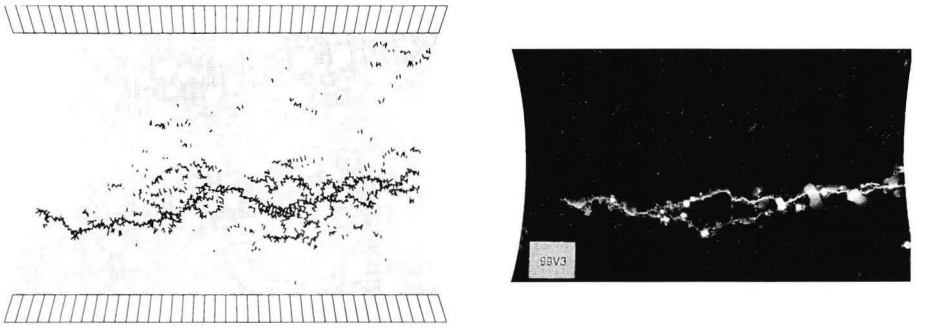
Figure 7.14 *Linear regression results for each specimen size separately, and for all test results of the DRY series (a) and the WET series (b).*

7.3 Simulations versus experiments

In Chapter 6 the lattice simulations were described which belong to the numerical part of this size effect study. The results obtained for regular and random triangular lattice models, with and without heterogeneity, showed that concrete fracture seems to be modelled best with a random lattice model on which an aggregate structure has been projected. Because of the random nature of the lattice itself, heterogeneity is then also included below the level of the smallest aggregates. Thus, the effect of sand grains and pores is implicitly modelled, leading to a more tortuous crack path which resembles experimental findings well. In Fig. 7.15 an example can be found of a crack pattern following from a lattice analysis and a typical crack pattern as found in the impregnation tests. In both cases the localized crack follows a path through the bond zones of the aggregates and the matrix. The numerical crack pattern shows in addition to the main crack also small micro-cracks along the right edge of the specimen, and distributed micro-cracks over the lattice area outside the localized crack. These micro-cracks were not found in the impregnated specimens at this level of observation. As for the micro-cracks inside the specimen this is due to the impregnation method, which can only be used to visualize cracks which have an open connection with the surface of the specimen *and* which are large enough to be impregnated. The same holds for the micro-cracks along the specimen edges. Only in thin sections which were made from this edge zone, small cracks were found which are likely to be due to a combination of shrinkage and loading. In the pictures of the specimen slices sometimes impregnated zones were visible along the specimen edges. As was already discussed in Section 5.5 this could indicate the presence of micro-cracks, although a lower concrete quality due to wall effect must be considered as well.

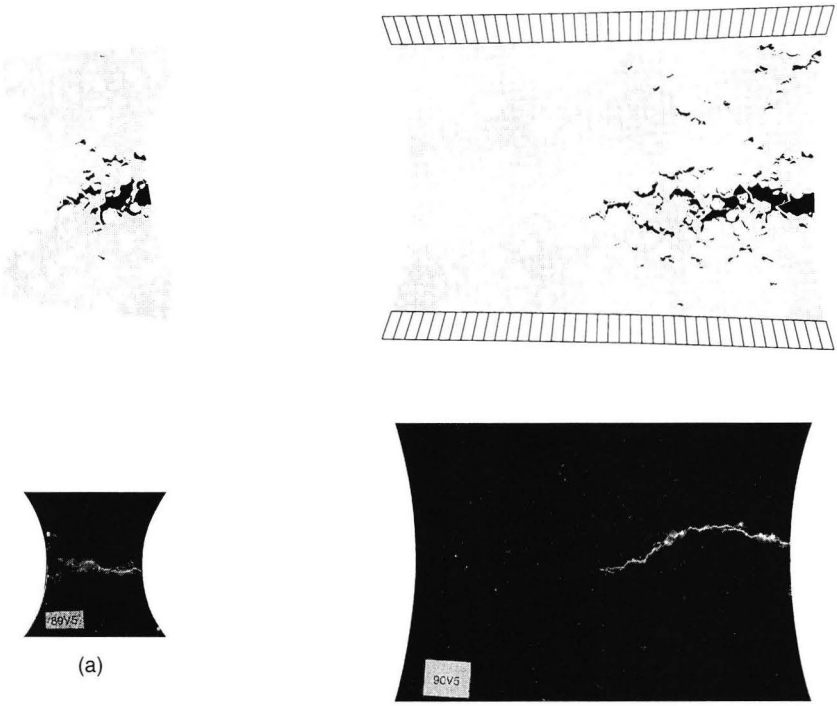
The lattice simulations on specimens of different sizes revealed different crack propagation stages when the same crack opening deformation was considered. Using results of the impregnation experiments a comparison can be made between the experiments and the simulations, which are found to be quite similar (Fig. 7.16). For the same maximum deformation smaller specimens contain a crack which is shorter, whereas the rotation angle between the two crack faces is larger (see also Figs. 6.21 and 6.22, where it must be noted that the deformations concern the upper lattice boundary rather than the crack face). Also the actual crack width is probably larger for the smaller specimens. This follows from the fact that less micro-cracks are found within the measuring length because of the larger curvature of the specimen edges. In summary, at specific deformation stages the distribution of deformations over the specimen width will be more linear for the small specimens, whereas for the larger specimens bending is found since a part of the specimen is still intact. Fig. 7.16a once more illustrates the significance of bridging in concrete cracks. Even though the A specimen seems to be completely fractured through, the load bearing capacity was still as high as 10% of the ultimate load level.

As for a size effect on the nominal strength, the numerical results for the three smallest specimen sizes were in agreement with the experimental findings. However, for larger models which incorporated an aggregate structure the nominal strength increased again. It was found that the constant, too small height of the zone with lattice elements restricted the amount of (micro-)cracking which could occur. Hence, the resulting value for the nominal strength became artificially high. In the lattice models without an aggregate structure, no increase of the nominal strength was found for the large model sizes. This is in agreement



(a) (b)

Figure 7.15 *Final crack pattern for a type* C *specimen modelled with a random lattice with aggregate structure (a) and laboratory specimen unloaded at a maximum deformation of 300 μm (b).*



(a)

(b)

Figure 7.16 *Numerical versus experimental crack patterns for a type* A *specimen (a) and a type* C *specimen (b). The laboratory specimens were unloaded at a maximum deformation of 100 μm . The* COD *of both lattice meshes is 5 μm .*

with the results of a size effect analysis which was previously carried out [99]. There, a random lattice with a cell size $s = 5$ mm was applied and specimen type A, B, C and D was fully modelled with a lattice mesh. Each simulation was repeated three times and the result showed a consistent decrease of the nominal strength. Depending on the lattice type, and thus on the amount of micro-cracking which can occur before ultimate load is reached, the size of the lattice region is more, or less critical. This observation is supported by lattice size effect analyses which were carried out by Bolander [14]. He simulated tensile splitting tests conducted by Wittmann [115] and although the width of the lattice zone increased with size, the largest ratio between the width and the beam length was still smaller than in the present analyses. Yet, the results did not indicate that the width of the lattice zone had been taken too small which can be attributed to the presence of the notch. This leads again to the conclusion that effects of the lattice zone width on the ultimate load only play a role in case of largely distributed micro-cracking. The amount of micro-cracking can be inherent to the applied material structure and to crack initiation from an unnotched surface.

In the previous sections the experimental size effect results were analyzed, leading to the discrimination of two main effects on the ultimate load. First of all a statistical size effect was found and secondly the effect of stress and/or strain gradients could have a profound influence of the ultimate load. As an explanation for the presence of these gradients served the shape of the specimens, the eccentricity of the external load and the inhomogeneity of the specimen's cross section. When relating the results of the numerical simulations to the experimental results, the latter effect could not be taken into account due to the two dimensional character of the lattice model. The effect of the load eccentricity was studied however, and showed a deterministic as well as a statistical aspect. If crack initiation occurred at the same spot in the mesh for both the centric and the eccentric loading case, the difference in ultimate load for both simulations approximately followed the effect of the eccentricity (Fig. 6.19). This simply means that with increasing eccentricity, the strength of the same weakest spot is already reached at a lower external load. If on the other hand for the centric case the crack initiated at a different spot in the mesh as for the eccentric case, the ultimate load

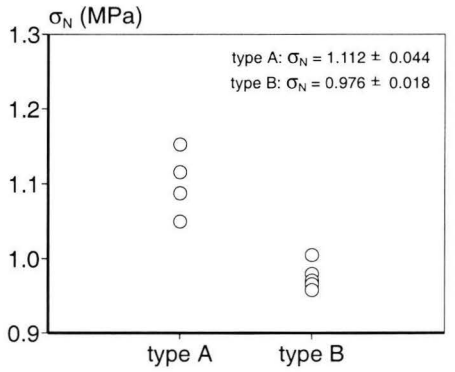


Figure 7.17 *Scatter in nominal strength values for five simulations on a type* A *specimen and five simulations on a type* B *specimen. Both specimens were modelled with a regular lattice with aggregate structure, and parameters as described in Section 6.2.4.*

could be lower than expected (Fig. 6.19). For that specific spot the combination of externally applied stress and local material strength was then obviously more critical, compared to the spot where failure took place in the eccentric loading case. This in fact illustrates the importance of statistical effects which will be present due to the heterogeneous nature of concrete. A variation of this statistical aspect was also found in the experimental strength results of the type A specimens, which exhibited a scatter much larger than that of the other specimen sizes (Fig. 5.9). As an explanation the influence of the aggregate structure was mentioned in relation to the smallest specimen size. This aspect ratio was likely to be too small for the A specimens. Later, this presumption was verified with a set of lattice simulations. These simulations comprised lattice analyses of a uniaxial tension test on a type A and a type B specimen, similar to the ones described in Chapter 6. Both specimens were modelled with a regular lattice on which an aggregate structure was projected. Five different aggregate structures were generated for the B specimen. After generating additional particles according to the procedure described in Section 6.2.3, the same aggregate structures were projected on the A specimen. The results of these simulations can be found in Fig. 7.17. Also in the lattice analyses the scatter in nominal strength values appears to be larger for the A specimens. Contrary to the experimental results however, the average nominal strength of the A specimens is higher compared to the B specimens. This can be explained by the fact that in the simulations no wall effect is present. Due to this wall effect, the concrete quality in the zone along the specimen edges can be expected to be poor compared to the middle of the specimen, which was indicated by the epoxy-penetrated edge zones in the impregnation tests. Since these zones are relatively large for the type A specimens, their average strength will be lower compared to larger specimens where the effect of the poor edge zones is restricted.

Chapter 8

Conclusion and future outlook

Laboratory experiments play a central role in processes like the drawing up of new design codes or the determination of material properties which have to be implemented in numerical models. Because of practical considerations, the size of the specimens that are used in these experiments is generally much smaller than the actual size of the structure that is subject of interest. Due to this size difference the experimental results can exhibit size effect, which in case of for instance the strength is reflected by measured values which are too high. As a consequence the experimentally determined values can not be applied directly to the full scale case. To overcome this problem the experimental results have to be corrected for the size difference, which however requires a thorough knowledge of the nature of the size effect.

Insight in the physical mechanisms underlying size effect can in the first place be obtained through experiments on specimens of different sizes. The experiments are conducted under controlled conditions, which gives the opportunity to closely monitor the processes leading to failure of the material. With increasing size the influence of the material structure decreases since the specimen becomes more homogeneous from a relative point of view. Investigating this situation is therefore especially interesting, since it comes closest to the case of real size structures. A restriction of an experimental approach for studying size effect is the total range of specimen sizes which can be tested. The effort which has to be made to test large size specimens is enormous, resulting in tested size ranges which might seem impressive but that are only a fraction of the total scale difference which is of interest. Whereas the foregoing holds for two dimensional similarity, the effort increases further for the case of three dimensional similarity which in fact represents the actual situation best. Moreover, in all these cases shape effects are neglected, which may be of significant influence as well.

A purely experimental approach can thus never fulfill the needs which are inherent to a size effect study. If in addition to the experiments numerical models are used, the possibilities to extend the size range increase, although it must be realized that also now restrictions apply in terms of computational capacity. Because of the ongoing hardware development however, these restrictions are less rigid than the experimental ones. When size effect is studied with a numerical model difficulties arise which are very similar to those encountered in experiments. These numerical difficulties mainly concern the correct way to scale the specimens while similarity is maintained. A natural way to circumvent scaling problems is to incorporate the meso-structure of the material in the model. This leaves a pure capacity problem which only deals with the maximum size to which the modelled material structure can be scaled. Besides the meso-structure, however, also the correct physical mechanisms

which take place in, and eventually lead to failure of the material should be incorporated in the model. After this has been achieved, material behaviour can be studied in such a way that the influence of for instance boundary conditions, shape effects and deformation state will be included automatically in the computational result.

In the present study it has been attempted to follow the previously sketched approach as much as possible. For the experimental part of the study a series of uniaxial tension tests was designed, which were conducted under deformation control while applying boundary conditions that allowed for free rotations of the specimen ends. The specific reason for selecting freely rotating boundary conditions was that a lower bound for the fracture energy is measured. The tested materials were concrete ($d_{max} = 8$ mm) cured under laboratory (20 °C , 60% R.H.) as well as controlled conditions (20 °C , 95% R.H.) and red Felser sandstone. For both concrete and sandstone six different specimens were tested with a constant thickness and the remaining sizes in a scale range of 1:32, which is the largest size variation in uniaxial tension tests on concrete to date. In addition to these main series of size effect tests a limited number of impregnation tests was carried out with the purpose to elucidate internal crack propagation as a function of crack opening. Three series of verification tests were carried out to get additional insight into material inhomogeneity due to casting effects, the rotational capacity of the hinge constructions and possible effects of the test set-up on the experimental result. In the numerical part of the study, the laboratory experiments were simulated with a lattice model. Regular and random triangular lattices were used, both with and without an aggregate structure incorporated in the mesh. In addition to the lattice simulations also a simple analytical model was derived, which was used to further explore the contribution of structural influences on the size effect which was observed in the experiments.

The study on size effect which is presented in this thesis, leads to the following main conclusions with respect to size effect of concrete and sandstone under uniaxial tension.

- Concrete specimens in a scale range of 1:16 (types B to F), cured under dry (laboratory) conditions, showed a consistent decrease of the nominal tensile strength up to 37%. The size effect for these specimens exactly followed the predicted strength decrease according to Weibull theory. For the concrete specimens cured under wet conditions on the other hand, the strength first increased for the three smallest specimens and then decreased again. The red Felser sandstone showed a very mild size effect on the nominal strength which already vanished for specimens of the third size.

- Through a combination of experiments, numerical simulations and an analytical model, the effect of stress and/or strain gradients on size effect could be determined. These gradients were found to be introduced by the shape of the specimens, the eccentricity of the external load, inhomogeneity of the specimen's cross section and eigenstresses due to differential drying. Hence, in the experiments on concrete specimens, three different causes could be distinguished for the observed size effect. In the smallest specimens the failure stress was governed by the concrete aggregate structure in combination with wall effect. With increasing size of the specimens, the role of the statistical strength distribution increased as well. The presence of flaws in the concrete therefore determined the ultimate stress, *unless* stress and/or strain gradients of a structural nature were present in the specimens, which were strong enough to overrule these material size effects.

- The fracture energy was found to increase with size going towards a horizontal asymptote for large sizes, irrespective of the type of material. The degree in which the fracture energy converged towards a constant value, depended on the place at the specimen were the deformations had been measured. Although for concrete the variation of the fracture energy with size was independent of the curing conditions, the highest values were found for the specimens cured under dry (laboratory) conditions.

- From experiments as well as from numerical simulations followed that for the smallest specimens used in this study, the aspect ratio of $D/d_{\max} = 3.75$ was too small. As a consequence the results showed a strong scatter. An implication of this observation is that discussions about a strength asymptote for very small specimen sizes are not of any practical interest.

- The size effect on strength and fracture energy which was found in simulations with a lattice model resembles the experimental results well for specimens up to the third size. For larger specimens the numerical results were influenced by the size of the lattice region which, for practical computational reasons, had been taken too small. It is however expected that the present problem is restricted to simulations of specimens without a notch. For those specimens micro-cracking will be more widely spread, which implies that the numerical result is more sensitive to the size of the lattice region compared to the case of notched specimens. Nevertheless, considering specimens without notches is more realistic since this is practical reality.

Besides the foregoing conclusions which specifically deal with size effect, also a number of more general conclusions can be drawn.

- The uniaxial tension tests were controlled using the maximum deformation rather than the average deformation measured on the specimen surface as feed-back signal. This type of test control, in combination with a measuring length of the control LVDTs which was kept constant throughout the size range, proved to be quite effective for conducting stable tests irrespective of the size of the specimen, and without applying a notch.

- Moisture gradients due to drying out of wet concrete specimens can occur within the first hours in which the specimens have been exposed to laboratory conditions. Depending on the size of the specimens, the consequent eigenstresses can completely overrule strength fluctuations due the material meso-structure.

- For given inhomogeneity, the shape of the cross section influences the deformation of, as well as the fracture initiation in a specimen.

- The outcome of a lattice analysis is purely determined by the ratios of strong and weak elements which are present in the mesh. The shape of the aggregate structure, as well as the length of the lattice beams in relation to the minimum aggregate size, hardly influence the global numerical result.

To come to a true understanding of the size effect phenomenon, looking only at global experimental results does not suffice. This study revealed that the size effect which is observed

in a series of experiments consists of different contributions, which all vary in magnitude. Especially size effect due to for instance the casting process, differential shrinkage and moisture gradients is seldom quantified. Yet, no matter how carefully the experiments are set up, these effects will always be present and can therefore have a pronounced influence on the experimental result. In order to estimate the contribution of these effects to the total size effect more research is needed. Simultaneously, numerical models must be extended to account for moisture transport and other possible causes of eigenstresses, resulting in stress gradients as well as non-mechanical damage. An analysis of these effects should be carried out prior to a mechanical analysis. Compared to this preferred situation, performing numerical simulations on specimens which are in a perfect state when the external load is applied, still seems to be far from reality. Taking all these mentioned points into account will take a lot of effort. Part of this effort is due to the fact that research can be very ineffective when it comes to fitting in the results of studies which were previously carried out. In this respect one can think of different material compositions, boundary conditions or environmental circumstances which make a true comparison difficult. If alternatively this effort would be put in a combined research program, with sub-programs focusing on a part of a central series of experiments, a quicker progress might be the result.

References

[1] ADAMSON, R.M., DEMPSEY, J.P., DEFRANCO, S.J., AND XIE, Y. Large-scale in-situ ice fracture experiments part I: experimental aspects. In *Ice Mechanics* (1995), J.P. Dempsey and Y.D.S. Rajapakse (eds.), ASME, pp. 107–128.

[2] ARSLAN, A. A study on effect of fracture law and porosity on concrete fracture under uniaxial tension. Report 25.5-95-8, Delft University of Technology, 1995.

[3] ARSLAN, A., SCHLANGEN, E., AND VAN MIER, J.G.M. Effect of model fracture law and porosity on tensile softening of concrete. In *Fracture Mechanics of Concrete Structures* (1995), F.H. Wittmann (ed.), AEDIFICATIO Publishers, pp. 45–54.

[4] BAKER, G. Interface fracture energy and aggregate size effects in particulate solids. In *Size-Scale Effects in the Failure Mechanisms of Materials and Structures* (1996), A. Carpinteri (ed.), E&FN Spon, pp. 171–186.

[5] BASCOUL, A., KHARCHI, F., AND MASO, J.C. Concerning the measurement of the fracture energy of a micro-concrete according to the crack growth in a three points bending test on notched beams. In *Fracture of Concrete and Rock* (1987), S.P. Shah and S.E. Swartz (eds.), Society for Experimental Mechanics, pp. 631–643.

[6] BAŽANT, Z.P. Size effect in blunt fracture: Concrete, rock, metal. *Journal of Engineering Mechanics (ASCE), 110*(4), 1984, pp. 518–535.

[7] BAŽANT, Z.P. Scaling of quasibrittle fracture: Asymptotic analysis. *International Journal of Fracture, 83*(1), 1997, pp. 19–40.

[8] BAŽANT, Z.P. Scaling of quasibrittle fracture: Hypotheses of invasive and lacunar fractality, their critique and Weibull connection. *International Journal of Fracture, 83*(1), 1997, pp. 41–65.

[9] BAŽANT, Z.P., AND CHEN, E.P. Scaling of structural failure. *Applied Mechanics Reviews, 50*(10), 1997, pp. 593–627.

[10] BAŽANT, Z.P., AND LI, Z. Modulus of rupture: size effect due to fracture initiation in boundary layer. *Journal of Structural Engineering, 121*(4), 1995, pp. 739–746.

[11] BAŽANT, Z.P., AND PLANAS, J. *Fracture and size effect in concrete and other quasibrittle materials*. CRC Press LLC, 1998.

[12] BAŽANT, Z.P., XI, Y., AND REID, S.G. Statistical size effect in quasi brittle structures: I. is Weibull theory applicable? *Journal of Engineering Mechanics (ASCE), 117*(11), 1991, pp. 2609–2622.

[13] BOLANDER, JR., J.E. An adaptive procedure for fracture simulation in extensive lattice networks. *Engineering Fracture Mechanics, 54*(3), 1996, pp. 325–334.

[14] BOLANDER, JR., J.E., HIKOSAKA, H., AND HE, W.-J. Fracture in concrete specimens of differing scale. *Engineering Computations, 15*(8), 1998, pp. 1094–1116.

[15] BONZEL, J., AND KADLEČEK, V. Einfluss der nachbehandlung und des Feuchtigkeitszustands auf die Zugfestigkeit des Betons. In *Betontechnische Berichte 1970* (1970), K. Walz (ed.), pp. 99–132 (in German).

[16] CARPINTERI, A., AND CHIAIA, B. Multifractal nature of concrete fracture surfaces and size effects on nominal fracture energy. *Materials and Structures (RILEM), 28*, 1995, pp. 435–443.

[17] CARPINTERI, A., CHIAIA, B., AND FERRO, G. Multifractal scaling law for the nominal strength variation of concrete structures. In *Size effect in concrete structures* (1994), M. Mihashi, H. Okamura, and Z.P. Bažant (eds.), E&FN Spon, pp. 173–185.

[18] CARPINTERI, A., CHIAIA, B., AND FERRO, G. Multifractal scaling law: an extensive application to nominal strength size effect of concrete structures. Report 51, Politecnico di Torino, Dipartimento di Ingegneria Strutturale, 1995.

[19] CEB TASK GROUP 2.7. Concrete tension and size effects. Bulletin 237, Comité Euro-International du Béton (CEB), 1997.

[20] COX, S.J.D., AND PATERSON, L. Tensile fracture of heterogeneous solids with distributed breaking strengths. *Physical Review B, 40*(7), 1989, pp. 4690–4695.

[21] COX, S.J.D., AND PATERSON, L. Damage development during rupture of heterogeneous brittle materials: a numerical study. In *Deformation Mechanisms, Rheology and Tectonics* (1990), R.J. Knipe and E.H. Rutter (eds.), no. 54 in Geological Society Special Publication, pp. 57–62.

[22] DAERGA, P.A. Some experimental fracture mechanics studies in mode I of concrete and wood. Licentiate Thesis, Luleå University of Technology, 1992.

[23] DEMPSEY, J.P., ADAMSON, R.M., AND MULMULE, S.V. Scale effects on the in-situ tensile strength and fracture of ice. Part II: First-year sea ice at Resolute, N.W.T. *International Journal of Fracture, 95*(1/4), 1999, pp. 347–366.

[24] DUXBURY, P.M., BEALE, P.D., AND LEATH, P.L. Size effects of electrical breakdown in quenched random media. *Physical Review Letters, 57*(8), 1986, pp. 1052–1055.

[25] ELICES, M., GUINEA, G.V., AND PLANAS, J. Measurement of the fracture energy using three point bend tests: Part 3 - influence of cutting the $p - \delta$ tail. *Materials and Structures (RILEM), 25*, 1992, pp. 327–334.

[26] FERRO, G. *Effetti di scala sulla resistenza a trazione dei materiali.* PhD thesis, Politecnico di Torino (in Italian), 1994.

[27] GUINEA, G.V., PLANAS, J., AND ELICES, M. Measurement of the fracture energy using three point bend tests: Part 1 - Influence of experimental procedures. *Materials and Structures (RILEM), 25*, 1992, pp. 212–218.

[28] HASEGAWA, T., SHIOYA, T., AND OKADA, T. Size effect on splitting tensile strength of concrete. In *Proceedings of the 7th conference of the Japan Concrete Institite* (1985), JCI, pp. 309–312.

[29] HASHIN, Z. On elastic behaviour of fibre reinforced materials of arbitrary transverse phase geometry. *Journal of the Mechanics and Physics of Solids, 13*, 1965, pp. 119–134.

[30] HASHIN, Z. Analysis of composite materials - A survey. *Journal of Applied Mechanics, 50*(9), 1983, pp. 481–505.

[31] HASSANZADEH, M., HILLERBORG, A., AND ZHOU, F.P. Tests of material properties in mixed mode I and II. In *Fracture of Concrete and Rock* (1987), S.P. Shah and S.E. Swartz (eds.), Society for Experimental Mechanics, pp. 353–358.

[32] HEILMANN, H.G. Zugspannung und dehnung in unbewehrten betonquerschnitten bei exzentrischer belastung. In *Deutscher Ausschuss für Stahlbeton* (1976), vol. 269, pp. 1–61 (in German).

[33] HEILMANN, H.G., HILSDORF, H., AND FINSTERWALDER, K. Festigkeit und Verformung von Beton unter Zugspannungen. In *Deutscher Ausschuss für Stahlbeton* (1969), vol. 203, pp. 1–94 (in German).

[34] HERRMANN, H.J., HANSEN, A., AND ROUX, S. Fracture of disordered, elastic lattices in two dimensions. *Physical Review B, 39*(1), 1989, pp. 637–648.

[35] HERRMANN, H., AND ROUX, S. *Patterns and Scaling for the Fracture of Disordered Media.* Elsevier Applied Science Publishers B.V., 1990.

[36] HETTEMA, M. *The thermo-mechanical behaviour of sedimentary rock: an experimental study.* PhD thesis, Delft University of Technology, 1996.

[37] HEYDEN, S. A network model applied to cellulose fibre materials. Licentiate Thesis, Luleå University of Technology, 1996.

[38] HILLERBORG, A. The theoretical basis of a method to determine the fracture energy G_F of concrete. *Materials and Structures (RILEM), 18*(106), 1985, pp. 291–296.

[39] HILLERBORG, A. Stability problems in fracture mechanics testing. In *Fracture of Concrete and Rock* (1989), S.P. Shah, S.E. Swartz, and B. Barr (eds.), Elsevier, pp. 369–378.

[40] HILLERBORG, A., MODÉER, M., AND PETERSSON, P.E. Analysis of crack formation and crack growth in concrete by means of fracture mechanics and finite elements. *Cement and Concrete Research, 6*, 1976, pp. 773–782.

[41] HILSDORF, H. Versuchstechnische Probleme beim Studium der Verformungseigenschaften des Betons. In *Materialprüfung* (1963), vol. 5 (11), (in German).

[42] HORDIJK, D.A. *Local Approach to Fatigue of Concrete*. PhD thesis, Delft University of Technology, 1991.

[43] HRENNIKOFF, A. Solution of problems of elasticity by the framework method. *Journal of Applied Mechanics (Transactions of the ASME), 8*, 1941, pp. A169–A175.

[44] HSU, T.T.C. Mathematical analysis of shrinkage stresses in a model of hardened concrete. *Journal of the American Concrete Institute, 60*(3), 1963, pp. 371–390.

[45] HSU, T.T.C., AND SLATE, F.O. Tensile bond strength between aggregate and cement paste or mortar. *Journal of the American Concrete Institute, 60*(4), 1963, pp. 465–485.

[46] HSU, T.T.C., SLATE, F.O., STURMAN, G.M., AND WINTER, G. Microcracking of plain concrete and the shape of the stress-strain curve. *Journal of the American Concrete Institute, 60*(2), 1963, pp. 209–224.

[47] HUGHES, B.P., AND CHAPMAN, G.P. The complete stress-strain curve for concrete in direct tension. *RILEM Bulletin, 30*, 1966, pp. 95–97.

[48] JIRASÉK, M., AND BAŽANT, Z.P. Macroscopic fracture characteristics of random particle systems. *International Journal of Fracture, 69*(3), 1994, pp. 201–228.

[49] KADLEČEK, V., AND ŠPETLA, Z. Effect of size and shape of test specimens on the direct tensile strength of concrete. *RILEM Bulletin, 36*, 1967, pp. 175–184.

[50] KARIHALOO, B.L. *Fracture Mechanics and Structural Concrete*. Longman Scientific & Technical, Harlow Essex, UK, 1995.

[51] LANDIS, E.N., AND SHAH, S.P. Experimental measurements of microfracture in cement-based materials. In *Fracture Mechanics of Concrete Structures* (1995), F.H. Wittmann (ed.), AEDIFICATIO Publishers, pp. 315–328.

[52] LEICESTER, R.H. Effect of size on the strength of structures. Report Paper No. 71, CSIRO Australian Forest Production Laboratory Division of Building Research Technology, 1973.

[53] LI, Z., KULKARNI, S.M., AND SHAH, S.P. New test method for obtaining softening response of unnotched concrete specimen under uniaxial tension. *Experimental Mechanics*(9), 1993, pp. 181–188.

[54] LILLIU, G., VAN MIER, J.G.M., AND VAN VLIET, M.R.A. Numerical characterization of the elastic properties of heterogeneous materials with a 3D lattice model. In *Computational Methods and Experimental Measurements IX* (1999), G.M. Cariomagno and C.A. Brebbia (eds.), WITpress, pp. 515–524.

[55] MECHTCHERINE, V., GARRECHT, H., AND HILSDORF, H.K. Effect of temperature and loading rate on fracture behaviour of concrete subjected to uniaxial tension. In *Fracture Mechanics of Concrete Structures* (1995), F.H. Wittmann (ed.), AEDIFICATIO Publishers, pp. 719–728.

[56] MECHTCHERINE, V., AND MÜLLER, H.S. Fracture mechanical and fractological investigations on normal and high-strength concrete. In *Brittle Matrix Composites 5* (1997), A.M. Brandt, V.C. Li, and I.H. Marshall (eds.), Woodhead Publishing Limited, Cambridge, pp. 231–240.

[57] MILLS, R.H. Strength-maturity relationships for concrete which is allowed to dry. In *Studies in concreting in hot countries* (1960), R. Shalon and D. Ravina (eds.), pp. 1–28.

[58] MÜLLER, R.K. Der Einfluss der Messlänge auf die Ergebnisse bei Dehnmessungen an Beton. *Beton*(5), 1964, pp. 205–208 (in German).

[59] MULMULE, S.V., DEMPSEY, J.P., AND ADAMSON, R.M. Large-scale in-situ ice fracture experiments part II: modeling aspects. In *Ice Mechanics* (1995), J.P. Dempsey and Y.D.S. Rajapakse (eds.), ASME, pp. 129–146.

[60] NEVILLE, A.M. *Properties of concrete.* Longman Scientific & Technical, Harlow Essex, UK, 1991.

[61] OŽBOLT, J. Size effect and ductility in concrete and reinforced concrete structures. Habilitation, Stuttgart University, Institut für Werkstoffe im Bauwesen, 1995.

[62] PASSCHIER, C.W., AND TROUW, R.A.J. *Microtectonics.* Springer, Berlin, 1996.

[63] PETERSON, R.E. *Stress concentration factors.* John Wiley & Sons Ltd., 1974.

[64] PETERSSON, P.E. *Crack growth and development of fracture zones in plain concrete and similar materials.* PhD thesis, Lund Institute of Technology, Division of Building Materials, 1981.

[65] PILKEY, W.D. *Peterson's stress concentration factors.* John Wiley & Sons Ltd., 1997.

[66] PLANAS, J., ELICES, M., AND GUINEA, G.V. Measurement of the fracture energy using three point bend tests: Part 2 - influence of bulk energy dissipation. *Materials and Structures (RILEM), 25*, 1992, pp. 305–312.

[67] SCHEIDLER, D. Experimentelle und analytische Untersuchungen zur wirklichkeitsnahen Bestimmung der Bruchschnittgrössen unbewehrter Betonbauteile unter Zugbeanspruchung. In *Deutscher Ausschuss für Stahlbeton* (1987), vol. 379, pp. 1–94 (in German).

[68] SCHLANGEN, E. *Experimental and Numerical Analysis of Fracture Processes in Concrete.* PhD thesis, Delft University of Technology, 1993.

[69] SCHLANGEN, E. Fracture simulations of brittle heterogeneous materials. In *Proceedings 10th ASCE-EMD Conference* (1995), ASCE, pp. 130–133.

[70] SCHLANGEN, E., 1998. Private communication.

[71] SCHLANGEN, E., AND GARBOCZI, E.J. Fracture simulations of concrete using lattice models: computational aspects. *Engineering Fracture Mechanics, 57*(2/3), 1997, pp. 319–332.

[72] SCHLANGEN, E., AND VAN MIER, J.G.M. Experimental and numerical analysis of micromechanisms of fracture of cement-based composites. *Cement and Concrete Composites, 14*, 1992, pp. 105–118.

[73] SCHLANGEN, E., AND VAN MIER, J.G.M. Numerical study of the influence of interfacial properties on the mechanical behaviour of cement-based composites. In *Interfaces in Cementitious Composites* (1992), J.C. Maso (ed.), E&FN Spon, pp. 237–246.

[74] SCHLANGEN, E., AND VAN MIER, J.G.M. Crack propagation in sandstone: Combined experimental and numerical approach. *Rock Mechanics and Rock Engineering, 28*(2), 1995, pp. 93–110.

[75] SCHORN, H., AND RODE, U. 3-D modeling of process zone in concrete by numerical simulation. In *Fracture of Concrete and Rock* (1987), S.P. Shah and S.E. Swartz (eds.), Springer Verlag, pp. 220–228.

[76] SHIOYA, T., IGURO, M., NOJIRI, Y., AKIYAMA, H., AND OKADA, T. Shear strength of large reinforced concrete beams. *ACI SP*(118), 1989, pp. 259–279.

[77] SNYDER, K.A., GARBOCZI, E.J., AND DAY, A.R. The elastic moduli of simple two-dimensional isotropic composites: Computer simulation and effective medium theory. *Journal of Applied Physics, 72*(12), 1992, pp. 5948–5955.

[78] STAUFFER, D. *Introduction to percolation theory*. Taylor & Francis, 1985.

[79] STROEVEN, M., AND STROEVEN, P. Structural evaluation of computer-made concrete. In *Proceedings 2nd international conference on Nondestructive testing of Concrete in the Infrastructure* (1996), pp. 177–184.

[80] STROEVEN, P. *Some Aspects of the Micromechanics of Concrete*. PhD thesis, Delft University of Technology, 1973.

[81] SWARTZ, S.E., AND REFAI, T. Cracked surface revealed by dye and its utility in determining fracture parameters. In *Fracture Toughness and Fracture Energy - Test Methods for Concrete and Rock* (1989), H. Mihashi, H. Takahashi, and F.H. Witmann (eds.), Balkema, pp. 509–520.

[82] TRUNK, B., AND WITTMANN, F.H. Experimental investigation into the size dependence of fracture mechanics parameters. In *Fracture Mechanics of Concrete Structures* (1998), H. Mihashi and K. Rokugo (eds.), AEDIFICATIO Publishers, pp. 1937–1948.

[83] VAN BEEK, A., LOKHORST, S.J., AND VAN BREUGEL, K. On-site determination of degree of hydration and associated properties of hardening concrete. In *Proceedings 3rd conference on Nondestructive Evaluation of Civil Structures and Materials* (1996), M.P. Schuller, D.B. Woodham, and Atkinson-Noland & Associates, Inc. (eds.), pp. 349–363.

[84] VAN MIER, J.G.M. Fracture of concrete under complex stress. *HERON, 31*(3), 1986, pp. 2–90.

[85] VAN MIER, J.G.M. Fracture process zone in concrete: a three dimensional growth process. In *ECF8 Fracture behaviour and Design of Materials and Structures* (1990), D. Firrao (ed.), EMAS Publishers, Warley, UK, pp. 599–604.

[86] VAN MIER, J.G.M. Crack face bridging in normal, high strength and lytag concrete. In *Fracture Processes in Concrete Rock and Ceramics* (1991), J.G.M. Van Mier, J.G. Rots, and A. Bakker (eds.), Chapman & Hall/E&FN Spon, pp. 27–40.

[87] VAN MIER, J.G.M. Mode I fracture of concrete: Discontinuous crack growth and crack interface grain bridging. *Cement and Concrete Research, 21*(1), 1991, pp. 1–15.

[88] VAN MIER, J.G.M. *Fracture processes of concrete*. CRC Press, 1997.

[89] VAN MIER, J.G.M., AND NOORU-MOHAMED, M.B. Geometrical and structural aspects of concrete fracture. *Engineering Fracture Mechanics, 35*(4/5), 1990, pp. 618–628.

[90] VAN MIER, J.G.M., AND SCHLANGEN, E. On the stability of softening systems. In *Fracture of Concrete and Rock* (1989), S.P. Shah, S.E. Swartz, and B. Barr (eds.), Elsevier, pp. 387–396.

[91] VAN MIER, J.G.M., SCHLANGEN, E., AND VERVUURT, A. Lattice type fracture models for concrete. In *Continuum models for Materials with Microstructure*, H.-B. Mühlhaus (ed.). John Wiley & Sons Ltd., 1995, pp. 341–377.

[92] VAN MIER, J.G.M., SCHLANGEN, E., AND VERVUURT, A. Tensile cracking in concrete and sandstone: Part 2 - effect of boundary rotations. *Materials and Structures (RILEM), 29*, 1996, pp. 87–96.

[93] VAN MIER, J.G.M., AND VAN VLIET, M.R.A. Experimentation, numerical simulation and the role of engineering judgement in fracture mechanics of concrete and concrete structures. *Construction and Building Materials, 13*, 1999, pp. 3–14.

[94] VAN MIER, J.G.M., VERVUURT, A., AND VAN VLIET, M.R.A. Materials engineering of cement-based composites using lattice type models. In *Computational Fracture Mechanics in Concrete Technology*, A. Carpinteri and M.H. Aliabadi (eds.). CMP Southampton, 1998, pp. 341–377.

[95] VAN VLIET, M.R.A., AND VAN MIER, J.G.M. Comparison of lattice type fracture models for concrete under biaxial loading regimes. In *Size-Scale Effects in the Failure Mechanisms of Materials and Structures* (1996), A. Carpinteri (ed.), E&FN Spon, pp. 43–57.

[96] VAN VLIET, M.R.A., AND VAN MIER, J.G.M. Concrete behaviour under uniaxial tension: Effect of casting and drying conditions. In *Brittle Matrix Composites 5* (1997), A.M. Brandt, V.C. Li, and I.H. Marshall (eds.), Woodhead Publishing Limited, Cambridge, pp. 329–339.

[97] VAN VLIET, M.R.A., AND VAN MIER, J.G.M. Size effect in tensile fracture of concrete: Effect of test-control. In *Ninth International Conference on Fracture* (1997), R.O. Ritchie, B.L. Karihaloo, and Y.M. Mai (eds.), Pergamon, Oxford, pp. 957–964.

[98] VAN VLIET, M.R.A., AND VAN MIER, J.G.M. Uniaxial tension tests on red and yellow felser sandstone. Report 25.5-97-9, Delft University of Technology, 1997.

[99] VAN VLIET, M.R.A., AND VAN MIER, J.G.M. Experimental and numerical investigation of size scale effects in concrete fracture. In *Material Instabilities in Solids*, R. de Borst and E. van der Giessen (eds.). John Wiley & Sons Ltd., 1998, pp. 185–206.

[100] VAN VLIET, M.R.A., AND VAN MIER, J.G.M. Experimental investigation of size effect in concrete under uniaxial tension. In *Fracture Mechanics of Concrete Structures* (1998), H. Mihashi and K. Rokugo (eds.), AEDIFICATIO Publishers, pp. 1923–1936.

[101] VAN VLIET, M.R.A., AND VAN MIER, J.G.M. Effect of strain gradients on the size effect of concrete in uniaxial tension. *International Journal of Fracture, 95*(1/4), 1999, pp. 195–219.

[102] VAN VLIET, M.R.A., VERVUURT, A., AND VAN MIER, J.G.M. Lattice model for simulating concrete fracture: Theory and applications. In *Second International DIANA Conference on Finite Elements in Engineering and Science* (1997), M.A.N. Hendriks, H. Jongedijk, J.G. Rots, and W.J.E. van Spanje (eds.), Balkema, Rotterdam, pp. 449–461.

[103] VERVUURT, A.H.J.M. *Interface Fracture in Concrete*. PhD thesis, Delft University of Technology, 1997.

[104] VERVUURT, A., VAN VLIET, M.R.A., VAN MIER, J.G.M., AND SCHLANGEN, E. Simulations of tensile fracture in concrete. In *Fracture Mechanics of Concrete Structures* (1995), F.H. Wittmann (ed.), AEDIFICATIO Publishers, pp. 353–362.

[105] VERWAAL, W., AND MULDER, A. Estimating rock strength with the Equotip hardness tester. *International Journal of Rock Mechanics and Mining Sciences and Geomechanics Abstracts, 30*(6), 1993, pp. 659–662.

[106] VISSER, J.H.M. *Extensile hydraulic fracturing of (saturated) porous materials*. PhD thesis, Delft University of Technology, 1997.

[107] VISSER, J.H.M., AND VAN MIER, J.G.M. Tensile hydraulic fracture of concrete and rock. In *Fracture Mechanics of Concrete Structures* (1995), F.H. Wittmann (ed.), AEDIFICATIO Publishers, pp. 261–270.

[108] WALRAVEN, J.C. *Aggregate Interlock: A Theoretical and Experimental Analysis.* PhD thesis, Delft University of Technology, 1980.

[109] WALSH, P.F. Fracture of plain concrete. *Indian Concrete Journal, 46*(11), 1972, pp. 469–470.

[110] WEIBULL, W. A statistical theory of the strength of materials. *Royal Swedish Academy of Eng. Sci. Proc., 151*, 1939, pp. 1–45.

[111] WEIBULL, W. A statistical theory of the strength of materials. *Journal of Applied Mechanics, 18*(9), 1951, pp. 293–297.

[112] WEILER, B., GROSSE, C., AND REINHARDT, H.W. Acoustic emission investigations of the damage zone in steel fibre reinforced beams. In *High Performance Fibre Reinforced Cement Composites (HPFRCC 3)* (1999), H.W. Reinhardt and A.E. Naaman (eds.), RILEM Publications S.A.R.L., pp. 487–496.

[113] WIJK, G. Some theoretical and experimental aspects of the uniaxial and point load tests of rock material. Thesis, Swedish Detonic Research Foundation, 1981.

[114] WIJK, G., REHBINDER, G., AND LOGDSTROM, G. The relation between the uniaxial tensile strength and the sample size for bohus granite. *Rock Mechanics, 10*, 1978, pp. 201–219.

[115] WITTMANN, F.H., MIHASHI, H., AND NOMURA, N. Size effect on fracture energy of concrete. *Engineering Fracture Mechanics, 35*(1/2/3), 1990, pp. 107–115.

[116] WITTMANN, F.H., SADOUKI, H., AND STEIGER, T. Experimental and numerical study of the effective properties of composite materials. In *Micromechanics of Concrete and Cementitious Composites*, C. Huet (ed.). Presses Polytechniques et Universitaires Romandes, Lausanne, 1993, pp. 59–80.

[117] ZECH, B., AND WITTMANN, F.H. A complex study on the reliability assessment of the containment of a PWR. Part II, Probabilistic approach to describe the behaviour of materials. *Nuclear Engineering and Design, 48*, 1978, pp. 563–593.

[118] ZHOU, F.P. Some aspects of tensile fracture behaviour and structural response of cementitious materials. Report TVBM-1008, Lund Institute of Technology, Division of Building Materials, 1988.

[119] ZHU, Y. The flexural strength for concrete beams without initial cracks. In *ECF8 Fracture behaviour and Design of Materials and Structures* (1990), D. Firrao (ed.), EMAS Publishers, Warley, UK, pp. 599–604.

Appendix A

Overview results size effect tests

A.1 Data of individual tests

Table A.1 Experimental data for the tests on the concrete specimens of the DRY series.

Specimen	D [mm]	E [GPa]	F_u [kN]	σ_N [MPa]	δ_u [μm]	G_F [N/m]
01a01n01	50	27.6	6.70	2.23	2.7	102.4
02a01n07	50	41.3	7.77	2.59	2.3	86.8
03a01n13	50	65.3	9.43	3.14	2.1	77.7
04a01n20	50	51.0	9.14	3.05	1.8	102.7
05a01n27	50	78.8	8.90	2.97	1.9	107.4
06a01n34	50	55.2	8.07	2.69	1.8	111.1
07a01n41	50	48.8	5.97	1.99	1.4	-
08a01n48	50	223.2	6.89	2.30	0.6	81.9
09a01n55	50	156.3	6.45	2.15	0.6	102.5
10a01n62	50	77.3	6.75	2.25	1.2	100.9
02b02n08	100	39.5	17.92	2.99	5.3	136.0
03b02n14	100	41.3	18.99	3.17	5.1	123.8
06b02n35	100	35.1	18.07	3.01	5.9	141.8
07b02n42	100	38.1	16.31	2.72	4.5	101.2
02c04n09	200	39.3	32.48	2.71	10.3	111.2
04c04n23	200	38.1	34.58	2.88	10.0	131.1
05c04n30	200	46.7	30.86	2.57	8.7	121.9
06c04n37	200	38.2	34.34	2.86	9.4	103.0
07c04n44	200	37.1	35.80	2.98	10.3	141.3
09c04n58	200	40.4	34.48	2.87	10.3	136.0
10c04n65	200	38.9	28.53	2.38	7.7	125.2

continued on next page

continued from previous page

Specimen	D [mm]	E [GPa]	F_u [kN]	σ_N [MPa]	δ_u [μm]	G_F [N/m]
01d08n04	400	42.5	53.36	2.22	15.5	119.9
02d08n10	400	52.4	53.48	2.23	12.8	121.8
05d08n31	400	41.6	54.70	2.28	13.6	109.4
06d08n38	400	40.0	58.88	2.45	15.9	146.4
07d08n45	400	37.5	55.51	2.31	16.1	128.6
06e16n40	800	44.4	99.99	2.08	23.2	152.2
08e16n54	800	48.7	106.53	2.22	19.0	149.7
09e16n61	800	43.7	99.49	2.07	22.2	130.8
10e16n68	800	46.2	92.34	1.92	23.7	136.5
01f32n06	1600	39.7	190.50	1.98	52.0	156.2
03f32n19	1600	45.0	173.32	1.81	39.3	134.1
04f32n26	1600	45.5	190.74	1.99	47.0	136.4
05f32n33	1600	40.0	158.65	1.65	39.3	137.7

Table A.2 Experimental data for the tests on the concrete specimens of the WET series.

Specimen	D [mm]	E [GPa]	F_u [kN]	σ_N [MPa]	δ_u [μm]	G_F [N/m]
12a01n69	50	25.4	5.97	1.99	2.4	69.3
13a01n73	50	28.1	6.11	2.04	2.6	119.5
14a01n77	50	42.2	5.97	1.99	1.5	78.8
15a01n81	50	73.4	6.84	2.28	1.7	96.1
16a01n85	50	33.3	7.72	2.57	2.7	93.7
12b02n70	100	41.6	13.48	2.25	4.0	114.2
13b02n74	100	38.0	13.13	2.19	3.4	88.7
14b02n78	100	40.5	13.33	2.22	4.3	102.3
15b02n82	100	41.0	14.50	2.42	4.2	101.8
16b02n86	100	37.9	12.40	2.07	4.6	91.3
12c04n71	200	42.0	32.34	2.69	9.7	82.6
13c04n75	200	41.4	29.30	2.44	8.4	97.6
14c04n79	200	45.5	28.73	2.39	7.9	101.9
15c04n83	200	38.6	27.55	2.30	7.7	71.8
16c04n87	200	44.4	30.77	2.56	8.1	90.7
12d08n72	400	40.4	56.03	2.33	16.1	110.8
14d08n80	400	39.7	58.82	2.45	16.6	91.2
15d08n84	400	41.4	55.78	2.32	15.0	-

continued on next page

continued from previous page

Specimen	D [mm]	E [GPa]	F_u [kN]	σ_N [MPa]	δ_u [μm]	G_F [N/m]
16d08n88	400	41.5	56.65	2.36	15.2	99.1

Table A.3 Experimental data for the tests on the red Felser sandstone specimens.

Specimen	D [mm]	E [GPa]	F_u [kN]	σ_N [MPa]	δ_u [μm]	G_F [N/m]
00a01r04	50	3.9	2.45	0.82	32.2	73.0
00a01r05	50	5.6	2.45	0.82	24.7	80.5
00b02r07	100	6.8	7.32	1.22	45.0	107.6
00b02r08	100	9.4	7.62	1.27	44.9	111.5
00b02r09	100	7.5	6.93	1.16	42.6	114.9
00c04r10	200	6.7	12.32	1.03	62.3	95.1
00c04r11	200	8.0	12.42	1.03	65.4	97.4
00c04r12	200	5.9	11.69	0.97	79.9	88.9
00d08r13	400	2.8	22.32	0.93	150.4	127.4
00d08r14	400	2.6	23.06	0.96	166.9	150.1
00d08r15	400	5.4	23.75	0.99	153.1	127.7
00e16r16	800	-	87.15	1.82	-	-
00e16r17	800	7.8	49.16	1.02	258.4	131.6
00e16r18	800	5.2	51.08	1.06	269.0	155.1
00f32r19	1600	6.4	94.53	0.98	402.9	86.7
00f32r20	1600	11.1	161.90	1.69	515.9	58.9
00f32r21	1600	7.2	88.93	0.93	385.3	99.8

A.2 Force-deformation curves

In this section an overview is given of the individual force-deformation curves of the size effect experiments. The curves which have been included are those of the DRY and WET concrete series, as well as the Felser sandstone series. The deformation in the curves is the average of the deformation measurements with scaled measuring length, measured in the middle of the specimens on the front and the back side respectively (see also Fig. 3.23).

A.2.1 Concrete tests (I): DRY series

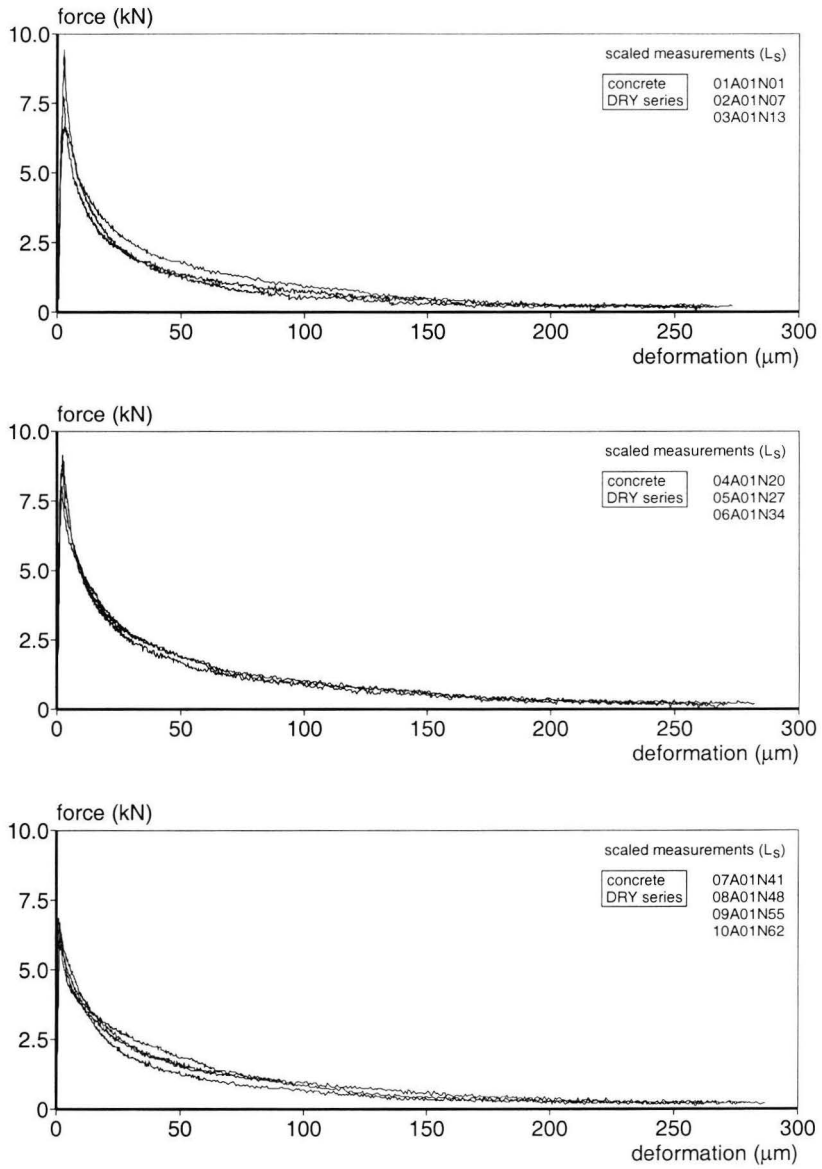


Figure A.1 Force-deformation curves of the A *specimens.*

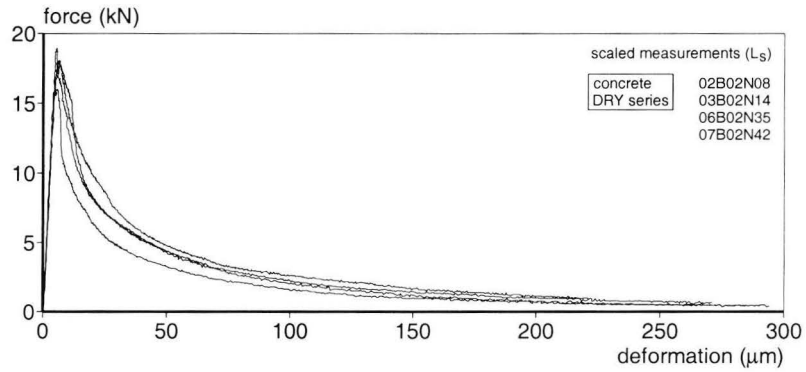
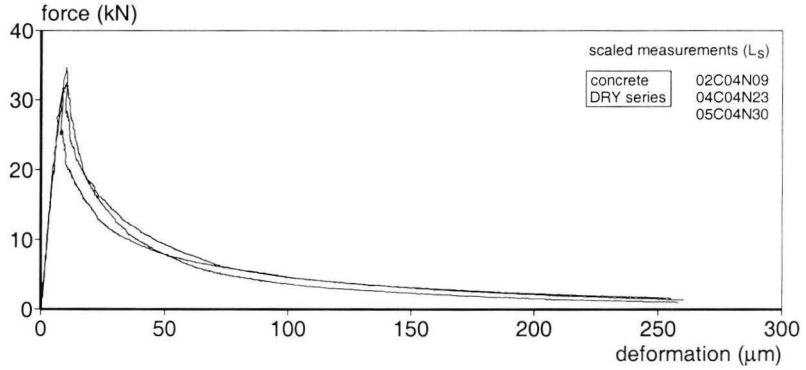


Figure A.2 Force-deformation curves of the B *specimens.*



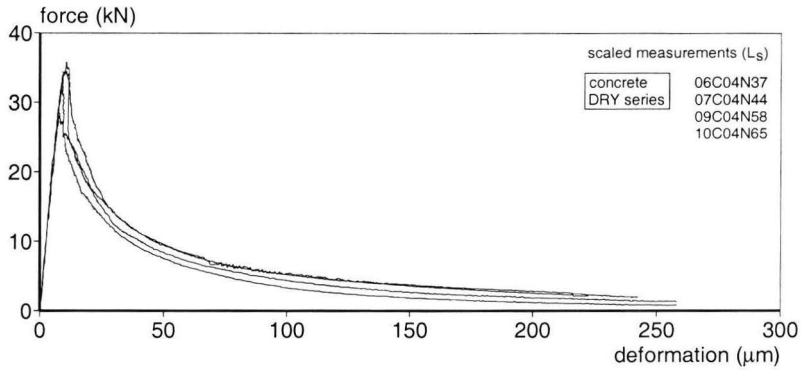


Figure A.3 Force-deformation curves of the C *specimens.*

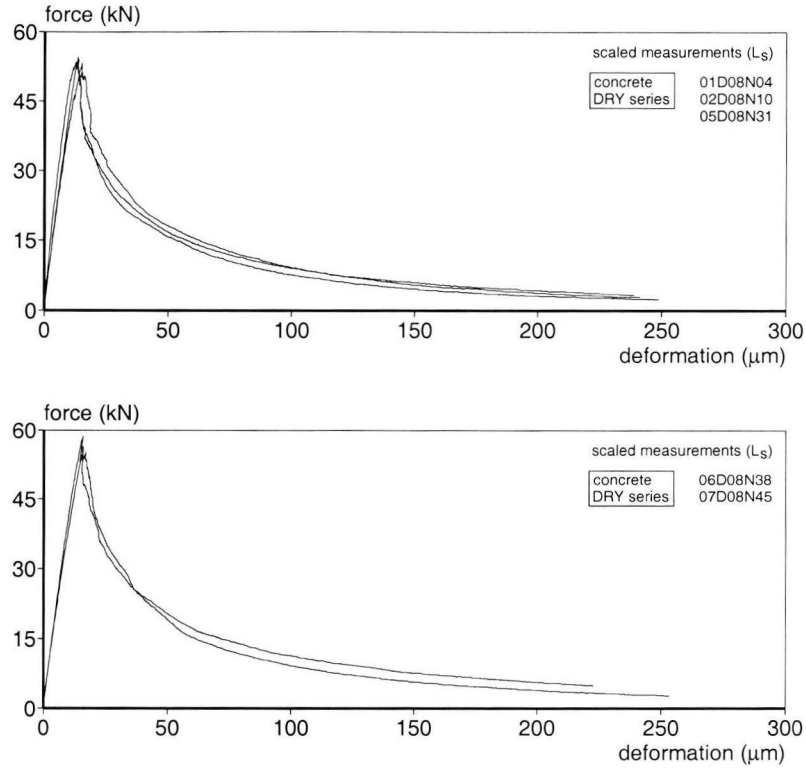


Figure A.4 Force-deformation curves of the D *specimens.*

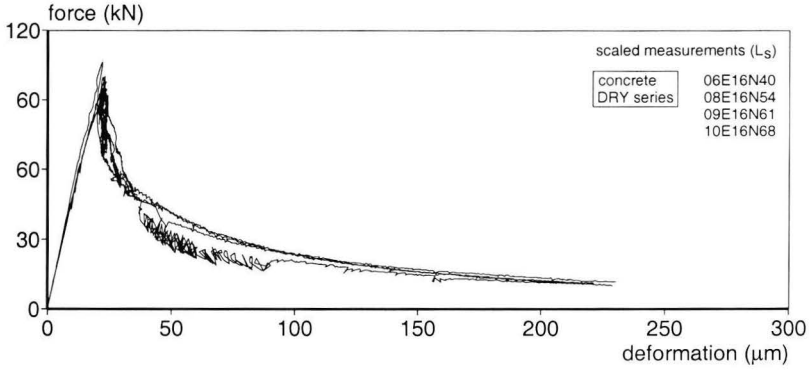


Figure A.5 Force-deformation curves of the E *specimens.*

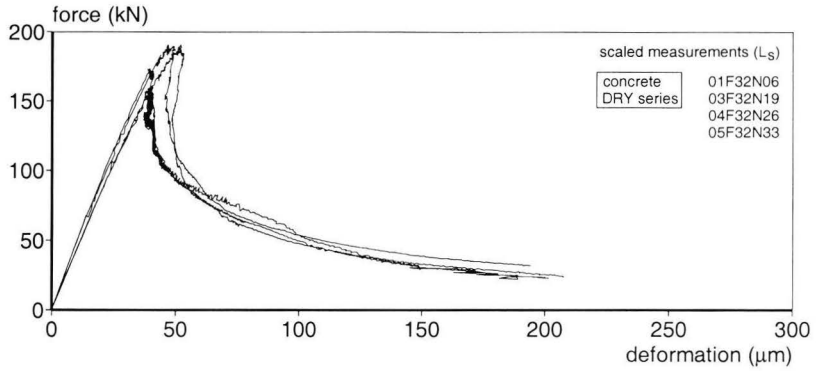
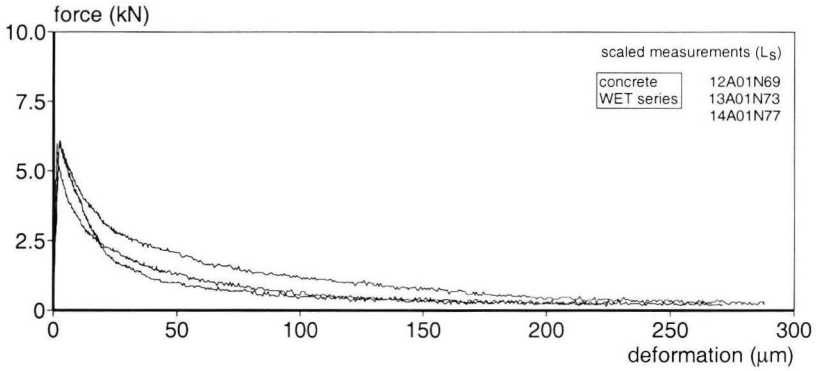


Figure A.6 Force-deformation curves of the F *specimens.*

A.2.2 Concrete tests (II): WET series



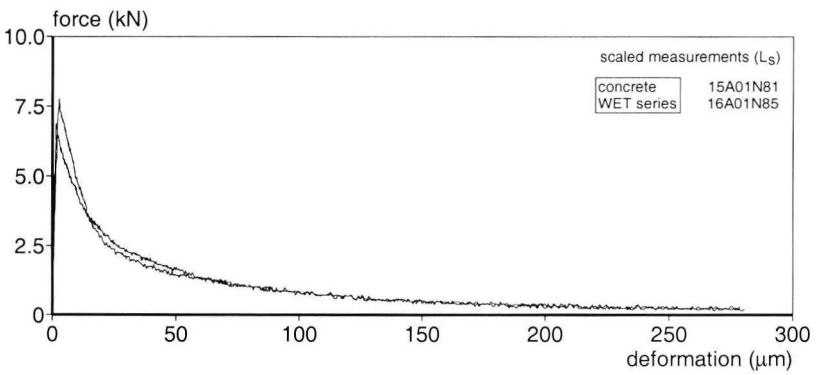


Figure A.7 Force-deformation curves of the A *specimens.*

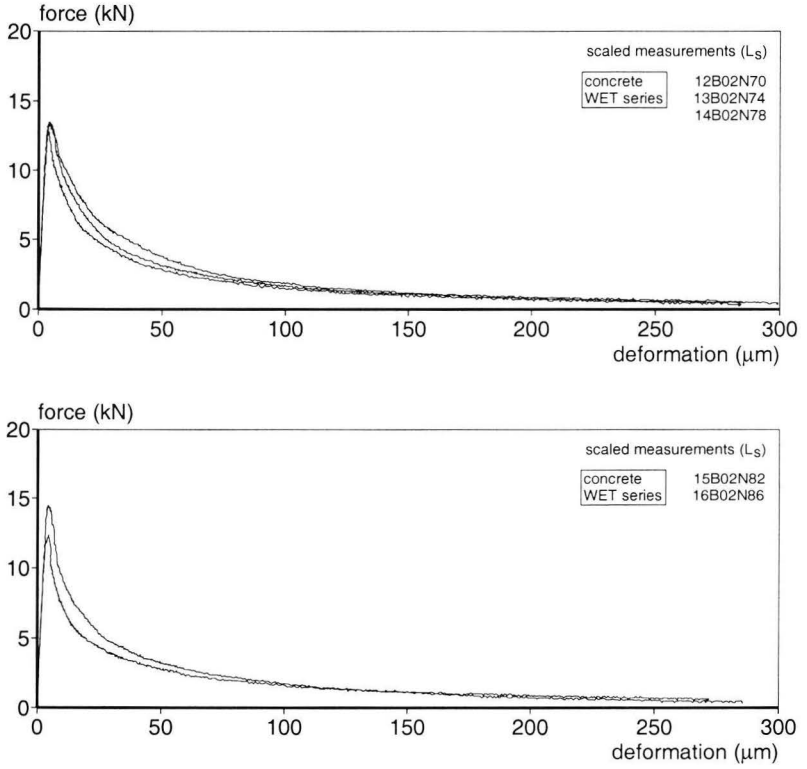


Figure A.8 Force-deformation curves of the B *specimens.*

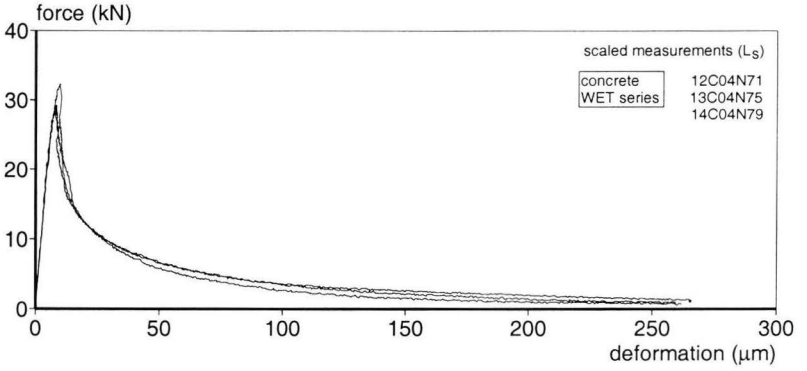


Figure A.9 Force-deformation curves of the C *specimens.*

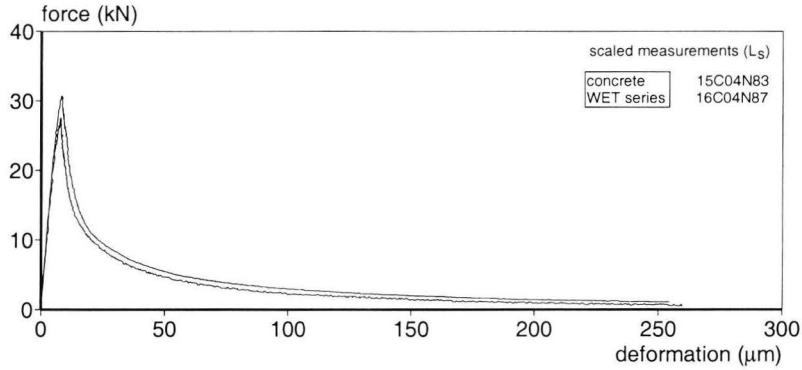


Figure A.10 Force-deformation curves of the C *specimens (continued).*

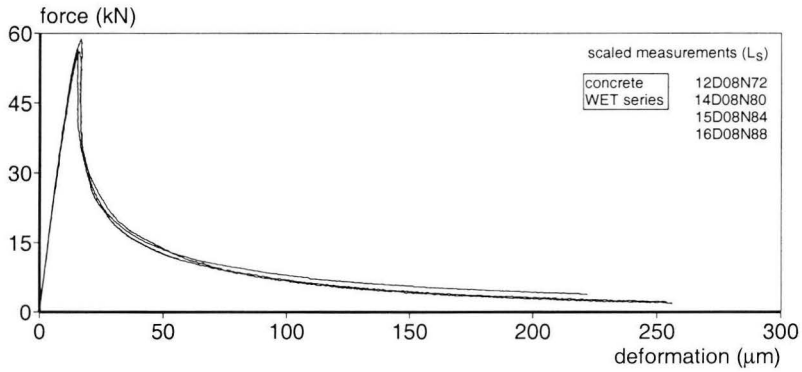


Figure A.11 Force-deformation curves of the D *specimens.*

A.2.3 Felser sandstone tests

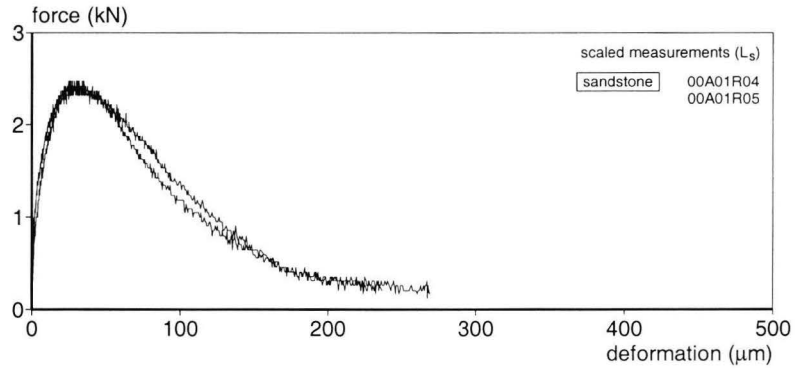


Figure A.12 Force-deformation curves of the A *specimens.*

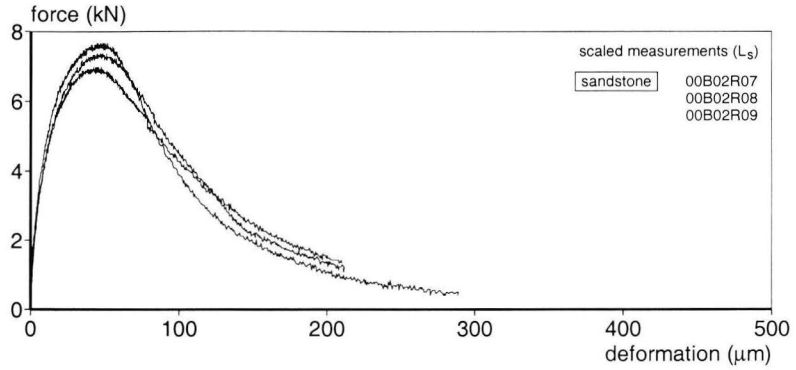


Figure A.13 Force-deformation curves of the B *specimens.*

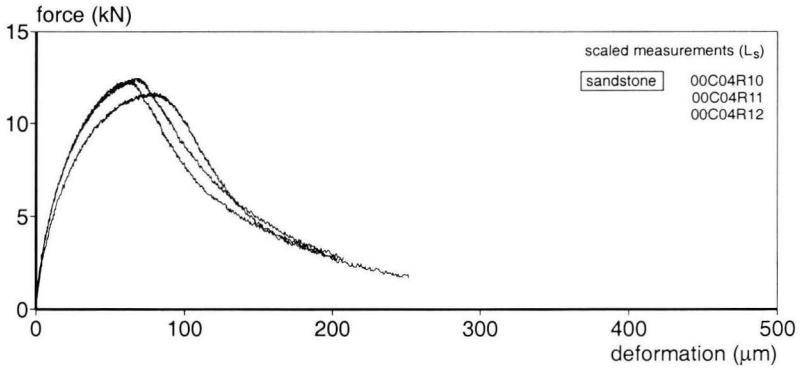


Figure A.14 Force-deformation curves of the C *specimens.*

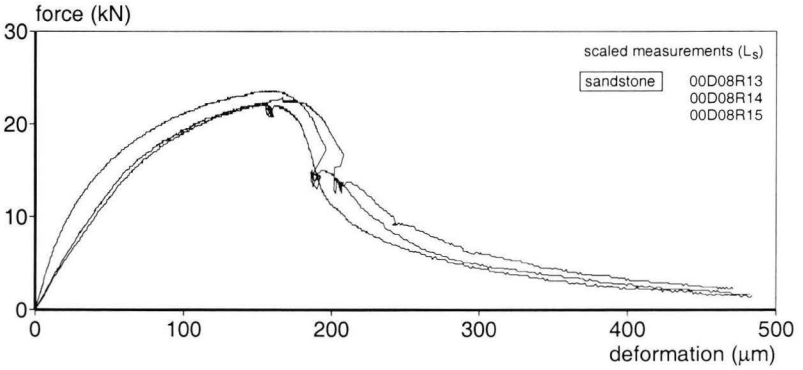


Figure A.15 Force-deformation curves of the D *specimens.*

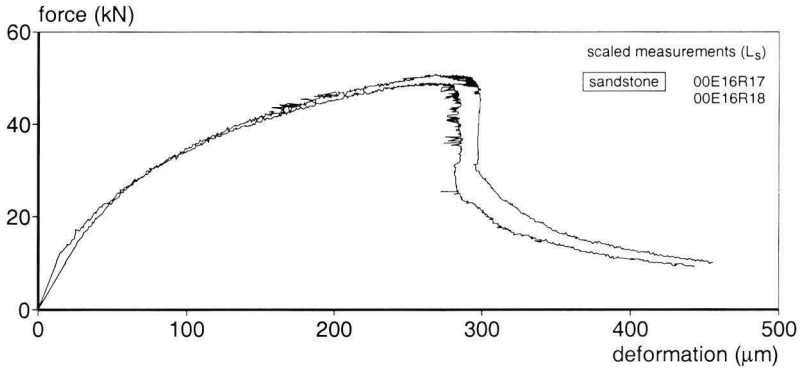


Figure A.16 Force-deformation curves of the E *specimens.*

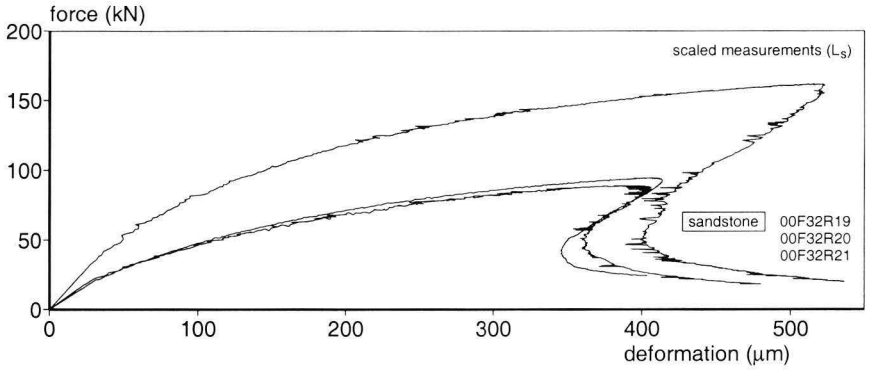


Figure A.17 Force-deformation curves of the F *specimens.*

Appendix B

Generation of an aggregate structure

The aggregate structures which have been used in the reported simulations are computer generated. As a basis for the generation of aggregates of different diameters served a cumulative distribution function derived by Walraven [108]. This function (Eq. B.1), which is based on a distribution (grading) of aggregate particles in a concrete mix according to a Fuller curve, represents the probability p_c that an arbitrary point in the concrete body, lying in an intersection plane, is located in an intersection circle with a diameter $d < d_0$.

$$p_c(d < d_0) = P_k \left[1.065\sqrt{\frac{d_0}{d_{\max}}} - 0.053\left(\frac{d_0}{d_{\max}}\right)^4 - 0.012\left(\frac{d_0}{d_{\max}}\right)^6 - 0.0045\left(\frac{d_0}{d_{\max}}\right)^8 - 0.0025\left(\frac{d_0}{d_{\max}}\right)^{10} \right] \tag{B.1}$$

In Eq. (B.1) P_k represents the ratio between the volume of the aggregate particles and the total volume of the concrete body. Analogous, P_k can be seen as the ratio between the total *area* of the aggregate particles in the intersection plane and the area of the intersection plane itself. A graphical representation of Eq. (B.1) is shown in Fig. B.1.

Although the actual distribution of aggregate diameters in the intersection plane is continuous, the generated aggregate diameters have been discretized to integer values. Thus, for a generation area A and an aggregate fraction P_k, the number of aggregate particles n_i with diameter d_i follows from

$$\begin{aligned} n_i &= \frac{\left[p_c(d < d_i + 0.5) - p_c(d < d_i - 0.5)\right] A P_k}{0.25\pi d_i^2}, \quad d_i < d_{\max} \\ n_i &= \frac{\left[p_c(d < d_i) - p_c(d < d_i - 0.5)\right] A P_k}{0.25\pi d_i^2}, \quad d_i = d_{\max} \end{aligned} \tag{B.2}$$

with as consequence that the area of the particles with $d < d_{\min} - 0.5$ is not discretized. The particles with $d < d_{\min} - 0.5$ can be regarded as an integral part of the cement matrix. Although this is quite reasonable from a physical point of view, the resulting aggregate area will be lower than the input value of P_k.

The smallest aggregate diameter which is to be generated and placed depends on the followed aggregate placement procedure. Here, the aggregate particles have been placed

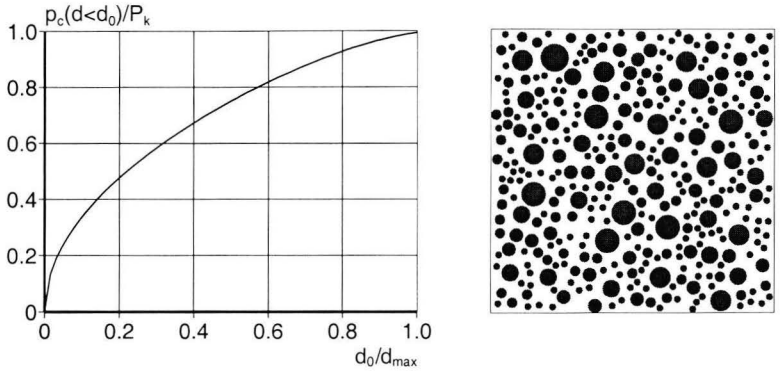


Figure B.1 *Cumulative distribution function for the diameter of intersection circles [108] (a), and generated particle structure for an area of* 80×80 mm^2, $2 \leq d \leq 8$ *mm and* $P_k = 0.75$ *(b).*

randomly in the generation area starting with the largest diameter [68]. The criterion for placement is that the distance between two particles A and B has to be equal, or larger than $1.1(d_A + d_B)/2$ (according to [44]). When using such a random placement procedure, like in the present study, generating and placing smaller aggregates than will be used eventually is not beneficial. Only aggregates with diameters equal to, or larger than twice the length of the lattice elements will be modelled (see Section C.2.3), and the random placement procedure ensures that also mutual distances larger than $1.1(d_A + d_B)/2$ will be present in the aggregate structure. This is however not the case when the aggregates are placed using an alternative procedure, based on dropping the particles in a box [104, 103]. In the latter case distances between particles do depend on the small particles, which consequently have to be generated, placed and again deleted from the aggregate structure before it is projected on a lattice mesh. The main advantage of this "dropping" procedure is that it is much faster than the random placement procedure, especially for simple rectangular generation areas.

Appendix C

Background of the lattice model

C.1 Elastic properties of a heterogeneous regular lattice

In this thesis a lattice model has been used to simulate fracture processes in concrete specimens of different sizes. In the lattice meshes a concrete material structure was introduced by assigning different stiffness and strength values to lattice elements representing the aggregate, bond and matrix phase respectively. Because of these different phases, already from an elastic point of view the material has to be treated as a *composite* material. The global or effective properties of such a material are composed from the properties of its constituents. On the meso-structural level, the local elastic properties influence the local stress distribution and thus the fracture process. For this reason, apart from fracture processes, also the elastic behaviour of a material model should resemble the behaviour of a composite material.

Analysis of the mechanical properties of composite materials goes back to work by Einstein in 1906, and incorporates analytical [30] as well as computer based approaches (see e.g. [77]) in addition to experimental work. In this section the results are outlined of a study on the elastic behaviour of a 2D regular lattice with aggregate structure. Since the beam elements are assigned two different Young moduli (E_a and $E_b = E_m$ respectively, see Section 6.1.3), the lattice can be considered a two-phase material. The study focuses on the effect of variations in aggregate content, aggregate composition and aggregate stiffness on the elastic properties of the composite. Part of this section can be found in [94, 93] as well.

C.1.1 Lattice model used in the calculations

The elastic computations were run on a regular lattice of 80×92 cells and a beam length $l = 1$ mm. Comparison of the numerically and analytically computed Young modulus and Poisson ratio had shown that only minor boundary effects were present in a homogeneous lattice of this size (Section 6.1.3). The input parameters are listed in Table C.1, where it is mentioned that the beam height followed from Eq. (6.3) after the choice for a global Poisson ratio $\nu = 0.2$. The applied supports as well as the loading scheme are shown in Fig. C.1.

After an elastic analysis E^* and ν^* have been computed by

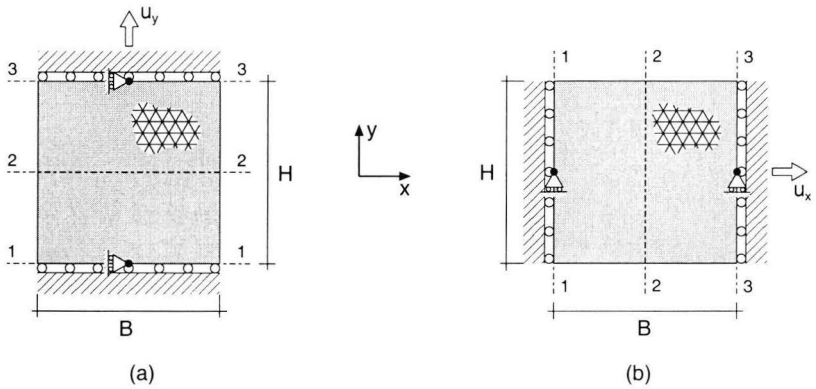


Figure C.1 Models for the computation of E_y^* and ν_x^* (a) and E_x^* and ν_y^* (b) respectively.

$$E_y^* = \frac{\sigma_y}{\varepsilon_y} = \frac{\sum F_{r,y}}{Bt}\frac{H}{u_y}, \qquad \nu_x^* = \frac{\varepsilon_x}{\varepsilon_y} = \frac{(\Delta u_{x1} + \Delta u_{x2} + \Delta u_{x3})}{3B}\frac{H}{u_y} \tag{C.1a}$$

$$E_x^* = \frac{\sigma_x}{\varepsilon_x} = \frac{\sum F_{r,x}}{Ht}\frac{B}{u_x}, \qquad \nu_y^* = \frac{\varepsilon_y}{\varepsilon_x} = \frac{(\Delta u_{y1} + \Delta u_{y2} + \Delta u_{y3})}{3H}\frac{B}{u_x} \tag{C.1b}$$

where $F_{r,y}$ and $F_{r,x}$ are the reaction forces of the supports in y and x direction respectively and t is the thickness. Δu_{xi} and Δu_{yi} ($i = 1$, 2 or 3) denote the deformations of the lattice in horizontal and vertical direction, computed along the lines 1, 2 and 3 respectively.

In the homogeneous case the lattice consists entirely of one phase which is considered the matrix. Within this matrix aggregates have been included representing the second phase. To see whether the elastic properties of the lattice are sensitive to variations in shape and size of the inclusions, the aggregate fraction was varied in three different ways, denoted by CASE I, II and III (see Table C.2). For CASE I, ten aggregate structures were generated with $1 \leq d \leq 16$ mm and aggregate fractions, denoted by P_k (Appendix B), of $0.10 \leq P_k \leq 1.00$. For CASE II, one aggregate structure was generated with $1 \leq d \leq 16$ mm and $P_k = 0.75$. Here, the aggregate fraction was varied by subsequently deleting the aggregates of the smallest diameter. CASE III comprises ten "aggregate" structures which simply consist of a certain percentage of beam elements with aggregate properties. These beam elements were generated randomly.

Table C.1 Geometrical and material input parameters for the elastic computations.

Measures in mm			Units in MPa		
l	h	t	E_M	E_A (normal concrete)	E_A (lightweight concrete)
1.0	0.577	1.0	31255	87514	12502

Table C.2 Applied methods for varying the aggregate fraction.

Case	Method	Values
I	variation of P_k	$P_k = 0.10, 0.20, ..., 1.00$
II	variation of $d_{\min}$	$d_{\min}$ = 1 mm, 2 mm ,..., 14 mm
III	variation of percentage aggregate beams	10%, 20%,..., 100% aggregate beams

In Appendix B it has already been mentioned that a difference exists between the P_k value used to generate the aggregate structure and the actual or effective P_k value. The latter value, $P_{k,\text{eff}}$ is always lower than P_k due to the procedure which was adopted for generating the aggregates. Hence, a value of $P_k = 1.00$, which theoretically means that the complete generation area consists of aggregate phase, results only in $P_{k,\text{eff}} = 0.80$. Even when generating aggregates with a total area of e.g. 90% of the generation area, they could not be placed. This was found in experiments conducted by Wittmann [116], and followed as well from the aggregate structures with $P_k = 0.90$ ($P_{k,\text{eff}} = 0.73$) and $P_k = 1.00$ ($P_{k,\text{eff}} = 0.80$) in CASE I. Since not all particles could be positioned with the random placement procedure, a numerical packing program developed by Stroeven [79] had to be used.

For the lattice meshes, the matrix and aggregate fraction are based on the number of beam elements which represent a certain phase. Thus, the aggregate fraction of the lattice ($P_{k,\text{lat}}$), is defined as the ratio of the number of aggregate beams and the total number of beams. Again the example of the generation value $P_k = 1.00$ is taken. After discretizing the aggregate particles this gives $P_{k,\text{eff}} = 0.80$, whereas after projecting the aggregate structure on the lattice only a value of $P_{k,\text{lat}} = 0.48$ is left. For all particle structures in CASE I and II, $P_{k,\text{lat}}$ is much smaller than P_k. Only the structures of CASE III give $P_k = P_{k,\text{lat}}$, since the desired aggregate fraction can be assigned directly.

In Figs. C.2, C.3 and C.4 four different lattice meshes are shown for each case. Because of the small scale of the pictures, only the aggregate beams are shown. For each of the meshes also the values for P_k, $P_{k,\text{eff}}$ and $P_{k,\text{lat}}$ are listed in Table C.3.

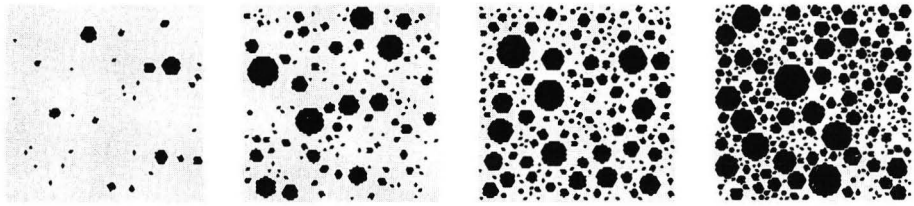
Using the aggregate structures of CASE I, II and III the effect of an increasing aggregate fraction on the global elastic properties was simulated for normal and lightweight concrete. For the normal concrete the global Young moduli 70 GPa (aggregate) and 25 GPa (matrix) have been used. For the lightweight concrete again a matrix stiffness of 25 GPa was taken, whereas the stiffness for the aggregates was decreased to 10 GPa. This low stiffness is typical for lightweight aggregates made from e.g. expanded clay. The values of the Young moduli which were assigned to the lattice beams are compiled in Table C.1, where E_M follows directly from Eq. (6.4) and E_A from Table 6.1.

C.1.2 Analytical models

The numerical results have been compared with predictions by well known analytical models. The most simple models in this respect are the parallel and serial model. They give the absolute upper and lower bound for the effective Young modulus of a material consisting of

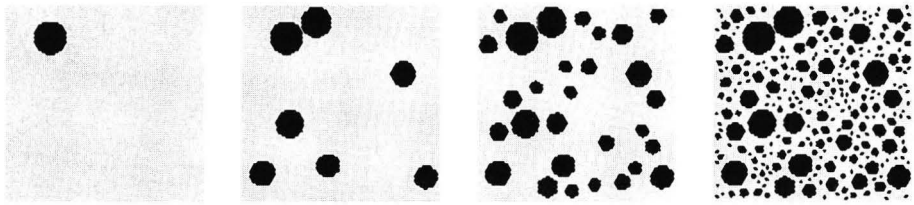
Table C.3 *Aggregate fractions for the generated aggregate structures, and after projection on the lattice for the meshes shown in Figs. C.2, C.3 and C.4.*

CASE I			CASE II			CASE III	
P_k	$P_{k,\text{eff}}$	$P_{k,\text{lat}}$	Aggr. diameters	$P_{k,\text{eff}}$	$P_{k,\text{lat}}$	Beam perc.	$P_{k,\text{eff}} = P_{k,\text{lat}}$
0.10	0.06	0.03	$14 \leq d \leq 16$ mm	0.02	0.02	10%	0.10
0.40	0.32	0.19	$10 \leq d \leq 16$ mm	0.12	0.11	30%	0.30
0.70	0.56	0.34	$6 \leq d \leq 16$ mm	0.25	0.22	60%	0.60
1.00	0.80	0.48	$2 \leq d \leq 16$ mm	0.47	0.35	90%	0.90



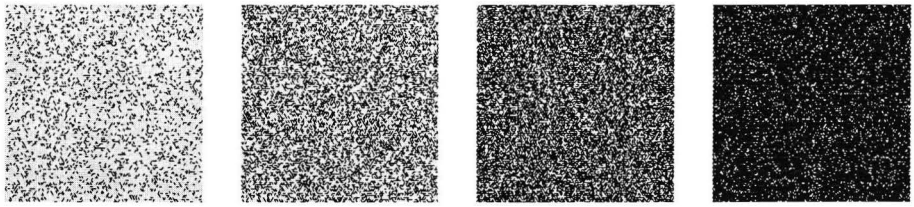
(a) $P_k = 0.10$ (b) $P_k = 0.40$ (c) $P_k = 0.70$ (d) $P_k = 1.00$

Figure C.2 *Four different lattice meshes for aggregate structures of* CASE I.



(a) $14 \leq d \leq 16$ mm (b) $10 \leq d \leq 16$ mm (c) $6 \leq d \leq 16$ mm (d) $2 \leq d \leq 16$ mm

Figure C.3 *Four different lattice meshes for aggregate structures of* CASE II.



(a) 10% aggr. beams (b) 30% aggr. beams (c) 60% aggr. beams (d) 90% aggr. beams

Figure C.4 *Four different lattice meshes for aggregate structures of* CASE III.

two layers, each layer with a volume (or area) fraction V_i and a Young modulus E_i. Depending on the direction in which the material is loaded, the effective or global Young modulus follows from

$$E = E_1 V_1 + E_2 V_2 \tag{C.2}$$

for the parallel model and

$$E = \frac{E_1 E_2}{E_2 V_1 + E_1 V_2} \tag{C.3}$$

for the serial model. These two basic models can be combined to chains of parallel and serial units, leading to tighter upper and lower bounds.

One of the best known analytical models, even giving an exact solution for the effective plane-strain bulk modulus of a two-phase material under certain conditions, is the model by Hashin. For the two-dimensional case, the lower and upper bound of the plane-strain bulk modulus K of a two-phase material are given by [29]

$$K^{(-)} = K_1 + \frac{V_2}{\dfrac{1}{K_2 - K_1} + \dfrac{V_1}{K_1 + G_1}} \tag{C.4a}$$

$$K^{(+)} = K_2 + \frac{V_1}{\dfrac{1}{K_1 - K_2} + \dfrac{V_2}{K_2 + G_2}} \tag{C.4b}$$

where G represents the shear modulus. The lower bound represents the case of inclusions of material 2 embedded in a matrix of material 1. For the upper bound, inclusion and matrix material have to be interchanged. By expressing K and G in terms of E and ν, Eqs. (C.4) can be rewritten into a lower and upper bound for the effective Young modulus. Furthermore, a simplification can be obtained when both materials have the same Poisson ratio. Since the lattice modelling of material 1 and 2 is the same, and the Poisson ratio of the lattice is set at 0.2 through the lattice geometry, this holds true. Hence, using

$$K_i = \frac{E_i}{2(1-\nu_i)}, \quad G_i = \frac{E_i}{2(1+\nu_i)}, \quad \nu_i = \nu \quad \text{with } i = 1,2 \tag{C.5}$$

Eqs. (C.4) can be written in the form

$$E^{(-)} = E_1 \frac{(1+\nu)E_2 + (1-\nu)E_1 + V_2(1-\nu)(E_2 - E_1)}{(1+\nu)E_2 + (1-\nu)E_1 - V_2(1+\nu)(E_2 - E_1)} \tag{C.6a}$$

$$E^{(+)} = E_2 \frac{(1+\nu)E_1 + (1-\nu)E_2 + V_1(1-\nu)(E_1 - E_2)}{(1+\nu)E_1 + (1-\nu)E_2 - V_1(1+\nu)(E_1 - E_2)} \tag{C.6b}$$

For the normal and lightweight concrete under consideration, values of 70 GPa and 10 GPa respectively apply for the aggregate phase (E_2), and 25 GPa for the matrix phase (E_1) whereas $\nu = 0.2$.

C.1.3 Results

The results for the effective Young modulus of the lattice model, loaded in y direction (Fig. C.1a), and for the case of normal and lightweight aggregates are shown in Figs. C.5a and b. In addition, also the analytical relations of the parallel, serial and Hashin model have been included. Only one simulation was carried out for each specific case. The fact that the results for the simulations of CASE I and CASE II are similar (Figs. C.5a and b), shows that E_y^* is not sensitive to variations in the aggregate structure. Moreover, a consistent relation is found between the aggregate fraction and the effective Young modulus, which matches the lower Hashin bound exactly for the normal weight aggregates. These observations could easily lead to the conclusion that the shape of the inclusions does not affect the global properties at all. If so, the results of the CASE III simulations should again be the same. Contrary to CASE I and CASE II however, the results for CASE III strictly follow the *upper* Hashin bound (Figs. C.5c and d).

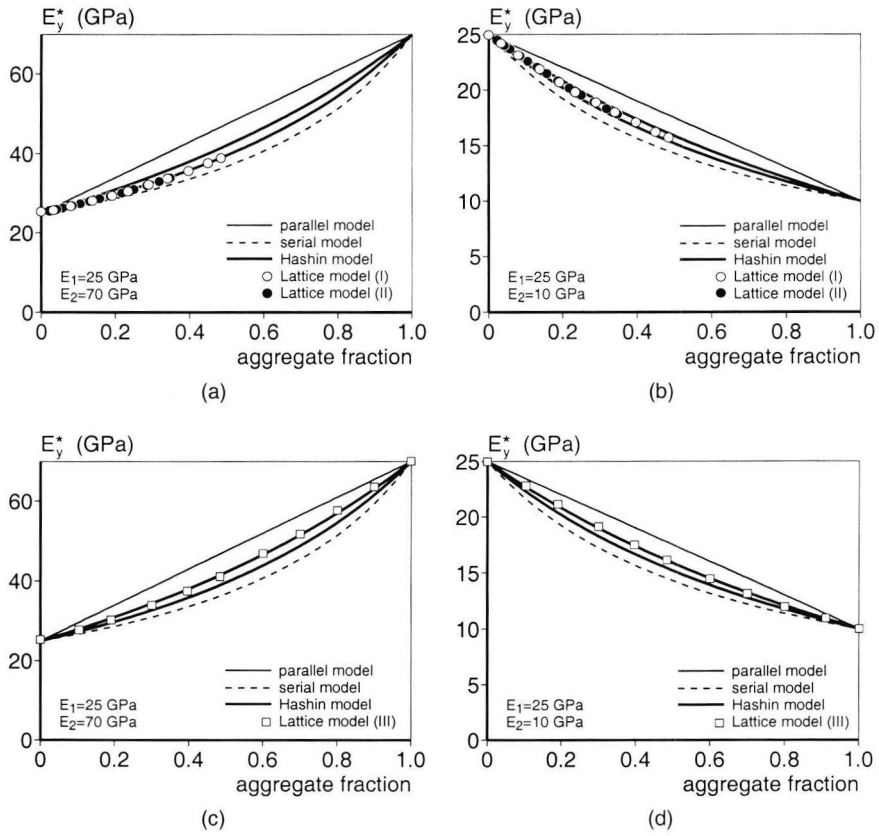


Figure C.5 *Effective Young modulus for a regular lattice with varying aggregate fraction and different aggregate structures. Normal weight aggregates: (a) and (c), light weight aggregates : (b) and (d).*

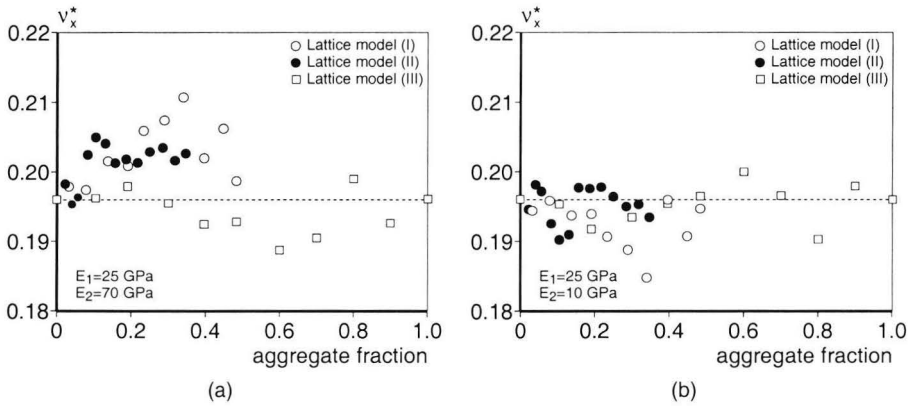


Figure C.6 *Effective Poisson ratio for a regular lattice with varying aggregate fraction and different aggregate structures. Normal weight aggregates: (a), light weight aggregates : (b).*

Besides the effective Young modulus, also the Poisson ratio of the subsequent aggregate structures was computed (Fig. C.6). The dashed line in Figs. C.6a and b is meant as a visual aid, and represents Poisson's ratio for the homogeneous case, i.e. for $V_2 = 0$ and $V_2 = 1$. No clear trend is found though, so that for conclusions with respect to the variation of ν^* with the aggregate fraction, the number of lattice calculations would have to be increased. Such a relation could very well exist though. Snyder et al. [77], studied among others the variation of ν^* with the inclusion fraction on a triangular lattice of spring elements with circular overlapping inclusions. Some of their findings can be found in Fig. C.7, showing a trend with a minimum and maximum for ν^*. Each point in the graph is the mean of ten computations, which illustrates the variation of ν^* which is to be expected. Contrary to the variations for ν^*, almost no scatter was present in the values for E^*.

Finally Fig. C.8 deals with the degree of anisotropy for the computed Young moduli and

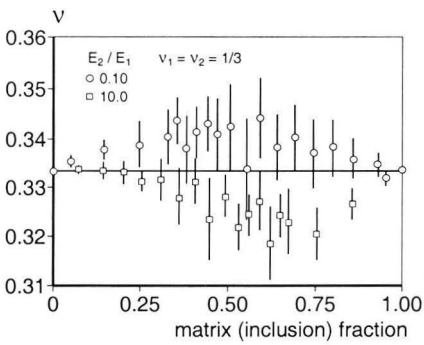


Figure C.7 *Variation of the effective Poisson ratio. For $E_2/E_1 = 10.0$ the data are plotted against V_2, for $E_2/E_1 = 0.10$ against V_1 [77].*

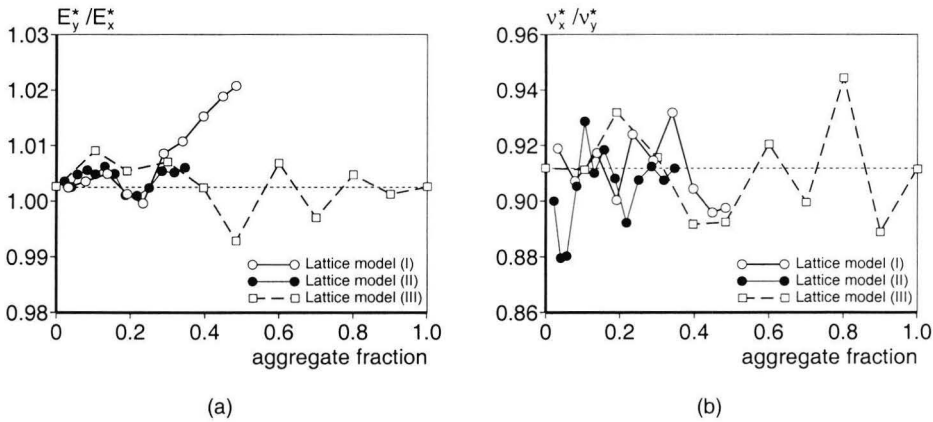


Figure C.8 *Degree of anisotropy for the Young modulus (a) and the Poisson ratio (b) of the normal weight concrete.*

Poisson ratios. Again, the horizontal dashed line connects the results for the homogeneous case, i.e. pure matrix and pure aggregate respectively. In general, the results show a random scatter which confirms that no structural effects were present in the computations. The only exception concerns the ratios of Young's modulus for the CASE I lattice meshes which increase consistently for large aggregate fractions. This could however be coincidental, and due to the fact that especially for the aggregate structures of $P_k = 0.90$ and $P_k = 1.00$ the large aggregates were positioned at one side of the mesh (see also Fig. C.2d). Consequently, a situation could be created which resembles the parallel and serial model. Because of the limited number of computations, this explanation is rather speculative though.

C.2 Fracture simulations with a regular lattice

The result of a fracture analysis with a lattice model strongly depends, as in any model, on the initial settings. These settings comprise of course the values of the input parameters, but also the lattice geometry, which influences the numerical result through the applied beam length. In addition to the work of Schlangen [68] and Vervuurt [103] on the determination of input values for the lattice model and the effect of parameter variations on the numerical result, this section discusses some new findings, as far as they affect the parameter settings that have been used in this thesis.

After some examples of typical observations in a lattice fracture analysis in general, the effect of variations of the strength and/or stiffness values of the lattice beams will be illustrated. The resulting fracture behaviour does not depend on the fact *that* a strength distribution is applied, but purely on the strength ratio between stronger and weaker elements. In addition, also the amount of weak elements in the mesh strongly influences the fracture behaviour.

C.2.1 General aspects of a fracture analysis

The present fracture analyses are characterized by the removal of one beam element per step of the analysis. The element which is to be removed is the one subjected to the highest stress with respect to its strength. By subsequently removing beam elements from the mesh a crack pattern develops, as well as a force-deformation relation for each set of two points in the mesh. These force-deformation curves have peculiar, irregular shapes. Some of the situations which lead to these typical shapes will now be discussed in more detail.

For a start the case of a homogeneous, regular triangular mesh will be taken. The fracture analysis of two specimens of type A and B is considered, with loading and boundary conditions as illustrated in Fig. C.9. The normalized force vs. deformation curves resulting from the analyses are shown in Fig. C.10a. Note that due to the fact that the deformation of specimen type B is based on a measuring length twice as long as for the type A specimen (see Fig. C.9), the initial slopes of the curves in Fig. C.10a also vary with a factor two after normalization of the force. For the A specimen, the crack starts at the right edge of the specimen and then grows continuously to the left side. Hence, each subsequent beam element which is removed is a neighbour of the element which was removed previously. The curve which results from this analysis has a smooth descending branch, as can be seen in Fig. C.10a. In the fracture analysis of the type B specimen some irregularities occurred. Again, the crack propagates from the right to the left specimen side, but now a couple of beams at the right edge remain intact (Figs. C.10b, c and d). During three stages of the analysis "the crack jumps back and forth" between this small intact spot at the right specimen edge and the "crack tip". These stages have been marked in Fig. C.10a by (b), (c) and (d), and correspond with Figs. C.10b, c and d where the element is shown which is to be removed in the next step. In other words, removal of the marked elements causes the typical drops in the force-deformation curve of the B specimen.

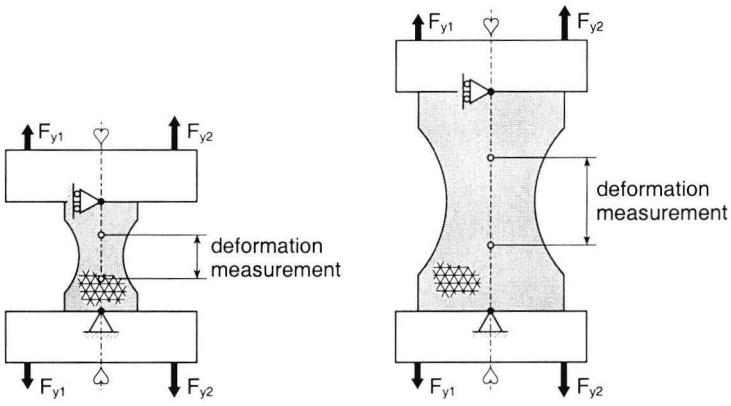


Figure C.9 *Loading and boundary conditions for lattice analyses on a specimen of type A (a) and type B (b).*

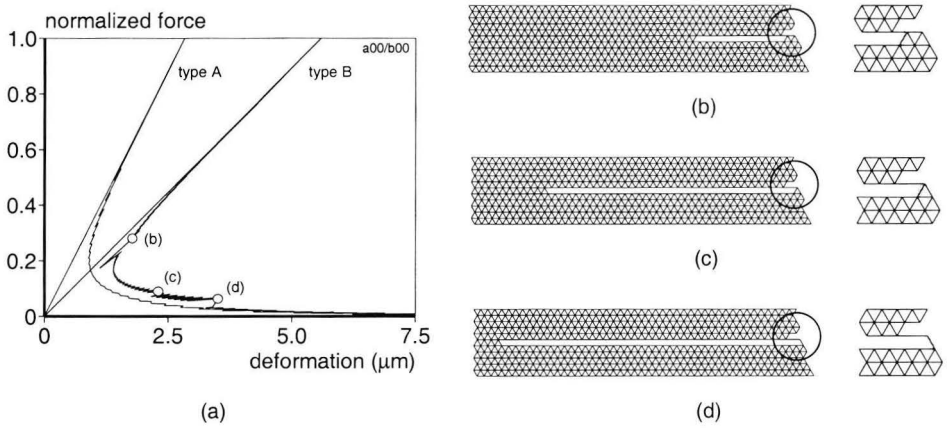


Figure C.10 *Normalized force vs. deformation curves of fracture analyses on a homogeneous* A *and* B *specimen (a). In figures (b), (c) and (d) the elements are marked which cause the irregularities in the analysis of the* B *specimen.*

The softening curves resulting from a lattice analysis which includes heterogeneity are much more irregular than the curves shown in Fig. C.10. Right after peak load for instance, sharp load-drops are observed. In Fig. C.11a four stages of such a load-drop are marked. The characters again correspond with the deformed meshes that include the lattice beams which will be removed next. What Fig. C.11 actually shows, is that crack growth starts at a (relatively) intact piece of material, e.g. an aggregate whose bond zone is still intact for the greater part. During the next steps of the analysis, bond beams fail which are situated close to each other. Hence, that specific spot in the material becomes weaker and due to stress

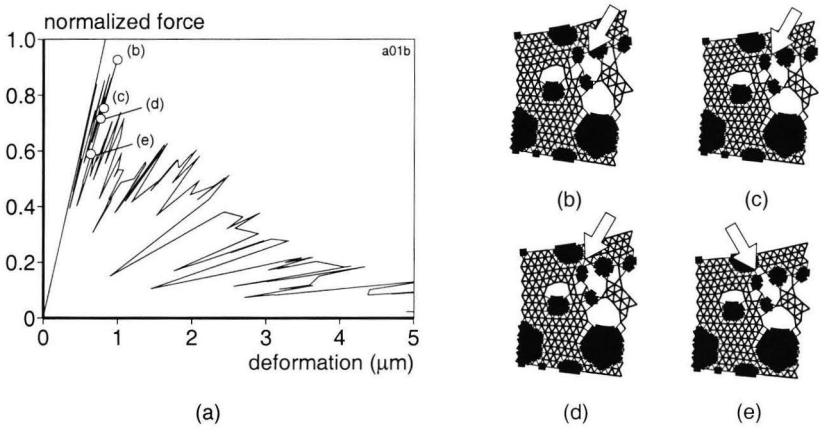


Figure C.11 *Failure right after peak load. The characters in the graph refer to the pictures which show the beams that will be removed at the indicated points.*

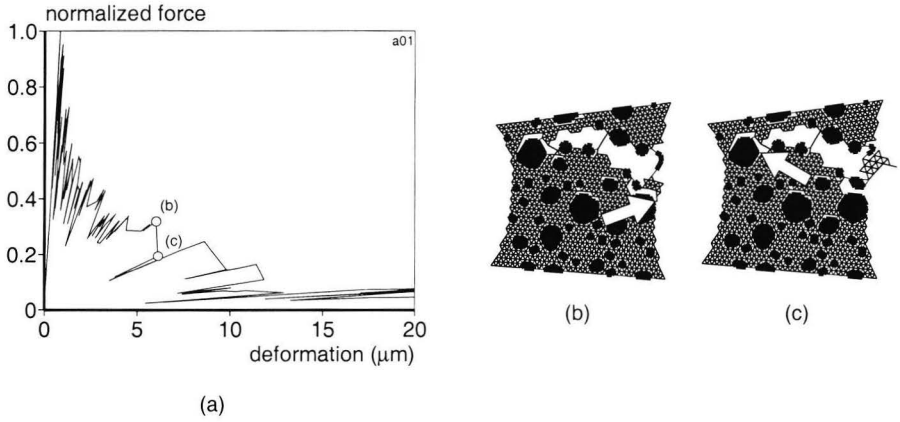


Figure C.12 *Partly failure of a bridge in the lattice mesh. The characters (b) and (c) in the graph refer to the crack stages shown in the accompanying pictures.*

concentrations at the crack tip, the external load which is needed to break the next lattice beam is lower. Although some beams are removed from the mesh the overall stiffness hardly changes, so that the computed deformations follow the external load on a one to one basis. When at some later instant cracking starts at another, intact, piece of the lattice the external load can and has to increase again. The process described before starts now all over again.

If we take a look at failure of the specimen in a more advanced stage of the computation, the observations are completely different. Bridges have developed between the crack faces, similar to observations in experiments, e.g. [86, 87]. These bridges can fail partly (Fig. C.12) or as a whole (Fig. C.13). In Fig. C.12 the case of a bridge which fails partly is

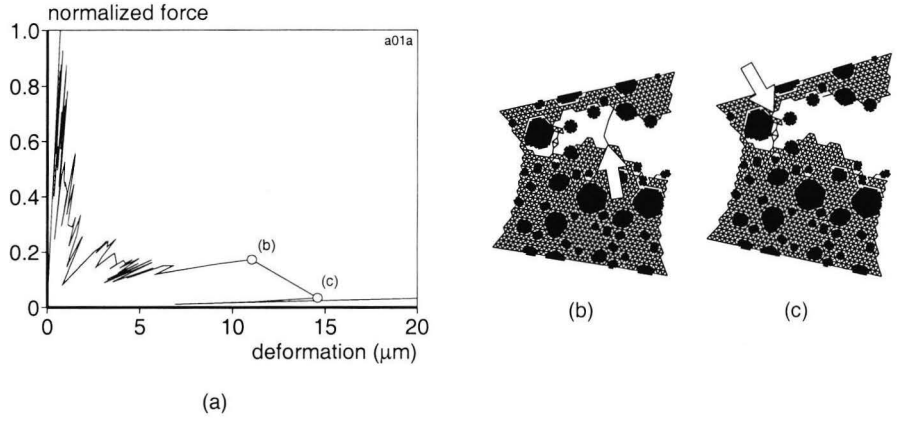


Figure C.13 *Complete failure of a bridge in the lattice mesh. The characters (b) and (c) in the graph refer to the crack stages shown in the accompanying pictures.*

considered. After failure of one of the beams the moment capacity of the bridge reduces. Consequently, the rotations of the specimen increase, which leads to a lower failure load for the next beam element which is removed. Despite the lower external load the deformations remain practically the same. This is due to other bridges inside the crack which are still intact, and thus prevent an increase of the deformations. When a bridge fails completely and no other bridges are present anymore (Fig. C.13), the failure load of the next beam decreases whereas the deformations increase strongly.

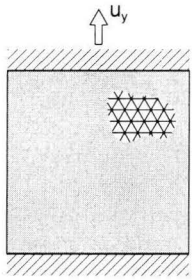
C.2.2 Effect of strength and stiffness variations of the lattice beams

When heterogeneity is introduced in a lattice, a transition takes place from regular crack growth by means of one straight crack, to irregular and distributed crack growth. Heterogeneity can be introduced by variations in the stiffness values which are assigned to the beams, variations in the beam strengths or a combination of both types of heterogeneity. Note that a distinct difference exists between the two ways of introducing heterogeneity, since variations of the beam strength do not influence the stress distribution within the lattice. Instead, the strength values come into play at the end of the linear elastic computation when the most critical beam element has to be selected.

In order to visualize the influence of strength and/or stiffness variations within a lattice mesh four analyses have been carried out. The lattice model which is used is shown in Fig. C.14 along with the input parameters. An aggregate structure ($2 \leq d \leq 8$ mm, $P_k = 0.75$) is projected on a regular lattice. Then material parameters are assigned to the lattice beams according to the four combinations which are shown in Fig. C.14. In Figs. C.15a, b and c the results are summarized and compared to the homogeneous case. The latter (gray shaded force-deformation curve in the graphs) is characterized by a maximum load which is already reached after the first beam element has been removed. Thereafter a straight crack develops through the mesh.

When the matrix beams are given a high stiffness while keeping the strength of all beams constant, the result of Fig. C.15a is obtained. Although small stress redistributions occur before peak load (13 aggregate beams have failed at peak load), the final crack is still straight. Note that due to the higher stiffness of the aggregates, which causes higher stresses, the crack runs through the aggregates. Varying the strength of the lattice beams instead of the stiffness has much more effect on the result (Fig. C.15b). At peak load 41 beams have been removed and the final crack pattern is not straight anymore but branches. The observation that strength variations have much more impact than variations of the elastic properties agree well with findings of Cox and Paterson [20, 21]. They arrived at the same conclusion for simulations on elastically brittle continuum elements with a stochastic distribution of the properties. Most stress redistributions and the highest ductility however, are found when strength as well as stiffness variations are applied. Peak load is only reached after failure of 131 lattice beams, and also the crack path is the most tortuous of the four, which is reflected in the force-deformation curve as well (Fig. C.15c).

In a majority of the simulations throughout this thesis the strength ratio between bond and matrix phase was taken $f_{t_B}/\ f_{t_M} = 0.30$ ($f_{t_B} = 1.50$ MPa and $f_{t_M} = 5.0$ MPa). Whether this specific ratio is best remains unclear though. Schlangen and Van Mier looked into the influence of the applied bond strength and found clear variations of the numerical result [73]. Together with $f_{t_M} = 5.0$ MPa the usually applied value for the bond strength became



	Units in MPa				
	E_A	E_B, E_M	f_{t_A}	f_{t_B}	f_{t_M}
hom	31255	31255	5.0	5.0	5.0
Evar	87514	31255	5.0	5.0	5.0
Ftvar	31255	31255	10.0	1.5	5.0
E+Ftvar	87514	31255	10.0	1.5	5.0

Figure C.14 *Model for studying the influence of strength and stiffness variations (see Table) of the lattice beams with geometry $l = 1.0$ mm, $h = 0.577$ mm.*

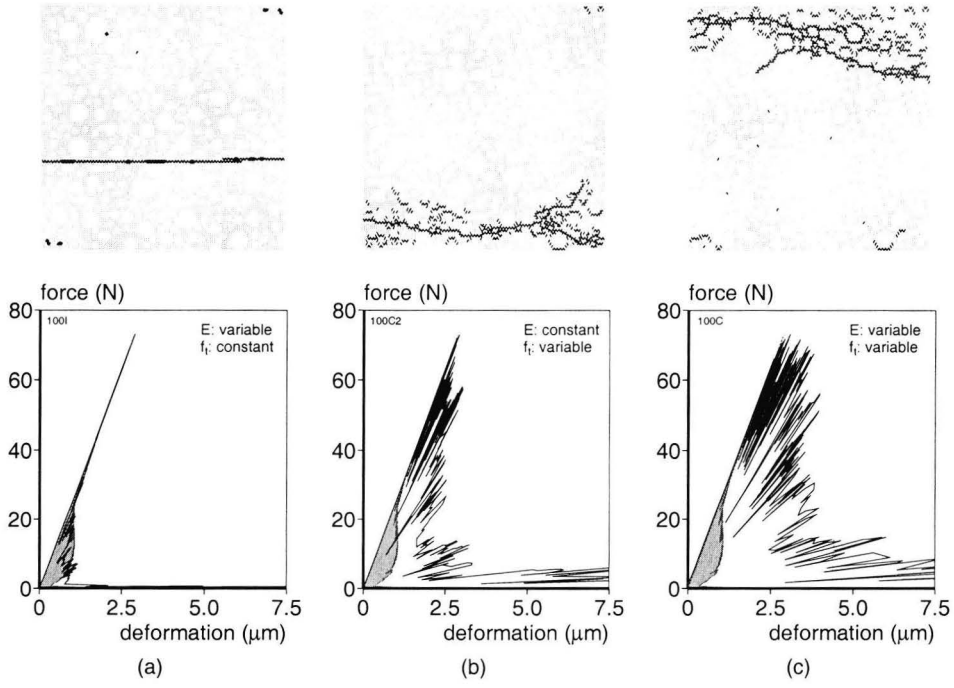


Figure C.15 *Influence of varying the Young modulus (a), the strength (b) and both Young modulus and strength (c). The crack patterns represent a deformation stage of 25 μm. The deformations of graph (a) and (c) have been multiplied with E^*/E^*_{hom} so that the initial slopes coincide with the slope for the homogeneous case, which is represented by the gray shaded area.*

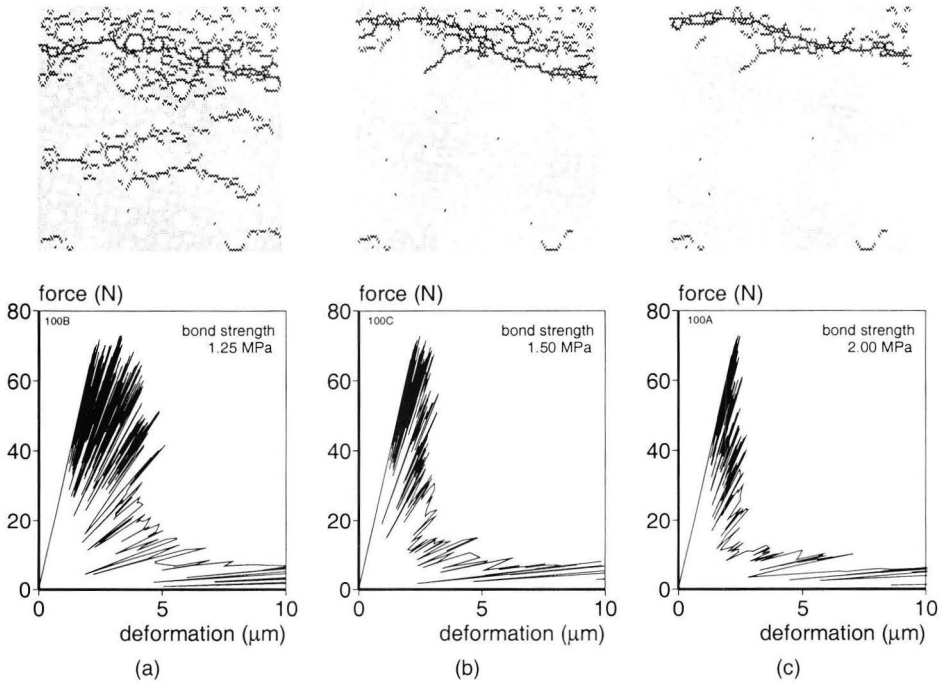


Figure C.16 *Effect of variation of the bond strength on the crack pattern and the force-deformation curve for the ratios $f_{t_B}/\ f_{t_M}$ = 0.25 (a), 0.3 (b) and 0.4 (c).*

f_{t_B}= 1.25 MPa [68]. Also Vervuurt studied the influence of variations of the bond strength [103]. He arrived at the conclusion that, in the case of granite or phosphorous aggregates, the upper bound for the bond strength equals half the matrix strength ($f_{t_B} < 0.5\ f_{t_M}$). In an experimental investigation by Hsu and Slate [45], it was found that the mortar-aggregate tensile bond strength varies from 33%-67% of the tensile strength of mortar, depending on the type of rock and the water-cement ratio. Still, no unique conclusion is available, also because the loading and boundary conditions as well as the specimen geometry play a role. Results that seem reasonable for certain cases may be questionable for others.

Fig. C.16 shows the results of three fracture analyses with the model of Fig. C.14. Apart from the bond strength, the values for the input parameters were the same as for case "E+Ftvar" in Fig. C.14. In the simulations the strength values f_{t_B}=1.25, 1.50 and 2.00 MPa ($f_{t_B}/\ f_{t_M}$= 0.25, 0.3 and 0.4 respectively) were applied. For f_{t_B}= 1.25 MPa excessive bond failure occurred, both before and after peak load. When the value for f_{t_B} was increased the result looked more reasonable, and especially more consistent within small variations of the bond strength. Thus, f_{t_B}= 1.50 MPa has been applied in most simulations, although experimental studies which include microscopy should give a final answer to the question which ratio $f_{t_B}/\ f_{t_M}$ has to be chosen.

C.2.3 Relation between beam length and minimum aggregate size

Where the previous section dealt with the influence of strength and stiffness variations of the lattice beams on the fracture behaviour, here the influence of the beam length will be discussed. For a lattice with particle overlay, a beam length l (or a cell size s) has to be chosen in combination with the minimum aggregate diameter $d_{\min}$ which is still incorporated in the aggregate structure. When restricting to a regular lattice for the sake of simplicity, the applied ratio $l/d_{\min}$ strongly influences the resulting fractions for the aggregate, bond and matrix phase respectively. To study this effect an aggregate structure ($2 \leq d \leq 8$ mm, $P_k = 0.75$) was projected on top of regular lattices of approximately 80×80 mm^2, and beam lengths varying from 0.25 mm to 4.5 mm. Depending on the beam length of the lattice the aggregates are schematized more, or less accurately, which is illustrated by Fig. C.17. The relation between the resulting phase fractions, i.e. the ratio of the number of beams representing a certain phase and the total number of beams, and the beam length is shown in Fig. C.18a. In case $l/d_{\min} \leq 0.5$ all particles will be discretized by at least three lattice beams. When this ratio is increased through an increase of the beam length, the number of aggregate beams will decrease whereas the number of bond beams strongly increases. This is a direct result from the method which is used to determine the phase to which lattice elements belong: elements intersecting an aggregate boundary are always assigned bond properties, independent of the fact whether any elements fall inside the aggregate or not. Hence, for $l/d_{\min} > 0.5$ clusters of 6 bond elements develop throughout the mesh. For $l/d_{\min} \ll 0.5$ the number of bond beams, and thus the dimension of the bond zone, decreases strongly. In addition, the aggregates become more isolated in the matrix and the number of interconnected bond zones decreases as well.

Despite clear differences in the schematization of the aggregate structure for different beam lengths, only small variations were found for both the effective Young modulus E^* and the ultimate load F_u. These latter properties are shown in Fig. C.18b for a beam length ranging from 0.75 mm to 2.5 mm. The fact that the ultimate load hardly depends on the beam length contradicts the findings of Schlangen [68], who concluded that the peak load strongly increased for $l/d_{\min} > 0.56$. This conclusion however, was based on simulations of notched specimens. Due to these notches, strong stress concentrations are introduced in a small area around the notch. When the beam length increases one beam element can ultimately even span the area with the higher stress, which results in a higher value of the failure load for this beam. This phenomenon therefore purely depends on the ratio between the beam length and

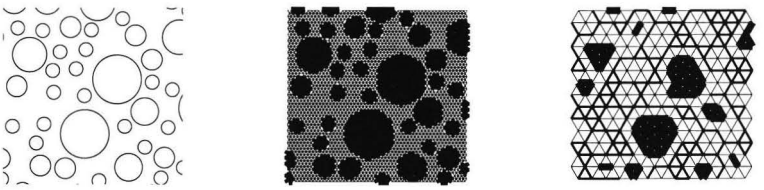


Figure C.17 *Original aggregate structure with $2 \leq d \leq 8$ mm (a) and projection on lattice with $l = 0.5$ mm (b) and $l = 2.0$ mm (c).*

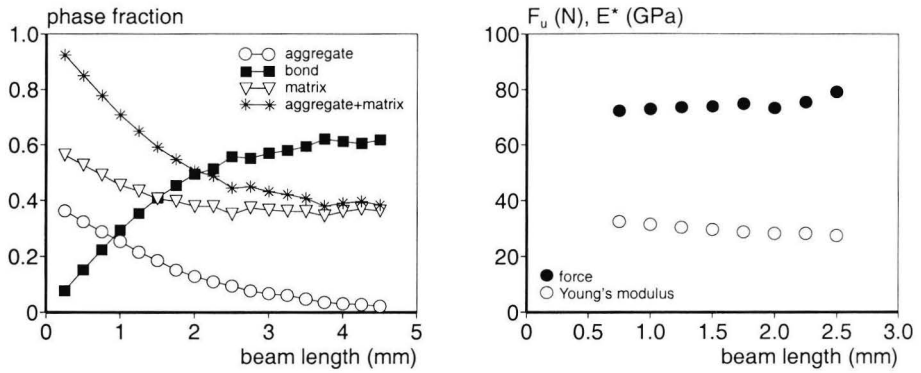


Figure C.18 *Dependence of the phase fractions (a) and the global stiffness and ultimate load (b) on the beam length. Aggregate overlay* $2 \leq d \leq 8$ *mm,* $P_k = 0.75$

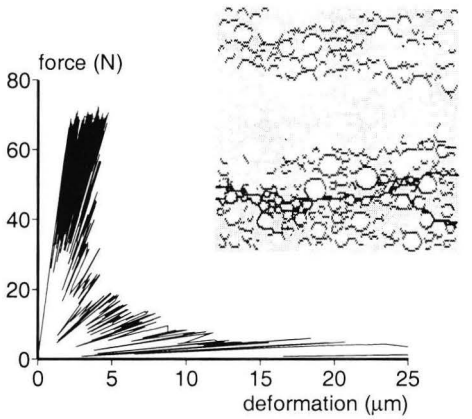
the notch size, and is not related to the minimum aggregate size.

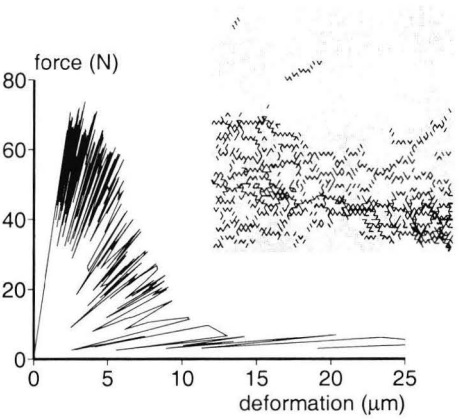
Although the ultimate load is rather insensitive for variations of the beam length, the fracture behaviour *is*. This is illustrated by Fig. C.19, showing the force-deformation curves as well as the fracture patterns at a deformation of 25 μm for lattice meshes with $l = 0.75$, 1.50 and 2.25 mm respectively. Some characteristic values of the computations are listed in the table which accompanies the figure. For $l = 0.75$ mm a large number of lattice beams fails before peak load, whereas for increasing beam length until 1.50 mm this number gradually decreases. Consequently, also the deformation at peak load (δ_u) decreases with increasing beam length. For beam lengths larger than 1.50 mm, a sharp transition is observed. Peak load is now reached after the failure of only a few lattice beams. Also with respect to the final crack pattern a transition takes place at the same beam length of 1.50 mm since little micro-cracking occurs anymore. Instead, localization takes place in an early stage of the computation leading to failure under the formation of discrete cracks (compare Figs. C.19a,b with c). The absence of micro-cracking and the formation of large bridges is also reflected by the maximum deformation (δ_{max}) which can be reached in a simulation. Note however that the maximum deformation is not a very consistent parameter (see the table in Fig. C.19), since it is very sensitive for the aggregate structure.

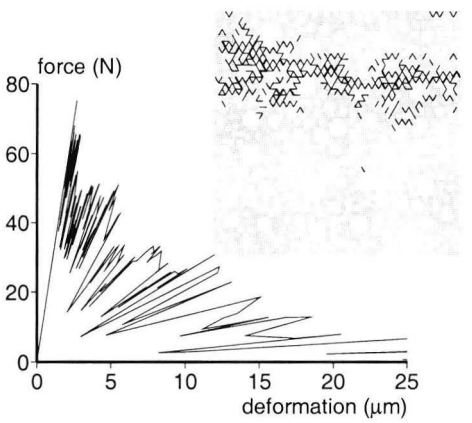
An explanation for the transition in fracture behaviour after a certain, critical beam length is exceeded, can be derived from Fig. C.18a. There it is found that for $l > 1.50$ mm the percentage of bond beams exceeds the percentage of matrix beams. The bond and the matrix thereby represent the two phases through which the cracks generally propagate, since with the present strength ratios failure of aggregate beams is hardly observed in any lattice analysis. Alternatively, also the percentage of weak beams with respect to the *total* amount of beams could be the main cause of the transition. If a certain, critical percentage of weak beams is exceeded, a chain of weak elements can be found in the mesh which causes immediate localization and thus a discrete crack. For a triangular lattice Stauffer [78] found this percolation threshold to be 35% for the case of intact and broken bonds, which resembles a two-phase material. This case was studied by Schlangen [71] as well, who performed

simulations on regular triangular lattices with different percentages of randomly distributed weak elements. Also he found more micro-cracks before localization in case of a low percentage of weak elements, and the formation of one localized crack for high percentages of weak elements. The reason for the percolation threshold being slightly higher than 35% in the present case, could be that apart from the three strength values also two different Young moduli were used in the simulations.

To conclude, no real optimum was found for the ratio between the beam length and the minimum aggregate diameter which should be applied. Depending on the ratio which is chosen, the aggregate structure will be modelled more or less accurately. For a regular lattice with $l \leq 0.5d$ each aggregate particle is modelled by at least three aggregate beams.







Lattice	scan	F_u [N]	δ_u [μm]	scan	δ_{max} [μm]
l=0.75	1897	72.2	4.1	2938	316.5
l=1.50	266	73.8	3.5	1083	997.7
l=2.25	2	75.4	2.7	398	124.6

Figure C.19 *Force-deformation curves and final crack patterns for lattices with beam lengths 0.75, 1.50 and 2.25 mm.* $f_{t_B}/\ f_{t_M}$ *= 1.25/5.00,* $2 \leq d \leq 8$ *mm and* $P_k = 0.75$

The phase fractions, and in particular the magnitude of the bond fraction, will eventually determine the outcome of the simulation.

C.2.4 Influence of the aggregate structure on the fracture behaviour

In the foregoing section the relation between beam length and aggregate size was studied, which eventually turned into a relation between the numerical result and the amount of weak lattice beams in the mesh. Although the amount of weak elements could be related to the composition of the aggregate structure, it also resulted from a schematization of the same aggregate structure by lattices with increasing beam length. To answer the question whether the (composition of) the aggregate structure influences the numerical result, it would be more natural to vary only the composition of the aggregate structure whereas the lattice mesh remains the same. The aggregate structures which are shown in this section are the same as were used for the elastic analyses described in Section C.1 (see Table C.1 for the beam properties). The phase fractions of these CASE I and CASE II meshes are shown in Fig. C.20a and b respectively.

First, the fracture behaviour for lattices with different aggregate content is considered. For this comparison lattices with aggregate structures of P_k = 0.20, 0.50 and 0.80 (CASE I) were loaded according to Fig. C.14. Note that contrary to the lattices with varying beam length (Fig. C.18a), here both the bond *and* the aggregate fraction increase with increasing P_k value (Fig. C.20a). The results of the three simulations, which are shown in Fig. C.21, show an interesting difference in fracture behaviour. Again, a transition takes place from localization through distributed micro-cracking for a low P_k value to immediate localization without micro-cracking for high P_k values. In addition, the behaviour around peak load is completely different. For P_k = 0.20 the force builds up due to micro-cracking in isolated bond systems, where crack propagation is prevented by the stronger matrix. Compared to the other two simulations, crack localization and propagation through the matrix takes only

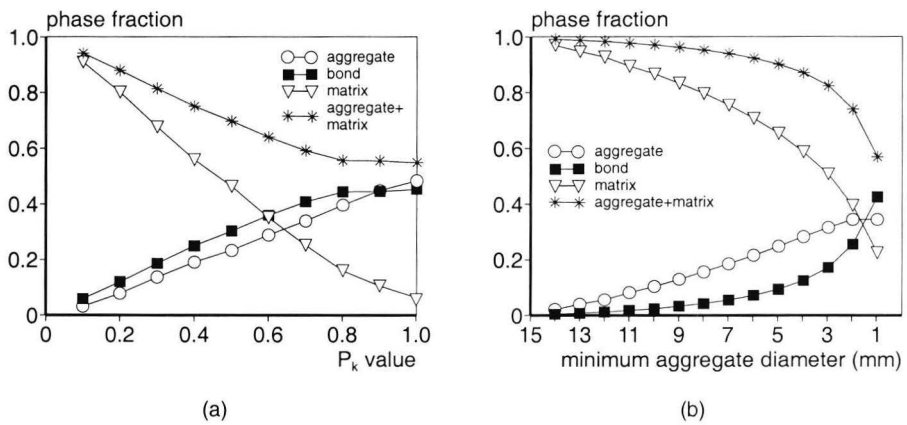


Figure C.20 *Phase fractions for the* CASE I *aggregate structures with different P_k values (a), and the* CASE II *aggregate structures in which d_{min} was varied (b).*

place at a much higher value for the ultimate load. In the case of $P_k = 0.50$ excessive failure of beams at ultimate load takes place, whereas for $P_k = 0.80$ a sharp peak is obtained which indicates that the percolation threshold of the lattice has been exceeded.

Fig. C.21 also shows the deformed meshes at a post-peak load level of approximately 25% of the ultimate load. Again, the differences in fracture behaviour are evident. In the mesh with $P_k = 0.20$ the fraction of (homogeneous) matrix beams is very large. Consequently, a rather smooth crack without many branches or bridges propagates through the matrix ignoring the previously formed micro-cracks. For $P_k = 0.50$ on the other hand, the

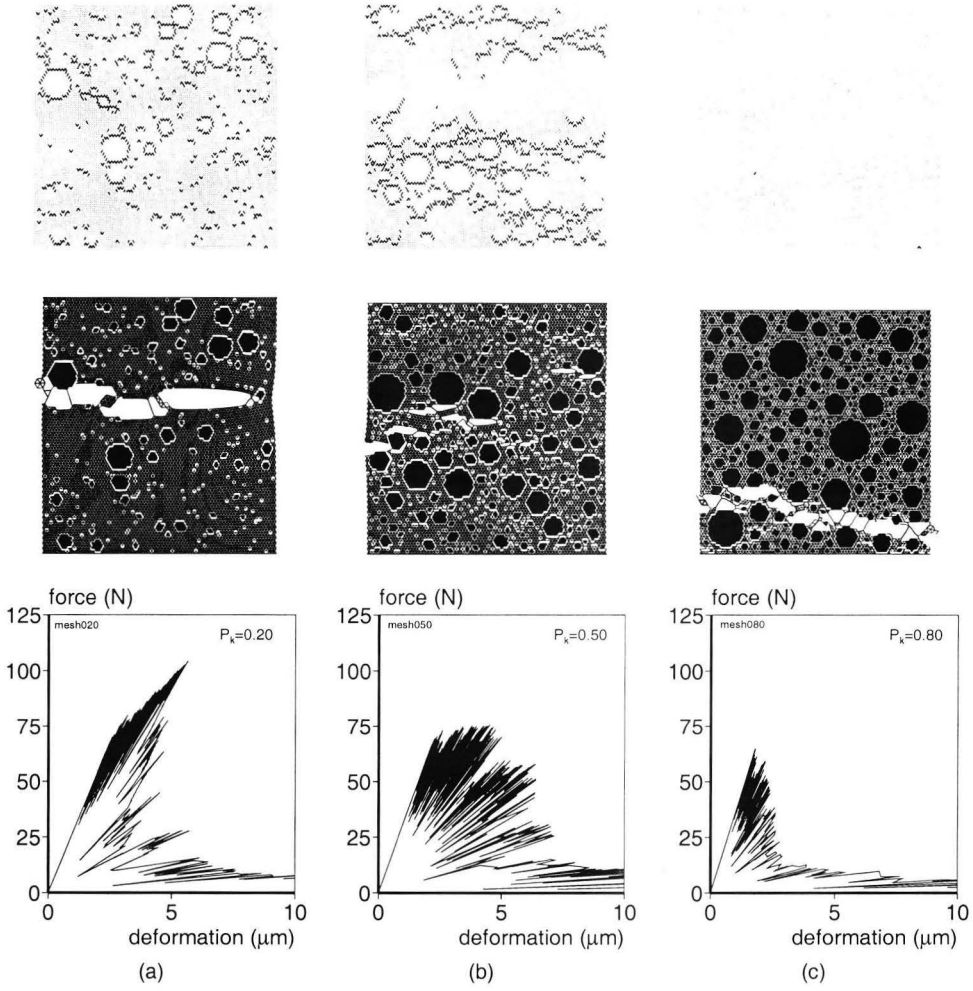


Figure C.21 *Effect of varying aggregate content on the fracture behaviour. The upper figures show the beams which have failed at peak load whereas the lower figures show the deformed mesh at a post-peak load level of $0.25F_u$ (a), $0.24F_u$ (b) and $0.19F_u$ (c) respectively, after [93].*

effect of the micro-cracking at ultimate load is still visible in the sense that the specimen deformation is distributed over more, smaller cracks. One localized crack is again found for P_k=0.80, which is curved and contains a large amount of bridges due to the extreme heterogeneity of the specimen.

The simulations for P_k = 0.20, 0.50 and 0.80, similar to the results of the previous section, showed that the magnitude of the *weak* fraction governs the computational result.

A second check concerns the influence of the shape of the aggregate structure on the fracture behaviour. For this purpose, a comparison was made between simulations for an aggregate structure with P_k = 0.10 (CASE I) and $7 \leq d \leq 16$ mm (CASE II) respectively. The two structures have a different aggregate fraction ($P_{k,\text{lat}}$ = 0.03 and 0.19 respectively), whereas the bond fractions are equal (6%). Comparison of Fig. C.22a and b learns that despite the

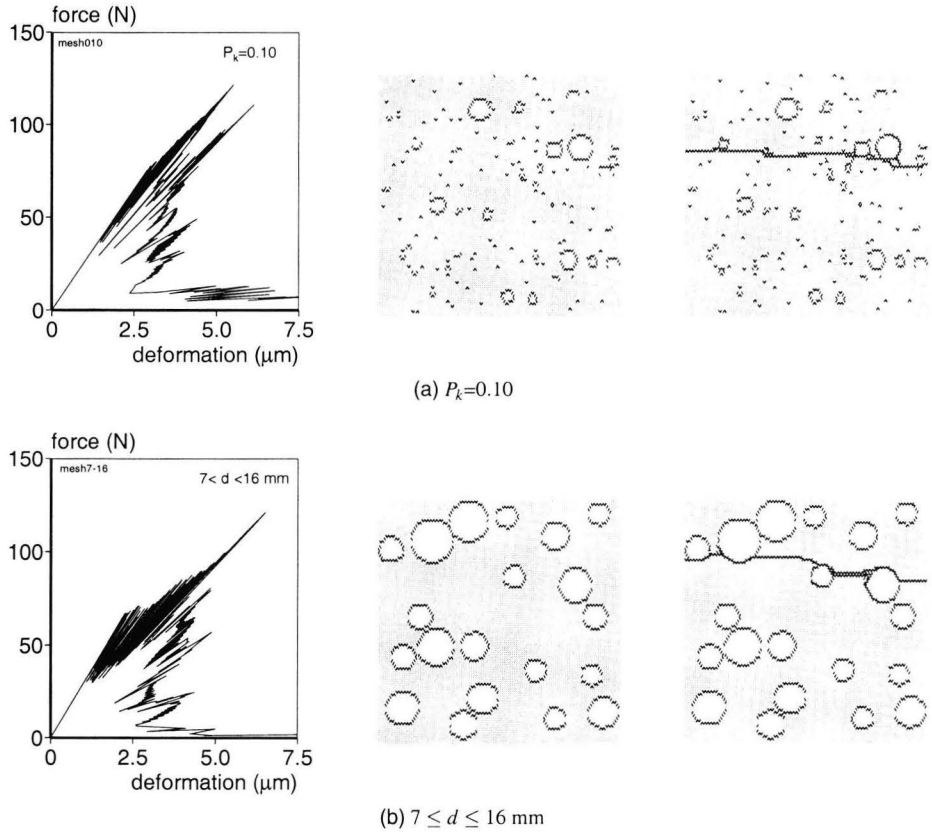


Figure C.22 *Effect of varying shape of the aggregate structure on the fracture behaviour. In (a) the results for an aggregate structure with P_k=0.10 (CASE I, Section C.1) are shown whereas (b) contains the result for an aggregate structure with $7 \leq d \leq 16$ mm (CASE II Section C.1). The crack patterns reflect the situation at ultimate load and the final crack pattern respectively.*

completely different composition of the two aggregate structures, the computational result is comparable in terms of pre-peak micro-cracking in isolated bond systems, as well as the same discrete final crack. Furthermore, before peak load is reached both simulations show the same typical increase of the external load. This shows once more that the percentage of weak elements in the model governs the result of a lattice simulation.

The knowledge which was gained on the effect of the amount of weak elements with respect to the computational result, can be used to generate specific material behaviour. This

Table C.4 *Re-assignment of bond properties to aggregate beams in order to obtain an equal bond fraction for lattices with l=1.0 mm and l=2.0 mm.*

	Fractions		
Lattice	aggregate	bond	matrix
l=1.0 mm	0.253	0.293	0.433
l=2.0 mm	0.128	0.494	0.378
l=1.0 mm*	0.253	0.494	0.253

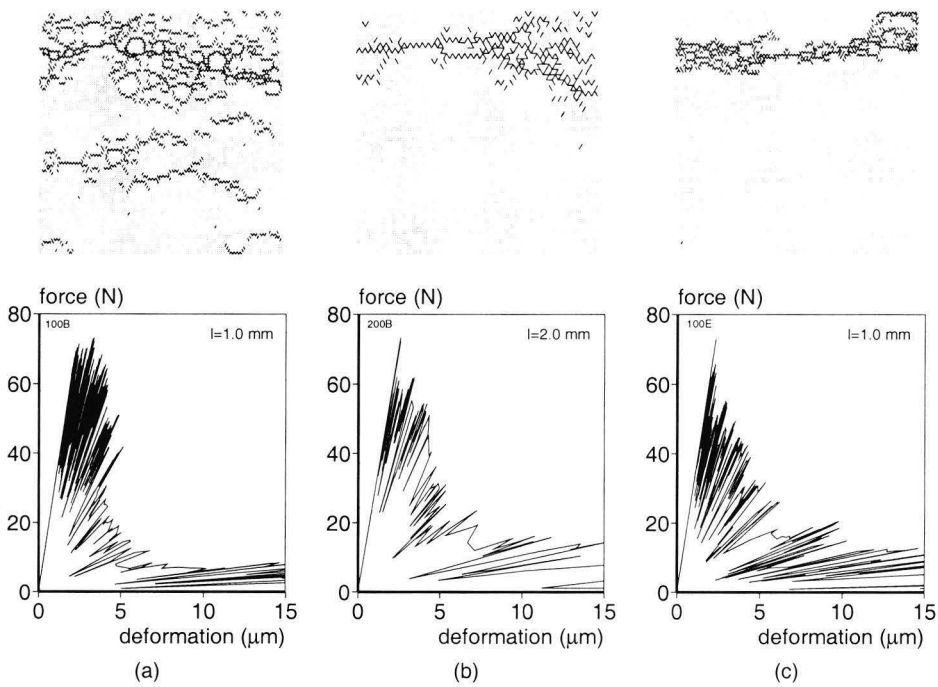


Figure C.23 *Force-deformation behaviour and crack pattern at a deformation of 25 μm for a lattice with l=1.0 mm (a), a lattice with l=2.0 mm (b) and again the lattice with l=1.0 mm in which the bond fraction has been increased so that it equals the bond fraction of the lattice with l=2.0 mm (c).*

is illustrated by the following example. Two lattices are taken like the ones which were discussed in the previous section, both with the same aggregate structure ($2 \leq d \leq 8$ mm and $P_k = 0.75$) and a strength ratio of $f_{t_B}/\ f_{t_M}$= 1.25/5.00. The first lattice has a beam length $l = 1.0$ mm whereas the second lattice has a beam length $l = 2.0$ mm. Figs. C.23a and b show the distinct difference in the force-deformation curve as well as the crack pattern at a deformation of 25 μm . It became evident that despite the differences in beam length and schematization of the aggregate structure, the result varies due to the different fractions of bond beams in each mesh. In Table C.4 the phase fractions are listed for both lattice meshes. Suppose that the fraction of bond beams in the lattice with $l = 1.0$ mm would be made equal to the fraction of bond beams in the lattice with $l = 2.0$ mm. Then the fracture behaviour in terms of crack pattern and force-deformation curve should become comparable as well. By randomly re-assigning a number of aggregate beams bond properties this situation has been created (lattice l=1.0 mm*, see Table C.4) and the convincing numerical result is shown in Fig. C.23c.

It could be interesting to investigate whether this dependence of the fracture behaviour on the fraction of weak elements in the lattice has a more general meaning. Suppose that this behaviour is similar to the behaviour of actual composite materials, then it would mean that in a rather easy way a material could be composed with fracture characteristics as desired. Using simple simulations as shown here, the behaviour of the composite could be tuned, and verified by laboratory experiments on the actual material.

C.3 Improving the computational efficiency

C.3.1 Problem description

For the intended size effect simulations, the mesh size would increase considerably for increasing specimen size because of the constant (average) beam length. In order to be able to simulate as many specimen sizes as possible the mesh sizes had to be reduced. A possible way to achieve this reduction is to model only the area where cracks (or damage in general) are expected with a fine mesh. For the remaining part of the structure a more coarse mesh can then be used. This approach is especially suited for continuum models, although it has been followed for some lattice simulations as well [104]. A consequence of the very coarse lattice beams in the outer specimen parts, however, is that the shape of the specimen can change considerably. This method of element reduction seems therefore less favorable. Alternative techniques comprise e.g. remeshing [104], or an interesting adaptive technique based on a combination of boundary elements and fuzzy logic, that was developed by Bolander [13]. These latter techniques have in common that they are best suited for localized fracture problems, and preferably for notched specimens in order to get a maximum profit.

A very simple, and therefore frequently used method to reduce the size of a lattice mesh, is to model only the preferential crack area with beam elements. Continuum elements are used to represent the remainder of the specimen, see e.g. [103] or [102] for an overview. For the dog-bone shaped specimens this means that only the middle part of the specimens is modelled with a lattice. The condition for this replacement of lattice beams by continuum elements, is that the result in terms of the ultimate load, the force-deformation curve and the crack pattern should remain unaffected. Furthermore, this condition applies both for a

random mesh and a regular mesh with particle overlay. For the latter case, it is mentioned that by replacing a part of the fine lattice micro-crack processes in those specimen parts are neglected (see [2]).

C.3.2 Modelling details

The problem which arises when a part of a lattice is replaced by continuum elements, is to make a smooth transition from the continuum mesh to the lattice mesh. Especially in case of a random lattice the way in which this connection should be made is not straightforward. In order to check whether a full lattice mesh and a combination of a lattice and a continuum mesh give identical results, a number of calculations has been carried out on the mesh of a type D specimen. One set of nodes was randomly generated for a rectangular area, according to the procedure described in Section 6.1.2. This nodal set was then used to construct the lattice meshes shown in Fig. C.24. The first mesh shown in Fig. C.24a (RAL5) consists purely of lattice elements and was used for reference. In the remaining three meshes a combination of lattice and continuum elements was used (Figs. C.24b,c and d) which were connected using to two different methods. In the first method (Fig. C.25a), which has originally been used [68], the coordinates of all nodes of the sub-lattice are identical compared to the large, original set of nodes. At the boundary of the random lattice continuum elements are placed, with a width and a height equal to the cell size s. By "tying" the nodes of the lattice boundary to the nodes of the continuum, i.e. specifying linear dependencies between degrees of freedom of the subsequent nodes, the two meshes are connected to each other (Fig. C.24b).

The second method is different in the sense that the positions of the lattice boundary nodes are slightly changed. Afterwards they match the center of the cells of the regular square grid which was used during generation (Fig. C.25b). This results in a straight boundary of the lattice mesh (Fig. C.24c) and nodal coordinates which are not identical anymore to the original set of nodes. As a consequence, the connectivities of the beam elements up to a distance of $3s$ from the lattice boundary can be different from the original mesh. This is due to the fact that the connectivities have to be generated again after re-positioning the boundary nodes, which can result in different connectivities in the boundary zone. Also in the second method the degrees of freedom of the lattice nodes are tied to the nodes of the continuum mesh.

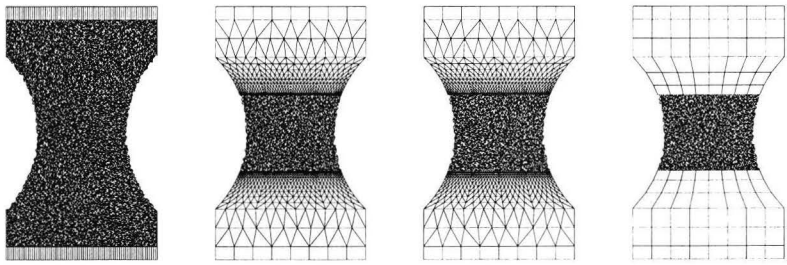


Figure C.24 Full lattice mesh (a) and combined lattice-continuum meshes (b,c and d).

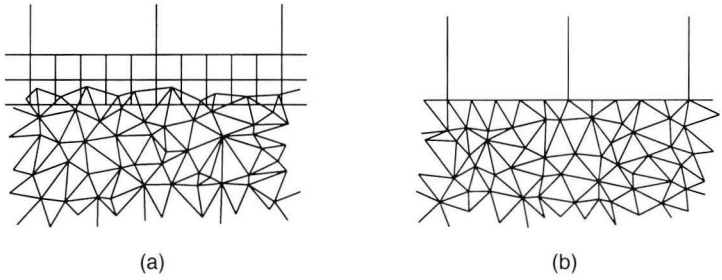
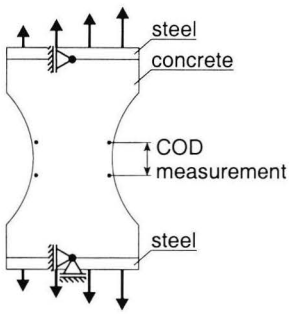


Figure C.25 *Connection of random lattice with original boundary nodes (a) and adjusted boundary nodes (b) to continuum mesh (after [103]).*

In the continuum parts of RALC2 and RALC1 (Figs. C.24b and c) three-noded plane stress elements with two translational degrees of freedom per node were applied. The continuum mesh of RALC8 on the other hand, was constructed from quadrilateral four-noded plane stress elements with two degrees of freedom per node. For the lattice nodes at the boundary of the mesh only the translational degrees of freedom of the lattice elements are tied, not the rotational degrees of freedom. It appeared that in case of uniaxial loading conditions the results remains the same whether the rotational degrees of freedom are tied or not. Whether this applies for other loading conditions as well has to be verified however. With respect to the method of tying, it is mentioned that in this thesis always linear tyings have been applied. Alternatively quadratic tyings could be used, which have not been considered here. Analogous to the degrees of freedom, it could be so that quadratic tyings *do* give a better result for more complicated loading conditions and/or other stress states than uniaxial tension.

Fig. C.26 shows the supports and the loading scheme which were applied in the calculations. The geometrical properties are summarized in the accompanying table (Fig. C.26) whereas Table C.5 lists the material properties. From Table C.5 again follows that it is crucial to assign the value of the global stiffness of the lattice mesh also to the continuum elements. When a different value is assigned, the stiffness difference will lead to stress concentrations at the boundary of the lattice mesh, and thus to crack growth towards this boundary.



		Measures in mm			
		s	A	h	t
Lattice		5.0	5.0	3.073	1.0
Continuum	concrete	-	-	-	1.0
	steel	-	-	-	1.0×10^5

Figure C.26 *Boundary conditions and geometrical properties for the simulations.*

Table C.5 Assigned material properties.

			Units in MPa	
		ν	E	f_t
Lattice*		-	30000	1.0
Continuum	concrete	0.2	23723	-
	steel	0.3	210000	-

* global lattice properties: E^*=23723 MPa, ν^*=0.2 determined according to Fig. 6.6

C.3.3 Results

The first results concern a comparison between the full lattice mesh of Fig. C.24a and the combined lattice-continuum mesh with the "original" way of tying (Fig. C.24b). The results are given in Figs. C.27a,b and Fig. C.28a, where the force-deformation curves in the latter figure are the "smoothened" versions of the original curves (see [68, 103] for more details), to enable a better comparison. Figure C.27 shows the first 175 beam elements that have been removed during the simulation. When comparing the crack patterns of Figs. C.27a and b, a distinct difference is found. This difference is also reflected by the computed force-COD curves shown in Fig. C.28a. Since at a certain moment the crack branches and continues to grow outside the zone where the deformations were measured, the force-COD curve for simulations RALC2 stops at a COD of 70 μm .

The differences that are found between simulation RAL5 and RALC2 are not surprising. At the boundary between continuum and lattice, the thickness of the mesh doubles since two meshes overlap. This results in a change of the local deformations at the boundary, and thus a situation comparable to the situation with stiffness differences between lattice and continuum which was mentioned before. Obviously, mesh overlaps should be refrained from so that another connectivity method has to be used. This leads to the mesh in Fig. C.24c, with a boundary like is shown in Fig. C.25b. The performance of this mesh has been compared to the reference mesh in Figs. C.27a, c and Fig. C.28b. It appears that the crack patterns are absolutely identical. Also the force-COD curves of simulations RALC1 and RAL5 are

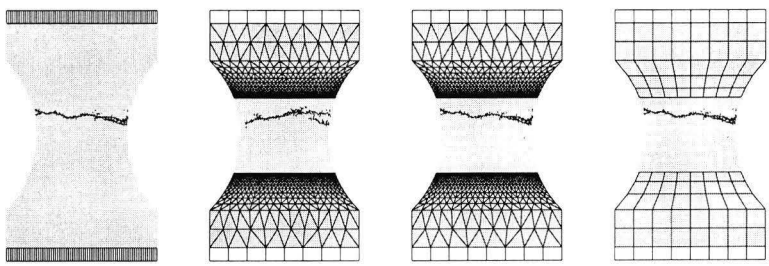


Figure C.27 Crack patterns after removal of 175 beams.

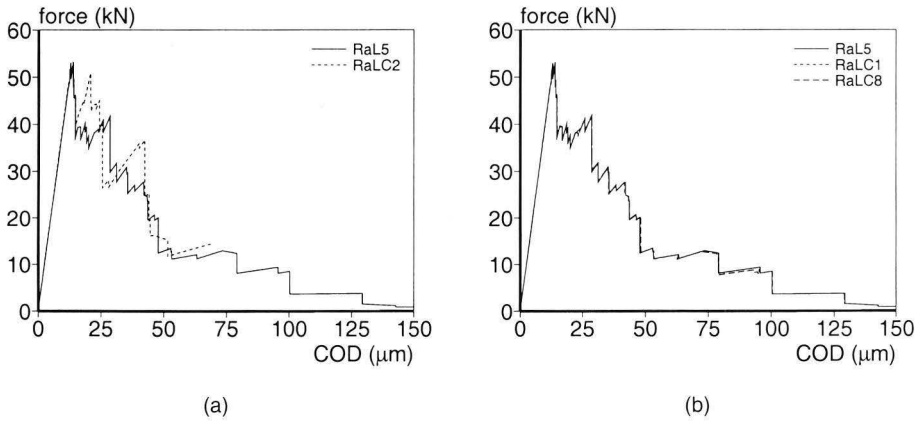


Figure C.28 *Comparison of computed force-*COD *curves of* RAL5 *and* RALC2 *(a) and* RAL5, RALC1 *and* RALC8 *(b).*

practically on top of each other. The only difference which is found in simulation RALC1, consists of the removal of 3 subsequent beams in a different sequence.

In the lattice mesh of simulation RALC1 the triangles at the boundary were open, i.e. the horizontal lattice beams in the boundary were omitted. Additional simulations showed that if this is not the case, again a situation comparable to simulation RALC2 is created.

The next question that arose was if equally good results could be obtained with a more coarse mesh of continuum elements. First, a coarse mesh of the same triangular elements was tried but the performance was rather poor. Despite the fact that a good agreement was found immediately after peak, the crack path diverged and the second part of the softening curve became completely different. Obviously the triangular elements perform well when they are of the same order of magnitude as the lattice, but when their dimensions are taken too big the displacement field at the boundary between lattice and continuum mesh is not accurate enough anymore. When quadrilateral 4-noded plane stress elements with two translational degrees of freedom per node were taken instead (Fig. C.24d), the performance improved considerably. At the boundary, the length of the continuum elements was approximately $6s$. The final crack path as shown in Fig. C.27d is again identical to that of the reference mesh

Table C.6 *Ultimate loads and CPU time needed for mesh* RALC1 *and* RALC8 *with respect to the reference mesh* RAL5.

	number of lattice elements	number of continuum elements	$F_u/F_{u,\text{RaL5}}$	$\text{CPU}/\text{CPU}_{\text{RaL5}}$
RAL5	23421	-	1.0000	1.000
RALC1	5883	1468 (3-noded)	1.0044	0.253
RALC8	5883	80 (4-noded)	1.0013	0.219

(Fig. C.27a). Only the order of removal was different for 13 elements out of 175. Finally, also the force-COD curve of simulation RALC8 is found to resemble the result of RAL5 well (Fig. C.28b).

The last check concerns the comparison of the computed ultimate loads. In Table C.6 the ultimate loads of RALC1 and RALC8 are shown relative to the ultimate load of the reference mesh RAL5. The performance of both meshes is thereby quite satisfactorily. With respect to the CPU time which is needed Table C.6 shows that for RALC1 a reduction of 75% is found with respect to the reference mesh. For a smaller number of continuum elements (RALC8), the CPU time reduces with an additional 3%. After these results had been obtained a simulation was made for a type B specimen, fully modelled with a regular lattice with particle overlay, as well as with a combined lattice-continuum mesh. Also this comparison gave an equally good result as for the random lattice.

The foregoing shows that the number of beam elements needed in a lattice calculation can be effectively reduced by replacing part of the lattice mesh by continuum elements. The zone of lattice elements should not be taken too narrow however, because this will influence the crack path. Whether the lattice mesh is large enough can be easily checked, since in those simulations where the area is selected too small, the crack will grow consistently towards the boundary of the lattice.

Summary

The material parameters of quasi-brittle materials like concrete and rock exhibit size effect. Due to this size effect, a considerable difference can occur between the values of material parameters which were obtained in the laboratory, and the actual values for real size structures. To take this difference correctly into account and to translate experimental results to field situations, a thorough knowledge of the nature of size effect is needed.

In a combined experimental and numerical approach, size effect of concrete and sandstone was studied under uniaxial tensile loading conditions. Due to the (supposedly) uniform stress field which is present in this type of loading, the influence of structural effects should be minimized, thus giving way to study the material size effect. In the course of the research however, it appeared that the stress field in the specimens was far from uniform. To investigate the influence of this non-uniformity on size effect, emphasis was put on a detailed analysis of the experimental results in order to get more insight into the contribution of material and structural effects to the observed size effect.

Uniaxial tensile size effect experiments have been conducted under freely rotating boundary conditions, on dog-bone shaped specimens of six different sizes. The thickness of the specimens was kept constant whereas the remaining dimensions doubled for each subsequent specimen size. Thus, a maximum size range of 1:32 was obtained, which for concrete is the largest range of sizes which has been tested in uniaxial tension to date. The specimens of these main size effect tests were made of concrete as well as red Felser sandstone. In principle, all concrete specimens were cured under laboratory conditions (20 °C , 60% R.H.). An additional series of size effect tests however, was carried out on concrete specimens cured in the climate room (20 °C , 95% R.H). This series comprised specimens in a size range of 1:8. Finally, a series of impregnation experiments has been carried out on specimens of three different sizes.

In order to conduct stable uniaxial tension tests on all specimens a new control system was developed. In this system the largest deformation measured by a number of LVDTs (each with a constant measuring length), is used as the feed-back signal (Chapter 3). Hence, besides the size effect on strength, the size effect on fracture energy could also be measured; the results of both are discussed in Chapter 5. In addition to the size effect experiments three series of verification tests were carried out. These tests focused on the rotational capacity of the hinge constructions, and on the influence of casting effects as well as possible effects of the loading frame on the outcome of a uniaxial tension test (Chapter 4).

Simulations with a lattice model were carried out to get more insight into observations which

were made in the experiments (Chapter 6). Furthermore, several additions were made to allow for accurate representation of material aspects by the lattice model (Appendix C). The size effect experiments were modelled with regular and random triangular lattices, both with and without an aggregate structure incorporated in the mesh. By applying the same aggregate structure and lattice dimensions for all specimen sizes, the influence of variations in material structure was excluded from the size effect which resulted from the simulations. The simulations clearly showed the influence of stress redistributions, as well as the eccentricity of the external load, on size effect.

Experimental as well as numerical results are combined in Chapter 7. Despite the fact that the size effect which had been found for the concrete specimens cured under laboratory conditions followed statistical strength theory exactly, the opposite was true for the specimens cured in the climate room. This observation led to the conclusion that the size effect which followed from the present experiments, did not consist of material or statistical size effect only.

To account for additional, structural, size effects a simple analytical model was derived. By means of this model the effect of the shape of the specimen, eccentricity of the external load and material inhomogeneity could be explicitly taken into account. As a result it was found that for the current tests three main causes were present for the size effect on the nominal strength. These are first of all the (meso-)structure of the material in combination with wall effect for small specimen sizes, and material size effect according to classical strength theory for specimens larger than the representative volume. The latter type of size effect however, can be overruled by structural size effects due to the presence of stress and/or strain gradients in the cross section of the specimen. For this reason these stress and/or strain gradients can not be excluded from any analysis of experimental size effect data.

From experiments as well as numerical simulations followed that the ratio between specimen dimension and material structure is bound by a minimum value. If the dimensions of the specimens are chosen too small, a large scatter will occur in the results. Hence, this observation implies that discussions about a strength asymptote for very small specimen sizes are not of any practical interest.

Samenvatting

De materiaalparameters van quasibrosse materialen zoals beton en gesteente zijn schaalafhankelijk. Als gevolg van deze schaalafhankelijkheid, kunnen de waarden van materiaalparameters die volgen uit laboratoriumproeven aanzienlijk verschillen van de waarden die gelden voor constructies op ware grootte. Een gedegen kennis van het schaaleffect is daarom noodzakelijk om dit verschil op de juiste manier in rekening te kunnen brengen, bij de vertaling van laboratoriumwaarden naar waarden die in praktijksituaties toepasbaar zijn.

Schaaleffect van beton en zandsteen onder éénassige trek is bestudeerd in een gecombineerd experimenteel en numeriek onderzoek. De spanningstoestand die het gevolg is van deze éénassige trekbelasting wordt in het algemeen gelijkmatig verdeeld verondersteld. Dit houdt in dat constructie-invloeden minimaal worden geacht, waardoor optimale mogelijkheden bestaan om zuivere materiaalinvloeden op schaaleffect te onderzoeken. Tijdens het onderzoek bleek echter dat de spanningstoestand in de laboratoriumproefstukken verre van gelijkmatig was. Om de invloed van deze spanningsvariaties in de proefstukdoorsnede op schaaleffect te onderzoeken, alsmede om meer inzicht te verkrijgen in de bijdrage van materiaal- en constructie-invloeden op het waargenomen schaaleffect, is een gedetailleerde analyse uitgevoerd van de experimentele resultaten.

De uitgevoerde experimenten bestonden uit éénassige trekproeven op "hondebot"vormige proefstukken van zes verschillende afmetingen, onder toepassing van vrij roterende randvoorwaarden. De dikte van de proefstukken was constant voor alle proefstukafmetingen, terwijl de resterende afmetingen verdubbelden voor elk opeenvolgend proefstuk. De verhouding tussen het kleinste en het grootste proefstuk was 1:32, wat voor beton tevens het grootste afmetingsverschil is dat tot op heden in een laboratorium onder éénassige trekcondities is beproefd. Zowel beton als rode Felser zandsteen zijn onderzocht. De standaard verhar-dingscondities voor de betonnen proefstukken waren laboratoriumcondities (20 °C , 60% R.V.). Daarnaast zijn ook schaaleffectexperimenten uitgevoerd op betonnen proefstukken, die zijn uitgehard in de verhardingskamer onder constante omgevingscondities (20 °C , 95% R.V). Het totale afmetingsverschil in deze laatste serie bedroeg 1:8. Tenslotte is een serie impregnatie-experimenten uitgevoerd op betonnen proefstukken van drie verschillende afmetingen.

Om het mogelijk te maken stabiele éénassige trekproeven uit te voeren op alle proefstukken is een nieuw stuursysteem ontwikkeld. De werking van dit systeem is gebaseerd op een stuursignaal, dat bestaat uit de grootste verplaatsing die gemeten wordt door één van meerdere verplaatsingsopnemers (LVDTs), elk met dezelfde meetlengte (zie Hoofdstuk 3). Aan de hand van de op die manier verkregen proefresultaten kon naast het schaaleffect van de

sterkte, ook het schaaleffect van de breukenergie bepaald worden. Beide resultaten worden behandeld in Hoofdstuk 5. Naast de schaaleffectexperimenten zijn ook drie series verificatie-experimenten uitgevoerd. In deze experimenten zijn de rotatiecapaciteit van de scharnieren, stortinvloeden en mogelijke effecten van het belastingsframe op het resultaat van een éénassige trekproef nader onderzocht (Hoofdstuk 4).

Om meer inzicht te verkrijgen in fenomenen die waargenomen werden tijdens de experimenten zijn simulaties uitgevoerd met een lattice model (Hoofdstuk 6). Naast deze schaaleffectsimulaties, zijn simulaties uitgevoerd die tot doel hadden de werking van het model verder te onderzoeken en de representatie van het materiaalgedrag van beton verder te verbeteren (zie Appendix C). De schaaleffectexperimenten zijn gemodelleerd met regelmatige en random driehoekslattices, beiden zowel met als zonder een korrelstructuur. Door dezelfde korrelstructuur en lattice afmetingen toe te passen voor alle te modelleren proefstukafmetingen, is de invloed van variërende materiaalstructuur op schaaleffect in de simulaties uitgesloten. Uit de simulaties volgde dat het optredende schaaleffect in sterke mate beinvloed wordt door de mogelijkheid tot herverdeling van spanningen, alsmede door de excentriciteit van de uitwendige kracht.

Experimentele en numerieke resultaten zijn gecombineerd in Hoofdstuk 7. Ondanks het feit, dat het optredende schaaleffect voor de betonnen proefstukken die waren uitgehard onder laboratoriumcondities exact overeenkwam met voorspellingen volgens de klassieke sterktetheorie, bleek dit niet het geval te zijn voor de proefstukken die uitgehard waren in de verhardingskamer. Dit gegeven leidde tot de conclusie dat het schaaleffect, dat volgde uit de uitgevoerde experimenten, niet zuiver uit materiaal- oftewel statistisch schaaleffect bestond.

Om ook de invloed van additionele, contructieve, schaaleffecten in de analyse van de experimentele resultaten te betrekken, is een eenvoudig analytisch model afgeleid. Met behulp van dit model kan het effect van de proefstukvorm, excentriciteit van de uitwendige kracht en materiaalinhomogeniteit in rekening worden gebracht. Uit de resultaten van het model volgde dat in de uitgevoerde experimenten drie hoofdoorzaken aanwezig waren voor het optredende schaaleffect van de nominale sterkte. Voor de kleinste proefstukken was dit allereerst de (meso-)materiaalstructuur, gevolgd door materiaalschaaleffect volgens de klassieke sterktetheorie voor proefstukken groter dan het representatieve volume. Dit laatste type schaaleffect kon echter overheerst worden door constructieve schaaleffecten tengevolge van de aanwezigheid van spannings- en/of vervormingsgradiënten in de proefstukdoorsnede (randeffecten). De invloed van deze spannings- en/of vervormingsgradiënten kan daarom niet buiten beschouwing gelaten worden in de analyse van experimentele schaaleffectresultaten.

Zowel uit de experimenten als uit simulaties volgde dat de verhouding tussen de proefstukafmeting en de materiaalstructuur gebonden is aan een minimale waarde. Wordt deze waarde onderschreden, dan heeft dit een grote spreiding van de resultaten tot gevolg. Deze waarneming impliceert daarom dat discussies over een asymptoot van de sterkte voor zeer kleine proefstukafmetingen geen praktische betekenis hebben.

Curriculum vitae

Naam	Marcel René Antoine van Vliet
15 september 1969	geboren te Maastricht
1988	Atheneum B diploma, Stedelijk Lyceum te Maastricht
1994	Diploma van civiel ingenieur, TU Delft, Faculteit der Civiele Techniek en Geowetenschappen, vakgroep Mechanica & Constructies, afdeling Betonconstructies
1994–1998	Assistent in opleiding, TU Delft, Faculteit der Civiele Techniek en Geowetenschappen, vakgroep Mechanica & Constructies, afdeling Betonconstructies
1998–1999	Toegevoegd onderzoeker, TU Delft, Faculteit der Civiele Techniek en Geowetenschappen, afdeling Mechanica Materialen en Constructies, sectie Constructiemechanica
1999–heden	Werkzaam bij TNO Bouw, divisie Constructies, afdeling Beton en Metselwerk